Atom-light couplers with one, two and ten billion atoms

Daniel Higginbottom

A thesis submitted for the degree of
Doctor of Philosophy of The Australian National University

Advisors: Prof. Ping Koy Lam, Prof. Ben Buchler and Prof. Rainer
Blatt

Department of Quantum Science

March 2018

This thesis is an account of research undertaken between September 2012 and March 2018 at The Department of Quantum Science, Research School of Physics, Faculty of Science, The Australian National University, Canberra, Australia and the Institut für Experimentalphysik, Leopold-Franzens-Universität Innsbruck, Innsbruck, Austria. Except where acknowledged in the customary manner, the material presented in this thesis is, to the best of my knowledge, original and has not been submitted in whole or part for a degree in any university.

Daniel Higginbottom
29 March 2018

Acknowledgements

It has been my pleasure to carry out the work of this thesis across two institutions, and with the help of two fantastic teams. For that reason I owe thanks to a great many people, without whom none of this would have been possible. If I have forgotten anyone—and I hope I haven't—please trust that the problem isn't a deficit of gratitude, but a surplus of debt.

I would first like to thank my supervisors, Prof. Ping Koy Lam, Prof. Ben Buchler and Prof. Rainer Blatt for their support, assistance and guidance. They have nurtured incredible research groups at their respective universities, and I have learned so much from their laboratory experience, scientific knowledge and perspectives on the field of quantum technology. In particular, I would like to thank them for allowing me the flexibility to pursue my research interests through the course of this PhD. It was Ben that first inspired me to pursue quantum physics, and for that too I am very grateful.

I would also like to offer a special thanks to two people in particular, Geoff Campbell and Gabriel Araneda. Geoff has been integral to the work of this thesis from beginning to end, a supervisor in all but name. Indeed, if Geoff hadn't glibly promised to lathe sub-lambda hemispheres for Rainer 'in a day' then this thesis would have a thoroughly different form. It has been my great pleasure to work with Gabriel too, whose knowledge and talent have been invaluable, and whose good company relieved the monotonous hours in a darkened lab.

At the ANU I worked alongside many wonderful students and researchers. It was a delight to work with Jiao Geng on the EIT and dual-rail GEM experiments, even when we were up all night baking-out vacuum chambers. Thanks to Nick Robins for his advice and assistance with all things MOT. Mahdi Hosseini has been an inspiration, and first proposed the dual-rail GEM. Thanks to Young-Wook Cho, who brought so much expertise to our experiments. It was also a great pleasure to work on the theory of stationary light with Jesse Everett, although the sheer number of ideas Jesse has can prove distracting. Thanks to Michael Hush for illuminating discussions about symmetry. Thanks to Pierre Vernaz-Gris for company, help and support, I wish we had been able to work together more!

I couldn't have hoped for a better second home than the quantum optics group in Innsbruck. A big thank you to Lukas Slodička and Gabriel Hétet, who welcomed me to Innsbruck and first introduced me to the wonderful worlds of trapped ions and rodelling. Markus Hennrich was a great help preparing the single-photon source manuscript. Thanks also to Yves Colombe for his guidance and attention to detail, and for first proposing to shape an emitter mode by near-hemispherical mirror. Working with Yves has been an education. Thanks to Muir Kumph for his help designing ion traps, to Ben Lanyon for his frequent advice and assistance, to Christian Roos (who always knows the answer) and to Tracy Northup for sharing her expertise in quantum networks. In the lab I relied at one stage or another on the help and good humour of Esteban Martinez, Kirill Lakhman-skiy, Martin van Mourik, Thomas Monz, Ben Ames, Regina Lechner, Bernardo Casabone and many others. Thank you everyone for the opportunity to work at your incredible

Abstract

Devices that harness the surprising properties of quantum systems at scale hold the possibility of revolutionary advances in information technology. Algorithms for quantum computers can take advantage of quantum parallelism to solve problems that are intractable with classical hardware, including prime factorization and simulating chemical processes. A quantum communication network that carries qubits instead of bits can leverage the irreversibility of projective measurement to guarantee secure communication. Because quantum states are fragile, building such devices requires exquisite control over many isolated quantum systems. One of the most critical capabilities is the interaction of stationary and flying qubits.

In this thesis we consider how to engineer atom-light interactions as an interface for networked quantum systems. Quantum atom-light couplers require the efficient and reversible interaction of atomic and optical qubits, but the natural interaction of atoms and photons is weak. It is this very lack of interaction between light and its environment that makes light such an excellent carrier of quantum information. There are three promising strategies for stronger coherent atom-light interactions. First, the light field may be confined to a cavity so that it interacts with the atom over a longer time. Second, the light field may be focussed to a small spot with high aperture optics and matched to the natural atomic radiation pattern. Third, we may pass the light field through an ensemble of many atoms and store the qubit in a distributed state. In practice, atom-light couplers employ some combination of all three strategies. We will focus our research on the second two approaches: first by coupling one and two trapped ions with high aperture optics, and then operating a quantum optical memory with an ensemble of ≈ 10 billion neutral atoms.

Atoms that have been ionized and trapped in a common electromagnetic potential are an advanced few-qubit computation platform. Qubit states are associated with an electronic excitation at each atom, controlled coherently with lasers, and made to interact in two (or many) qubit gates by mutual Coulomb repulsion. One path to quantum advantage with ion-trap quantum processors is to scale small qubit registers by distributing entanglement with photonic interconnects. We consider the feasible efficiency of free-space atom-light couplers for atomic dipole transitions, and derive the atomic image by common free-space couplers.

We couple a trapped-ion register with high-aperture lenses and operate a single trapped ion as a photon source. We model the dynamic character of the source and show spin-orbit coupling in the single-photon spatial mode. Although the total collection efficiency is only $\eta \approx 0.01$, the source has exceptional photon-number purity $\mathbb{A} = (1.9 \pm 0.2) \times 10^{-3}$ such that the higher-order quantum nature of the field persists even after most of the field has been discarded. We derive an efficient quantum non-Gaussian witness and surpass it, the first such demonstration for a trapped-atom single-photon source. We entangle two trapped atoms by single-photon detection, and observe an interference pattern in the spatial mode of the bipartite state. Constructive interference between the entangled components enhances the emission probability by up to 29%, an example of collective enhancement by a two-atom ensemble.

The efficiency of free-space atom-light couplers is limited by our capability to engineer high-precision, high-aperture optics. We fabricate ultra-precise hemispheric mirrors with numerical aperture 0.996 by single point diamond turning. The mirrors are amongst the smoothest hemispheric surfaces ever manufactured with root-mean-square (RMS) errors consistently below 25 nm. The smoothest of our mirrors has a RMS error of 14 nm and peak-to-valley error of 88 nm. A mirror with this surface is capable of suppressing or enhancing the spontaneous emission of an atom into free space by 96% in a proposed quantum electrodynamics experiment. We show how these mirrors, with a simple modification, can shape the spatial mode of a trapped atom by similar vacuum-mode engineering. We derive a near-hemispheric mirror coupling scheme that should be 72% efficient with mirrors as precise as ours. We design an ion trap for use with such high-aperture optics.

With careful conditioning and control, ensembles of many atoms can be made to store and release photonic qubits on demand. Such optical quantum memories leverage the collective interaction of a light field with many billions of atoms to achieve storage and recall efficiencies approaching unity. We show how stationary light fields for photonic phase gates can be generated in optically deep ensembles, an effect which has since been observed.

We implement the gradient echo memory (GEM) scheme in an ultra-high optical depth cold-atom ensemble. The performance of a practical quantum memory is contingent on the chosen qubit encoding. We extend the GEM protocol to allow the simultaneous storage of frequency separated signals and demonstrate that this 'dual-rail' memory is suitable for high-fidelity frequency qubits. Dual-rail signals are recalled with 35% efficiency, 82% interference fringe visibility and 6° phase stability. We describe how the fidelity of the scheme is limited by frequency-dependent polarization rotation and how this may be addressed in an improved configuration. Finally, we demonstrate single-rail storage by GEM with 87% efficiency and 1 ms memory lifetime. Our memory surpasses the no-cloning limit for up to 600 μs of storage, out-performing an optical fibre delay line by a factor of six. This is the first quantum memory to beat this important benchmark.

Contents

List of Figures

List of Tables

Publications

Some of the work in this thesis has appeared in the following publications.

Publications covered in this thesis

1. D. B. Higginbottom, J. Geng, G. T. Campbell, M. Hosseini, M. T. Cao, B. M. Sparkes, J. Bernu, N. P. Robins, P. K. Lam, and B. C. Buchler. Dual-rail optical gradient echo memory, *Opt. Express* **23**, 24937 (2015).

2. D. B. Higginbottom, L. Slodička, G. Araneda, L. Lachman, R. Filip, M. Hennrich, and R. Blatt. Pure single photons from a trapped atom source *New J. Phys.* **18**, 93038 (2016).

3. Y.-W. Cho, G. T. Campbell, J. L. Everett, J. Bernu, D. B. Higginbottom, M. T. Cao, J. Geng, N. P. Robins, P. K. Lam, and B. C. Buchler. Highly efficient and long-lived optical quantum memory with cold atoms *Optica* **3**, 100 (2016).

4. D. B. Higginbottom, G. T. Campbell, G. Araneda, F. Fang, Y. Colombe, B. C. Buchler, and P. K. Lam. Fabrication of ultrahigh-precision hemispherical mirrors for quantum-optics applications *Sci. Rep.* **8**, 221 (2018).

5. G. Araneda, D. B. Higginbottom, L. Slodička, Y. Colombe and R. Blatt. Interference of single photons emitted by entangled atoms in free space, *Phys. Rev. Lett.* **120**, 193603 (2018)

6. G. Araneda, S. Walser, Y. Colombe, D. B. Higginbottom, J. Volz, R. Blatt, and A. Rauschenbeutel. Wavelength-scale errors in optical localization due to spin-orbit coupling of light, *Nat. Phys.* (2018).

Publications authored during my PhD not covered in this thesis

1. O. Pinel, M. Hosseini, B. M. Sparkes, J. L. Everett, D. B. Higginbottom, G. T. Campbell, P. K. Lam, and B. C. Buchler. Gradient echo quantum memory in warm atomic vapor *J. Vis. Exp.* **e50552** (2013).

2. J. Geng, G. T. Campbell, J. Bernu, D. B. Higginbottom, B. M. Sparkes, S. M. Assad, W. P. Zhang, N. P. Robins, P. K. Lam, and B. C. Buchler. Electromagnetically induced transparency and four-wave mixing in a cold atomic ensemble with large optical depth *New J. Phys.* **16**, 113053 (2014).

3. J. L. Everett, G. T. Campbell, Y.-W. Cho, P. Vernaz-Gris, D. B. Higginbottom, O. Pinel, N. P. Robins, P. K. Lam, and B. C. Buchler. Dynamical observations of self-stabilizing stationary light *Nat. Phys.* **13** 68-73 (2017).

Introduction and motivation

...nature isn't classical, dammit, and if you want to make a simulation of nature, you'd better make it quantum mechanical, and by golly it's a wonderful problem, because it doesn't look so easy.

– Richard Feynman, *Simulating physics with computers* (1981)

If computers that you build are quantum / Then spies of all nations will want 'em. / Our codes will all fail, and they'll read our email, / Till we've crypto that's quantum, and daunt em'.

– Jennifer and Peter Shor, *Science News poetry competition* (1996)

Devices that harness the surprising properties of quantum systems at scale hold the possibility of revolutionary advances in information technology. Quantum bits, or 'qubits' can be prepared in a superposition of classical bit values 0 and 1. Multiple qubits may exist in a combined superposition state that cannot be divided into separate, independent local states. We call this type of correlated superposition an 'entangled' state. Algorithms for quantum computers have the ability to solve problems that are intractable with classical hardware, including prime factorization and simulating chemical processes. Furthermore, a quantum communication network that carries qubits instead of bits can take advantage of superposition states to guarantee secure communication. However, because superposition states are fragile and 'decohere' under interaction with the environment, building such devices requires exquisite control over many isolated quantum systems. One of the most critical capabilities is the efficient interaction of stationary atomic and flying optical qubits.

In this chapter we make a broad survey from high above the field of quantum information. This survey has a dual purpose: to provide much needed context and motivation for a general audience, and to offer an informed perspective on the field for researchers. Such perspective seems timely given the surge of private investment and public interest in quantum information technology. With one eye to each of these tasks we describe the separate but related goals of quantum computation and communication, discuss the physics and engineering challenges that must be overcome to achieve these goals, and map a course to these twin destinations in light of recent advances—before finally gliding gracefully back to ground level to outline the work of this thesis and its role in the wider field. The background provided in this chapter is necessarily brief, but it is hoped that the references included provide a comprehensive introduction to the field of quantum information and the need for efficient and coherent atom-light couplers.

1.1 Superposition, entanglement and you

The classical information technology that is now ubiquitous operates by the storage and manipulation of discrete, binary units of information: the bit, which can be in either of two states that we choose to label 0 and 1. However, it is a property of quantum mechanics that even binary systems with only two measurable configurations can exist along a continuous spectrum of possible 'superpositions'. That is to say, a quantum bit (or qubit) can be in any combination of 0 and 1 simultaneously [10]. When the superposed qubit is measured, it will be found in either state 0 or 1 with probabilities determined by the nature of the initial superposition. Extending the principle of superposition to systems of multiple particles, a truly curious phenomena emerges.

Superposition states of multiple particles can be correlated in ways that are simply impossible within the framework of classical physics. Measurements made on one qubit depend on the outcomes of measurements on the second qubit. Two qubits, no matter how far apart, may be in a combined state such that neither particle can be described completely in isolation, and we say they are 'entangled'. Entanglement is so counter to our intuition of the natural world that Einstein, late in his life, was moved to repurpose a three hundred-year-old criticism of Newtonian gravity and describe entanglement derisively as "spukhafte Fernwirkung"—spooky action at a distance [11]. Indeed, any physical theory that preserves both the locality and realism of classical mechanics is inconsistent with not only quantum mechanics [12], but also with the outcomes of experiments [13–16]. Entanglement, and related quantum correlations [17], are not only startling phenomena, but also potentially very useful.

1.2 Quantum algorithms

An N-qubit register may be in a simultaneous superposition of all 2^N classical configurations. A quantum computer operating on such a register can take advantage of this quantum parallelism to perform calculations that are classically intractable [18]. The quantum circuit, in which qubits interact by a series of one and two qubit gates including a complete set of single-qubit rotations and the controlled-not gate, is a universal quantum computer equivalent to the quantum Turing machine [19]. There is a known class of problems that can be solved in polynomial time on any universal quantum computer, but require more than polynomial time on a classical computer [20]. This provides an information-theoretic guarantee of superiority for a sufficiently large universal quantum computer. Today there is a veritable zoo [21] of tasks for such a quantum computer, including checking for balanced functions [18], searching lists [22] and solving linear systems of equations[1] [23].

Peter Shor proposed one of the earliest and most startling algorithms for a universal quantum computer, the factorization of large numbers [24]. This application is startling because easily factoring large numbers would fatally undermine the most common encryption algorithms in use today, but the hardware required is considerable. Factoring numbers beyond the capabilities of existing supercomputers requires a quantum computer with qubits $\times$ gates $= 10^{15}$ [25]. Furthermore, performing such a task on proposed fault-tolerant circuit architectures requires millions of physical qubits [25]. Existing quantum

---

[1]It's noteworthy that even after decades of theoretical research, entirely new algorithms with quantum speed-up are being proposed. It inspires hope that developing small-scale quantum computers will stimulate the discovery of even more novel applications.

computers are a long way from out-factorizing classical supercomputers, but there are applications that are within sight of existing devices.

The most immediate use for quantum computers may be closer to their first identified application [26], solving outstanding problems in the chemical reactions of large molecules. Problems in quantum chemistry are notoriously hard for exactly the same reason that quantum computers are powerful, they involve many interacting quantum systems. Exactly calculating the ground state of molecules with more than ten electrons is already beyond today's supercomputers. Efficiently simulating a complicated quantum process requires a quantum device [27]. Variational quantum eigensolvers are a hybrid quantum-classical approach to elucidating complex chemical reaction mechanisms on noisy, intermediate scale quantum computers [28, 29]. Enormously significant problems including biological nitrogen fixation are within the capability of a 1000-qubit quantum computer, even without fault-tolerant architecture [30].

A key landmark in the development of quantum computers will be 'quantum advantage'[2], the demonstration of a quantum computation that outperforms the best classical hardware (even if the computation itself is not useful). To do so should not require outrageous resources. The possible configurations of a 50-qubit register are already beyond the storage capacity of existing supercomputers.

There are two popular alternatives to the quantum circuit architecture: photonic computation and quantum annealing. Photonic quantum computing is an alternative measurement-based universal architecture that we discuss in Sec. 1.4.4. Quantum annealing [31] is a non-universal computing architecture that has already been commercialized [32]. Although quantum annealing may provide an advantage over classical computers for specific classes of problems, identifying suitable problems for existing annealers has proved evasive [33, 34].

1.3   Decoherence

The challenge facing any quantum information device is that decoherence, the randomization of a quantum state by interaction with its environment, limits the useful lifetime of qubits. Decoherence turns the quantum 'and' to a classical 'or'—the qubit to merely a bit—and is the reason that superposition and entanglement are typically (but not only) seen with small numbers of well-isolated particles. Decoherence is the problem that quantum device engineers must overcome, and the coherence time is the critical metric for comparing physical implementations of qubits as quantum information platforms. The more robust the physical qubit, the more operations can be performed in sequence during it's lifetime.

It is now possible to keep some physical qubits, such as qubits in the electronic state of trapped ions as we investigate in Part II, well insulated from their environment on timescales long enough for a computation. Moreover, control engineering techniques for stabilizing qubits against decoherence can improve the passive robustness of quantum systems [35–37]. For systems like these, imperfect gate operations are the critical source of decoherence that must be considered. The theory of quantum error correction is directed at combating the errors most common in gates. Gates beyond the error-correction threshold can be concatenated in a fault-tolerant calculation of any required length [38, 39].

---

[2]Although the rather unfortunate term 'quantum supremacy' is more common in the literature, we prefer 'quantum advantage' in this thesis.

1.4   Quantum computers

The approach most research takes to building a quantum computer described above begins with building and controlling small numbers of material qubits with sufficient gate fidelity for fault-tolerant universal quantum computing, before finding a means to scale the number of qubits to out-perform classical devices. The simultaneous requirements that qubits are isolated from their environment but also controllable restrict potential quantum hardware to a handful of systems, ranging from trapped atoms [40–43], to photons [44, 45], to novel engineered qubits including superconductors [46–48] and spin donors in silicon [49–51] or diamond [52].

1.4.1   Trapped-atom computers

The most natural stationary qubit is an individual atom. Atoms are standards, and can be isolated in a vacuum so that they do not interact with background gases or surfaces. At ultra-high vacuum (UHV) pressures background collisions occur $\approx$1/hour. With cryogenically-cooled vacuum chambers these collisions can be eliminated completely. Trapped atoms are well isolated mechanical systems, a very good approximation of the ideal harmonic oscillator, and may be laser-cooled to low temperatures, or even the motional ground-state [53].

The valence electron of hydrogen-like atoms may have Zeeman or hyperfine split ground states, and metastable dipole-forbidden excited states. These narrow-linewidth transitions have long coherence times suitable for quantum information. The state of a qubit encoded into an atom's electronic configuration can be controlled coherently with narrow-linewidth laser fields.

Ion traps, which hold charged atoms in oscillating electric fields, are a well developed few-qubit computation platform. In a linear 'Paul' trap of the sort we use in Part II a hundred atoms may be confined in a one-dimensional string along the axis of an harmonic potential. Macroscopic ion traps can have deep potentials, holding the same atoms for months. The alkaline earth ions (Be^+, Mg^+, Ca^+, Sr^+ and Ba^+) along with some transition metals (Yb^+) have strong closed optical transitions for cooling, preparing and reading the state of the ion.

The mutual Coulomb repulsion between cold ions in the same trap provides a means of coupling qubits by their shared, quantized motional modes. In contrast to the first trapped-ion qubit gates proposed by Cirac and Zoller [54], recent trapped-ion gates do not require ground-state cooling [55]. Trapped-ion two-qubit gates can be performed with fidelities over 99% [56] at a rate of up to 100 kHz, currently limited by the period of the ions oscillating in the trap potential. An ion-trap quantum computer of 11 qubits has realized the Shor algorithm to factor the number 15 [42].

High fidelity operations have not been performed on larger ion chains because the gate time scales with the square root of the number of ions. Controlling crystals of more than 100 ions is considered to be infeasible [57]. Nevertheless powerful, high repetition-rate pulsed lasers should provide a means of increasing the gate speed to GHz [58] at which point even a trapped-ion processor of 100 qubits can outperform existing classical computers at certain tasks [59]. Prospects for further scaling trapped-ion processors include propagating entanglement between separate registers by shuttling chosen ions between adjacent traps [60] or optically coupling qubits in separate registers with optical gates [61].

1.4.2   Optically coupled qubits

One path to scaling ion-trap quantum processors to a useful size is the use of photonic interconnects for distributing entanglement between smaller registers. This requires an efficient interface between the atoms in a trapped-atom processor and optical qubits, ideally travelling in an optical fibre. If optical and stationary qubits can be coupled efficiently, then photon-atom gates can be a tool for generating and distributing quantum information. With entanglement purification protocols even an imperfect optical link can distribute a high degree of entanglement. This capability would go some way towards extending the size of linear ion trap quantum computers into the realm of quantum advantage [62].

1.4.3   Artificial atoms

We can identify a class of solid-state qubits that mimic the electronic properties of atoms, of which quantum dots (QDs) and vacancy centres are the most promising examples for quantum information. Like atoms, these systems have confined electrons restricted to discrete energy levels that may be configured and manipulated by optical fields. The coherence time of these 'artificial atom' qubits is lower than the coherence time of atomic qubits in a vacuum. Unlike clean atomic qubits, artificial atoms are embedded in a host material which decoheres the qubit by interaction with the bulk. However, artificial atoms may be designed with more convenient or manipulatable energy levels (for example, the host material can be fabricated with electrical contacts for tuning the field around the qubit) and, like solid state atomic systems, artificial qubits have an obvious path towards scalability.

1.4.4   Photonic computers

Photonic quantum computing provides for an alternative computing paradigm to the atom-based circuit processor. The photonic quantum computer replaces the deterministic gates with probabilistic, measurement-based operations on photonic cluster states produced passively by beam-splitter interference [44, 45]. There is an enormous overhead associated with this approach because it requires hundreds of photons interacting by probabilistic linear optical gates to produce a single computational qubit equivalent. Furthermore, this architecture requires optical switches and phase shifters, and the losses and errors caused by these active components are not negligible.

However, in contrast to the matter-based quantum computer architecture described above, the architecture of a photonic quantum computer—being a precise, lossless, multiphoton interferometer—is relatively easy to manufacture on-chip and scale. Today photonic integrated circuits are being built with thousands of components on chips 100s of microns across, but recent advances indicate that much more complicated circuits can be built with existing fabrication techniques [63]. Hybrid systems combining measurement-based photonic computing and atomic circuit operations may be able to leverage and combine the advantages of each physical system [64]. The development of atom-light interfaces between the two systems is critical for this approach.

1.5   Quantum networks

Flying photonic qubits may be a challenging platform for quantum computing, but they are the essential component of quantum communication networks. Today's global com-

munication network operates by the distribution of bits encoded in light fields that travel through optical fibres. Where necessary, we secure this communication by encryption. However, the only way to guarantee unconditional cryptographic security between two parties, we call them Alice and Bob, is to ensure they start with identical copies of a secret key to use as a one-time pad [65]. Public-key cryptography relies on the assumed difficulty of some asymmetric computation, such as factorization, and is vulnerable to attack by a an eavesdropper (Eve) with sufficient computational power.

Quantum cryptography leverages the unique properties of quantum systems to guarantee cryptographic security by quantum key distribution (QKD). Measuring a quantum system, as an eavesdropper must, irreversibly disturbs the system. Any information that Eve might gain by intercepting a stream of qubits between Alice and Bob will measurably distort the shared state. Alice and Bob can establish a one-time pad with any required level of security by sharing a stream of qubits, some proportion of which will be used to check for eavesdroppers. Alice and Bob can distil a secure key by classical error correction and privacy amplification so long as the error rate on their communication link is below a certain threshold [66].

1.5.1   Quantum key distribution

The first method of QKD to be proposed, the famous BB84 protocol [67], is an example of a discrete-variable QKD scheme (DV-QKD). DV-QKD schemes utilize qubits encoded on single photons to generate secure keys between Alice and Bob. The qubits may be encoded on any photonic degree of freedom with two non-orthogonal bases, but qubits are most commonly encoded in the polarization, time bins or orbital angular momentum.

In any network link there is some degree of signal attenuation and photon loss. In principle, noiseless QKD schemes can handle any attenuation, but the presence of noise limits the tolerable losses and sets an upper limit on the range of secure communication. Noise sources can include crosstalk with bright signals and detector errors. For example, dark counts are an unavoidable source of noise present in every realistic single-photon detector.

Single-photon sources are required for QKD, much as they are required for photonic quantum computation, because multi-photon pulses are not only a source of noise, they are also vulnerable to photon-number splitting attacks by Eve [68]. The amount of common secret key that can be distilled from each bit of raw key by error correction and privacy amplification is called the 'secret fraction'. Given a particular QKD scheme and well characterized single-photon sources the secret fraction can be bounded for known attacks, guaranteeing a certain rate of secure communication.

1.6   Single photon sources

Photon sources are devices for producing a single photon (and never more than one photon) on demand, and they have various applications across the field of quantum information. Prepare-and-measure DV-QKD schemes like BB84 leverage the indivisibility of single photons to guarantee security. Similarly, photonic quantum computers require sources of pure photons that can be entangled to produce cluster states for photonic computing. Moreover, any atom-light interface for coupling qubits between registers of trapped-atom quantum computers is necessarily a type of single photon source. The operation of a single-photon source is an essential step in efficient coupling of qubits between atoms and light. In

Chap. 5 we explore existing single-photon sources and quantum atom-light networks, and compare their capabilities to performance benchmarks for QKD and photonic quantum computing.

1.7   Quantum repeaters and memories

Signals travelling through telecommunications fibre are attenuated by at least 0.2 dB/km [69], and this limits the range of direct, telecommunications fibre-based QKD to less than 400 km [70]. Where classical signals are simply amplified periodically to travel long distances, quantum signals cannot be amplified deterministically without decoherence, a consequence of the no-cloning theorem. One dramatic way of circumventing this problem is to use satellite-based QKD, as demonstrated recently in Ref. [71].

We need not give up on optical fibre quantum networks completely; quantum repeaters have been proposed to create long-distance entanglement by entanglement swapping between nodes along a fibre network [72]. Qubits can be teleported between the remote entangled pair, or the entanglement itself can be used to generate a cryptographic key [73, 74]. An integral component of these repeaters is a quantum memory for storing and retrieving quantum states of light on demand. Like single-photon sources, quantum memories require efficient atom-light interactions. In Chap. 14 we take a close look the capabilities of existing quantum memories, and what more is required to build a useful quantum repeater.

1.8   The structure of this thesis

In this thesis we consider how the atom-light interaction can be engineered to provide an interface for networked quantum systems. Such an interface requires the efficient and reversible interaction of atomic and optical qubits, but the natural interaction of atoms and photons is weak. It is this very lack of interaction between light and its environment that makes light such an excellent carrier of quantum information.

There are three promising strategies for stronger atom-light interactions, shown schematically in Fig. 1.1. First, the light field may be confined to a high-finesse cavity so that it interacts with the atom over a longer time. Second, the light field may be focussed to a small spot with high aperture optics and matched to the natural atomic radiation pattern. Third, we may pass the light field through an ensemble of many atoms and store the qubit in a distributed state. In this thesis we explore experimental and theoretical approaches to efficient atom-light coupling using first free-space optics with one or two atoms and then atom ensembles with about ten billion atoms (strategies (b) and (c) in Fig. 1.1).

The thesis is divided into three parts, in Part I we review the necessary physics for understanding the interaction of quantum light fields and atomic qubits. In Chap. 4 we introduce the optical field of an atomic dipole, and the image of this dipole by a number of common free-space atom-light couplers.

In Part II we consider a free-space atom-light coupler for networking one or two trapped ions in a qubit register. In Chap. 7 we demonstrate a trapped-ion single-photon source coupled by high aperture lenses. We model the dynamic character of the source and show manifestation of spin-orbit coupling in the single-photon spatial mode. Although the total coupling efficiency is low, the source has exceptional photon-number purity and the higher-order quantum nature of the field persists even after most of it has been dis-
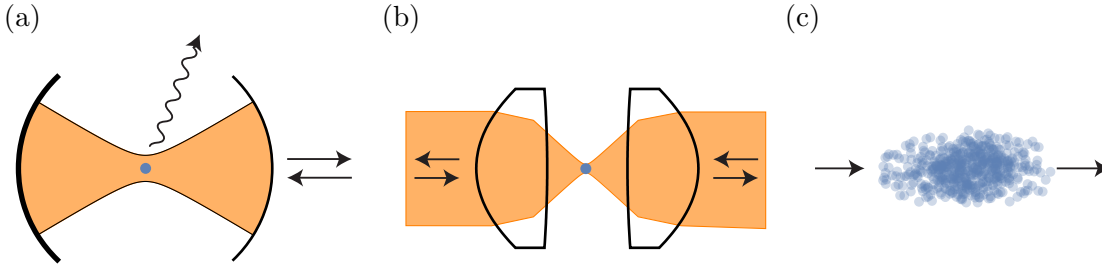
Figure 1.1: The interaction between photons and atoms is weak, but there are three broad strategies for enhancing the interaction. (a) Resonators increase the atom-light interaction time by holding the light field in a resonator mode. (b) Focussing the optical field into a small area increases the field per photon. (c) The collective interaction strength between a light field and an ensemble of atoms can be large. Most implementations involve some combination of these approaches. For example, resonators can both confine the photon mode and increase the interaction time, and tight focussing into an atomic ensemble increases the collective interaction strength.

carded. In Chap. 8 we derive a quantum non-Gaussian witness and measure violation of this witness, the first such demonstration for a trapped-atom single-photon source. The same apparatus can be used to entangle two trapped ions by single-photon detection. In Chap. 9 we observe spatial interference in single-photon emission from an entangled state. Interference-enhanced emission from the collective excitation of this two-atom ensemble is the first step towards coherent ensemble-light interactions with many atoms.

The availability of high-precision, high-aperture optics is one of the limits for efficient free-space atom-light coupling. In Chap. 10 we fabricate ultra-precise hemispheric mirrors for experiments in quantum electrodynamics. We show that a mirror with this surface is capable of suppressing or enhancing the spontaneous emission of an atom into free space by 96%, and that a variation of these mirrors can be used to efficiently couple the atomic dipole mode to a fibre with only low aperture optics. In Chap. 11 we design an ion trap for use in combination with such mirrors.

In Part III we trap and cool approximately 10 billion neutral atoms to demonstrate the storage and retrieval of light in an atomic ensemble quantum memory. We show how such ensemble quantum memories are able to leverage the simultaneous interaction of light with many billions of atoms to achieve efficiencies approaching unity in Chap. 13. We demonstrate a gradient echo memory (GEM) in an ultra-high optical depth cold-atom ensemble that equals the best demonstrated quantum memory efficiency. In Chap. 16 we extend the GEM protocol to allow the simultaneous storage of frequency separated signals and demonstrate that this 'dual-rail' memory is suitable for high-fidelity frequency qubits. Finally, in Chap. 17 we increase the coherence time of our memory to surpass the performance of an optical fibre delay line in the no-cloning regime.

Given that this thesis will be a little on the hefty side by the time we have completed the ambitious agenda above, code samples and other supporting derivations that might normally be included as a printed Appendix will instead be made available as a digital appendix at the following GitHub repository: https://github.com/dhigginbottom/thesis-appendices.git. The appendices at that address include Mathematica scripts for simulating dipole images, deriving the wavefronts of an elliptical dipole field, Python scripts for simulating the eight-level atomic Bloch dynamics, and XMDS2 scripts for simulating GEM.

Bibliography - Introduction and motivation

10. C. Ferrie, and Whurley, *Quantum computing for babies* (Sourcebooks Jabberwocky, 2018).

11. A. Einstein, M. Born, and H. Born, *The Born-Einstein letters; correspondence between Albert Einstein and Max and Hedwig Born from 1916 to 1955.* (Walker, New York, 1971).

12. J. S. Bell, On the Einstein Podolsky Rosen paradox, *Physics* **1**, 195–290 (1964).

13. A. Aspect, J. Dalibard, and G. Roger, Experimental test of Bell's inequalities using time-varying analyzers, *Phys. Rev. Lett.* **49**, 1804–1807 (1982).

14. B. Henson, et al., Loophole-free Bell inequality violation using electron spins separated by 1.3 kilometres, *Nature* **526**, 682–686 (2015).

15. L. K. Shalm, et al., Strong loophole-free test of local realism, *Phys. Rev. Lett.* **115**, 250402 (2015).

16. M. Giustina, et al., Significant loophole-free test of Bell's theorem with entangled photons, *Phys. Rev. Lett.* **115**, 250401 (2015).

17. H. Ollivier, and W. H. Zurek, Quantum discord: A measure of the quantumness of correlations, *Phys. Rev. Lett.* **88**, 017901 (2001).

18. D. Deutsch, Quantum theory, the Church-Turing principle and the universal quantum computer, *Proc. Royal Soc. A* **400**, 97–117 (1985).

19. A. Chi-Chih Yao, Quantum circuit complexity, in *Proceedings of the IEEE 34th Annual Foundations of Computer Science* (1993), pp. 352–361.

20. S. Aaronson, *Quantum computing since Democritus* (Cambridge University Press, 2013).

21. S. Jordan, *Quantum algorithm zoo*, 2018.

22. L. K. Grover, A fast quantum mechanical algorithm for database search, *Proceedings of the twenty-eighth annual ACM symposium on theory of computing*, 212–219 (1996).

23. A. W. Harrow, A. Hassidim, and S. Lloyd, Quantum algorithm for linear systems of equations, *Phys. Rev. Lett.* **103**, 150502 (2009).

24. P. Shor, Algorithms for quantum computation: discrete logarithms and factoring, in *Proceedings of the {IEEE} 35th Annual Foundations of Computer Science* (1994), pp. 124–134.

25. J. O'Gorman, and E. T. Campbell, Quantum computation with realistic magic-state factories, *Phys. Rev. A* **95**, 032338 (2017).

26. R. P. Feynman, Simulating physics with computers, *Int. J. Theor. Phys.* **21**, 467–488 (1982).

27. S. Lloyd, Universal quantum simulators, *Science* **273**, 1073–1078 (1996).

28. A. Kandala, et al., Hardware-efficient variational quantum eigensolver for small molecules and quantum magnets, *Nature* **549**, 242–246 (2017).

29. J. Preskill, Quantum computing in the NISQ era and beyond, 1–22 (2018).

30. M. Reiher, et al., Elucidating reaction mechanisms on quantum computers, *Proc. Natl. Acad. Sci.* **114**, 7555–7560 (2017).

31. S. Boixo, et al., Evidence for quantum annealing with more than one hundred qubits, *Nat. Phys.* **10**, 218–224 (2014).

32. E. Gibney, D-Wave upgrade: How scientists are using the world's most controversial quantum computer, *Nature* **541**, 447–448 (2017).

33. J. Job, and D. Lidar, Test-driving 1000 qubits, *Quantum Sci. Technol.* **3**, 030501 (2018).

34. H. G. Katzgraber, Viewing vanilla quantum annealing through spin glasses, *Quantum Sci. Technol.* **3**, 030505 (2018).

35. J. W. Clark, D. G. Lucarelli, and T.-J. Tarn, Control of quantum systems, *Int. J. Mod. Phys. B* **17**, 5397–5411 (2003).

36. H. M. Wiseman, and A. C. Doherty, Optimal unravellings for feedback control in linear quantum systems, *Phys. Rev. Lett.* **94**, 070405 (2005).

37. H. I. Nurdin, M. R. James, and I. R. Petersen, Coherent quantum LQG control, *Automatica* **45**, 1837–1846 (2009).

38. D. Aharonov, and M. Ben-Or, Fault-tolerant quantum computation with constant error, in *Proceedings of the twenty-ninth annual ACM symposium on Theory of computing* (1997), pp. 176–188.

39. J. Preskill, Fault-tolerant quantum computation, *arXiv:quant-ph/9712048v1* (1997).

40. T. P. Harty, et al., High-fidelity preparation, gates, memory, and readout of a trapped-ion quantum bit, *Phys. Rev. Lett.* **113**, 220501 (2014).

41. D. Nigg, et al., Quantum computations on a topologically encoded qubit, *Science* **345**, 302–305 (2014).

42. T. Monz, et al., Realization of a scalable Shor algorithm, *Science* **351** (2016).

43. S. Debnath, et al., Demonstration of a small programmable quantum computer with atomic qubits, *Nature* **536**, 63–66 (2016).

44. E. Knill, R. Laflamme, and G. J. Milburn, A scheme for efficient quantum computation with linear optics., *Nature* **409**, 46–52 (2001).

45. P. Kok, et al., Linear optical quantum computing with photonic qubits, *Rev. Mod. Phys.* **79**, 135–174 (2007).

46. J. M. Chow, et al., Universal quantum gate set approaching fault-tolerant thresholds with superconducting qubits, *Phys. Rev. Lett.* **109**, 060501 (2012).

47. J. Kelly, et al., State preservation by repetitive error detection in a superconducting quantum circuit, *Nature* **519**, 66–69 (2015).

48. Y. Wang, et al., 16-qubit IBM universal quantum computer can be fully entangled, *arXiv:1801.03782v2* (2018).

49. B. E. Kane, A silicon-based nuclear spin quantum computer, *Nature* **393**, 133–137 (1998).

50. M. Veldhorst, et al., A two-qubit logic gate in silicon, *Nature* **526**, 410–414 (2015).

51. M. Fuechsle, et al., A single-atom transistor, *Nat. Nanotechnol.* **7**, 242–246 (2012).

52. M. W. Doherty, et al., The nitrogen-vacancy colour centre in diamond, *Phys. Rep.* **528**, 1–45 (2013).

53. D. Leibfried, et al., Quantum dynamics of single trapped ions, *Rev. Mod. Phys.* **75**, 281–324 (2003).

54. J. I. Cirac, and P. Zoller, Quantum computations with cold trapped ions, *Phys. Rev. Lett.* **74**, 4091–4094 (1995).

55. A. Sørensen, and K. Mølmer, Quantum computation with ions in thermal motion, *Phys. Rev. Lett.* **82**, 1971–1974 (1999).

56. J. Benhelm, et al., Towards fault-tolerant quantum computing with trapped ions, *Nat. Phys.* **4**, 463–466 (2008).

57. C. Monroe, and J. Kim, Scaling the ion trap quantum processor, *Science* **339**, 1164–9 (2013).

58. J. J. García-Ripoll, P. Zoller, and J. I. Cirac, Speed optimized two-qubit gates with laser coherent control techniques for ion trap quantum computing, *Phys. Rev. Lett.* **91**, 157901 (2003).

59. R. L. Taylor, et al., A study on fast gates for large-scale quantum simulation with trapped ions, *Sci. Rep.* **7**, 46197 (2017).

60. D. Kielpinski, C. Monroe, and D. J. Wineland, Architecture for a large-scale ion-trap quantum computer, *Nature* **417**, 709–711 (2002).

61. I. L. Chuang, and D. Gottesman, Demonstrating the viability of universal quantum computation using teleportation and single-qubit operations, *Nature* **402**, 390–393 (1999).

62. A. Bermudez, et al., Assessing the progress of trapped-ion processors towards fault-tolerant quantum computation, *Phys. Rev. X* **7**, 041061 (2017).

63. I. M. Georgescu, S. Ashhab, and F. Nori, Quantum simulation, *Rev. Mod. Phys.* **86**, 153–185 (2014).

64. O. Mandel, et al., Controlled collisions for multi-particle entanglement of optically trapped atoms, *Nature* **425**, 937–940 (2003).

65. C. E. Shannon, Communication theory of secrecy systems, *Bell Labs Tech. J.* **28**, 657–715 (1949).

66. C. A. Fuchs, et al., Optimal eavesdropping in quantum cryptography . I. Information bound and optimal strategy, *Phys. Rev. A* **56**, 1163–1172 (1997).

67. C. H. Bennett, and G. Brassard, Quantum cryptography: Public key distribution and coin tossing, *Theor. Comput. Sci.* **175**, 8 (1984).

68. G. Brassard, et al., Limitations on practical quantum cryptography, *Phys. Rev. Lett.* **85**, 1330–1333 (2000).

69. G. P. Agrawal, *Optical fibers* (John Wiley & Sons, Inc., Hoboken, 2011).

70. H.-L. Yin, et al., Measurement-device-independent quantum key distribution over a 404 km optical fiber, *Phys. Rev. Lett.* **117**, 190501 (2016).

71. J.-G. Ren, et al., Satellite-to-ground quantum key distribution, *Nature* **549**, 43–47 (2017).

72. H.-J. Briegel, et al., Quantum repeaters: The role of imperfect local operations in quantum communication, *Phys. Rev. Lett.* **81**, 5932–5935 (1998).

73. A. K. Ekert, Quantum cryptography based on Bell's theorem, *Phys. Rev. Lett.* **67**, 661–663 (1991).

74. A. Acín, N. Gisin, and L. Masanes, From Bell's theorem to secure quantum key distribution, *Phys. Rev. Lett.* **97**, 120405 (2006).

Part I

Foundations

Quantum states of light

Wo viel Licht ist, ist starker Schatten.
  – Johann Wolfgang von Goethe, *Götz von Berlichingen* (1773)

The purpose of the experiments in this thesis is to explore means of preparing, manipulating and storing quantum states of light. To describe these experiments we require an understanding of the useful quantum states of light and the properties that distinguish them from classical fields as described by Maxwell's equations. In this chapter we introduce a mathematical description of the discrete nature of light, and the ubiquitous concept of an optical 'mode'. For this we rely on the seminal work of Refs. [75–78] which provide a more comprehensive discussion of these fundamental subjects than is feasible here.

A great deal of the work in this thesis will regard single-photon optical states, the most fundamental demonstration of the discrete nature of light. In this chapter we relate the photon-number field states to the coherent light fields produced by lasers, and to the squeezed quantum light fields that may be produced parametrically from coherent sources. Although the experiments in this thesis won't generate any squeezing, we require a description of squeezed states to distinguish the various quantum properties of squeezed and photon-number fields. We describe the theory behind experiments for characterizing quantum light fields including measurements of first and second-order coherence, and consider how various illustrative fields perform under such measurements.

2.1   Quantizing the optical field

A quantum description of light begins with observing that the electromagnetic field may be represented as an infinite set of independent harmonic oscillators with quantized excitations [77]. Each independent oscillator is a 'mode' of the electromagnetic field: a solution to Maxwell's equations that comprises all of the classical properties of light, namely the spatial and temporal distribution of the field (including polarization). This classical mode becomes a framework in space and time for describing the excitation of quantum light fields [75]. Associated with each mode is a harmonic oscillator with discrete energy levels corresponding to its possible excitation amplitudes so that the electric field strength in mode $\mathbf{u}(\mathbf{r}, t)$ is

$$\hat{\mathbf{E}} = \mathbf{u}(\mathbf{r}, t)\hat{a} + \mathbf{u}^*(\mathbf{r}, t)\hat{a}^\dagger \qquad (2.1)$$

where the c-number α describing the phase and amplitude of the classical field has been replaced by the Bosonic annihilation operator $\hat{a}$. The non-Hermitian operators $\hat{a}$ and $\hat{a}^\dagger$ are ladder operators for the associated quantum harmonic oscillator obeying the commutation

relation

$$[\hat{a}, \hat{a}^\dagger] = 1 \,, \tag{2.2}$$

and the Hermitian number operator

$$n = \hat{a}^\dagger \hat{a} \tag{2.3}$$

gives the photon occupation of a given mode. The field strength per photon in a given standing wave mode with a narrow frequency range about ω is

$$\epsilon_\omega = \sqrt{\frac{\hbar\omega}{\epsilon_0 V}} \,, \tag{2.4}$$

where ϵ_0 is the vacuum permittivity and V is the mode volume. By incorporating ϵ_ω into the mode definition we normalize $\mathbf{u}(\mathbf{r}, t)$. We can separate the mode into vector and scalar terms $\mathbf{u}(\mathbf{r}, t) = \mathbf{e}(\mathbf{r}, t)u(\mathbf{r}, t)$ where the vector $\mathbf{e}$ is the field polarization, which may depend on position and time. For example, tightly focused beams may have a spatial polarization dependence, and the field from a point source is best expanded in a basis of spherical multipole moments with spatial polarization dependence. We treat the spatial distribution of the dipole mode in Chap. 4.

2.1.1   Optical quadratures

In addition to the creation and annihilation operators, we can also introduce Hermitian operators for field quadratures $\hat{x}$ and $\hat{p}$ corresponding to the real and imaginary components of the complex field amplitude in a given mode

$$\hat{x} = \frac{1}{\sqrt{2}}(\hat{a}^\dagger + \hat{a}) \tag{2.5}$$

$$\hat{p} = \frac{i}{\sqrt{2}}(a^\dagger - \hat{a}) \tag{2.6}$$

which, following from Eqn. 2.2, are canonically conjugate

$$[x, p] = i \,. \tag{2.7}$$

These are analogous to the position and momentum operators of a harmonic oscillator.

2.1.2   Plane wave mode basis

The electromagnetic field exists in a Hilbert space that may be decomposed over any arbitrary orthonormal basis of modes and single-mode quantum states. A natural mode basis is usually suggested by the measurement being made. One basis of light modes that we will use extensively in our analysis is the set of plane waves in a vacuum

$$\mathbf{u}(\mathbf{r}, t) = \mathbf{e}\sqrt{\frac{\hbar\omega}{\epsilon_0 V}}e^{i(\mathbf{k}\cdot\mathbf{r} - \omega t)} \tag{2.8}$$

with fixed polarization $\mathbf{e}$, frequency ω, and wave vector $\mathbf{k}$ where $k^2 = \omega^2/c^2$. Strictly speaking, plane waves are not normalizable in $\mathbb{R}^3$ and are restricted to an 'interaction volume' of size V for the purpose of constructing a valid Hilbert space. Although it is included here for the sake of clarity, in practice we will avoid this slight of hand by

considering only normalizable modes when applying the Born rule. We can write any field as a sum of of plane waves inside a box of volume V with periodic boundary conditions

$$\hat{\mathbf{E}} = \sum_{\mathbf{k}} \sqrt{\frac{\hbar\omega_{\mathbf{k}}}{2\epsilon_0 V}} \mathbf{e}_{\mathbf{k}} \left(\hat{a}_{\mathbf{k}} e^{i(\mathbf{k}\cdot\mathbf{r}-\omega_{\mathbf{k}}t)} + \hat{a}_{\mathbf{k}}^\dagger e^{-i(\mathbf{k}\cdot\mathbf{r}-\omega_{\mathbf{k}}t)} \right) , \tag{2.9}$$

or as an integral in the continuous limit [77]

$$\sum_{\mathbf{k}} \rightarrow \frac{V}{(2\pi)^3} \int \mathrm{d}^3 k \tag{2.10}$$

$$\hat{\mathbf{E}} = \frac{1}{(2\pi)^3} \sqrt{\frac{\hbar V}{2\epsilon_0}} \int \mathrm{d}^3\mathbf{k}\, \mathbf{e}_{\mathbf{k}} \sqrt{\omega_{\mathbf{k}}} \left(\hat{a}_{\mathbf{k}} e^{i(\mathbf{k}\cdot\mathbf{r}-\omega_{\mathbf{k}}t)} + \hat{a}_{\mathbf{k}}^\dagger e^{-i(\mathbf{k}\cdot\mathbf{r}-\omega_{\mathbf{k}}t)} \right) . \tag{2.11}$$

It will occasionally be convenient to separate the optical field into positive and negative frequency components.

$$\hat{\mathbf{E}} = \hat{\mathbf{E}}^+ + \hat{\mathbf{E}}^-, \qquad \hat{\mathbf{E}}^- = (\hat{\mathbf{E}}^+)^\dagger \tag{2.12}$$

where $\hat{\mathbf{E}}^+$ is the sum of annihilation operator terms oscillating with frequency $e^{i\omega t}$ and $\hat{\mathbf{E}}^-$ is the sum of creation operator terms oscillating with frequency $e^{-i\omega t}$.

2.2 Quantum states of light

A great deal of this thesis concerns the design of quantum devices which, as the name suggests, take advantage of the uniquely quantum properties of light fields. We have already introduced technologies such as the single-photon source, quantum memory and quantum computer in Chap. 1, albeit without the essential theory of their operation. In the remainder of this chapter we will explore key properties of light which cannot be explained in terms of classical fields: for instance the degree of anti-bunching, quadrature squeezing and entanglement. To do so we will need to introduce the most elementary single-mode, pure states of the light field and their properties.

2.2.1 Fock states

The Fock states $|n\rangle$ are eigenstates of the photon number operator with photon number n

$$|n\rangle = \frac{(\hat{a}^\dagger)^n}{\sqrt{n!}} |0\rangle \tag{2.13}$$

$$\hat{n} |n\rangle = n |n\rangle \tag{2.14}$$

and form an orthonormal Hilbert space basis for single mode states of the quantum field. Although a foundational concept for quantum optics and an elementary component of proposed quantum technologies, pure Fock states are difficult to generate in the lab (we'll explore this problem in some detail when we discuss single photon sources in Chap. 7). Fock states of a fixed frequency mode, such as plane waves, are also energy eigenstates with energy

$$\hat{\mathcal{H}} |n_{\mathbf{k}}\rangle = \hbar\omega_{\mathbf{k}}(\hat{n} + 1/2) |n_{\mathbf{k}}\rangle \tag{2.15}$$

where the factor of 1/2 is the zero-point energy of the zero-photon Fock state, or 'vacuum field', $|0\rangle$. In this thesis we will usually consider energy exchange between atomic and

optical systems, and in this context the constant factor can be neglected from the Hamiltonian, but it shouldn't be forgotten that the vacuum is a meaningful optical state of a mode. For example, the uncertainty in the electric field strength of the nth Fock state is [77]

$$\Delta \mathbf{E} = \sqrt{\langle \mathbf{E} \rangle^2 - \langle \mathbf{E}^2 \rangle} \tag{2.16}$$

$$= \sqrt{2} \mathbf{u}(\mathbf{r}, t) \sqrt{n + 1/2} \,. \tag{2.17}$$

Even the field strength of the $n = 0$ 'vacuum' state fluctuates. These vacuum fluctuations are responsible for both the spontaneous decay and energy level shifts of excited atomic states. Importantly, even the vacuum fluctuations depend on the allowed mode amplitudes $\mathbf{u}(\mathbf{r}, t)$ such that the vacuum fluctuations may be shaped by surfaces with appropriate boundary conditions. We will take advantage of this fact for the design of experiments with precision fabricated mirrors in Chap. 10.

2.2.2 Coherent states

According to Eqn. 2.7, the amplitude and phase quadratures of the optical field do not commute, so we can see that the product of phase and amplitude uncertainty has a lower limit fixed by Heisenberg's uncertainty relation. Coherent states are the optical states that minimize this uncertainty product, they have the smallest possible quadrature fluctuations. In this sense, they are the closest possible quantum state to the noiseless classical field. They are eigenstates of the annihilation operator

$$\hat{a} \left| \alpha \right\rangle = \alpha \left| \alpha \right\rangle \tag{2.18}$$

and can be expanded in the Fock state basis

$$\left| \alpha \right\rangle = e^{-\frac{1}{2} |\alpha|^2} \sum_{n=0}^{\infty} \frac{\alpha^n}{\sqrt{n!}} \left| n \right\rangle \tag{2.19}$$

which is to say that the coherent state $\left| \alpha \right\rangle$ is a Poissonian superposition of photons with mean intensity α^2 as shown in Fig 2.3(b). Coherent states have the same quadrature uncertainty as the vacuum, and can be described as a displaced vacuum state with amplitude $|\alpha|$ and phase $\arg(\alpha)$

$$\hat{D} = \exp\left[\alpha \hat{a}^\dagger - \alpha^* \hat{a} \right] \tag{2.20}$$

$$\left| \alpha \right\rangle = \hat{D}(\alpha) \left| 0 \right\rangle \,. \tag{2.21}$$

Coherent states are not mutually orthogonal, because they are not the eigenstates of a Hermitian operator, but coherent states with $\Delta\alpha > 2$ are approximately orthogonal. Because coherent states are not eigenstates of the creation operator, any physical operation (Hamiltonian or unitary operator) containing $\hat{a}$ necessarily changes the energy in a coherent state. An ideal laser produces a coherent optical field in a single mode, usually a Gaussian mode with a narrow bandwidth.

2.2.3   Squeezed states

Squeezed states, like coherent states, have only the minimum quadrature uncertainty necessary to satisfy Heisenberg's relation. Unlike coherent states, the squeezed states distribute this uncertainty asymmetrically between the two quadratures, reducing uncertainty in one quadrature at the expense of a corresponding increase in the complementary quadrature. We can write the set of single-mode quadrature-squeezed states in terms of the operator $\hat{S}(\zeta)$ [79]

$$
\begin{align}
|\zeta, \alpha\rangle &= \hat{D}(\alpha)\,\hat{S}(\zeta)\,|0\rangle \tag{2.22}\\
\hat{S}(\zeta) &= \exp\left[(\zeta\hat{a}^2 - \zeta^*\hat{a}^{\dagger 2})/2\right], \tag{2.23}
\end{align}
$$

where $\zeta = re^{i\phi}$ is the squeezing parameter with magnitude r at angle ϕ. The squeezing operator contains only even powers of creation and annihilation operators, and may be written as the action of a Hamiltonian

$$
\hat{H} = i\hbar r(\hat{a}^2 - \hat{a}^{\dagger 2})/2 \tag{2.24}
$$

that creates or annihilates photons in pairs. Applied to the vacuum state, the squeezing operator produces pairs of photons with a Poissonian distribution as shown in Fig. 2.3(a). For this reason, an early name for the squeezed-vacuum state was a 'two photon coherent state'.

In practice, any unitary Hamiltonian that is at least quadratic in the ladder operators can generate some degree of squeezing. The most common means of generating squeezed light is spontaneous parametric down-conversion (SPDC), in which a bright pump field propagates through a medium with a second-order nonlinear optical response. Each pump photon has some probability to be split into two photons of lower energy, with modes that satisfy a phase-matching condition.

The squeezing operation $\hat{S}$ is best pictured as a Bogoliubov transformation of the creation and annihilation operators, corresponding to compression and elongation of the two quadratures by a factor $R = e^r$. The quadrature variances of a squeezed coherent state are

$$
\begin{align}
\Delta x^2 &= 1/(2R^2), \tag{2.25}\\
\Delta p^2 &= R^2/2, \tag{2.26}
\end{align}
$$

although the squeezing operator also changes the field amplitude α for all $|\alpha| > 0$. This operation may be visualized by stretching the plane of the Wigner quasi-probability distribution $W(x, p)$ which we shall now introduce. We will make further use of these Wigner functions by deriving the photon-number distribution of a general squeezed state.

2.3   The Wigner function

So far we have quantized the optical field and considered the elementary single-mode quantum states of light, starting with the vacuum field, in terms of the photon-number basis. The density operator of a general mixed state can always be written as a density matrix in this basis. However it will now prove more convenient to work with an alternative representation of the field, the so-called 'Wigner function' which is a phase space distribution

for the field in the two quadrature values x and p.

We may write all physical density matrices in terms of a coherent state expansion

$$\hat{\rho} = \int d\alpha \, P(\alpha) \, |\alpha\rangle \langle\alpha| \,, \tag{2.27}$$

where $P(\alpha)$ is a normalized, real-valued function of the complex variable α. It represents the relative weight of the coherent state $|\alpha\rangle$ with $\alpha = (x + ip)/\sqrt{2}$ in a coherent state expansion of the field. The Wigner function is an integral transform of the P function

$$W(\alpha) = \frac{2}{\pi} \int d\beta \, P(\beta) e^{-2|\alpha-\beta|^2} \tag{2.28}$$

and therefore the Fourier transform of the symmetrically ordered characteristic function $C(\gamma)$

$$W(\alpha) \;=\; \frac{1}{\pi^2} \int d\gamma \, e^{\alpha\gamma^* - \alpha^*\gamma} C(\gamma) \,, \tag{2.29}$$

$$C(\gamma) \;=\; \mathrm{Tr}\left[\hat{\rho}\, e^{\gamma\hat{a}^\dagger - \gamma^*\hat{a}}\right] \,, \tag{2.30}$$

which is the expectation value of the displacement operator for state ρ.

Because the quadratures are conjugate, the Wigner function cannot be construed as a literal probability distribution. The Wigner function is normalized, but not positive-definite; it may have negative values. However, a useful property of the Wigner function is that the probability distributions for the quadratures x and p are the projection of the Wigner function onto each axis

$$P_x(x) \;=\; \int dy \, W(x,p) \quad \geq 0 \quad \forall \, x \,, \tag{2.31}$$

$$P_p(p) \;=\; \int dx \, W(x,p) \quad \geq 0 \quad \forall \, p \,. \tag{2.32}$$

2.3.1   Squeezed state Wigner functions

The general, pure squeezed state is the product of squeezing and displacement operators on the vacuum (Eqn. 2.22). We can write these operations as a series of coordinate transforms of the vacuum state Wigner function

$$W_v(x,p) = \frac{1}{\pi} e^{-(x^2+p^2)} \,. \tag{2.33}$$

The squeezing operator $\hat{S}(\zeta)$ at angle ϕ is a Bogoliubov transformation of quadrature coordinates $\hat{x}$ and $\hat{p}$ (illustrated in Fig. 2.1)

$$W_R(x,p) = W_v(Rx, \frac{p}{R}) \tag{2.34}$$

followed by a rotation with angle ϕ

$$W_{R,\phi}(x,p) = W_R(x\cos\phi + p\sin\phi, -x\sin\phi + p\cos\phi) \,. \tag{2.35}$$
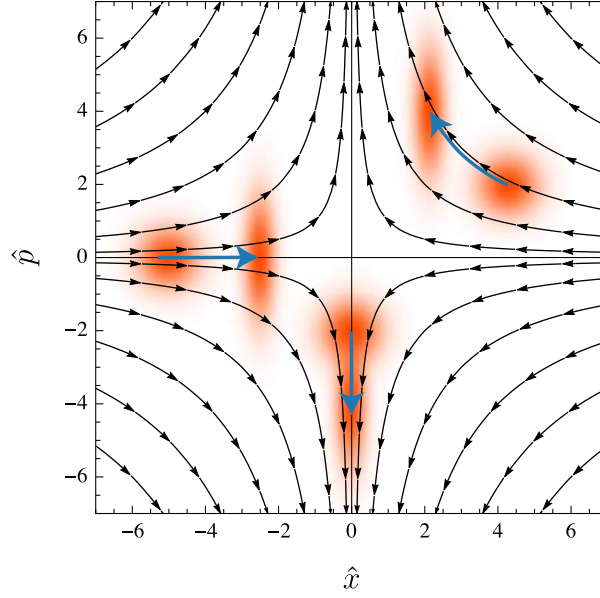
Figure 2.1: Action of the squeezing operator on a coherent state. The squeezing operator is a Bogoliubov transformation of the quadrature phase space (streamlines) that both squeezes and displaces (blue arrows) coherent states as shown.

Finally, the displacement operator $\hat{D}(\alpha)$ displaces the squeezed Wigner distribution $\hat{x}$ coordinate by $\sqrt{2}\alpha$

$$W_s(x, p) = W_{R,\phi}(x - \sqrt{2}\alpha). \tag{2.36}$$

Combining these transformations yields the Wigner distribution of a pure squeezed state (up to a global phase)

$$W_s(x, p) = \frac{1}{\pi} \exp\left[-R^2 \left(p \sin\phi + \left(x - \sqrt{2}\alpha\right)\cos\phi\right)^2 - \frac{\left(p\cos\phi + \left(\sqrt{2}\alpha - x\right)\sin\phi\right)^2}{R^2}\right]. \tag{2.37}$$

The Wigner distributions of several squeezed states are plotted in the third column of Fig. 2.3. The coherent ($R = 1$) and squeezed ($R \neq 1$) states are known collectively as 'Gaussian states' for the shape of their Wigner functions. The Gaussian states satisfy $W_s(x, p) \geq 0 \forall x, p$. More generally, we'll refer to any convex mixture of Gaussian states as Gaussian.

2.3.2 Fock state Wigner functions

The Wigner function of the n-photon Fock state is [80]

$$W_n(x, p) = \frac{(-1)^n e^{-p^2 - x^2} L_n\left(2\left(p^2 + x^2\right)\right)}{\pi}, \tag{2.38}$$

where L_n is the n-th order Laguerre polynomial. Fig. 2.2 shows the Wigner functions for the first three Fock states. Although the Wigner functions themselves may be negative, the x and p projections (Eqn. 2.31) are always positive. The overlap between an arbitrary Wigner function and these n-photon 'projectors' gives the probability of finding the field in an n photon state $P_n = |c_n|^2$.
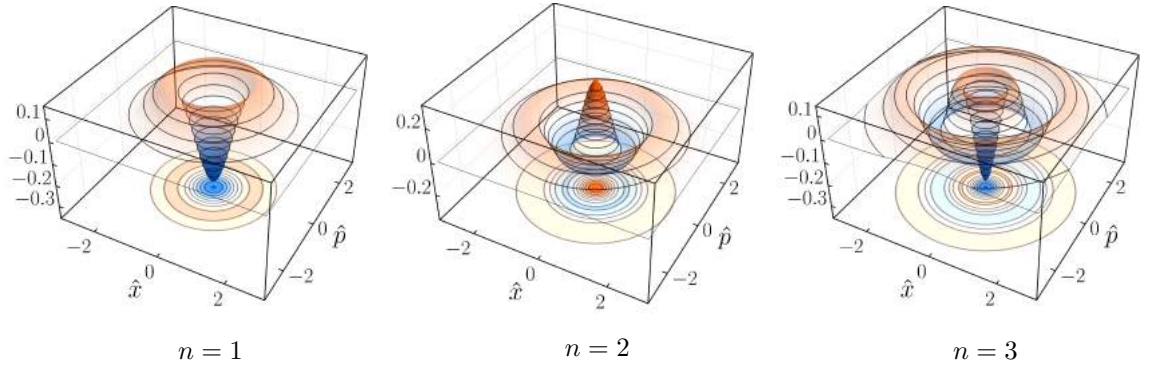
Figure 2.2: Fock state Wigner functions $W_n(x, p)$ for $n = 1, 2, 3$ as surface and contour plots. The Fock states are phase symmetric, as required for energy eigenstates. Every Fock state $n > 0$ has negative values (blue).

2.4 Photon-number distribution of a general squeezed state

In Chap. 8 we will derive a statistical non-Gaussian witness for optical states using a photon-number distribution for the general Gaussian states. In contrast to the photon-number distribution of the single-mode squeezed-vacuum (two-photon coherent) state, the general Gaussian state contains both odd and even photon numbers. The probability P_n of measuring this general, pure squeezed state with photon number n is the overlap of the state with projectors W_n for the n photon Fock state

$$P_n = \int_{-\infty}^{\infty} W_n W_{V,\phi,r} \, \mathrm{d}x \mathrm{d}p \,, \tag{2.39}$$

which yields the vacuum and single photon probabilities

$$P_0 = \frac{2R}{R^2 + 1} e^{-\alpha^2 \left(\frac{(R^2 - 1)\cos(2\phi)}{R^2 + 1} + 1 \right)} \,, \tag{2.40}$$

$$P_1 = P_0 \frac{2\alpha^2 \left(\left(R^4 - 1\right)\cos(2\phi) + R^4 + 1 \right)}{\left(R^2 + 1\right)^2} \,, \tag{2.41}$$

$$\tag{2.42}$$

as plotted in Fig. 2.4.

The integral Eqn. 2.39 becomes a little involved for $n \geq 1$, we direct the interested reader to derivations by G. S. Agarwal [81], and resign ourselves to simply reporting here the photon-number distribution according to the more compact notation of V. V. Dodonov [82]

$$P_n = P_0 \frac{(T^2 - 4d)^{\frac{n}{2}}}{(2T + 4d + 1)^n} \sum_{k=0}^{n} \left(\frac{4d - 1}{\sqrt{T^2 - 4d}} \right)^k \frac{n!}{[(n-k)!]^2 \, k!} |H_n(\gamma)|^2 \,, \tag{2.43}$$

where

$$\gamma = \frac{(T+1)\alpha + (\sigma_{pp} - \sigma_{xx} - 2i\sigma_{xp})\alpha^*}{\sqrt{2(T+1)(\sigma_{pp} - \sigma_{xx} - 2i\sigma_{xp})}} \tag{2.44}$$
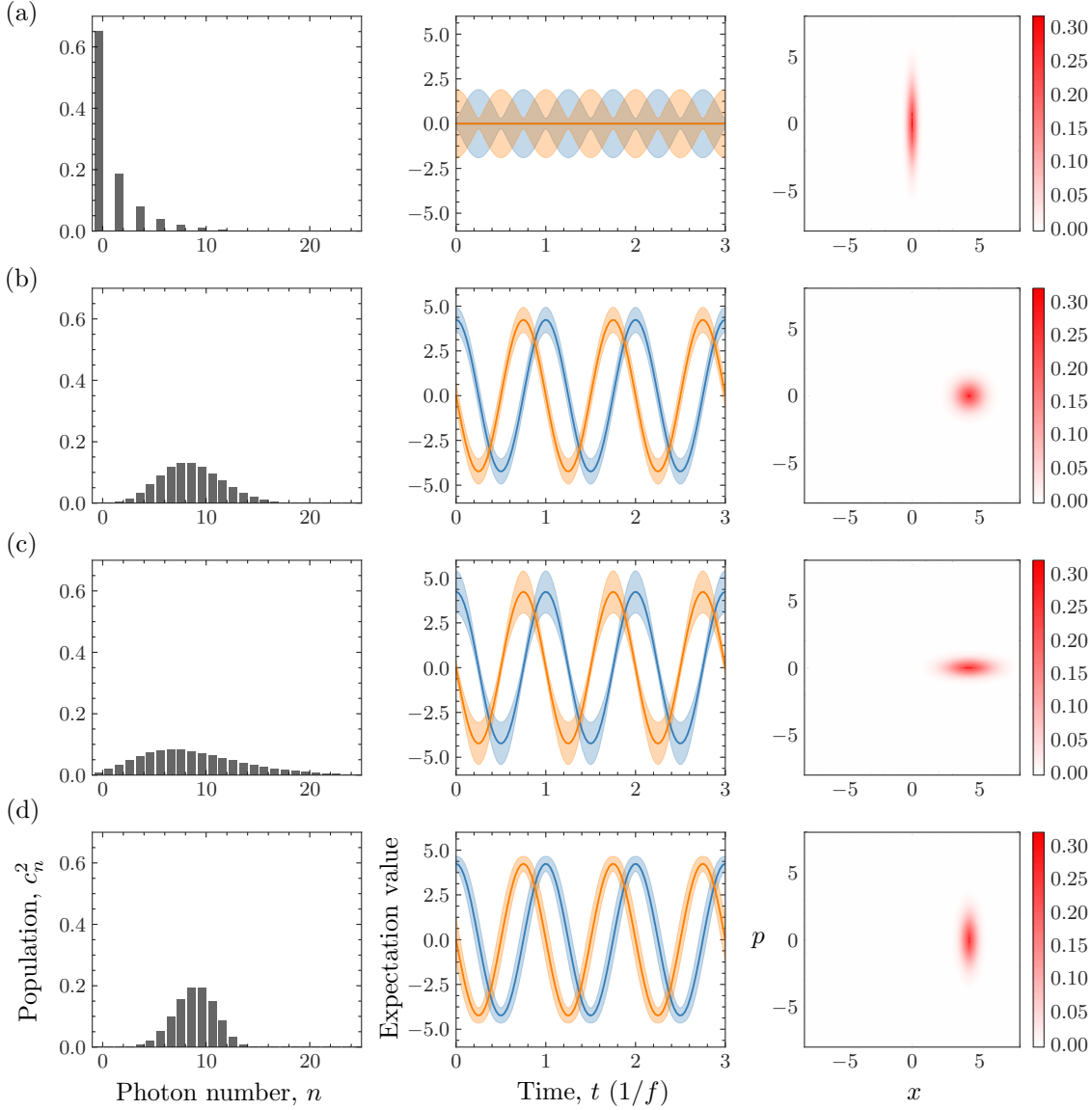
Figure 2.3: Squeezed states of the optical field. (a) The squeezed vacuum: $\alpha = 0$, $R = 2.7$. (b) Coherent state: $\alpha = 3$, $R = 0$. The photon number distribution is Poissonian. (c) Phase squeezed state: $\alpha = 3$, $R = 0.6$. The photon number distribution is super-Poissonian. (d) Amplitude squeezed state: $\alpha = 3$, $R = 1.7$. The photon-number distribution is sub-Poissonian. Each state is shown by its photon-number distribution (left), quadrature expectation values and uncertainty in a stationary frame (centre), and Wigner distribution (right). The squeezed vacuum consists of even number Fock states. Although the expectation value of each quadrature is zero, the energy is non-zero. The coherent state photon number is Poissonian, and uncertainty is evenly distributed between the quadratures. The phase squeezed state photon-distribution is super-Poissonian and uncertainty is distributed unevenly between the quadratures. Compared to a coherent state with same mean, the photon number uncertainty is larger, and quadrature uncertainty is low (high) when the quadrature value is low (high). The amplitude squeezed state photon-distribution is sub-Poissonian. Compared to a coherent state with the same mean, the photon number uncertainty is low, and the quadrature uncertainty is high (low) when the quadrature value is low (high).
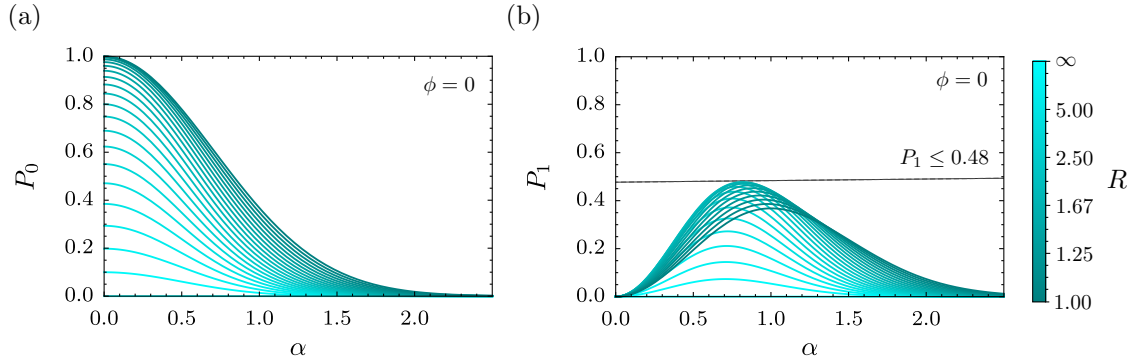
Figure 2.4: The (a) vacuum and (b) single-photon probabilities of number-squeezed ($\phi = 0$) Gaussian states as a function of displacement α. The coherent state ($R = 1$) single photon probability is maximum at $\alpha = 1$. The squeezed state single-photon probability is maximum at $R = 1.73, \alpha = 0.82$. The single photon component is bounded, $P_1 \leq 0.48 \quad \forall \alpha, R, \phi$.

d and T are the determinant and trace of the Wigner function variance matrix M

$$d = \left| M \right| , \qquad T = \text{Tr}[M] , \qquad M = \begin{bmatrix} \sigma_{pp} & \sigma_{xp} \\ \sigma_{xp} & \sigma_{xx} \end{bmatrix} . \tag{2.45}$$

For pure states, $d = \frac{1}{4}$, and Eqn. 2.43 reduces to

$$P_n = \frac{P_0}{2^n n!} \left(\frac{T-1}{T+1} \right)^{\frac{n}{2}} \left| H_n \left(\gamma \right) \right|^2 \tag{2.46}$$

and the variances become

$$\sigma_{xx} = \Delta x^2 = \frac{1}{2} \left(R^2 \sin[2]\phi + \frac{\cos^2(\phi)}{R^2} \right) , \tag{2.47}$$

$$\sigma_{pp} = \Delta p^2 = \frac{1}{2} \left(\frac{\sin^2(\phi)}{R^2} + R^2 \cos(\phi) \right) , \tag{2.48}$$

$$\sigma_{xp} = -\sqrt{\sigma_{xx}\sigma_{pp} - \frac{1}{4}} , \tag{2.49}$$

where the quadrature covariance $\sigma_x p$ is given by the Schrödinger-Robertson uncertainty relation for a pure Gaussian state. The photon-number distribution of various squeezed states is shown in Fig. 2.3.

2.5   Optical correlation functions

So far we have quantized the optical field and considered the elementary quantum states of light by their Wigner functions and photon-number distributions. In this section we will introduce the first of several detection methods that we will use to identify and distinguish these states in experiments: the optical correlation functions. These correlation functions probe orders of 'coherence' of light fields. According to Glauber's unifying treatment we can define the general n-th order correlation function as the Heisenberg picture expectation

value [83]

$$G^{(n)}(\mathbf{r}_1, ..., \mathbf{r}_{2n}; t_1, ..., t_{2n}) \equiv \left\langle \hat{\mathbf{E}}^-(\mathbf{r}_1, t_1) ... \hat{\mathbf{E}}^-(\mathbf{r}_n, t_n) \hat{\mathbf{E}}^+(\mathbf{r}_{n+1}, t_{n+1}) ... \hat{\mathbf{E}}^+(\mathbf{r}_{2n}, t_{2n}) \right\rangle \tag{2.50}$$

where $\hat{\rho}$ is the density operator of the optical field. It will usually be more convenient to work with the normalized correlation functions $g^{(n)}$, which are defined as follows

$$g^{(n)}(\mathbf{r}_1, ..., \mathbf{r}_{2n}; t_1, ..., t_{2n}) \equiv \frac{G^{(n)}(\mathbf{r}_1, ..., \mathbf{r}_{2n}; t_1, ..., t_{2n})}{\sqrt{G^{(1)}(\mathbf{r}_1; t_1)...G^{(1)}(\mathbf{r}_{2n}; t_{2n})}} . \tag{2.51}$$

This is the most general form of the n-th order optical correlation function, but we will frequently be able to make some simplifying assumptions. First, we will usually be interested in the single-point correlation function

$$G^{(n)}(\mathbf{r}; t_1, ..., t_{2n}) \equiv G^{(n)}(\mathbf{r}_1, ..., \mathbf{r}_{2n}; t_1, ..., t_{2n}) \tag{2.52}$$

for $\mathbf{r}_1, ..., \mathbf{r}_{2n} = \mathbf{r}$. For single-mode fields we may replace the field operators $\hat{\mathbf{E}}^+$ and $\hat{\mathbf{E}}^-$ with the annihilation and creation operators for the field mode so that the spatial dependence is removed entirely

$$G^{(n)}(t_1, ..., t_{2n}) = \left\langle \hat{a}^\dagger(t_1) ... \hat{a}^\dagger(t_n) \hat{a}(t_{n+1}) ... \hat{a}(t_{2n}) \right\rangle . \tag{2.53}$$

Finally, for stationary fields, meaning that $\left[\hat{H}, \hat{\rho}\right] = 0$, we may integrate over one time parameter and express the others as time differences $\tau_{n-1} = t_n - t_1$.

We'll consider now the first and second-order ($n = 1, 2$) correlation functions, which are pivotal concepts for the characterization of quantum light fields.

2.5.1 First-order coherence

The first order correlation function $G^{(1)}$ quantifies the capacity for the field at two different points in space and time to interfere. This is the sense in which 'coherence' is used in classical optics, for example in Young's double slit experiment. A field with $\left|g^{(1)}\right| = 1$ is coherent, and may interfere with unit visibility. An ideal photo-detector, with bandwidth much broader than the incident field and negligible spatial extent, at coordinate $\mathbf{r}$ records a count-rate proportional to $G^{(1)}(\mathbf{r}; t, t)$ at time t. The two-time correlation function $G^{(1)}(\mathbf{r}; t_1, t_2)$ expresses the phase fluctuations of the light field. The power spectrum of the field $S(\mathbf{r}, \omega)$ is therefore related to the first-order correlation function by the Wiener-Khinchin theorem

$$S(\mathbf{r}, \omega) = \frac{\epsilon_0 c}{2\pi} \lim_{T \to \infty} \int_0^T \mathrm{d}t_1 \int_0^T \mathrm{d}t_2 \, G^{(1)}(\mathbf{r}; t_1, t_2) e^{i\omega(t_2 - t_1)} . \tag{2.54}$$

For stationary fields the spectrum becomes

$$S(\mathbf{r}, \omega) = \frac{\epsilon_0 c}{2\pi} \mathrm{Re} \int_0^\infty \mathrm{d}\tau \, G^{(1)}(\mathbf{r}; \tau) e^{i\omega\tau} \tag{2.55}$$

where we have written the time-difference correlation function $G^{(1)}(\mathbf{r}; \tau) \equiv G^{(1)}(\mathbf{r}; 0, \tau)$. We will see in the following chapter that the first-order coherence of atomic fluorescence is determined by competition between two internal atomic processes, elastic and inelastic

scattering. This is a critical consideration for atom-light quantum networks. which require the control of coherent, and suppression of incoherent, atom-light processes.

2.5.2   Second-order coherence

We can further elucidate the properties of the light field by extending the concept of coherence to higher orders, and it is by doing so that the consequences of a quantized optical field become clear. Given n ideal detectors we can measure the n-th fold coincidence rate

$$G^{(n)}(\mathbf{r}_1, ..., \mathbf{r}_n; t_1, ..., t_n) \equiv G^{(n)}(\mathbf{r}_1, ..., \mathbf{r}_n, \mathbf{r}_n, ..., \mathbf{r}_1; t_1, ..., t_n, t_n, ..., t_1). \tag{2.56}$$

In principle, a single broad-bandwidth, zero-deadtime and n-photon discriminating detector can measure the n-th fold, single-point coincidence rate $G^{(n)}(\mathbf{r}; t_1, ..., t_n)$. Making the typical assumptions outlined above, we can write the second-order, single-point normalized coherence function for stationary fields

$$g^{(2)}(\tau) = \frac{\langle \hat{a}^\dagger(0)\hat{a}^\dagger(\tau)\hat{a}(\tau)\hat{a}(0)\rangle}{\langle \hat{a}^\dagger(0)\hat{a}(0)\rangle^2}. \tag{2.57}$$

2.5.3   Hanbury-Brown and Twiss measurement

Hanbury-Brown and Twiss pioneered the use of the second-order correlation function in an experimental configuration that now bears their names [84, 85]. The Hanbury-Brown Twiss (HBT) configuration, shown schematically in Fig. 2.5(a), is a means of measuring the second order coherence of a field with realistic detectors, below the detector dead time limit. In a HBT measurement a beam splitter divides an optical field into two output arms that are measured continuously and simultaneously by photon detectors. Let us consider two stationary, single mode fields $\hat{\rho}_{1,2}$ mode matched through a beam splitter. The normalized Hanbury-Brown and Twiss (HBT) detector correlation function is

$$g^{(2)}_{\text{HBT}}(\tau) = \frac{\langle \hat{a}^\dagger_3(0)\hat{a}^\dagger_4(\tau)\hat{a}_4(\tau)\hat{a}_3(0)\rangle}{\langle \hat{a}^\dagger_3(0)\hat{a}_3(0)\rangle \langle \hat{a}^\dagger_3(0)\hat{a}_3(0)\rangle}, \tag{2.58}$$

where we have reduced the field operators to the scalar single-mode annihilation operators $\hat{a}_{3,4}$ for the orthogonal beam splitter output modes and the expectation value is taken over the output state

$$\hat{\rho}_{\text{out}} = \hat{B}\left(\hat{\rho}_1 \otimes \hat{\rho}_2\right)\hat{B}^\dagger. \tag{2.59}$$

We can write the beam splitter operation $\hat{B}$ as a relationship between annihilation operators in the input and output modes [75]

$$\begin{aligned}
\hat{a}_3 &= \tfrac{1}{\sqrt{2}}\left(\hat{a}_1 + i\hat{a}_2\right), \\
\hat{a}_4 &= \tfrac{1}{\sqrt{2}}\left(i\hat{a}_1 + \hat{a}_2\right)
\end{aligned} \tag{2.60}$$

and with these substitutions the normalized HBT correlation function (Eqn. 2.58) is a ratio of expectation values of the input state operators on the input states. When one of the fields is the vacuum state $\hat{\rho}_2 = |0\rangle\langle 0|$ then the normalized HBT correlation function
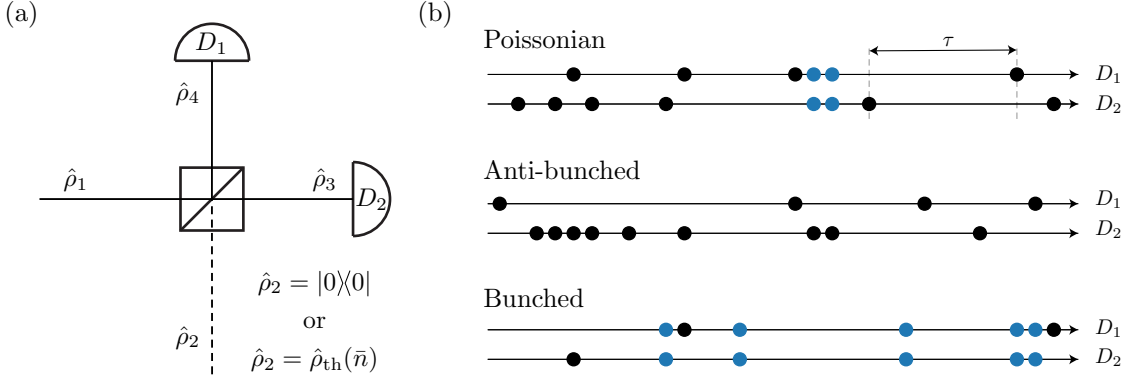
Figure 2.5: Schematic of the Hanbury-Brown and Twiss (HBT) measurement. (a) An input field $\hat{\rho}_1$ is divided evenly between two output modes $\hat{\rho}_{3,4}$ by a balanced beam splitter. Photon arrival times are measured independently and continuously at the two detectors $D_{1,2}$. In an ideal HBT measurement the field at the second beam splitter input port is the vacuum, but to model detector dark noise we can inject a thermal state at $\hat{\rho}_2$. (b) Simulated photon arrival times at each HBT detector given Poissonian (coherent), sub-Poissonian (anti-bunched) and super-Poissonian (bunched) fields $\hat{\rho}_1$ with the same intensity. Coincidence events ($\tau = 0$) are shown in blue.

reduces to the normalized correlation function of the non-vacuum input field [86, 87]

$$g_{\text{HBT}}^{(2)}(\tau)\left[\rho \otimes |0\rangle\langle 0|\right] = g^{(2)}(\tau)\left[\rho\right]. \tag{2.61}$$

A realistic detector has some detection noise which can be modelled as a thermal state injected at the dark port of the beam splitter. Including this noise state produces a dark count rate related proportional to the mean photon number of the thermal state $\bar{n}_{\text{th}}$. When $\bar{n}_{\text{th}} \ll \langle n \rangle$ the dark noise contributes a Poissonian coincidence rate proportional to $\bar{n}_{\text{th}}$. Detector inefficiencies can be modelled with an additional beam splitter before each detector.

We can define the anticorrelation parameter of a field with measured HBT coincidence probability P_c and individual detector rates $P_{1,2}$

$$\mathbb{A} = \frac{P_c}{P_1 P_2} = \frac{4P_c}{P_s^2} \tag{2.62}$$

where the single detection event probability $P_s = 2P_1 = 2P_2$ for perfectly balanced detection. Even with inefficient detectors (but neglecting detector noise) $\mathbb{A} \to g^{(2)}(0)$ in the weak-field limit.

2.5.4 Photon anti-bunching

We can consider how various elementary fields introduced above will perform under $g^{(2)}(\tau)$ measurement at zero time delay. The single-mode coherent state is an eigenstate of the annihilation operator, and so the operators in the correlation function simply factorize to leave us with $g^{(2)}(0) = 1$. In fact, the coherent state is coherent for all orders of coherence n, $g^{(n)}(0) = 1 \; \forall \; n \in \mathbb{Z}^+$.

In contrast, the second-order coherence of the n-photon Fock state is less than one for all photon numbers n. We can expand a general pure state in the Fock basis with

n-photon coefficients a_n so that we have

$$g^{(2)}(0) \quad = \quad \frac{\sum_{n=0}^{\infty} \langle n|\hat{a}^\dagger \hat{a}^\dagger \hat{a}\hat{a}|n\rangle}{\left(\sum_{n=0}^{\infty} \langle n|\hat{a}^\dagger \hat{a}|n\rangle\right)^2} \tag{2.63}$$

$$= \quad \frac{\sum_{n=2}^{\infty} n(n-1)a_n^2}{\left(\sum_{n=1}^{\infty} n a_n^2\right)^2} \tag{2.64}$$

therefore the n-photon Fock state has

$$g^{(2)}(0) = 1 - \frac{1}{n} < 1 \tag{2.65}$$

The photons of the Fock state light field are less likely to arrive at a detector together than you would expect for a classical light field. This so-called 'anti-bunching' is a strictly quantum phenomenon, a direct consequence of the quantization of the light field.

For a single-photon Fock state the interpretation of the $g^{(2)}$ measurement is clear. Because of the fundamental indivisibility of the photon the $g^{(2)}(0)$ of the $n = 1$ Fock state is necessarily zero. A single photon may only register on only one detector at a time, and given noiseless detectors the coincidence rate will be zero. A necessary (but not sufficient) criteria for a single-photon source is therefore that the $g^{(2)}(0)$ of the source is sufficiently close to zero, where 'sufficient' depends considerably on the application. In Sec. 8 we explore how the number of nodes in a single-photon QKD network is constrained by the $g^{(2)}(0)$ of available single-photon sources.

Fock states are not the only states which exhibit anti-bunching. We've already seen that optical states may be amplitude-squeezed so that the photon-number distribution is sub-Poissonian, Fig. 2.3(d). For a weak field $\langle n \rangle \ll 1$ we can write Eqn. 2.63 reduces to

$$g^{(2)}(0) = \frac{2|a_2|^2}{|a_1|^4 + 2|a_2|^2} \approx \frac{2|a_2|^2}{|a_1|^4} \ . \tag{2.66}$$

For a sub-Poissonian distribution we must have $g^{(2)}(0) < 1$, which implies that weak, amplitude squeezed fields are also anti-bunched. Although squeezed states must have $g^{(2)}(0) > 0$, they can in fact be arbitrarily close to zero, even without an arbitrarily high degree of squeezing. Consider the general, single-mode squeezed state $|R, \alpha\rangle = \hat{D}(\alpha)\hat{S}(e^r e^{i\phi})|0\rangle$. Fig. 2.6 shows the $g^{(2)}(0)$ as a function of α and R for the phase, $\phi = \pi/2$, and amplitude, $\phi = 0$ squeezed states. There exists a set of low amplitude-squeezed states close to the squeezed vacuum which are anti-bunched and can have arbitrarily low $g^{(2)}(0)$.

2.6   Homodyne and heterodyne measurements

Homodyne and heterodyne detection are alternatives to direct photon-number detection in which the quadrature components are measured instead of the intensity [88, 89]. In these schemes the signal field is mixed with a bright coherent reference field, called the 'local oscillator', at a balanced beam splitter. The intensity at each output is measured by photodetectors, usually linear photodiodes. The signal and reference fields interfere such that the output intensity in each arm depends on the amplitude and phase of the signal. The output intensities are noisy because of fluctuations in the bright field, but taking the difference of the two measured intensities leaves only the interference term between the two fields.
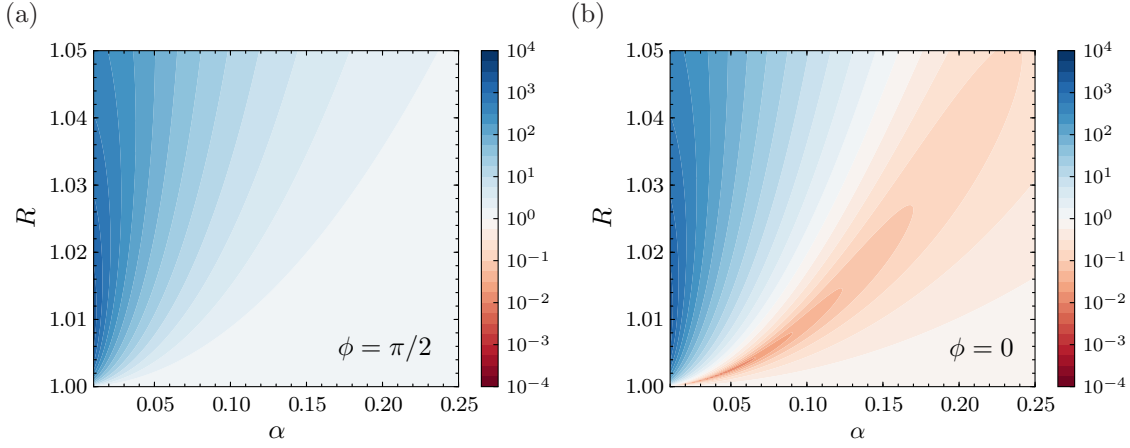
Figure 2.6: (a) $g^{(2)}(0)$ of the phase-squeezed state, $\phi = \pi/2$, as a function of the displacement α and squeezing factor R. Blue regions are bunched, $g^{(2)}(0) > 1$, and red regions are anti-bunched, $g^{(2)}(0) < 1$. Coherent states, $R = 0$, have $g^{(2)}(0) = 1$. Squeezed vacuum, $\alpha = 0$, contains only photon pairs and must be bunched. The general phase-squeezed state is super-Poissonian and must also have some degree of bunching. (b) $g^{(2)}(0)$ of the amplitude-squeezed state, $\phi = 0$. Weak amplitude-squeezed states are sub-Poissonian and there exists a region in α, R where the amplitude squeezed states are anti-bunched.

The measured quadrature is the projection of the signal field onto the local oscillator [75]. In this way the local oscillator is amplifying the input signal. Because the oscillator (ideally) contributes no noise to the difference signal, it is possible to amplify the signal above the noise floor of the photodiodes and measure up to the standard quantum limit. Because this is an interference effect, the local oscillator defines the spatio-temporal mode of the signal that is amplified and measured. For efficient measurement the overlap between the signal and oscillator modes should be substantial. If the two fields are at the same frequency (homodyne) this is a stable measurement of the generalized quadrature component $\hat{q}_\theta$ with reference phase θ defined with respect to the local oscillator. If the signal frequency is detuned slightly (heterodyne) then the interference term is the beat signal between the two.

Bibliography - Quantum states of light

75. U. Leonhardt, *Measuring the quantum state of light* (Cambridge University Press, 1997).

76. D. F. Walls, and G. J. Milburn, *Quantum optics*, 2nd ed. (Springer, Berlin, 2008).

77. P. Lambropoulos, and D. Petrosyan, *Fundamentals of quantum optics and quantum information* (Springer, Heidelberg, 2007).

78. M. Orszag, *Quantum optics including noise reduction, trapped ions, quantum trajectories and decoherence* (Springer, Berlin, Heidelberg, New York, 2008).

79. A. I. Lvovsky, Squeezed light, in *Photonics Sci. Found. Technol. Appl. Vol. 1*, edited by D. L. Andrews, (John Wiley & Sons, Inc., Hoboken, NJ, 2015), pp. 121–163.

80. M. Hillery, et al., Distribution functions in physics: Fundamentals, *Phys. Rep.* **106**, 121–167 (1984).

81. G. Agarwal, Wigner-function description of quantum noise in interferometers, *J. Mod. Opt.* **34**, 909–921 (1987).

82. V. V. Dodonov, O. V. Man'ko, and V. I. Man'ko, Photon distribution for one-mode mixed light with a generic Gaussian Wigner function, *Phys. Rev. A* **49**, 2993–3001 (1994).

83. R. J. Glauber, The quantum theory of optical coherence, *Phys. Rev.* **130** (1963).

84. R. Hanbury Brown, and R. Twiss, Correlation between photons in two coherent beams of light, *Nature* **177**, 27–29 (1956).

85. R. Hanbury Brown, and R. Q. Twiss, A test of a new type of stellar interferometer on Sirius, *Nature* **178**, 1046–1048 (1956).

86. H. Kimble, M. Dagenais, and L. Mandel, Photon antibunching in resonance fluorescence, *Phys. Rev. Lett.* **39**, 691–695 (1977).

87. P. Grangier, G. Roger, and A. Aspect, Experimental evidence for a photon anti-correlation effect on a beam splitter: A new light on single-photon interferences, *Europhys. Lett.* **1**, 173–179 (1986).

88. H. P. Yuen, and V. W. S. Chan, Noise in homodyne and heterodyne detection, *Opt. Lett.* **8**, 177 (1983).

89. G. L. Abbas, V. W. S. Chan, and T. K. Yee, Local-oscillator excess-noise suppression for homodyne and heterodyne detection, *Opt. Lett.* **8**, 419 (1983).

Atom-light interactions

I am a quantum engineer, but on Sundays I have principles.
– John Bell, *The Underground Colloquium* (1983)

The most fundamental interaction between light and matter is the emission and absorption of single photons by single quantum emitters. This elementary process is the essential physics underlying many phenomena, and controlling this interaction is the basis for diverse applications in quantum technology. For these reasons, complete control of the light-matter interaction at the single-quanta level is one of the central goals of quantum optics.

Novel materials with coherent transitions are being manufactured for quantum technologies, but such transitions occur naturally in atomic systems. The valence electron of hydrogen-like atoms may have Zeeman or hyperfine split ground states, and metastable dipole-forbidden excited states. These narrow-linewidth transitions have long coherence times suitable for quantum information. Dipole-forbidden transitions can be addressed coherently with narrow-linewidth lasers, and Zeeman split transitions can be driven with RF fields. Where the metastable state cannot be addressed directly, or where it is inefficient to do so, we can couple two long-lived states via a two-photon Raman process through a third, short-lived excited state.

The physics of atom-light interactions will be essential to the work of this thesis. In this chapter we introduce the interaction between single atoms and light fields, which will be sufficient for the trapped-atom experiments in Chaps. 7 and 8. Later in Chap. 13, we will expand this theory to include the interaction of light fields and large atomic ensembles. A complete and self-consistent description requires that we treat both the fields and atoms quantum mechanically, but in many cases a 'semi-classical' approach, in which some or all fields are classical will be sufficient.

3.1 The Jaynes-Cummings model

The simplest atom-light system is a single atom interacting with a single-mode field near resonance. The dynamics of an atom-field system are given by solutions to the Schrödinger equation with the system Hamiltonian

$$\hat{H} = \hat{H}_{\mathrm{a}} + \hat{H}_{\mathrm{f}} + \hat{H}_{\mathrm{int}} \tag{3.1}$$

comprising the atom, field and interaction Hamiltonians. We have already described the quantum field in some detail in the previous chapter, and from Eqn. 2.15 we have the

Hamiltonian for a monochromatic single mode field of frequency ω,

$$\hat{H}_{\mathrm{f}} = \hbar\omega a^{\dagger}a \tag{3.2}$$

where we have set the zero-point energy of the field to zero for convenience. Now to understand the interaction of this field we must introduce the atomic configuration energy and the corresponding operators as well.

3.1.1 Atomic operators

The energy eigenstates of hydrogen-like atoms consist of an infinite number of discrete levels corresponding to the bound states of the atomic electron. The lowest energy configuration of electrons in the atomic potential is the ground state $|g\rangle$. The simplest non-trivial atomic system is the two-level atom with excited state $|e\rangle$ and ground state atomic transition frequency ω_0. For convenience, we will choose the zero-point energy half way between the energy of the two atomic states. We introduce atomic spin operators for the two-level system in terms of the Pauli spin matrices $\sigma_{x,y,z}$

$$\hat{\sigma}_+ = \tfrac{1}{2}\left(\hat{\sigma}_x + i\hat{\sigma}_y\right) = |e\rangle\langle g| \; , \tag{3.3}$$

$$\hat{\sigma}_- = \tfrac{1}{2}\left(\hat{\sigma}_x - i\hat{\sigma}_y\right) = |g\rangle\langle e| \; , \tag{3.4}$$

$$\hat{\sigma}_z = |e\rangle\langle e| - |g\rangle\langle g| \; . \tag{3.5}$$

The spin operators $\hat{\sigma}_{\pm}$ are also called raising and lowering operators because they represent transitions between the two states of our spin-$\tfrac{1}{2}$ equivalent system. The Hamiltonian of the atomic system is simply

$$\hat{H}_{\mathrm{a}} = \tfrac{1}{2}\hbar\omega_0\sigma_z \; . \tag{3.6}$$

It remains only to find the interaction Hamiltonian of the atom-field system.

3.1.2 Dipole approximation

In the classical dipole approximation the energy of the system is the energy of the electron-nucleus dipole in an external electric field. The quantum dipole operator $\hat{\mathbf{d}} = e\hat{\mathbf{r}}$ is proportional to the position operator $\hat{\mathbf{r}}$. The Coulomb potential about the atomic nucleus is spherically symmetric, and therefore the electronic eigenstates $|g\rangle$ and $|e\rangle$ have no net dipole moment. Writing the dipole operator in the spin-operator basis, the diagonal terms $\langle g|\hat{\mathbf{d}}|g\rangle$ and $\langle e|\hat{\mathbf{d}}|e\rangle$ are zero. The off-diagonal terms are $\langle e|\hat{\mathbf{d}}|g\rangle = \mathbf{d}_{eg} = \mathbf{d}_{ge}^* = \mathbf{d}\hat{\sigma}_-$ where $\mathbf{d}$ is the transition dipole moment. The interaction Hamiltonian is therefore

$$\hat{H}_{\mathrm{int}} = -\hat{\mathbf{d}} \cdot \hat{\mathbf{E}} \tag{3.7}$$

$$= \hbar g(\hat{\sigma}_- + \hat{\sigma}_+)(\hat{a} + \hat{a}^{\dagger}) \tag{3.8}$$

where the atom-field coupling constant g is given by

$$g = \frac{1}{\hbar}\left(\mathbf{u}(\mathbf{r}) \cdot \mathbf{d}_{eg}\right) \tag{3.9}$$

at the position **r** of the atom. For a plane wave the coupling constant g depends on the mode volume V and polarization **e**

$$g = \frac{\epsilon_\omega}{\sqrt{2\hbar}}(\mathbf{e} \cdot \mathbf{d}_{eg}) = \sqrt{\frac{\omega}{2\hbar\epsilon_0 V}}(\mathbf{e} \cdot \mathbf{d}_{eg}) \,. \tag{3.10}$$

Dipole transitions can involve the exchange of angular momentum. The angular momentum of the atomic configuration about the quantization axis is given by the magnetic quantum number m. Dipole transitions with $\Delta m = 0$ (π transitions) do not change the total angular momentum of the atomic system, but transitions with $\Delta m = \pm 1$ ($\sigma_\pm$ transitions) involve the exchange of one unit of angular momentum from the field to the atom (or vice versa). Higher order multipole transitions may involve the exchange of even more angular momentum. We explore the particular spatial field associated with dipole transitions and the way this field may carry angular momentum in Chap. 4.

3.1.3   The interaction picture

The atom and field are interacting subsystems, with their own internal configuration energies H_a and H_f. It is convenient to solve such problems in the interaction picture. Compared to the Schrödinger picture, the interaction picture allows us to separate dynamics with different timescales. We define the total subsystem energy $H_0 = H_\mathrm{a} + H_\mathrm{f}$. In the interaction picture states and operators transform according to the free evolution operator

$$\hat{U} = e^{i\hat{H}_0 t/\hbar} \tag{3.11}$$

$$|\tilde{\psi}\rangle = \hat{U}^\dagger |\psi\rangle \tag{3.12}$$

$$\hat{\tilde{o}} = \hat{U}^\dagger \hat{o} \hat{U} \tag{3.13}$$

and these states evolve according to a system Hamiltonian given by the transformed interaction Hamiltonian

$$\hat{\tilde{H}} = \hat{U}^\dagger \hat{H}_\mathrm{int} \hat{U} \,, \tag{3.14}$$

$$i\hbar \frac{\mathrm{d}|\tilde{\psi}\rangle}{\mathrm{d}t} = \hat{\tilde{H}}|\tilde{\psi}\rangle \,. \tag{3.15}$$

3.1.4   The rotating wave approximation

The optical and atomic subspaces commute, which allows us to decompose the unitary transformation as follows

$$\hat{U} = \left(e^{\frac{1}{2}i\hbar\omega_0}\hat{\sigma}_{gg} + e^{-\frac{1}{2}i\hbar\omega_0}\hat{\sigma}_{ee} \right) \otimes \left(e^{-i\omega\hat{a}^\dagger\hat{a}} \right) \,. \tag{3.16}$$

Transforming the dipole interaction Hamiltonian $\hat{H}_i$ into the interaction picture we

have

$$\hat{\tilde{H}} = \hat{U}^\dagger \hat{H}_i \hat{U} \tag{3.17}$$

$$= \hbar g \left(e^{-i\omega_0 t} \hat{\sigma}_+ + e^{i\omega_0 t} \hat{\sigma}_- \right) \otimes \left(e^{-i\omega t} \hat{a}^\dagger + e^{i\omega t} \hat{a} \right) \tag{3.18}$$

$$= \hbar g \left(\hat{a}^\dagger \hat{\sigma}_- e^{i(\omega-\omega_0)t} + \hat{\sigma}_+ \hat{a} e^{-i(\omega-\omega_0)t} + \hat{a}^\dagger \hat{\sigma}_+ e^{i(\omega+\omega_0)t} + \hat{\sigma}_- \hat{a} e^{i(\omega+\omega_0)t} \right) . \tag{3.19}$$

This Hamiltonian has near-resonant terms $\hat{a}^\dagger \hat{\sigma}_-$ and $\hat{\sigma}_+ \hat{a}$ that correspond to atomic relaxation and photon creation, and atomic excitation and photon destruction respectively. These terms oscillate with frequency $\Delta = \omega - \omega_0$ corresponding to the detuning of the field from the atomic transition. For near-resonance fields $|\Delta| \ll \omega$. The remaining terms $\hat{a}^\dagger \sigma_+$ and $\hat{\sigma}_- \hat{a}$ describe non-resonant processes in which the atom and field gain or lose excitations simultaneously. These terms do not conserve energy, and only contribute to higher-order processes in which energy conservation may be violated at intermediate steps.

The non-resonant terms oscillate with frequency $\omega_0 + \omega \approx 2\omega \gg |\Delta|$. We will be interested in the dynamics of the system over timescales much longer that the optical period such that the contribution of the non-resonant terms will quickly average to zero. In the 'rotating wave' approximation we neglect these terms from the Hamiltonian completely

$$\hat{\tilde{H}} = -\hbar g \left(e^{-i\Delta t} \hat{\sigma}_+ \hat{a} + e^{i\Delta t} \hat{\sigma}_- a^\dagger \right) . \tag{3.20}$$

This approximation will remain valid so long as we describe weak interactions near resonance. Transforming back into the Schrödinger picture by reversing Eqns. 3.11 leaves us with the Jaynes-Cummings Hamiltonian [90]

$$\hat{H} = \tfrac{1}{2}\hbar \omega_0 \sigma_z + \hbar \omega \hat{a}^\dagger \hat{a} + \hbar g \left(\hat{\sigma}_+ \hat{a} + \hat{a}^\dagger \hat{\sigma}_- \right) . \tag{3.21}$$

3.2 Semi-classical atom-light interactions

The Jaynes-Cummings model above provides a complete description of the interaction between a two-level atom and a monochromatic field, treating both the field and the atom quantum mechanically [90, 91]. However, in this thesis we will often consider the interaction of atoms with laser beams, and when the laser field is bright we can simplify the Hamiltonian considerably. At optical frequencies, even a low power (1 μW) beam contains many orders of magnitude more photons than the scattering rate of an atomic transition. In this case, excitation and relaxation by the atom have a negligible impact on the energy of the field, leaving it essentially unchanged by the interaction, and we can eliminate H_f from the Hamiltonian completely. Additionally, the laser field is coherent (see Sec. 2.2.2) and bright coherent states have the same effect as a classical monochromatic wave. We can therefore replace the quantum field of Eqn. 3.21 with a classical field, but continue treating the atomic system as quantum, in the so called 'semi-classical' approach.

Replacing the quantum light field with a classical plane-wave field with polarization $\mathbf{e}$, complex amplitude E_0 and phase ψ we have

$$\mathbf{E} = 2\mathbf{e}|E_0| \cos\left(\omega t - \psi\right) = \mathbf{e}\left(E_0 e^{-i\omega t} + E_0^* e^{i\omega t}\right) . \tag{3.22}$$

The dipole interaction Hamiltonian (Eqn. 3.7) with this classical field becomes

$$\hat{H}_i = -\hat{\mathbf{d}} \cdot \mathbf{E} \tag{3.23}$$

$$= -\hbar\hat{\sigma}_+ \left(\Omega e^{-i\omega t} - \Omega e^{i\omega t}\right) + h.c. , \tag{3.24}$$

where we have introduced the Rabi frequency

$$\Omega \equiv (\mathbf{d}_{eg} \cdot \mathbf{e})|E_0|/\hbar , \tag{3.25}$$

which is the semi-classical equivalent of the positive frequency quantum field and coupling strength

$$g\hat{a} \rightarrow \Omega . \tag{3.26}$$

We can make the rotating wave approximation with classical fields, just as we did for the quantized field in the Jaynes-Cummings Hamiltonian, or alternatively we can make the above classical wave substitution directly to Eqn. 3.20. In the semi-classical limit we therefore have the interaction picture Hamiltonian

$$\hat{\tilde{H}} = -\hbar \left(\Omega e^{-i\Delta t}\hat{\sigma}_+ + \Omega^* e^{i\Delta t}\hat{\sigma}_-\right) . \tag{3.27}$$

To isolate only the slowly varying components of the system, we write the Schrödinger picture Hamiltonian in a frame that rotates with the optical field. To move into a frame rotating at frequency ω we make transformations

$$|\psi\rangle' = \hat{U}^\dagger |\psi\rangle , \tag{3.28}$$

$$\hat{H}' = -i\hbar\hat{U}^\dagger\frac{\mathrm{d}\hat{U}}{\mathrm{d}t} + \hat{U}^\dagger\hat{H}\hat{U} , \tag{3.29}$$

$$\hat{U} = e^{i\omega t} . \tag{3.30}$$

Leaving us with [77]

$$\hat{H}' = -\hbar\Delta\hat{\sigma}_{ee} - \hbar\left(\Omega\hat{\sigma}_+ + \Omega^*\hat{\sigma}_-\right) , \tag{3.31}$$

where $\hat{\sigma}_{ee} = \hat{\sigma}_+\hat{\sigma}_- = |e\rangle\langle e|$. This is the Hamiltonian that we will use to model the interaction of atoms with coherent, bright light fields provided by laser systems.

3.3   Spontaneous emission and damping

To this point we have considered only the reversible unitary evolution of the atom-field system given by the Schrödinger equation. In this description the field was restricted to a single (unspecified) quasi-resonant mode. All possible degrees of freedom are included in the atom-field state operator and so coherence is always maintained. However, in realistic situations the atomic system is not perfectly isolated. The atom is almost always interacting with a reservoir of infinitely many closely-spaced (or continuum) energy states. To describe the interaction of an atom with such reservoir fields we must trace over the external degrees of freedom (sometimes called the reservoir 'bath') and consider exclusively the dynamics of our chosen subsystem. Information about the complete system is lost in this process so that even pure initial states of the subsystem evolve to statistical mixtures. The spontaneous decay of an atomic excited state, cavity field losses and other sources of decoherence will be included in our model in terms of such reservoir interactions.

The evolution of the reduced atomic density operator $\hat{\rho}$ is given by a master equation [77]

$$\frac{\partial}{\partial t}\hat{\rho} = -\frac{i}{\hbar}\left[\hat{H}, \hat{\rho}\right] + \hat{\mathcal{L}}(\hat{\rho}).$$ (3.32)

where the first term is the reversible Schrödinger evolution derived above, and the second is the Liouvillian superoperator containing all dissipative system dynamics. In general the Liouvillian has Lindblad form

$$\hat{\mathcal{L}} = \sum_i \tfrac{1}{2}\left(2\hat{C}_i\hat{\rho}\hat{C}_i^\dagger - \hat{C}_i^\dagger\hat{C}_i\hat{\rho} - \hat{\rho}\hat{C}_i^\dagger\hat{C}_i\right),$$ (3.33)

where the jump operator $\hat{C}_i$ that models the dynamics of the i-th decay process contains relaxation rate Γ_i. Since the Liouvillian is linear in the components of $\hat{\rho}$ we can write the evolution as a system of coupled linear equations for the components of $\hat{\rho}$, these are the optical Bloch equations.

Spontaneous emission is modelled with the atomic transition jump operator $\hat{C}_{eg} = \sqrt{\Gamma_{eg}}\hat{\sigma}_-$. The free-space atomic decay rate of a two level atom in the dipole limit is given by [92]

$$\Gamma_{eg} = \frac{4\omega^3\alpha|\hat{\mathbf{r}}_{eg}|^2}{3c^2} = \frac{4\omega^3\alpha d_{eg}^2}{3e^2c^2} = \frac{\omega^3 d_{eg}^2}{3\times 2\pi\epsilon_0\hbar c^3},$$ (3.34)

where α is the dimensionless fine structure constant

$$\alpha = \frac{1}{4\pi\epsilon_0}\frac{e^2}{\hbar c} \approx 137.$$ (3.35)

The probability to find an atom initially prepared in the excited state decays as $e^{-\Gamma_{eg}t}$. In addition to this spontaneous decay term, the coupling between the atom and the vacuum modes of the reservoir produces an atomic energy level shift called the Lamb shift [77, 93]. In the model described so far we incorporate the Lamb shift by assuming it is already included in the atomic energy eigenvalues.

Solving the system for the steady state condition $\frac{\mathrm{d}}{\mathrm{d}t}\hat{\rho} = 0$ yields the free space atomic scattering rate under continuous excitation

$$\Gamma_{\mathrm{sc}} = \tfrac{1}{2}\Gamma_{eg}\frac{I/I_{\mathrm{s}}}{1 + I/I_{\mathrm{s}} + 4\left(\frac{\Delta}{\Gamma_{eg}}\right)^2},$$ (3.36)

where I_{s} is the saturation intensity

$$I_{\mathrm{s}} = \frac{\hbar\omega^3\Gamma_{eg}}{4\pi c^2}$$ (3.37)

and the intensity and Rabi frequency are related by $I/I_{\mathrm{s}} = 2\Omega^2/\Gamma^2$. Without coherent control the mean excited state population over time is bounded to $\langle\rho_{ee}\rangle \leq \tfrac{1}{2}$ and $\Gamma_{\mathrm{sc}} \leq \tfrac{1}{2}\Gamma_{eg}$.

Atomic coherences relax with rate $\gamma_{eg} = \tfrac{1}{2}\Gamma_{eg} + 2\Gamma_{ee}$ where Γ_{ee} contains the contributions of all possible decoherence mechanisms, for example by phase fluctuations of the driving field or by elastic atomic collisions [77]. Decoherence terms are incorporated by including jump operator $\hat{C}_{ee} = \sqrt{\gamma_{ee}}\hat{\sigma}_z$ where γ_{ee} is, for example, the linewidth of the driving laser $\Delta\omega$.
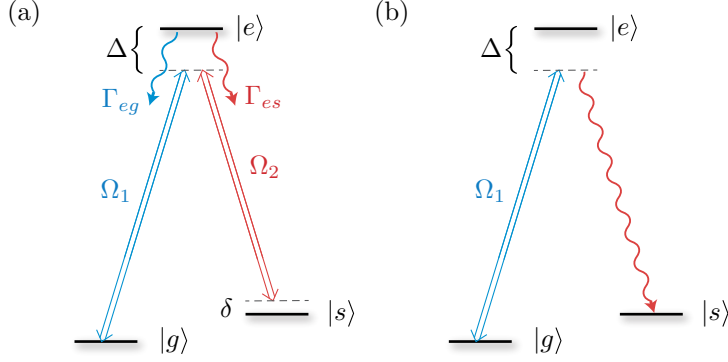
Figure 3.1: (a) Energy level configuration of a Λ-type three-level atom driven by two classical fields. (b) Raman scattering a stokes photon from the Λ-atom by driving with a single classical field.

3.4   The Λ configuration

So far we have considered only a two-level atom interacting with optical fields. This is a suitable model for cyclic transitions between ground and excited states driven by a single near-resonant field, but in this thesis we will explore systems with multiple levels and decay pathways, and drive those systems with multiple fields. Where necessary we will use a complete many-level model of the atomic system, but most of the important phenomena we will explore can be captured by a straightforward extension of the two level atom: the three level atom in a Λ configuration. In this configuration, the excited state $|e\rangle$ couples not only to the ground state $|g\rangle$, but also to an additional low energy state $|s\rangle$. The state $|s\rangle$ couples only weakly (or not at all) to $|g\rangle$ (this transition may, for example, be dipole-forbidden) and so we say the state $|s\rangle$ is metastable. Two fields addressing the atomic transitions $|g\rangle \rightarrow |e\rangle$ and $|s\rangle \rightarrow |e\rangle$ together can drive a two-photon 'Raman' transition between the ground and metastable states shown in Fig. 3.1(a).

We introduce atomic operators $\hat{\sigma}_{ij} = |i\rangle\langle j|$ for the multilevel system analogous to raising and lowering operators for the $|i\rangle \rightarrow |j\rangle$ transition. The atomic Hamiltonian of the three level system is

$$\hat{H}_{\mathrm{a}} = \hbar \left(\omega_g \hat{\sigma}_{gg} + \omega_e \hat{\sigma}_{ee} + \omega_s \hat{\sigma}_{ss} \right) \tag{3.38}$$

and the interaction Hamiltonian of the atom with two classical fields is

$$\hat{H}_{\mathrm{int}} = \hat{\mathbf{d}}_{ge} \cdot \mathbf{E}_1 + \hat{\mathbf{d}}_{se} \cdot \mathbf{E}_2 \,. \tag{3.39}$$

Following the same method we took for the two-level atom above, we can write the semi-classical Hamiltonian of the Λ-configured atom with the rotating wave approximation, but in the frame rotating with the optical fields [77]

$$\hat{H} = -\hbar \left(\Delta \hat{\sigma}_{ee} + \delta \hat{\sigma}_{ss} \right) - \hbar \left(\Omega_1 \hat{\sigma}_{eg} + \Omega_2 \hat{\sigma}_{es} + \mathrm{H.c.} \right) \tag{3.40}$$

where H.c. stands for Hermitian conjugate, $\Omega_{1,2}$ are the Rabi frequencies of the classical fields addressing transitions $|g\rangle \rightarrow |e\rangle$ and $|s\rangle \rightarrow |e\rangle$ respectively, and the two-photon detuning is $\delta = \Delta_1 - \Delta_2$. The system also has jump operators corresponding to spontaneous emission into the two low-energy states $\hat{C}_{eg} = \sqrt{\Gamma_{eg}}\hat{\sigma}_{eg}$ and $\hat{C}_{es} = \sqrt{\Gamma_{es}}\hat{\sigma}_{es}$, and decoherence terms $\hat{C}_{gg} = \sqrt{\Gamma_{gg}}\hat{\sigma}_{gg}$ and $\hat{C}_{ss} = \sqrt{\Gamma_{ss}}\hat{\sigma}_{ss}$ that are included in the Liouvillian
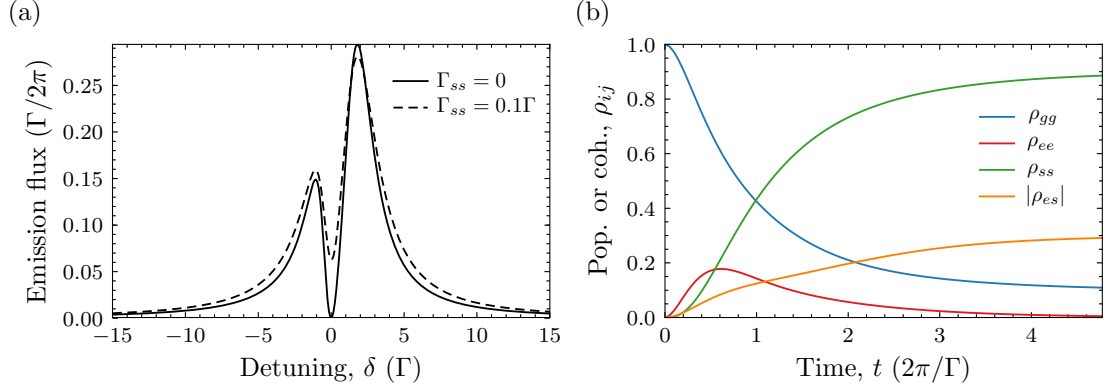
Figure 3.2: Characteristic behaviour of the Λ-atom. (a) Resonance fluorescence spectrum of the atom near saturation showing the dark resonance at $\delta = 0$ with and without decoherence. The parameters are $\Gamma_{eg} = \Gamma_{es} = \Gamma/2$, $\Delta = \Gamma$, $\Omega_1 = \Gamma$, $\Omega_2 = 0.7\Gamma$. (b) Continuous driving with $\delta = 0$ pumps the atom to the dark state. The atom is prepared in ground state $|g\rangle$ and converges to the steady-state superposition $|D\rangle$ under continuous weak excitation. In this state the excited population $\rho_{ee} = 0$ and the atom goes dark. Increasing the field powers beyond saturation produces no improvement in pumping time, but may induce Rabi oscillations. The parameters are $\Gamma_{eg} = \Gamma_{es} = \Gamma/2$, $\Delta = \Gamma$, $\Omega_1 = 0.3\Gamma$, $\Omega_2 = 0.1\Gamma$, $\Gamma_{ss} = 0$.

(Eqn. 3.33).

3.4.1   Dark resonances, optical pumping and Raman scattering

The two-photon Raman transition occurs when the two-photon detuning is small. With $\delta \approx 0$ and $\Delta \lesssim \Omega_{1,2}$ the eigenstates of Eqn. 3.40 are

$$
\begin{aligned}
|D\rangle &= \frac{1}{\sqrt{\Omega_1^2 + \Omega_2^2}} \left(\Omega_2 |g\rangle - \Omega_1 |s\rangle \right) , \\
|B_\pm\rangle &= \frac{1}{\sqrt{\Omega_1^2 + \Omega_2^2 + \lambda_\pm^2}} \left(\Omega_1 |g\rangle - \lambda_\pm |e\rangle + \Omega_2 |s\rangle \right) ,
\end{aligned}
\tag{3.41}
$$

where $\lambda_\pm = \pm\sqrt{\Omega_1^2 + \Omega_2^2 + (\Delta/2)^2} - \Delta/2$ are the two non-zero energy eigenvalues. The excited state population of the so-called 'dark' eigenstate $|D\rangle$ is zero, it is completely decoupled from the two driving fields. So long as the only damping terms included are spontaneous emission from the excited state, the dark state is the stationary state of the Λ system. Continuous driving with two-photon resonant fields prepares the atom in the low-energy state superposition $|D\rangle$ and the atomic fluorescence goes to zero. Decoherence between the states $|g\rangle$ and $|s\rangle$ upsets the superposition $|D\rangle$ and in this case the excited state population of the stationary state and the atomic fluorescence rate are non-zero. This dark resonance is a distinctive feature of the resonance spectrum of multi-level atoms, in Chap. 7 we use the depth, width and position of dark resonances in the atomic spectrum to identify the driving parameters of a trapped-atom photon source. Fig. 3.2 shows the resonance fluorescence spectrum of a Λ-atom under continuous driving as a function of the two-photon detuning δ with and without decoherence between the low-energy states.

When one of the driving fields is zero the dark state is the bare atomic state $|g\rangle$ (for $\Omega_1 = 0$) or $|s\rangle$ (for $\Omega_2 = 0$). In this configuration the atom is driven until it decays to the

unaddressed bare state, in which it is trapped. Such optical 'pumping' is characteristic of multi-level atoms. For example, atoms with multiple Zeeman-split ground states can be prepared in one of the extremal Zeeman states by pumping with $\sigma_\pm$ fields that drive only $\Delta_m = \pm 1$ transitions. Throughout this thesis we will use optical pumping to prepare atomic systems in a chosen pure state so that we may control the subsequent coherent evolution of the system.

The same process can be used to control the emission of single photons from the Λ atom system by Raman scattering. During Raman scattering, incident fields interact with an atomic system to cause the generation of a field at a different frequency. For example, the Λ-atom prepared in the ground state and driven only by field $\mathbf{E}_1$ will eventually Raman-scatter a single-photon to the vacuum field $\hat{\mathbf{E}}_2$ with energy difference $\hbar(\omega_g - \omega_s)$ as shown in Fig. 3.1(b).

3.4.2 Stimulated Raman adiabatic passage

When the field amplitudes $\Omega_{1,2}$ are allowed to vary in time, the instantaneous dark state $|D\rangle$ follows. If the rate of change is slow compared to the dressed state energy splitting, that is

$$\left| \frac{\dot{\Omega}_1 \Omega_2 - \Omega_1 \dot{\Omega}_2}{\Omega_1^2 + \Omega_2^2} \right| \ll |\lambda_+ - \lambda_-|, \tag{3.42}$$

then an atom prepared in one dark state will follow the instantaneous dark state adiabatically such that $\rho = |D\rangle \langle D|$ and $\rho_{ee} = 0$ at all times. For example, an atom initially in state $|g\rangle$ can be coherently transferred to state $|s\rangle$ by two partially overlapping time-dependent pulses, an Ω_2 pulse followed by an Ω_1 pulse because $|g\rangle$ is an eigenstate when $\Omega_1 = 0$. This coherent population transfer technique, called stimulated Raman adiabatic passage (StiRAP) [94], is an essential technique of coherent control with atom-like systems. In strongly coupled atom-light systems, the vacuum-StiRAP process can be used to generate a photon coherently and deterministically from an atomic excitation.

3.5 Numerical modelling

Under some circumstances the optical Bloch equations of the Λ-atom allow analytic solutions. In this thesis we will prefer analytic solutions when they exist, but for many more complicated scenarios we will resort to numerically solving the system dynamics. In this case we will rely on the Quantum Toolbox in Python (QuTiP) [95] which is an open source solver for open quantum systems that leverages the well-known Numpy, SciPy and Cython libraries. QuTiP allows the numerical integration quantum systems with time-dependent Hamiltonians and collapse operators given a Linblad master equation of the sort derived in this chapter. QuTiP allows for an enormous amount of flexibility with ensemble and Monte-Carlo solvers, steady-state solvers, correlation calculators and parallel processing support.

Bibliography - Atom-light interactions

77. P. Lambropoulos, and D. Petrosyan, *Fundamentals of quantum optics and quantum information* (Springer, Heidelberg, 2007).

90. E. Jaynes, and F. Cummings, Comparison of quantum and semiclassical radiation theories with application to the beam maser, *Proc. IEEE* **51**, 89–109 (1963).

91. L. Allen, and J. H. Eberly, *Optical resonance and two-level atoms* (Wiley, 1975).

92. D. A. Steck, *Quantum and atom optics* (2007).

93. W. E. Lamb, and R. C. Retherford, Fine structure of the hydrogen atom by a microwave method, *Phys. Rev.* **72**, 241–243 (1947).

94. U. Gaubatz, et al., Population switching between vibrational levels in molecular beams, *Chem. Phys. Lett.* **149**, 463–468 (1988).

95. J. Johansson, P. D. Nation, and F. Nori, QuTiP: An open-source Python framework for the dynamics of open quantum systems, *Comput. Phys. Commun.* **183**, 1760–1772 (2012).

Imaging atomic transitions

...some [atoms] make no effort to look like their pictures.

– Salvador Dalí

The quantum information protocols introduced in Chap. 1 require the efficient and reversible interaction of light with atomic systems as a prerequisite. One of the most promising demonstrated approaches to this problem is to use protocols that reversibly couple a photon into a collective excitation across an ensemble of atoms. We will explore this in detail in Part III, but in general there is a trade off between the number of entangled components and the degree of isolation and control that is possible over the entangled state. Single trapped atoms make excellent qubits, but have a small interaction cross-section with travelling light fields. We've already discussed a second, and very successful, strategy to enhance the coupling strength of optical qubits to single-atoms systems: the use of optical resonators. However, in principle the resonator—and the accompanying bandwidth compromise—are not necessary to achieve this single-photon π pulse.

The time reversal symmetry of Schrödinger's and Maxwell's equations implies that there exist conditions for the perfect absorption of an incident photon by an atom in free-space. Because the emission of a photon from an atom prepared in the excited state happens with perfect efficiency, it follows that the the inverse process is sufficient for efficient absorption. To realize this prediction of quantum optics it is necessary to engineer photons with the time-reversed temporal wave-packet of the spontaneously emitted photons [96], in a spatial and polarization mode matched to the radiation pattern of the atomic transition. An atom at the centre of these converging, time-reversed fields produces a non-propagating near-field by back-action until the travelling field converges to atomic dimensions [97].

Therefore an optical network of free-space atoms requires collection optics that are not only close to a complete 4π steradian geometry, but the optics must also map the radiation pattern of the atomic fluorescence to a convenient optical mode. We can impose these criteria: we would prefer a spatial mode that is easy to manipulate with available optics and travels well in fibre. Due to the symmetry of the atom-photon system, the problem of optically networking atoms is intimately connected to the problem of accurately and efficiently imaging atoms, and indeed to the field of sub-wavelength optical microscopy [98]. Even in the absence of an atomic emitter, the time-reversed far-field dipole radiation pattern derived below converges until the wavefronts reach sub-wavelength dimensions, surpassing the typical focal spot size resolution limits of Abbe and Rayleigh. Such tight focussing is desirable not only for atom-light coupling and imaging, but also for optical trapping and tweezers [99].

In this chapter we will derive the spatial distribution of the atomic dipole radiation

field using Bliokh's vectorial method [100] and explore how this radiation field is coupled by common imaging systems. Once we have derived the polarization associated with each partial wave emitted from the source we will map these rays through the imaging system to calculate the output field distribution. In particular, we derive the output field for both a spherical lens and a parabolic mirror. We will compare the travelling photon modes produced when each system images a single atom, and the feasibility of coupling these modes to fibres for optical networks. These are key to understanding the limitations of free-space ion-photon networks, and will be relevant specifically to this thesis when we analyse results from the single ion-imaging apparatus in Chap. 7 and then when we consider the design of the improved ion-imaging apparatus in Chap. 11. Parts of the following theoretical results have been published in

[6] "**Wavelength-scale errors in optical localization due to spin-orbit coupling of light** G. Araneda, S. Walser, Y. Colombe, D. B. Higginbottom, J. Volz, R. Blatt, and A. Rauschenbeutel, *Nature Physics* **14** (2018). "

4.1   Spatial distribution of the atomic dipole

The atomic transitions that couple most strongly to optical fields are dipole transitions, either π transitions with internal angular momentum change $\Delta m = 0$ or σ transitions with $\Delta m = \pm 1$. For the purpose of this analysis we will exclusively consider the spatial distribution of atomic dipole transitions, according to the method of [100]. The far-field spatial mode $\mathbf{u}_{\mathrm{dip}}(\mathbf{r})$ of a photon emitted from an atomic dipole transition with Heisenberg picture dipole operator $\hat{\mathbf{d}}$ is the classical field emitted by the classical dipole oscillating with corresponding dipole moment $\mathbf{d}$[1] [92]:

$$\mathbf{E}^+(\mathbf{r}, t) = \frac{1}{4\pi\epsilon_0}[(\hat{\mathbf{d}} \cdot \hat{\mathbf{r}})\hat{\mathbf{r}} - \hat{\mathbf{d}}]\frac{\dddot{d}^+(t_r)}{c^2 r} \,, \qquad (4.1)$$

where $t_r = t - r/c$ is the retarded time, $\hat{\mathbf{d}}$ is the unit vector of the dipole $\mathbf{d}$ with magnitude d and the dipole is at the coordinate origin. The far-field, or 'radiation limit', is the field distribution after evanescent field terms have decayed, valid when $d \ll \lambda \ll r$. Because this field consists of a narrow spectrum $\Delta|\mathbf{k}| \ll |k|$ of plane waves with $\mathbf{k}$-vectors spherically distributed about the source, we can separate out the normalized angular component expressed in the momentum space of $\mathbf{k}$

$$\tilde{\mathbf{E}} = \sqrt{\frac{3}{8\pi}} \left(\hat{\mathbf{k}} \times (\hat{\mathbf{k}} \times \hat{\mathbf{d}}) \right) \qquad (4.2)$$

where $\hat{\mathbf{k}} = \hat{\mathbf{r}}$ for a source at the origin, we've neglected the time dependence, and we have re-written the dot-difference vector operation from Eqn. 4.1 as a double cross product. In contrast to the common dot-difference form, the double cross product is explicit that the polarization and amplitude of the partial wave emitted by the atomic dipole in direction $\hat{\mathbf{k}}$ is the spherical projection of the dipole $\mathbf{d}$ onto the unit sphere at position $\hat{\mathbf{r}}$. We can

---

[1]On the subject of hats: now that we have replaced the dipole and field operators with their classical equivalents, and can safely proceed through this chapter without doing much further quantum physics, we will use hats almost exclusively to denote unit vectors rather than quantum operators. The exceptions will be limited and clearly marked. We will also distinguish between vector fields in momentum space and position space by accenting momentum space fields with a tilde.

(a)

(b)
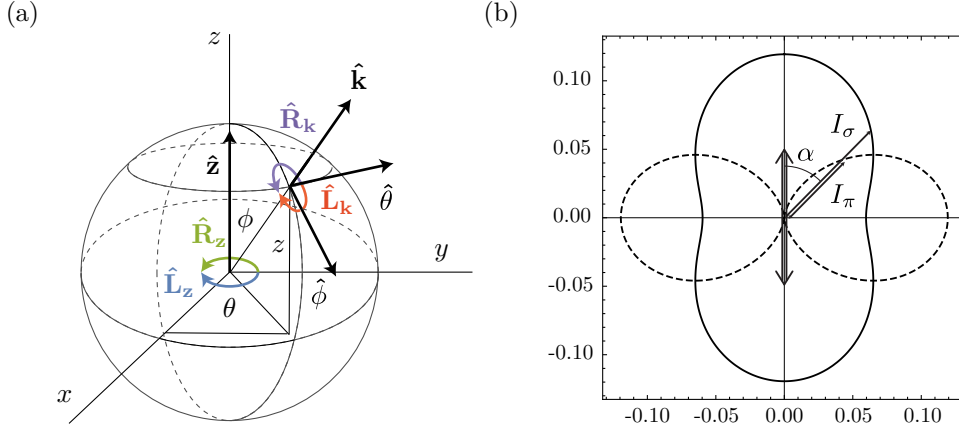
Figure 4.1: (a) The coordinate system and polarization frames in this chapter. The laboratory frame consists of $\hat{\mathbf{z}}$ and the two circular polarizations about $\mathbf{z}$: $\hat{\mathbf{R}}_{\mathbf{z}}$ and $\hat{\mathbf{L}}_{\mathbf{z}}$. When the quantization axis is aligned with $\mathbf{z}$ these basis vectors are the unit dipoles associated with atomic transitions between angular momentum eigenstates. The helical frame is associated with each partial wave with wave vector $\mathbf{k}$ and consists of $\hat{\mathbf{k}}$ and the two circular polarizations about $\mathbf{k}$: $\hat{\mathbf{R}}_{\mathbf{k}}$ and $\hat{\mathbf{L}}_{\mathbf{k}}$. (b) Plot of the dipole intensities I_σ (solid) and I_π (dashed) from Eqn. 4.10. The intensities are shown as a radial function of the angle α from the quantization axis ($\alpha = \phi$ when quantized along the z axis).

therefore treat the dipole geometrically to derive the far-field intensity and polarization distributions. To do so, it will prove convenient to write polarizations in the circular basis $[R_z, L_z, z]$ consisting of the Cartesian basis vector ($\hat{\mathbf{z}}$) along the z-axis and the right ($\hat{\mathbf{R}}_{\mathbf{z}}$) and left ($\hat{\mathbf{L}}_{\mathbf{z}}$) circular basis vectors about the $\hat{\mathbf{z}}$ axis, see Fig. 4.1(a). These basis vectors are the unit dipole vectors associated with transitions between angular momentum eigenstates of an atom quantized along the z axis.

The triple cross product projection in Eqn. 4.2 can be written as the operation of a rotation operator U and the orthogonal plane projection operator P. The rotation operator consists of a zenithal rotation by angle ϕ and two azimuthal rotations by angle θ to transform the basis vector $\hat{\mathbf{z}}$ to the position vector on the unit sphere $\hat{\mathbf{r}} = \hat{\mathbf{r}}(\phi, \theta)$ in spherical coordinates. Explicitly, the rotation operator U in the Cartesian polarization basis is

$$U_L(\phi, \theta) = R_z(-\theta) R_y(-\phi) R_z(\theta) \tag{4.3}$$

$$= \begin{bmatrix} (a-b)\cos^2(\theta) + \sin^2(\theta) & -b\sin(2\theta) & \cos(\theta)\sin(\phi) \\ -b\sin(2\theta) & \cos^2(\theta) + (a-b)\sin^2(\theta) & \sin(\theta)\sin(\phi) \\ -\cos(\theta)\sin(\phi) & -\sin(\theta)\sin(\phi) & a-b \end{bmatrix} \tag{4.4}$$

where substitutions $a = \cos^2(\phi/2)$ and $b = \sin^2(\phi/2)$ have been made for readability. To convert U into our preferred circular polarization basis we apply the unitary transformation

$$V = \frac{1}{\sqrt{2}} \begin{bmatrix} 1 & 1 & 0 \\ -i & i & 0 \\ 0 & 0 & \sqrt{2} \end{bmatrix}, \tag{4.5}$$

giving us

$$U_C(\phi, \theta) = V^\dagger U_L V \tag{4.6}$$

$$= \begin{bmatrix} a & -be^{-2i\theta} & \sqrt{2ab}e^{-i\theta} \\ -be^{2i\theta} & a & \sqrt{2ab}e^{i\theta} \\ -\sqrt{2ab}e^{i\theta} & -\sqrt{2ab}e^{-i\theta} & a-b \end{bmatrix}. \tag{4.7}$$

The projection operator is

$$P = \mathrm{diag}(1, 1, 0). \tag{4.8}$$

We can write the polarization associated with each partial wave propagation vector **k** in either the laboratory reference frame defined above or the helicity frame $[R_k, L_k, k]$ consisting of circularly polarized vectors $\hat{\mathbf{R}}_\mathbf{k}$ and $\hat{\mathbf{L}}_\mathbf{k}$ about the propagation vector $\hat{\mathbf{k}}$ as shown in Fig. 4.1(a). For TEM modes $\mathbf{E} \cdot \mathbf{k}$ is necessarily zero, so only two basis vectors orthogonal to **k** are required in the helicity frame. These reference frames are related by an additional operation of U, which means that the electric field of the dipole fluorescence in the helicity basis and the laboratory reference basis are respectively

$$\tilde{\mathbf{E}}^H(\mathbf{k}) \propto PU^\dagger\hat{\mathbf{d}}, \qquad \tilde{\mathbf{E}}^L(\mathbf{k}) \propto UPU^\dagger\hat{\mathbf{d}}. \tag{4.9}$$

We note here that the $\hat{\mathbf{z}}$ component of $\tilde{\mathbf{E}}^L(\mathbf{k})$ is non-zero (projection in the laboratory frame is followed by a second rotation) which is to say that the dipole field is not paraxial. This is consequential for applications in which the field interacts with inhomogeneous materials, but in this thesis we will restrict ourselves to imaging systems that collimate spherical waves without distorting polarization in the local frame (Sec. 4.3).

From Eqn. 4.9 we can derive the intensity distributions, illustrated in Fig. 4.1(b), of fields due to π and σ transitions quantized along the z axis. At an angle α from the quantization axis the normalized intensity of each transition are the familiar dipole intensity distributions

$$I_\pi = \frac{3}{8\pi}\sin^2(\alpha), \qquad I_\sigma = \frac{3}{16\pi}(1 + \cos^2(\alpha)). \tag{4.10}$$

The projections of two perpendicular vectors onto the unit sphere are also perpendicular, so I_σ can be derived directly from I_π by adding the distributions of two perpendicular linear dipoles.

We can characterize the dipole field more completely by the spatial distribution of Stokes parameters $(S_0 = I, S_1, S_2, S_3)$ which are related to orthogonal field components in the Cartesian (E_x, E_y), diagonal (E_a, E_b) and circular (E_R, E_L) bases and the polarization ellipse parameters ψ and χ by

$$\begin{aligned} I &= E_x^2 + E_y^2 \\ S_1 &= \langle E_x^2 \rangle - \langle E_y^2 \rangle = Ip\cos 2\psi \cos 2\chi \\ S_2 &= \langle E_a^2 \rangle - \langle E_b^2 \rangle = Ip\sin 2\psi \cos 2\chi \\ S_3 &= \langle E_R^2 \rangle - \langle E_L^2 \rangle = Ip\sin 2\chi. \end{aligned}$$

In Fig. 4.2 we plot the Stokes parameters of the spatial fields of two atomic dipoles in the helicity basis. Each disk in this figure is an azimuthal equidistant projection of a hemisphere $\phi \in [0, \pi/2]$ centred on the z-axis showing how the polarization of the dipole field changes as a function of ϕ and θ.
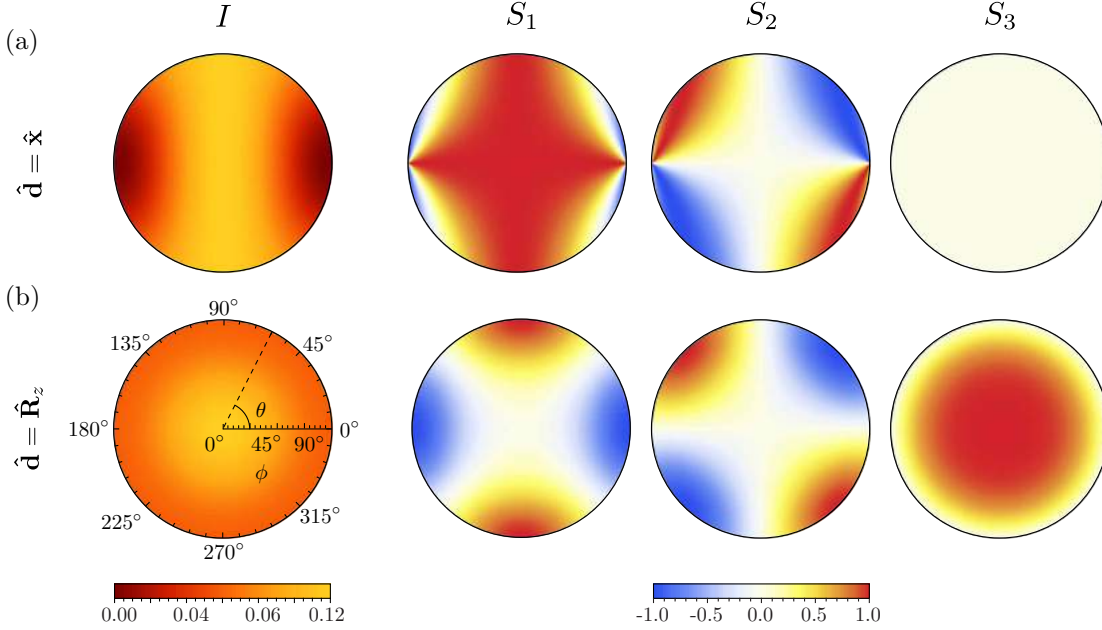
Figure 4.2: Stokes parameters of the optical field emitted by (a) π and (b) σ^+ atomic dipole transitions. The Stokes fields are presented as azimuthal equidistant projections of the hemisphere $\phi \in [0, \pi/2], \theta \in [0, 2\pi]$ such that the z axis is at the centre of the projection and the radial displacement is equal to the zenithal angle ϕ. The quantization axis is aligned with the x axis for the π transition and along the z axis for the σ^+ transition such that the intensity distribution peaks in each case at $\phi = 0$.

With Eqn. 4.9 we can now derive the spatial distribution of an arbitrary atomic dipole transition. Ultimately we will consider how best to image such transitions, but before we move on it's worth considering some noteworthy properties of the dipole fields.

4.2 Optical angular momentum

The total angular momentum of the atom-photon system must be conserved in any photon absorption or emission process. A photon emitted from a transition with internal angular momentum change Δm must carry the opposite angular momentum to compensate. In an external magnetic field, the atomic energy eigenstates are also angular momentum eigenstates, with angular momentum m about the quantization axis. A photon emitted from a dipole transition between these states is also an angular-momentum eigenstate, carrying precisely $+\hbar, -\hbar$ or 0 angular momentum about the quantization axis

$$\hat{J}_z |\psi\rangle = -\Delta m \hbar |\psi\rangle \, , \tag{4.11}$$

where $\hat{J}_z$ [2] is the total angular momentum operator about the quantization axis and $|\psi\rangle$ is the photon state. We can therefore write the single photon field associated with the transitions $\hat{\sigma}_\pm$ about the i-axis as $\left|\sigma_i^\mp\right\rangle = \sigma_i^\mp(\mathbf{r}) |1\rangle$, where $\sigma_i^\mp(\mathbf{r})$ is the spatial mode of a right-handed circular dipole $\mathbf{d} = \hat{\mathbf{R}}_i$ and $|1\rangle$ is the single-photon Fock state. Here we follow the convention that the spin of a $\hat{\mathbf{R}}$ circularly polarized beam is positive. The

---

[2] $\hat{J}_z$ $\hat{l}_z$ and $\hat{s}_z$ are not unit, these are quantum operator hats

photonic angular momentum exists as some combination of spin $\hat{s}_z$ (polarization) and orbital angular momentum $\hat{l}_z$ (spatial phase)

$$\hat{J}_z = \hat{l}_z + \hat{s}_z \,. \tag{4.12}$$

The orbital angular momentum (OAM) operator and spin operator (in the circular basis and laboratory frame) are [100–102]

$$\hat{l}_z = -i\hbar\frac{\partial}{\partial\theta}, \qquad \hat{s}_z = \mathrm{diag}(\hbar, -\hbar, 0) \,. \tag{4.13}$$

The spin $\hat{s}$ may only carry angular momentum about the direction of propagation. These are operators of the normalized photon spatial mode $\mathbf{u}(\mathbf{r})$.

4.2.1   Angular momentum per photon

Where we collect only a portion of the single-photon mode, it is pertinent to ask the angular momentum per collected photon. Once again, we express the momentum as a distribution in $\mathbf{k}$. Because the plane-wave photon component of $|\psi\rangle$ in direction $\hat{\mathbf{k}}$, $|\psi_{\mathbf{k}}\rangle = \mathbf{E}(\mathbf{k})\,|\mathbf{k}\rangle$ is not normalized, asking the momentum per photon in this direction requires renormalization. Formally, the local value of the angular momentum per photon is the weak value [103]

$$J_z^{\mathbf{k}} = \mathrm{Re}\,\frac{\langle\psi_{\mathbf{k}}|\hat{J}_z|\psi\rangle}{\langle\psi_{\mathbf{k}}|\psi\rangle} = \frac{J_z(\mathbf{k})}{I(\mathbf{k})} \,, \tag{4.14}$$

and the same renormalization can be performed to define local values of s_z and l_z.

If the total field is an angular momentum eigenstate, then $|\psi_{\mathbf{k}}\rangle$ is also an eigenstate of $\hat{J}_z$ and $J_z^{\mathbf{k}} = J_z \; \forall\, \mathbf{k}(\phi,\theta)$. When the total field is not an angular momentum eigenstate, interference between the components of superposed momentum eigenstate fields can produce spatial dependence in the momentum per photon (local wave vector) of the total field, and even lead to local values of $J_z^{\mathbf{k}}$ that exceed the eigenstate spectrum where the field intensity is weak. Such 'supermomentum' is an example of superoscillation in interfering fields [103, 104]. We show how supermomentum manifests in dipole fields in Sec. 7.5.2 and in Ref. [6].

4.2.2   Dipole angular momentum distribution

Even when the total field is an angular momentum eigenstate, the partial wave components are not generally an eigenstate of $\hat{l}_z$ and $\hat{s}_z$ [104]. With operators $\hat{l}_z$ and $\hat{s}_z$ from Eqns. 4.13 and dipole field given by Eqn. 4.9 we can calculate the expectation value of the spin and OAM of light from an atomic dipole quantized along the z axis [105]

$$\left\langle \hat{l}_z \right\rangle = \hbar\Delta m \frac{\sin^2(\phi)}{1 + \cos^2(\phi)} \tag{4.15}$$

$$\left\langle \hat{s}_z \right\rangle = \hbar\Delta m \frac{2\cos^2(\phi)}{1 + \cos^2(\phi)} \,. \tag{4.16}$$

Conservation of angular momentum requires that the sum of these expectation values is $-\hbar\Delta m$ for every partial wave, that is $\forall\,\mathbf{k}(\phi,\theta)$. Furthermore, this must also be true for each polarization component of the field in any (laboratory) basis.
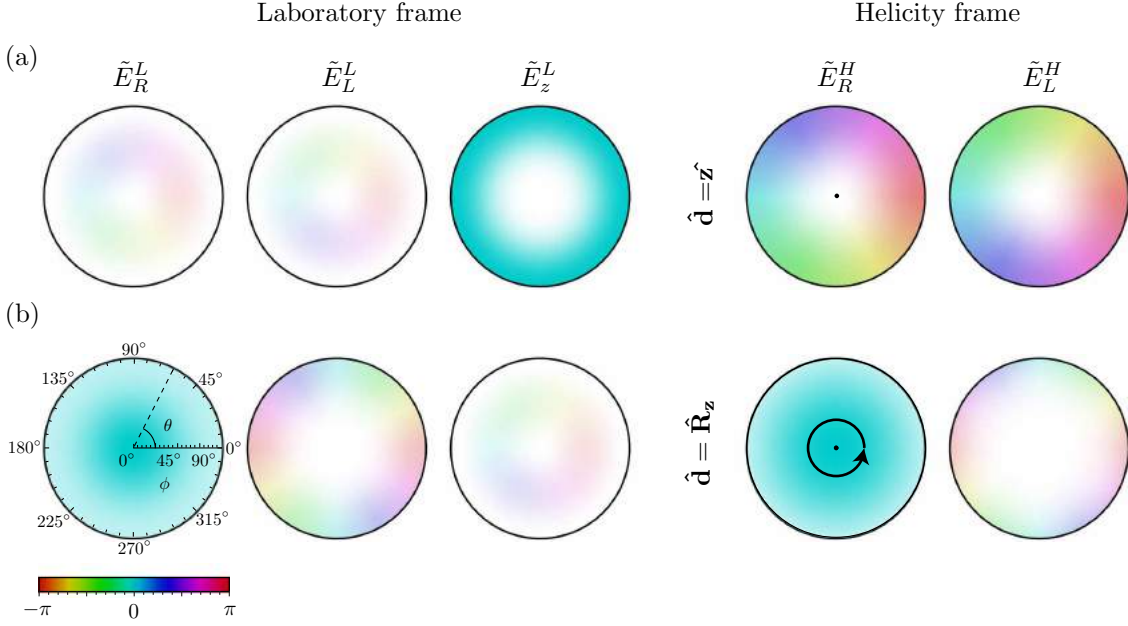
Figure 4.3: Optical field components of (a) π and (b) σ_+ dipoles quantized along z. The fields are shown as azimuthal equidistant projections of a hemisphere centred on the optical axis, directed out of the page. Polarization components $E_{x=R,L,z}$ are plotted with hue $\underline{/E_x}$ according to the colourbar and opacity $|E_x|^2$. The third helicity frame component ($\tilde{E}_k^H$) is always zero.

Let's consider how the angular momentum is distributed for π and σ transitions quantized about the z-axis. Although the fields are not $\hat{s}_z$ or $\hat{l}_z$ eigenstates, they are a superposition of simultaneous $\hat{s}_z$, $\hat{l}_z$ eigenstates with eigenvalues l_z and s_z. The coeffecients of these components in the total field are angle dependent, we can see their relative weights by plotting $\hat{\mathbf{R}}_z$ and $\hat{\mathbf{L}}_z$ polarized components of the field in the laboratory frame. Fig. 4.3(a) maps the field distribution of a π ($\hat{\mathbf{d}} = \hat{\mathbf{z}}$) transition in the laboratory and helicity frames. The $\hat{\mathbf{R}}_z$ and $\hat{\mathbf{L}}_z$ polarized components of the laboratory frame field must have OAM opposite and equal to to their spin. This appears as a spiral phase $e^{\mp i\theta} \to l_z = \pm\hbar$ about the z axis. Translating from the laboratory to helicity frames, the π transition emits a superposition of $\hat{\mathbf{R}}_k$ and $\hat{\mathbf{L}}_k$ photons with $l_z = \pm\hbar$ and equal intensity distributions.

Fig. 4.3(b) maps the field distribution of a σ_+ ($\hat{\mathbf{d}} = \hat{\mathbf{R}}$) transition. The z component of the field has a $l_z = \hbar$ spiral phase to carry the necessary angular momentum. The spin of the L_z component is $s_z = -\hbar$, and so this component has a steeper spiral phase gradient $l_z = 2\hbar$. In the helicity frame, the circularly polarized dipole field is the superposition of a $\hat{\mathbf{R}}_k$ field with $l_z = 0$ and a $\hat{\mathbf{L}}_k$ field with an azimuthally dependent phase and $l_z = 2\hbar$.

The azimuthal phases are explicit in the off-diagonal vortex terms of U_C (Eqn. 4.6). Geometrically, they originate because the rotation operations that constitute U do not commute. In the paraxial limit ($\phi \ll \pi/2$) the projection operation can be neglected, and the off-diagonal phase is a Berry phase accumulated during the parallel transport rotation U, but for larger angles this analogy breaks down.

4.2.3   Optical spin-orbit coupling

The mapping between the spin associated with the transition and the spatial mode of the field described above manifests in a high numerical aperture imaging system as optical spin-orbit coupling [106]. In the non-paraxial, tightly focused regime necessary for efficiently

imaging sub-wavelength emitters, the spin and OAM of light become coupled and this gives rise to phenomena in which the angular momentum associated with an atomic transition determines the spatial distribution and propagation path of scattered light, so-called 'chiral quantum optics', with applications for optical nano-devices and quantum networks [107].

Another manifestation of spin-orbit coupling in light emitted from an atomic dipole can be seen if the quantization axis is instead oriented perpendicular to the optical axis. In this configuration the component of the field circularly polarized about the quantization axis shows a distinctive linear spatial phase that corresponds to a wave front tilt in the collimated beam and a focal point shift in the focal plane. We measure this effect for the dipole single-photon field emitted by our source in Sec. 7.5.1 and Ref. [6]. In the following section we will see how spin-orbit coupling manifests in realistic imaging systems, and how it imposes an upper limit on the fibre coupling efficiency of atomic σ transitions.

4.3   Imaging beyond the paraxial limit

Perfect single-quantum atom-light transfer by focussing optics requires a travelling photon field identical to the image of the atomic transition to be excited. This spatial-mode maximizes the energy density at the focus. In Ref. [108] a Gaussian mode is optimized for efficient focussing with an aspheric lens, and in Ref. [109] a similar optimization procedure is followed for focussing the radially polarized 'doughnut mode' with a parabolic mirror. This experimental procedure is equivalent to matching the incident field to the image of a dipole at the focus. Following Ref. [110], an atom-photon network with focussing optics requires only that we know the image field of the atomic transition and match it with a travelling photon mode (neglecting the temporal mode).

Consider an atom at the coordinate origin imaged by an axially symmetric collimating optic of half-aperture angle ϕ_a and focal length f a distance f from the atom along the optical axis z as shown in Fig. 4.4. An external magnetic field determines the quantization axis of the atom at some angle δ to the optical axis in the z, y plane, but we'll continue working in the basis of circular dipoles about z to take advantage of their axial symmetry with respect to the imaging system. The collimating optic transforms spherical waves at the origin to collimated plane waves with wave vector $\mathbf{k_c} \approx k\,\mathbf{z}$ at the Fourier plane. In Sec. 4.1 we derived the dipole field in terms of the momentum space coordinates $\hat{\mathbf{k}}$. We can describe the momentum transformation of any focussing optic by a bijection $M : \rho \to \mathbf{k}$ that maps to this coordinate system from the polar Fourier plane coordinate system, with an axially symmetric system the map M reduces to a function $\phi = m(\rho)$ that is contingent on the optic.

In this and the following sections we derive the field distributions of dipoles imaged by high-NA optics, and feasible fibre-coupling efficiencies for each optic. This problem has been considered before, notably by Ref. [110]. We will expand on this work with an emphasis on spherical lenses. We consider two important optical elements: a spherical lens, which we take as a model of both the confocal lens objectives used in Chap. 7 and the aspheric lens for the system in Chap. 11, and a parabolic mirror, which is a leading candidate for efficient free-space atom-light coupling [111]. We will derive mapping functions m, apodizations A and Fourier plane distributions E for these systems. We will also consider the image plane field distribution E' as a function of aperture and the fibre-coupling efficiency of various fields. However, for lossless optics the intensity collection efficiency η_I depends only on the half aperture angle ϕ_a, so we can derive η_I as a function of δ in general before considering the details of any particular system.
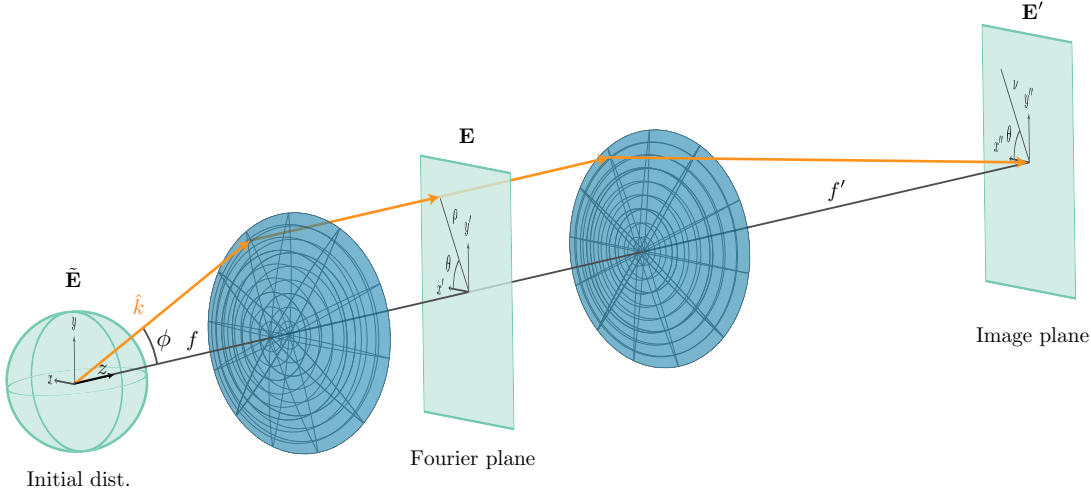
Figure 4.4: Coordinates and frames for an atomic imaging scheme. In the text we consider collimating the atomic dipole field with a spherical lens (shown) and a parabolic mirror (not shown). Although the collimating optic NA should be large, we may image the collimated field with a low-NA lens ($f' \gg f$) in which case the image field E' is paraxial.

4.3.1 Intensity collection efficiency

By integrating over the dipole intensity distributions from Eqn. 4.10 in a frame rotated by angle δ in the y,z plane we determine the intensity collection efficiency of a dipole at angle δ from the optical axis on the y,z plane.

$$\eta_I = \int_0^{2\pi} \mathrm{d}\theta \int_0^{\phi_a} \mathrm{d}\phi \; I(\alpha)\sin(\phi), \tag{4.17}$$

where the angle α between the area element angle and the quantization axis is given by $\alpha = \arccos\left[\cos(\phi)\cos(\delta) + \cos(\theta)\sin(\phi)\sin(\delta)\right]$. Evaluating this expression for each case yields

$$\eta_I^\pi = \frac{1}{64}\left(-3\cos(\phi_a)\left(4\cos(2\delta)\sin^2(\phi_a) + 11\right) + \cos(\phi_a) + 32\right), \tag{4.18}$$

$$\eta_I^\sigma = \frac{1}{128}\left(3(\cos(2\delta) - 21)\cos(\phi_a) - (3\cos(2\delta) + 1)\cos(3\phi_a) + 64\right), \tag{4.19}$$

which we have plotted in Fig. 4.5. This shows the image intensity of a dipole at various angles δ between zero (darkest) and $\pi/2$ (brightest). We have also plotted the collected solid angle $\Omega = (1 - \cos(\phi_a))/2$ and the solid angle advantage $\eta_c - \Omega$ which indicates the advantage in collecting a directed dipole compared to a uniform spherical wave. The σ intensity distribution is less directional than the π distribution, but for NA< 1 the optimally oriented detection scheme collects an equal amount from each transition. For NA> 1 there is an advantage in collecting fluorescence from a π transition.

For applications in networks it is not enough to know the total collected intensity. The closer a spatial mode is to Gaussian, the easier it is to manipulate and propagate without distortion. Similarly, the closer a mode is to a fibre mode the easier it is to transmit coherently over distances. For a fibre-coupled network then the more meaningful
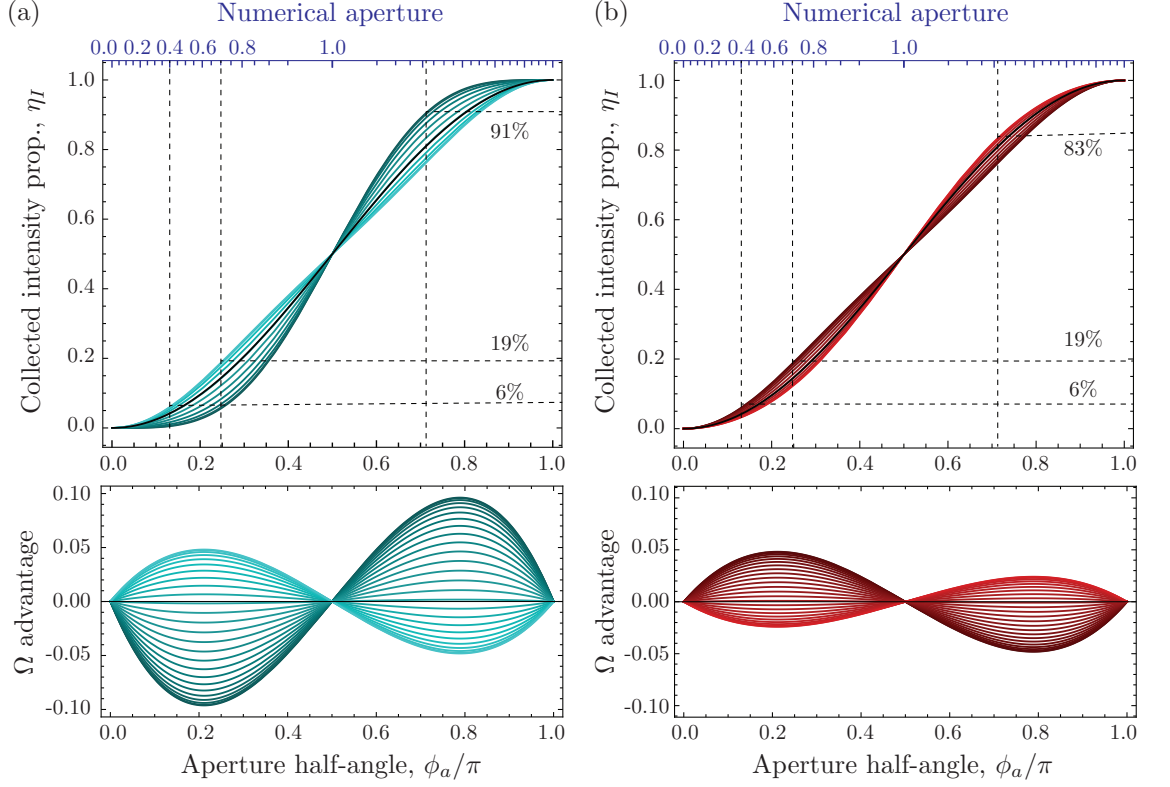
Figure 4.5: Proportion of total intensity collected from (a) π and (b) σ transitions for various collection angles α as a function of aperture half-angle. The angle α between the quantization and optical axes varies from zero (darkest) to $\pi/2$ (brightest). The top axis indicates the corresponding numerical aperture and dashed lines identify key configurations from the body of this thesis. The solid angle Ω at each aperture is plotted as a solid black line for reference. The difference between the collected intensity proportion and the solid angle is the Ω advantage plotted in the two bottom figures with corresponding axes and colours. For NA < 1 the optimally oriented π and σ transitions have the same intensity collection efficiency, but for NA > 1 the π transition may be collected more efficiently.

parameter is the total collection efficiency into the relevant fibre mode

$$\eta = \eta_I \, \eta_c \,, \tag{4.20}$$

which is equal to the product of the collected intensity η_I and the mode matching η_c. In the following subsections we will consider the feasible coupling efficiency between free-space trapped atoms and fibre communication networks. We will see that mode distortion originating from optical spin-orbit coupling limits the advantage of ever higher aperture imagining systems.

4.3.2   Apodization

Conservation of energy requires that atomic dipole field $\tilde{\mathbf{E}}(\mathbf{k})$ and the collimated field distribution $\mathbf{E}(\rho)$ at the pupil of the imaging system are related by an 'apodization' factor. Recall that the total power in the field is

$$P = \int \mathrm{d}\Omega \; I = \frac{c\epsilon_0 n}{2} \int \mathrm{d}\Omega \; E^\dagger E \,, \tag{4.21}$$

where $d\Omega$ is the area element of the unit sphere about the atom. The area elements of the unit sphere and the pupil aperture are

$$d\Omega = \sin(\phi)\ d\theta\ d\phi\ , \tag{4.22}$$

$$d\mathbf{A} = \rho\ d\theta\ d\rho\ . \tag{4.23}$$

Therefore the field distributions must be related by the apodization factor $A(\rho)$ where

$$\mathbf{E}(\theta,\rho) = \sqrt{A(\rho)}\ \tilde{\mathbf{E}}(\theta, m(\rho))\ , \tag{4.24}$$

$$A(\rho) = \frac{\sin(m(\rho))}{\rho}\frac{\partial m}{\partial \rho}\ . \tag{4.25}$$

The apodization factor depends on the design of the imaging system. Below we derive the apodization factors for spherical lenses, thin lenses and parabolic mirrors.

4.3.3 Image field

For imaging lens focal length $f' \gg f$, the image plane field is paraxial, and

$$\mathbf{E}' = \mathcal{F}[\mathbf{E}]\ . \tag{4.26}$$

With axially symmetric optics imaging a dipole on axis the azimuthal field dependence of $\tilde{\mathbf{E}}$ is unchanged by the map m. We have already seen that U is θ, ϕ separable in the basis of circular dipoles about z, with θ terms of the form $e^{il\theta}$. We can therefore reduce the two-dimensional, complex Fourier transform to a one-dimensional, real Hankel transform [112]. Writing the image plane field in terms of a Green's function given by the Hankel transform of $\mathbf{E}$ we have

$$\mathbf{E}'(\nu,\theta) = \mathcal{F}\left[\sqrt{A}M^{-1}\left[PU^{\dagger}\mathbf{d}\right]\right] \tag{4.27}$$

$$= G(\nu,\theta)\mathbf{d} \tag{4.28}$$

$$G(\nu,\theta) = \begin{bmatrix} \mathbb{H}_0\left[\sqrt{A}a\right] & -\mathbb{H}_{-2}\left[\sqrt{A}b\right]e^{-2i\theta} & \mathbb{H}_{-1}\left[\sqrt{2Aab}\right]e^{-i\theta} \\ \mathbb{H}_2\left[\sqrt{A}b\right]e^{2i\theta} & \mathbb{H}_0\left[\sqrt{A}a\right] & \mathbb{H}_1\left[\sqrt{2Aab}\right]e^{i\theta} \\ 0 & 0 & 0 \end{bmatrix}\ . \tag{4.29}$$

4.4 Confocal lenses

Interferometrically stable confocal lenses are a common approach to single-pass atom-light coupling [98] and the primary approach taken in this thesis. In the experiments described in Chap. 7 we collect fluorescence from a trapped atom with confocal lens objectives, and in Chap. 11 we design an improved apparatus that couples the atom to a collimated mode with a high-NA asphere. Confocal lenses are also used in scanning two and three-photon microscopy where the imaging resolution depends on the size of the focal spot. Although immersion lenses can reach numerical apertures larger than one, free space lenses and lens objectives are restricted by the limits of optical manufacturing to NA< 0.9, and diffraction-free lenses are unavailable beyond NA$= 0.8$. Nevertheless, a confocal lens system can take advantage of the degree of direction in the dipole emission to outperform its solid angle proportion, as we can see from Fig. 4.5, and achieve significant coupling.

We will model lenses according to the Debye-Wolf theory [113, 114] in which partial
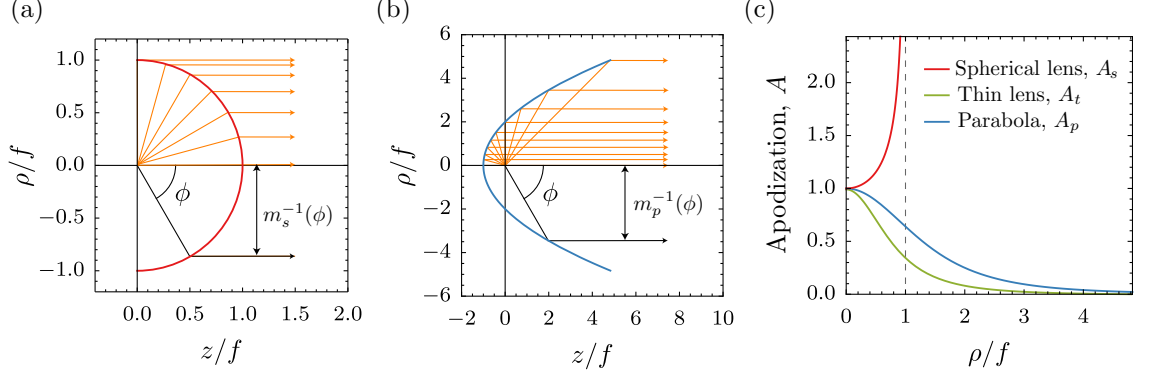
Figure 4.6:   Collimating by (a) a spherical lens (b) a parabolic mirror. Beam paths are traced at intervals of $15°$. The path density at the Fourier plane is the apodization factor A. (c) The apodization function of a spherical lens (red), a thin lens (green) and a parabolic mirror (blue).

waves retain their helicity through the lens. Real large-aperture objectives are necessarily more complicated than this model; broadband anti-reflection coatings are less effective at large angles, and this contributes to Fresnel losses and polarization distortion in the elements of any high-aperture objective [115] which we will neglect in this treatment.

4.4.1   Spherical lens apodization

Small-aperture collimating objectives can be approximated by a spherical lens, illustrated in Fig. 4.6(a). A spherical lens relates the initial and collimated field coordinates by a mapping function

$$\phi = m_s(\rho) = \arcsin(\rho) \tag{4.30}$$

equivalent to an orthographic projection of the helicity frame field $\tilde{\mathbf{E}}$ scaled by the appropriate apodization according to Eqn. 4.24

$$E_s(\rho, \theta) = \sqrt{A_s}\, \tilde{\mathbf{E}}(\arcsin(\rho), \theta) \tag{4.31}$$

$$A_s = \frac{1}{\cos(\phi)} = \frac{1}{\sqrt{1 - \rho^2}}\,. \tag{4.32}$$

The spherical lens is a poor model at large angles; Fig. 4.6(c) illustrates how A_s diverges at $\phi_a = \pi/2$, but because an exact map m depends on the details of the objective design, we will take the spherical lens model as an indicative first-order illustration of collimating lens systems in general (Fresnel lenses are a noteworthy exception that we will consider below).

4.4.2   Spherical lens fields

The spherical lens Fourier plane fields calculated with Eqn. 4.31 are shown for illustrative dipoles in Fig. 4.7. Each field is shown as an intensity distribution, and as weighted phase plots in the appropriate basis. The parallel dipoles (a) $\mathbf{d} = \hat{\mathbf{R}}_z$ and (b) $\mathbf{d} = \hat{\mathbf{z}}$ are plotted in the circular polarization basis and the perpendicular dipoles (c) $\mathbf{d} = \hat{\mathbf{x}}$ and (d) $\mathbf{d} = \hat{\mathbf{R}}_x$ are plotted in the linear polarization basis. Of these, (a) and (c) have the best collection efficiency.

The collimated field distribution of the linear dipole perpendicular to the optical axis

$(\mathbf{d} = \hat{\mathbf{x}})$ has linear basis components

$$\mathbf{E}_s^\pi = \sqrt{\frac{3}{2\pi}} \frac{1}{4(1-\rho^2)^{\frac{1}{4}}} \times$$
$$\left((1 + \sqrt{1-\rho^2} + (\sqrt{1-\rho^2} - 1)\cos(2\theta))\hat{\mathbf{H}} + (\sqrt{1-\rho^2} - 1)\sin(2\theta)\hat{\mathbf{V}} \right) , \quad (4.33)$$

where we have chosen $\hat{\mathbf{H}}$ parallel to the x-axis and $\hat{\mathbf{V}}$ parallel to the y-axis. A circular dipole aligned with the optical axis is necessarily axially symmetric, and can be written in the circular basis

$$\mathbf{E}_s^\sigma = \sqrt{\frac{3}{2\pi}} \frac{1}{4(1-\rho^2)^{\frac{1}{4}}} \left((1 + \sqrt{1-\rho^2})\hat{\mathbf{R}} + (\sqrt{1-\rho^2} - 1)e^{2i\theta}\hat{\mathbf{L}} \right) . \qquad (4.34)$$

A circular dipole imaged by a typical collimating lens and with the quantization axis aligned with the optical axis produces an almost uniform intensity distribution over the output pupil for $NA < 0.8$. For numerical apertures larger than this the field begins to diverge, and the intensity distribution becomes concentrated far from the centre of the beam. As with any high-NA image of the atomic dipole the optical spin and orbital angular momentum of the output field are coupled. In the NA $= 1$ limit, $7/8$ of the total power is in the field with circular polarization aligned parallel to the atomic transition $s_z = \hbar\Delta m$, but the remaining $1/8$ is in the orthogonal polarization. The orthogonally polarized light is produced in a spatial mode with $l_z = 2\hbar\Delta m$ in order to conserve angular momentum. The polarization of the field changes smoothly from circular at the centre, to azimuthally polarized at the extreme edge.

Fig. 4.7 also shows the image plane intensity distribution of each dipole for $\phi_a = \frac{1}{4}$ (NA$= 0.7$, dashed line on phase figures) and $\phi_a = \frac{1}{2}$ (NA$= 1$). In cases a,b and c the intensity collected by a lens with NA< 0.7 is close to uniform, and so the image is close to the point spread function of the aperture. In the case of d, $\mathbf{d} = \hat{\mathbf{R}}_x$, the centre of the intensity distribution is displaced in order to conserve angular momentum about the quantization axis [105].

4.4.3 A note on Fresnel lenses

Before we move on, we note for the sake of completeness that Fresnel lenses are another method of atom-light coupling in use [116, 117]. The Fresnel lens may be modelled as an ideal thin lens with map m_t and apodization a_t

$$\phi = m_t(\rho) = \text{atan}\left(\frac{\rho}{f}\right), \qquad (4.35)$$

$$A_t = \cos^3(\phi) = \frac{1}{(1+\rho^2)^{\frac{3}{2}}} . \qquad (4.36)$$

In contrast to a spherical lens above, the thin lens does not diverge and remains a relatively accurate model of high-NA Fresnel lenses. The thin lens system is inconsequential to the original work in this thesis, and we will not present this case in detail, but the same method may be applied to calculate the Fourier plane and image fields of a Fresnel lens coupler. We note only that the long tail of the thin lens apodization function A_t shown in Fig. 4.6(c) produces fields which couple less efficiently to fibre modes than the spherical lens or parabolic mirror images derived in this chapter. Curious readers can find a comparable

derivation of the thin lens dipole image in Ref. [110].

4.5 Parabolic mirror

Parabolic mirrors are being successfully pursued as a means of atom-photon coupling [111, 118, 119]. The defining characteristic of a parabolic mirror is that it perfectly focusses an incident plane wave to a spherical wave converging at the focal point [120]. In contrast to the spherical lenses above the parabolic mirror may have arbitrarily high numerical apertures (although we will see in Chap. 10 that manufacturing such optics is challenging), and does not diverge for any critical aperture. Parabolic mirrors are being pursued for strong atom-light coupling. Spherical mirrors may be used in combination with aspheric correctors to mimic the performance of a parabolic mirror [121].

The surface of an axially symmetric parabola is entirely specified by the distance f from the vertex to the focus

$$z = \frac{\rho^2}{4f} - f \,, \tag{4.37}$$

and the aperture is

$$\rho_a = f \frac{\sin(\phi_a)}{\cos^2(\phi_a/2)} \,. \tag{4.38}$$

4.5.1 Parabolic mirror apodization

Given that $z = f^2 \cos(\phi) \sec^2(\phi/2)$ we can derive the coordinate map of the parabola m_p and, according to Eqn. 4.24, the associated apodization factor A_p

$$\phi = m_p(\rho) = 2 \operatorname{atan}\left(\frac{\rho}{2f}\right) \tag{4.39}$$

$$A_p = \left(\frac{\cos^2(\phi/2)}{f}\right)^2 = \left(\frac{4f}{4f^2 + \rho^2}\right)^2 \,. \tag{4.40}$$

4.5.2 Parabolic mirror fields

In general the phase shift of a partial wave on reflection is a function of the incidence angle, this introduces a radial phase shift to a parabolic mirror image that must be corrected with a phase plate [122]. Although this correction isn't trivial, we will take it for granted that a radial phase may be corrected and neglect this term in our calculations.

Fig. 4.8 shows the Fourier plane fields calculated with Eqn. 4.39 for the same illustrative dipoles and in the same polarization bases as Fig. 4.7. The field is collected most efficiently when a linear dipole at the focus is oriented parallel to the optical axis, Fig. 4.8(b). The collected field at the pupil is the superposition of two circularly polarized angular momentum eigenfields with $l_z = -s_z = \pm\hbar$. The total field is radially polarized with a central dark spot

$$\mathbf{E}_p^\pi = \frac{\rho}{f}\sqrt{\frac{3}{\pi}}\left(\frac{2}{\frac{\rho^2}{f^2} + 4}\right)^2 \left(e^{-i\theta}\hat{\mathbf{R}} + e^{i\theta}\hat{\mathbf{L}}\right) \tag{4.41}$$

$$= \frac{\rho}{f}\sqrt{\frac{3}{\pi}}\left(\frac{2}{\frac{\rho^2}{f^2} + 4}\right)^2 \hat{\rho} \,. \tag{4.42}$$
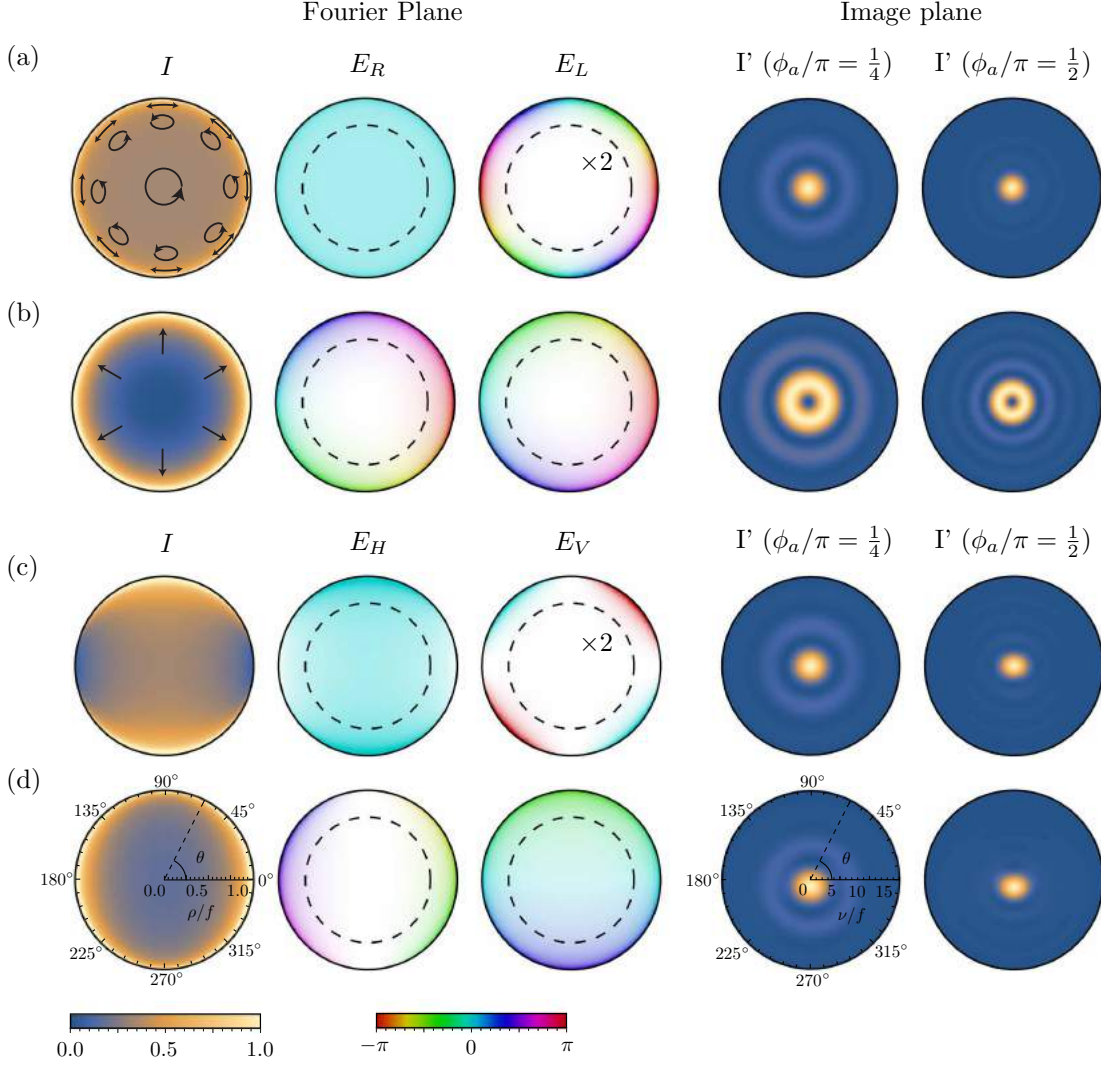
Figure 4.7: Intensity and field distributions of atomic dipoles imaged by a spherical lens. Fields are shown in both the Fourier and image planes (for two aperture sizes ϕ_a). Polarization components $E_{x=R,L,H,V}$ are plotted with hue $\angle E_x$ according to the colourbar and opacity $|E_x|^2$. Some weak field components are scaled with multipliers as shown for visibility. Image plane intensity distributions are peak-normalized. (a) $\mathbf{d} = \hat{\mathbf{R}}_z$ produces a $\hat{\mathbf{R}}$ polarized field along the optical axis which becomes elliptical and finally azimuthally polarized as $\rho \to f$. A polarization vector field is drawn over the Fourier-plane intensity distribution. (b) $\mathbf{d} = \hat{\mathbf{z}}$ is the least efficiently collected dipole with intensity at the extreme edge of the Fourier plane field. The Fourier plane field is radially polarized everywhere as indicated. (c) $\mathbf{d} = \hat{\mathbf{x}}$ is the efficiently oriented linear dipole. The Fourier plane field is $\hat{\mathbf{H}}$ polarized on the optical axis and azimuthally polarized at $\rho \to f$. The high aperture image plane field is elongated along the quantization axis. (d) $\mathbf{d} = \hat{\mathbf{R}}_x$ is the inefficiently oriented circular dipole. The Fourier plane field is $\hat{\mathbf{V}}$ polarized on axis with a phase gradient that is approximately linear and equates to a vertical displacement in the image plane.
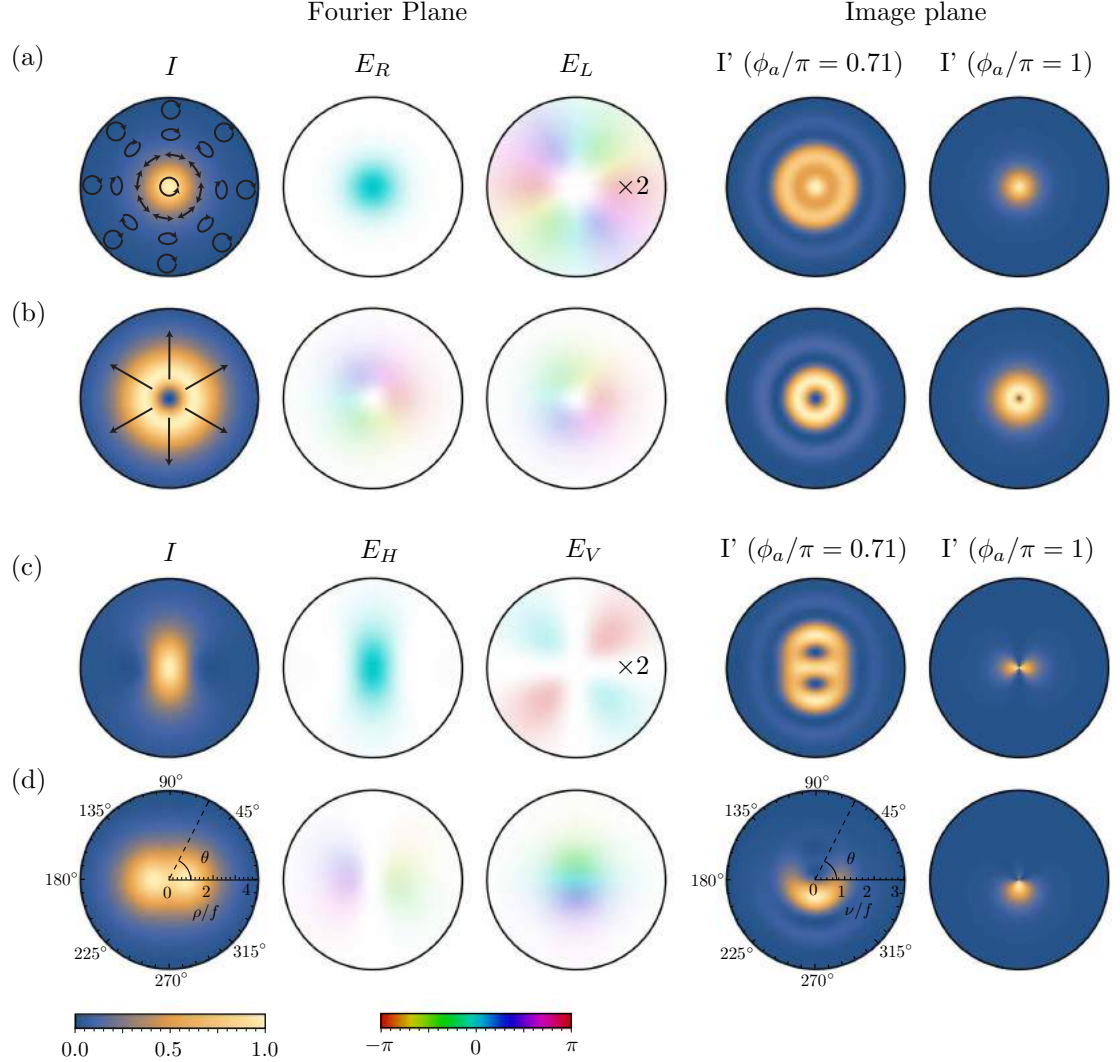
Figure 4.8: Intensity and field distributions of atomic dipoles imaged by a parabolic mirror. The Fourier plane fields are plotted to $\rho = 4$ ($\phi_a = 0.71\pi$). Image plane intensity distributions are peak-normalized. (a) the inefficiently oriented circular dipole $\mathbf{d} = \hat{\mathbf{R}}_z$ produces a central $\hat{\mathbf{R}}$ polarized field that transitions to first azimuthally and then $\hat{\mathbf{L}}$ polarization with increasing ρ. A polarization vector field is drawn over the Fourier-plane intensity distribution. The infinite aperture image of this field is a radially polarized Bessel function of the second kind. (b) The efficiently oriented linear dipole $\mathbf{d} = \hat{\mathbf{z}}$ produces a radially polarized mode similar to the doughnut mode. A polarization vector field is drawn over the Fourier-plane intensity distribution. As the aperture increases the image approaches another Bessel function. (c) The inefficiently oriented linear dipole $\mathbf{d} = \hat{\mathbf{x}}$ produces a Fourier plane field that is $\hat{\mathbf{H}}$ polarized on axis and azimuthally polarized for large ρ. (d) In the Fourier plane the efficiently oriented circular dipole $\mathbf{d} = \hat{\mathbf{R}}_x$ is predominantly $\hat{\mathbf{V}}$ polarized with a phase gradient that corresponds to a displacement of the image.

We will see in the following section that this field is similar to the so-called 'doughnut mode', and that it couples efficiently to a low-loss single-mode fibre.

If instead we consider a σ transition in the same configuration, we see the following distribution at the output pupil

$$\mathbf{E}_p^\sigma = \sqrt{\frac{6}{\pi}} \left(\frac{1}{4 + \frac{\rho^2}{f^2}} \right)^2 \left(4\hat{\mathbf{R}} - \frac{\rho^2}{f^2} e^{2i\theta} \hat{\mathbf{L}} \right) . \tag{4.43}$$

Like the confocal spherical lens image of the σ transition, Eqn. 4.34, this is a circularly polarized mode at $\phi_a = 0$ and transitions smoothly to an azimuthal linear polarization at $\phi_a = \pi/2$ before continuing to the opposite circular polarization with an orbital angular momentum of $l_z = 2\hbar\Delta m$ as ϕ_a is increased further. While exactly half of the total power is in each component, the peak intensity in the $\hat{\mathbf{L}}$ field is 0.12 and the peak intensity in the $\hat{\mathbf{R}}$ field is 0.015. In the next section we derive fibre-coupling efficiencies for these two distributions and see that while the parabolic mirror image of π transition couples efficiently to fibre, the σ transition is a more challenging proposition.

4.6 Fibre coupling efficiency

To efficiently network atomic photon sources we require that the spatial mode of our imaging system is close to the propagation mode of a convenient single- or few-mode fibre or waveguide and that the mode can be manipulated with typical Gaussian optics. That is, for some normalized fibre mode $\mathbf{E}_f$ we require the mode overlap

$$\eta_c = \left| \int \mathrm{d}\mathbf{A} \ \mathbf{E}^\dagger \mathbf{E}_f \right|^2 = \left| 2\pi \int \mathrm{d}\rho \ \rho \mathbf{E}^\dagger \mathbf{E}_f \right|^2 \tag{4.44}$$

to be close to one. We will consider the best-match fibre mode for the optimally oriented atomic transition images derived above and calculate the mode matching η_c possible for each scheme. Although a complete survey of optical fibre engineering is outside the scope of this chapter, it is necessary to introduce a few typical fibre modes. If the fibre has radial symmetry, the propagation mode depends only on the radial refractive index profile. The simplest case to consider is the step-index profile between the refractive index of the core and the cladding. In this case the lowest-order guided (LP_m^l) modes of the fibre are very close to low order Laguerre-Gauss (LG_m^l) modes with normalized transverse beam waist profiles given by [123]

$$\mathrm{LG}_m^l = \sqrt{\frac{m!}{(|l| + m)!} \frac{2}{\pi w^2}} \left(\frac{\sqrt{2}\rho}{w} \right)^{|l|} \mathrm{L}_m^{|l|} \left(\frac{2\rho^2}{w^2} \right) e^{-il\theta - \frac{\rho^2}{w^2}} \tag{4.45}$$

where w is the beam waist size, and L_m^l the Laguerre polynomial with order m and topological charge l. These profiles join continuously with exponentially decaying fields in the cladding. Optical quantum networks, being interferometers, require fibres in which intermode dispersion is very low or —in the case of single-mode fibres—completely forbidden. Typical single mode fibres have a core size on the order of a few λ and a small refractive index difference between core and cladding. In this case it is only the fundamental mode LP_0^0 that we need to consider, and it is almost perfectly Gaussian. The propagation mode in the fibre is linearly polarized, but we can efficiently map any uniform polariza-
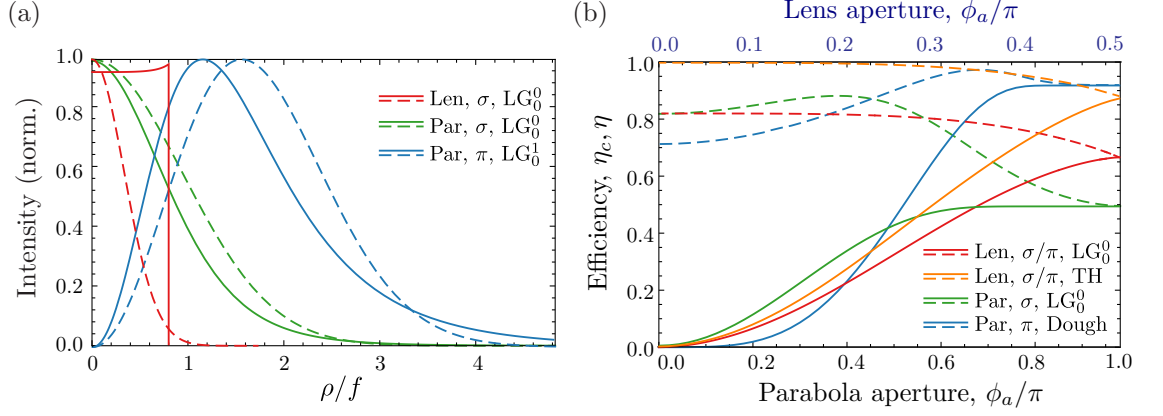
Figure 4.9: (a) Radial intensity distribution of three atom fluorescence images by spherical lens and parabola (solid lines) and mode matched fibre modes (dashed lines). Only the intensity in the polarization mode of the fibre is shown (see text for discussion) and each distribution is peak-normalized. The spherical lens image distribution is shown only for NA= 0.8. The radial distributions are matched over the collection aperture with $dA = \rho \, d\theta \, d\rho$, which produces an apparent shift towards higher ρ in the radial profiles. (b) Total fibre collection efficiency η (solid lines) and mode overlap η_c (dashed lines) for various atomic fluorescence images by spherical lens and parabola as a function of aperture angle.

tion distribution to the fibre mode with waveplates. However, the atom images derived above are neither perfectly Gaussian nor uniformly polarized. We will calculate the mode overlap with common Gaussian mode fibres as well as considering more exotic fibres with non-uniform polarization and non-Gaussian irradiance profiles as necessary.

Fig. 4.9 summarizes the maximum possible fibre coupling efficiency of the atomic fluorescence images derived above for spherical lenses and parabolic mirrors as a function of aperture. Fig. 4.9(a) shows the intensity distribution of the images (solid lines) and the best-fit fibre mode (dashed lines) and Fig. 4.9(b) shows the mode matching η_c (dashed lines) and the total coupling efficiency $\eta = \eta_I \eta_c$ (solid lines) as a function of the collection aperture angle ϕ_a. We will now proceed to consider each of the cases shown.

As we saw above (Sec. 4.4), at NA< 0.8 the image of a σ_z transition through a spherical lens has uniform intensity and near-uniform circular polarization over the lens aperture. The closest typical fibre mode is the fundamental Gaussian mode LG_0^0 mapped to a fixed circular polarization with waveplates. The radial profile of the $\hat{\mathbf{L}}$ polarized component and the closest Gaussian mode are shown in Fig. 4.9(a) (red lines). Fig. 4.9(b) shows η_c (dashed red line) and η (solid red line) as a function of aperture angle for spherical lens images of atomic transitions. Because the perpendicularly polarized π transition can be decomposed into the sum of two parallel σ dipoles (compare Fig. 4.2(a) and (b), linear and circular components) the perpendicular linear dipole fibre couples to linearly polarized, radially symmetric modes with the same efficiency that the parallel circular dipole couples to the same, but circularly polarized, modes. For this reason coupling efficiencies for parallel σ and perpendicular π polarized transitions are shown together on Fig. 4.9(b).

The Gaussian mode coupling efficiency is the relevant fibre coupling efficiency for the experiments carried out with confocally imaged trapped ions in Chap. 7, but it is possible to do better. Several techniques exist for engineering single mode, polarization maintaining fibres that support a more uniform, 'top hat' irradiance profile [124–126], and free form optics are also available for coupling top hat distributions into regular fibre modes [127–

129]. With these it is possible to reach $\eta_c > 0.99$ for spherical lenses of up to NA= 0.8. To efficiently fibre-couple atomic fluorescence beyond this numerical aperture it is necessary to correct the increasingly non uniform polarization as it becomes elliptical at the edge of the image. In principle this can be achieved with either a spatially inhomogeneous wave plate assembled from sections of birefringent crystal or a spatial light modulator [130]. However, any such correction necessarily introduces further losses and disturbances. Without these corrections the efficiency approaches 85% as the confocal lens system approaches the total solid angle.

The parabolic mirror image of a π transition is similar to a radially polarized doughnut mode $\mathbf{D} = \frac{1}{\sqrt{2}}(\mathrm{LG}_0^1 + \mathrm{LG}_0^{-1})$, but with a long-tailed radial intensity distribution, see Fig. 4.9(a) (blue lines). We note that the adapted doughnut mode matched to the distribution here (dotted blue line) differs from that presented in Ref.[131], in which the radial profile was matched without radially weighting the area element. The peak of the appropriately matched mode doesn't coincide with the peak of the image, instead it is shifted by broadening the mode to overlap with the extended tail of the image. The mode overlap between the mirror image of a large aperture parabola and LG_0^1 is 0.92 with $w = 2.36f$, the total collection efficiency and mode matching η are shown in Fig. 4.9 (blue lines). In conventional step-index fibres the azimuthally and radially polarized doughnut modes are near-degenerate and unstable to small perturbations, but an optical fibre with an annular, high-index ring profile is able to lift this degeneracy so that the radial doughnut mode can be coupled efficiently and propagated purely [132] in a few-mode fibre. The parabolic mirror is therefore a promising avenue for fibre-coupled π transitions.

Unfortunately the parabolic image of a σ transition in the same configuration does not couple to fibres so conveniently. The closest fibre mode to the σ transition image is the fundamental Gaussian mode LG_0^0 with circular polarization orthogonal to the transition dipole orientation. The radial intensity distribution of the $\hat{\mathbf{R}}$ circular component of the image (also plotted in Fig. 4.9(a) (green lines)) is close to Gaussian, albeit with an extended tail. However because half of the fluorescence is mapped to the orthogonal polarization, the mode overlap is considerably reduced; compare the intensity in the appropriate polarization to the total intensity profile derived in Ref. [118]. For this reason the σ transition collection efficiency of the parabolic mirror system tops out at 0.49 with $w = 1.88f$, as shown in Fig. 4.9(b)(green lines). The spatial polarization variation can in-principle be corrected using the same methods discussed for the case of the spherical lens image.

4.7   Summary

We have now established all of the theory that we need to quantify the performance limits of the atom imaging experiments used in this thesis, as well as the limits of even ideal free-space atom-network links. The biggest challenge to efficiently and coherently couple a light field to an atom in free-space remains the difficulty of capturing a large proportion of the total solid angle, and the simplest way to achieve this is a parabolic reflector [118, 131]. A parabolic mirror of infinite extent encloses the complete solid angle and captures 100% of the atomic fluorescence. But as we saw above, only 92% of the field collected from a π transition overlaps with a useful fibre mode. The parabolic mirror is even worse at coupling σ transitions, as optical-spin orbit coupling produces a pupil field with spatially inhomogeneous polarization that is difficult to correct. The fibre coupling efficiency of a σ transition, infinite-parabola image is only 0.49. Prof. Gerd Leuchs and his team

Optic	ϕ_a/π	NA	$\Omega/4\pi$	η_I	$\hat{\mathbf{d}}$	Matched mode	η_c	η
Lens	0.13	0.4	0.04	0.06	σ/π	LG_0^0	0.81	0.1
						Tophat	1.00	0.12
	0.25	0.7	0.30	0.38	σ/π	LG_0^0	0.81	0.15
						Tophat	0.99	0.19
Parabola	0.71	-	0.81	0.76	σ	LG_0^0	0.65	0.49
				0.90	π	Doughnut	0.97	0.88

Table 4.1: Key figures of merit for imaging systems referred to in this thesis, including NA 0.4 and NA 0.7 confocal lens systems and a parabolic mirror coupler of the same dimensions as Ref. [111]. For each system we calculate the total solid angle included Ω, the total collected intensity η_I, the matched mode for each transition image, the mode-matching η_c, and the total collection efficiency η.

have pioneered the use of parabolic mirror atom-light couplers and have the most efficient free-space atom-light collection yet demonstrated with a parabola of aperture $\phi_a = 0.71\pi$ [111, 133]. The corresponding collection efficiencies for an ideal parabolic mirror of those dimensions are shown in Tab. 4.7.

In this thesis we will consider two variations of a confocal lens imaging system. In Chap. 7 we will image trapped ions with a two-lens system of numerical aperture 0.4. This system collects 12% of the total ion fluorescence, and couples at most 10% into the single-mode fibre network, see Tab. 4.7. The improved imaging system we describe in Chap. 11 combines an asphere with numerical aperture 0.7 and a hemispherical mirror to collect 38% of the total fluorescence and will couple at most 30% into a step-profile single mode fibre, although this could be improved to 38% with a top hat fibre mode. These are critical figures for the efficiency of atom-imaging with these systems and limit our capacity to network these atomic qubits with optical links, but increasing the numerical aperture of a lens system beyond 0.8 is a challenging proposition with diminishing returns. In Chap. 10 we will consider an alternative means of efficiently coupling atom light sources to optical networks with near-hemispheric mirrors that shape the vacuum mode density in the vicinity of an atom to favour efficiently collected spatial modes. In this case it is not necessary to collect a large proportion of the solid angle, but rather to suppress emission outside of the collected aperture.

Bibliography - Imaging atomic transitions

6. G. Araneda, et al., Wavelength-scale errors in optical localization due to spin-orbit coupling of light, *Nat. Phys.* **14**, 1–6 (2018).

92. D. A. Steck, *Quantum and atom optics* (2007).

96. V. Leong, et al., Time-resolved scattering of a single photon by a single atom, *Nat. Commun.* **7**, 13716 (2016).

97. S. Quabis, et al., Focusing light to a tighter spot, *Opt. Commun.* **179**, 1–7 (2000).

98. Y.-S. Chin, M. Steiner, and C. Kurtsiefer, Nonlinear photon-atom coupling with 4Pi microscopy, *Nat. Commun.* **8**, 1200 (2017).

99. N. Schlosser, et al., Sub-Poissonian loading of single atoms in a microscopic dipole trap, *Nature* **411**, 1024–1027 (2001).

100. K. Y. Bliokh, et al., Spin-to-orbital angular momentum conversion in focusing, scattering, and imaging systems., *Opt. Express* **19**, 26132–49 (2011).

101. J. H. Poynting, The wave motion of a revolving shaft, and a suggestion as to the angular momentum in a beam of circularly polarised light, *Proc. Royal Soc. A* **82**, 560–567 (1909).

102. R. A. Beth, Mechanical detection and measurement of the angular momentum of light, *Phys. Rev.* **50**, 115–125 (1936).

103. M. V. Berry, Optical currents, *J. Opt. A* **11**, 094001 (2009).

104. K. Y. Bliokh, and F. Nori, Transverse and longitudinal angular momenta of light, *Phys. Rep.* **592**, 1–38 (2015).

105. G. Moe, and W. Happer, Conservation of angular momentum for light propagating in a transparent anisotropic medium, *J. Phys. B* **10**, 1191 (1977).

106. K. Y. Bliokh, et al., Spin–orbit interactions of light, *Nat. Photonics* **9**, 796–808 (2015).

107. R. Mitsch, et al., Quantum state-controlled directional spontaneous emission of photons into a nanophotonic waveguide, *Nat. Commun.* **5**, 5713 (2014).

108. M. K. Tey, et al., Interfacing light and single atoms with a lens, *New J. Phys.* **11**, 043011 (2009).

109. N. Bokor, and N. Davidson, 4π Focusing with single paraboloid mirror, *Opt. Commun.* **281**, 5499–5503 (2008).

110. M. Sondermann, N. Lindlein, and G. Leuchs, Maximizing the electric field strength in the foci of high numerical aperture optics, *Arxiv Prepr. 0811.2098v3*, 1–9 (2011).

111. R. Maiwald, et al., Collecting more than half the fluorescence photons from a single ion, *Phys. Rev. A* **86**, 043431 (2012).

112. N. Baddour, 2D Fourier transforms in polar coordinates, *Adv. Imaging Electron Phys.* **165**, 1–45 (2011).

113. E. Wolf, Electromagnetic diffraction in optical systems. I. An integral representation of the image field, *Proc. Royal Soc. A* **253**, 349–357 (1959).

114. B. Richards, and E. Wolf, Electromagnetic diffraction in optical systems. II. Structure of the image field in an aplanatic system, *Proc. Royal Soc. A* **253**, 358 LP –379 (1959).

115. S. Inoué, Characterizing high numerical aperture microscope objective lenses, in *Optical imaging and microscopy: Techniques and advanced systems*, edited by P. Török, and F.-J. Kao, (Springer Berlin Heidelberg, 2003).

116. E. W. Streed, et al., Imaging of trapped ions with a microfabricated optic for quantum information processing, *Phys. Rev. Lett.* **106**, 10502 (2011).

117. E. W. Streed, et al., Absorption imaging of a single atom, *Nat. Commun.* **3**, 933 (2012).

118. M. Sondermann, et al., Design of a mode converter for efficient light-atom coupling in free space, *Appl. Phys. B* **89**, 489–492 (2007).

119. M. Fischer, et al., Efficient saturation of an ion in free space, *Appl. Phys. B* **117**, 797–801 (2014).

120. D. Korsch, *Reflective optics.* (Elsevier Science, 1991).

121. G. Shu, et al., Efficient fluorescence collection from trapped ions with an integrated spherical mirror, *Phys. Rev. A* **81**, 042321 (2010).

122. V. S. Ignatovsky, Diffraction by a parabolic mirror having arbitrary opening, *Trans. Opt. Inst. Petrogr.* **1** (1920).

123. L. Allen, et al., Orbital angular momentum of light and the transformation of Laguerre-Gaussian laser modes, *Phys. Rev. A* **45**, 8185–8189 (1992).

124. C. Valentin, et al., Top-hat beam output of a single-mode microstructured optical fiber: Impact of core index depression, *Opt. Express* **21**, 23250 (2013).

125. P. Gouriou, et al., Polarization maintaining single-mode fiber delivering a flat top intensity profile, *Opt. Express* **23**, 32496 (2015).

126. I. Gris-Sánchez, D. Van Ras, and T. A. Birks, The Airy fiber: an optical fiber that guides light diffracted by a circular aperture, *Optica* **3**, 270 (2016).

127. B. R. Frieden, Lossless conversion of a plane laser wave to a plane wave of uniform irradiance, *Appl. Opt.* **4**, 1400–1403 (1965).

128. M. Mayeh, and F. Farahi, Laser beam shaping and mode conversion in optical fibers, *Photonic Sensors* **1**, 187–198 (2011).

129. T. Gissibl, et al., Sub-micrometre accurate free-form optics by three-dimensional printing on single-mode fibres, *Nat. Commun.* **7**, 11763 (2016).

130. S. Quabis, R. Dorn, and G. Leuchs, Generation of a radially polarized doughnut mode of high quality, *Appl. Phys. B* **81**, 597–600 (2005).

131. N. Lindlein, et al., A new 4π geometry optimized for focusing on an atom with a dipole-like radiation pattern, *Laser Phys.* **17**, 927–934 (2007).

132. S. Ramachandran, P. Kristensen, and M. F. Yan, Generation and propagation of radially polarized beams in optical fibers, *Opt. Lett.* **34**, 2525–2527 (2009).

133. G. Leuchs, and M. Sondermann, Light–matter interaction in free space, *J. Mod. Opt.* **60**, 1–7 (2013).

Part II

Few atoms

Single photon sources: a review

According to the assumption to be contemplated here, when a ray of light is spreading from a point, the energy is not distributed continuously over ever-increasing spaces, but consists of a finite number of energy quanta that are localized points in space, move without dividing, and can be absorbed or generated only as a whole.
– Albert Einstein, *Concerning the production of light* (1905)

Evidence for the quantization of light has existed for over a hundred years [134, 135] and photons have been detected individually for over 60 years [136], but devices capable of producing photons on demand are a relatively recent innovation. Such definite, single-excitation light fields are an elementary tool for quantum information and a key feature in schemes for encoding, manipulating and communicating quantum information. There are two broad applications for single-photon sources in quantum information: networking stationary qubits and as a resource for photonic quantum computing (see Sec. 1.4.4)[1]. We can draw a further distinction between two networking applications: interfacing modular registers of qubits within a quantum computer, and as flying qubits for long-range quantum key distribution (QKD).

In the following chapters we will implement a trapped-atom single-photon source and consider its properties and limitations. Because trapped atoms are themselves excellent stationary qubits, trapped-atom photon sources are a path to implementing quantum memories, and to networking registers of trapped-atom qubits in a quantum computer as described in Sec. 1.4.1. To put this work in its proper context, we will review in this chapter the various demonstrated single-photon technologies, their advantages and disadvantages as sources for quantum information networks and for optical quantum computing, recent noteworthy results, and the future prospects of each.

5.1 Photon source performance criteria

An ideal single photon source emits on demand a single photon (and never more than one photon) into a well defined spatio-temporal mode, with 100% probability and desirably with high brightness (meaning the attainable single-photon rate) [136, 137]. We can measure the photon-number purity with the second-order correlation function $g^{(2)}(0)$ measured in a HBT experiment as introduced in Sec. 2.5.4. Multi-photon components of the optical state contribute to the HBT coincidence rate, and in this sense the HBT anti-correlation parameter $\mathbb{A} = 4P_c/P_s^2$ from Eqn. 2.62 is a measure of the photon-number purity of states close to the single photon Fock state.

---

[1]Single-photon interferometry is another noteworthy application of single-photon sources, but we'll restrict this review to the broad applications of photon sources.

The photon wave-packet should be Fourier-limited such that subsequent pulses from the same source are indistinguishable and interfere with high visibility. We may measure the indistinguishability M via Hong-Ou-Mandel interferometry. Linear optical quantum computing further requires that photons produced by parallel sources are also indistinguishable [44], although a single source of sufficient brightness may be temporally multiplexed across a large number of modes to achieve the same result. Apart from any technical limitations to our capacity to efficiently multiplex sources, this necessarily requires a trade-off between the brightness of the source and the number of modes it is required to multiplex.

The brightness of on-demand sources is a function of their repetition rate and efficiency η, which we may divide into two components: the generation and collection efficiencies η_g and η_I. Additionally, many sources are inherently multi-mode, producing (for example) a mixture of polarizations, which caps the feasible single-mode generation efficiency. Single-mode sources are required for network applications, and we will only compare single-mode efficiencies below. Following the treatment of atom-light coupling efficiencies given in Chap. 4, we can write the total single-mode efficiency

$$\eta = \eta_g \eta_I \eta_c \,, \tag{5.1}$$

where η_c is the mode matching parameter. Finally, because the repetition rate is fundamentally limited by the source bandwidth, we usually prefer the spectral brightness, the ratio of brightness to bandwidth, as a more meaningful measure of comparative brightness than the raw brightness.

We must treat the brightness of probabilistic sources a little differently. The brightness of probabilistic sources scales with the pump power, which can be large. Because lower pump powers are more practical, and because multi-photon noise often scales with pump power (as it does for spontaneous parametric down conversion and four-wave mixing based photon sources, see Sec. 5.2) the brightness of probabilistic sources is often reported as a ratio of spectral brightness and pump power, that is in units of photons s^{-1} mW^{-1} MHz^{-1}.

5.2 Probabilistic sources

The most salient distinction between single photon sources is between on-demand and probabilistic sources. Probabilistic sources produce pairs of correlated photons with low probability. One half of the pair, the 'idler', is detected to herald the existence of the other 'signal' photon with some herald efficiency η_h that may be improved by multiplexing several identical sources [138]. Probabilistic sources are sufficient for QKD over low-loss links, but are not scalable sources for photonic computers. Over communication channels with substantial losses, we require photon sources to be compatible with quantum memories for storage and synchronization. In combination with a suitable quantum memory, probabilistic sources may be multiplexed to overcome the unpredictable generation times. Multiplexing schemes are limited by the herald, switch and storage efficiencies. The most developed probabilistic photon sources are spontaneous parametric down conversion (SPDC) and spontaneous four wave mixing (FWM) in a nonlinear optical medium.

5.2.1 SPDC

The workhorse of current quantum information experiments [139] is spontaneous parametric down conversion (SPDC) which probabilistically produces correlated pairs of photons across two modes, one of which can be used to herald a single photon in the other. A nonlinear crystal produces phase matched photon pairs from a pump beam, with conversion efficiency up to 5×10^{-6} [140]. Herald efficiencies of about $\eta_h = 0.75$ recently allowed for loophole-free Bell tests with polarization entangled photon pairs from SPDC sources [15, 16].

To operate on-demand, SPDC sources must be combined with a suitable quantum memory, but the broadband photons produced by typical SPDC sources are incompatible with leading memories. Memory schemes such as EIT, GEM and AFC[2] in alkali or rare-Earth ion ensembles store fields with bandwidth ≈ 1MHz and resonant with an atomic transition (in Chap. 14 we review quantum memory research in detail). Typical SPDC sources have bandwidths on the order of 100s of GHz. To reduce the single-photon bandwidth by filtering alone requires an impractical reduction in brightness.

Cavity-enhanced SPDC produces narrow linewidth photon pairs, usually across several frequency modes, at the cost of total brightness. In most cases a chosen frequency mode must be spectrally filtered by an additional external cavity [141], but two recent cavity-SPDC sources have shown near-single mode operation by double-passing the pump through the crystal [142, 143]. Ref. [143] is a noteworthy memory-compatible SPDC source with pair generation rate 7.24×10^5 pairs s^{-1} mW^{-1} and bandwidth of $2\pi \times 6.6(6)$ MHz for a spectral brightness of 1.06×10^5 pairs s^{-1} mW^{-1} MHz^{-1}. This is, to our knowledge, the spectrally-brightest single-mode SPDC source. With an external filter cavity, Ref. [141] demonstrates single photon generation with bandwidth $2\pi \times 0.66(2)$ MHz, $g^{(2)}(0) = 0.016(2)$ and heralding rate 5 kHz.

Even as a probabilistic source SPDC has important limitations. Unless efficient photon number resolving detectors are available to discriminate single-pair from multi-pair events at the herald, SPDC sources produce fields with an intrinsic multi-photon component that scales with the pair generation rate [144], therefore requiring SPDC sources to operate at low brightness. For example, the telecom SPDC source in Ref. [145] produced photons with bandwidth of 6.9 nm. For $\mathbb{A} = 0.01$ the feasible heralding rate was only 403 kHz, yielding a spectral brightness of less than 4 pairs MHz^{-1}. For this reason quantum information experiments with even small numbers of photons generated by SPDC can take hundreds of hours [146, 147]. In Chap. 8 we compare the multi-photon rates of SPDC, quantum dot and trapped-atom photon-sources and show that the intrinsic multi-photon rate of SPDC sources is detrimental to performance in QKD networks. Finally, photon pairs produced by SPDC are simultaneously entangled in several degrees of freedom. This entanglement between the photon pairs limits indistinguishability [148, 149].

5.2.2 FWM

Correlated photon pairs can also be produced using four-wave mixing (FWM) in which two pump photons are converted to correlated signal and idler photons. Because the required nonlinearity is small, optically dense media are required. FWM in waveguides and fibres is a source of broadband photons at telecom frequencies, although FWM sources are typically noisier than SPDC due to Raman scattering processes that can be difficult

---

[2]Although AFC delay lines are broadband, on-demand AFC storage is not.

to suppress and may require cryogenic cooling [150]. Fibre-based FWM sources have been operated with herald efficiency up to $\eta_h = 0.26$ [151] and $\mathbb{A} = 0.01$ [152] at a spectral brightness up to 10^4 pairs s^{-1} mW^{-1} MHz^{-1} [137]. FWM in optically dense cold-atom ensembles is a source of narrowband photon pairs. Autonomous FWM sources have been made to interfere with $V = 0.83$ [153].

5.3   On-demand sources

Natural or artificial single emitters are a means of producing single-photons on demand such that a separate quantum memory becomes unnecessary. This simplifies the technical overhead of optical quantum computing substantially. If the single emitters are themselves suitable qubits for computation, then photon emission is a means of optically coupling and entangling separate quantum registers. Similarly, well-coupled single emitters may function as quantum memories for optical networks.

Atomic transitions are natural single emitters, and the focus of research in this thesis. In the following section we review the leading techniques for achieving efficient atom-light interfaces including optical resonators and free-space couplers. Engineered systems including semi-conductor quantum dots (QDs) and crystal defects replicate some of the useful properties of atomic transitions, and are sometimes called 'artificial atoms'. We will also review recent advances with these leading engineered systems. Recent research on solid-state photon sources has expanded to include novel two-dimensional materials and carbon nano-tubes. Such less-developed sources are outside the scope of this review but interested readers can see Ref. [154].

5.4   Trapped atoms

Single trapped atoms are a natural candidate for the nodes of a quantum network. We've already seen how long-lived qubits can be implemented with the electronic configuration of atoms in Chap. 3 and we will discuss our particular implementation with trapped Barium ions in Chap. 6. Atoms of the same isotope are naturally identical in all respects and, if the atoms are well insulated from their environment, photons scattered from atoms can be made to interfere with high visibility. Experimental techniques for isolating, manipulating and addressing single trapped atoms are well developed. Furthermore, although scaling trapped-ion quantum computers is challenging, they are currently the most advanced platform for universal quantum computation [42, 155]. Atom-light interfaces with trapped atoms are a means of networking such systems, and perhaps a feasible path to scaling trapped-atom processors by networking small quantum processors [57]. Apart from their advantages as photon sources for quantum networks, this provides an additional motivation for trapped-ion based atom-light couplers in particular.

However, the interaction cross section of atoms and photons in free space is small. To couple atomic and photonic qubits deterministically requires an efficient atom-light interface. Enormous progress has been made towards this goal in the last decade, particularly in the field of cavity QED. In the sections below we will consider the relative advantages of cavity and free-space based atom-light couplers, and review recent results with rudimentary optical networks of trapped atoms.
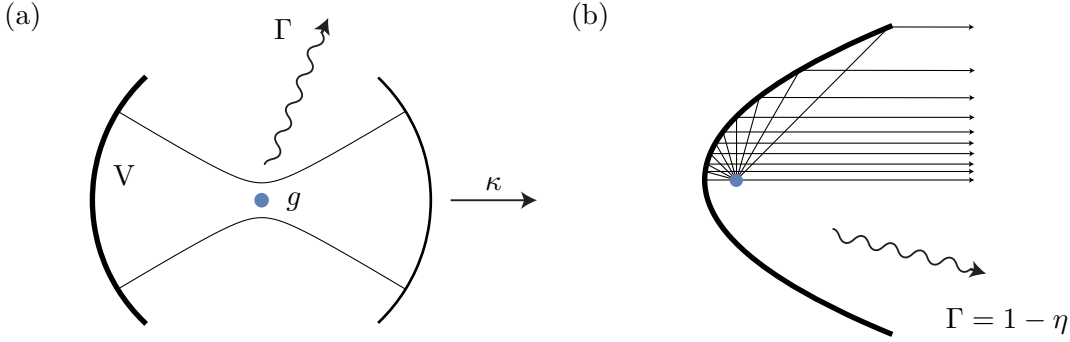
Figure 5.1: (a) Schematic of a resonator-coupled atom showing the important cavity parameters. (b) Free space coupling by a parabolic mirror.

5.4.1   Coupling with optical resonators

Resonators can be used to couple atoms to either optical or microwave photons, but we will restrict this review to atom-light couplers for optical photonic networks, which have longer coherence times. When an atom is positioned at an anti-node of a cavity standing wave, the atom-photon interaction strength can be much larger than in free space. Resonators effectively increase the interaction strength in two ways: by confining the photon to a small resonator mode and by increasing the interaction time. We call the regimes dominated by one or the other of these effects the 'Purcell' and 'strong' coupling regimes respectively [156].

The important cavity parameters are the coherent atom-field coupling constant for the cavity field g, the free-space atomic emission rate Γ and the cavity decay rate κ, which is inversely related to the cavity finesse $\mathscr{F}$ shown in Fig. 5.1(a). Together these give the cooperativity $C = g^2/(\kappa\Gamma)$ and Purcell emission rate enhancement $P = 1 + 2C$. The collection efficiency in such a cavity is the product of three probabilities [157]

$$\eta = T\left(\frac{2C}{1+2C}\right)\left(\frac{2\kappa}{2\kappa + \Gamma}\right),\tag{5.2}$$

where T is the transmission of the cavity, the second term is the cavity capture proportion and the third term is the cavity loss proportion of the atom-cavity system. Written in this way, it becomes clear that efficient atom-cavity coupling requires both large g and κ.

There are two typical strategies for designing resonator-based atom-light couplers. First, improving the cavity finesse allows photons to interact with the atom over many cavity round-trips or, equivalently, to interact with many mirror images of the atom at the same time. This is the strong coupling regime, $g > \kappa, \Gamma$ and $C \gg 1$, typified by oscillatory exchange between the atom and cavity field. In this regime the coupling strength g has been increased so that it exceeds all the dissipative processes in the system, but at the cost of lower cavity linewidth κ.

In practice many implementations fall short of strong coupling. However, high-finesse cavity sources can be operated efficiently with Λ-atoms and Raman coupling schemes, even when the free-space spontaneous emission rate Γ is faster than the cavity dynamics. This is achieved by taking advantage of the different detuning dependence between the coherent and incoherent Raman processes and is sometimes called the 'intermediate' regime [158].

The effective Raman atom-cavity coupling and spontaneous decay rates are

$$g_{\text{eff}} = g \frac{\Omega_e}{2\Delta} \, , \tag{5.3}$$

$$\Gamma_{\text{eff}} = \Gamma \left(\frac{\Omega_e}{2\Delta} \right)^2 . \tag{5.4}$$

By choosing the excitation power Ω_e and detuning Δ such that $\kappa > g_{\text{eff}} > \Gamma_{\text{eff}}$, the atomic excitation may be efficiently transferred to the field. However, the repetition rate of the source is still restricted by the cavity decay rate κ. There is an implicit trade-off in the design of both strong and intermediate resonator coupled photon sources: the better the cavity finesse, the lower the linewidth and the lower the speed of the network.

The second route to resonator-based networks is reducing the cavity mode volume. In quantizing the electric field we saw that the field strength per photon depends on the mode volume V, Eqn. 2.4. As the mode volume of a single photon decreases, the strength of the field increases. Confining photons to a smaller mode therefore improves the interaction strength according to $g \propto 1/\sqrt{V}$. With sufficiently small mode volume even leaky cavities can be efficient couplers. This is the Purcell regime of small, leaky cavities with $\kappa \gg g \gg \Gamma$ and $C \gg 1$. In this regime the cavity increases the atom-light coupling strength by shaping the photonic spatial mode density in the vicinity of the atom. In Sec. 10.7.2 we consider a single-pass approach to atom-light coupling which uses the same technique, and realizes an extreme of the Purcell resonator regime.

As we described in Sec. 3.4.2, photons can be generated reversibly from Λ-atoms in cavities by vacuum StiRAP with the cavity mode. This has been performed with cold neutral atoms falling through cavities [159, 160], neutral atoms in optical traps [161, 162] and trapped ions [163]. Compared to electromagnetically trapped ions, optically trapped atoms have limited trapping time and are less well localized, which compromises atom-cavity coupling and is an additional source of decoherence. On the other hand, trapped ions are restricted by the geometries of large ion traps (a problem that we will also face in Chap. 11) and coupling ions to small cavities is difficult because charged particles interact strongly with nearby surfaces. To date no trapped-ion photon-source has been operated in the strong or Purcell cavity QED regimes.

Here we will highlight recent experiments with resonator-based atom-light couplers. Refs. [156, 164] contain a historical overview and further detail for readers interested in the landmark results in this field. StiRAP has been performed with trapped ions in Fabry-Pérot cavities with collection efficiency $\eta_I = 0.88$ and total efficiency $\eta = 0.045$ at a rate of 2.4 kHz [165]. The source is essentially dark count limited, with $\mathbb{A} = 0.015$. The photon source may be operated as a unidirectional atom-light qubit interface with $\eta = 0.01$ and fidelity $F = 0.66$[166] and to demonstrate atom-photon entanglement [167].

StiRAP has also been demonstrated with neutral atoms in large cavities with $\eta_I = 0.56$ and $\eta = 0.15$ at a rate of 100 kHz[168]. Once again, the number-purity of the source is essentially dark-count limited, $\mathbb{A} = 0.02$. Operated as a unidirectional atom-light qubit interface the fidelity is $F = 0.93$[169]. The trapped atom source has been operated as a deterministic quantum memory with efficiency $\eta = 0.17$ and fidelity $F = 0.93$ [169, 170] as well as a heralded quantum memory with $\eta = 0.39$ and $F = 0.86$[171].

To this point, a state of the art atom-light quantum network consists of two nodes universally coupled (read and write) to a single network link. Teleportation has been performed with neutral trapped atoms in Fabry-Pérot cavities in this configuration with

fidelity $F = 0.88$ and success probability $P = 0.001$ at an attempt rate of 10 Hz [172]. The interference visibility in that experiment was limited by inhomogeneous transition broadening to $V = 0.64$. Ground state cooling has since been demonstrated with trapped neutral atoms in optical cavities [173] which would improve the source indistinguishability considerably.

Although these elementary atom-light networks have been constructed from relatively large cavities, miniaturization is the route to fast, high efficiency single photons from atom-resonator systems. To this end atoms have been coupled to fibre-based Fabry-Pérot cavities [174, 175], microtoroidal resonators [176, 177] and photonic crystal cavities [178]. Fibre cavities are a promising path towards coupling trapped ions in particular because the dielectric surface required can be small, and shielded using metal fibre sleeves [179, 180].

5.5   Free-space coupling

The operation of an atom-light quantum network does not, however, require optical resonators. In Chap. 4 we derived the free-space dipole field and the necessary optics for efficiently collecting and networking a photon in this dipole mode. As we noted at the time, such free-space optics are not only capable of efficient single photon collection, they are also capable of the reverse process: efficient single photon absorption by a single atom [181–183]. Furthermore, a free-space coupled atom is also capable of efficiently switching or even phase shifting an input field by up to π [133, 184]. Confocal lenses have even applied the techniques of 4π-microscopy to achieve almost 40% extinction by a single atom, and observed nonlinear atom-photon interactions in this regime. Free-space coupling may be seen as an extreme limit of the cavity QED Purcell regime, in which the mode confinement is provided by tight focussing and the $\kappa \to \infty$. In this limit the discrete cavity modes approach the continuum of free-space modes.

Efficient free-space atom-light coupling requires diffraction-limited collection optics capturing as close to the complete 4π-steradian solid angle as possible. Recent efforts towards this goal have been reviewed in detail by Refs. [133, 185, 186]. Common approaches include high-aperture lenses and lens objectives [187–192], thin Fresnel lenses [116, 193], spherical mirrors [194] and parabolic mirrors [111, 118] as shown in Fig. 5.1(b). It is the parabolic mirror apparatus in Ref. [111] that is closest to collecting the complete fluorescence from a single trapped atom. We calculated the collection efficiency limit for a parabolic mirror with the same dimensions in Sec. 4.7. For the optimally oriented π-transition the collection limit is $\eta_I = 0.97$. Ref. [111] demonstrates a collection efficiency of $\eta_I = 0.55$, limited by the reflectivity of the mirror surface, for a total collection efficiency of $\eta = 0.031$. As we discussed in the context of cavity-based trapped-atom photon sources, trapped ions have the advantage of tighter confinement, but require novel trap designs that allow sufficient optical access. We'll consider this problem further in Chap. 11.

With sufficient atom-field coupling a single atom has been shown to extinguish more than 10% [187] and impart a phase shift of up to 2° [195] to a coherent incident field [195–197] and up to 75° to the scattered field [198]. Similar extinction and phase shift results have been shown by focussing fields on to single molecules [199, 200] and quantum dots [201]. In this coupling regime single atoms produce phenomena typically associated with optically dense ensembles including electromagnetically induced transparency [202], coherent back-scattering [203] and Faraday rotation [196].

Although high efficiency free-space collection remains an outstanding challenge, many

of the rudimentary operations of a quantum network have already been demonstrated with free-space coupled atoms. Efficient excitation of a trapped-atom free-space node requires not only high-aperture optics, but also perfect time reversal of the atomic decay process. This means generating photons matching both the spatial and time-reversed temporal modes. Free-space excitation has been performed with rising exponential pulses and achieved an excitation probability of $\eta = 0.05$ by coherent pulses with $\langle n \rangle \approx 3$ [204].

Free-space coupled single-atom photon sources have been used to demonstrate atom-photon entanglement [205] as well as atom-atom entanglement through photonic links. Ref. [206] achieved an entanglement fidelity of $F = 0.63$, however this entanglement scheme requires simultaneous detection of photons from each atom, and the success probability is therefore limited by the collection efficiency to $P = 3.6 \times 10^{-9}$ at an attempt rate of 550 kHz. Similarly, heralded teleportation has been performed with free-space atom-light couplers at an attempt rate of 75 kHz and fidelity $F = 0.9$ and success probability $\eta = 1.9 \times 10^{-8}$ [207]. A similar coincidence-based approach with neutral atoms achieved fidelity $F = 0.81$, beating the Bell's inequality threshold, with success probability 5×10^{-7} and rate 50 kHz [208]. Ref. [190] uses the single-photon entanglement herald proposed in Ref. [209] to improve the success probability to $P = 1.1 \times 10^{-4}$ at an attempt rate of 2.3 kHz with fidelity $F = 0.64$. However, in the efficient-collection limit the advantage of single-photon detection schemes diminishes.

Finally, the same technique has been applied to entangle small trapped-ion registers with a photonic entanglement rate faster than the observed decoherence rate [192]. In this miniature of a distributed-computing scheme the motional entangling gates between trapped ions in the same register can be used in concert with the optical remote entanglement operation. As with cavity-based networks, networks of free-space coupled atoms are currently no larger than two nodes separated by a single link.

5.6 Artificial atoms

5.6.1 Quantum dots

Semiconductor quantum dots (QDs) are the most promising practical on-demand photon sources because these 'artificial atoms' may be integrated into semiconductor technologies, including high Q-micro-cavities, and because they may be triggered to spontaneously scatter photons either optically or electrically [210]. While QDs are in principle single emitters, multi-photon noise in these systems may be poor compared to trapped atoms due to interactions with the bulk material or surface charge noise [211]. QDs must operate at cryogenic temperatures (≈ 4K) to suppress thermal bulk interactions. Currently, electrically driven QDs are substantially noisier than optically driven dots with $g^{(2)}(0) \geq 0.08$ [212].

Quantum dots may be integrated with optical microcavities [213–216] to improve collection efficiency and narrow linewidth by the Purcell effect. The record collection efficiency for QDs is $\eta_c = 0.79$ which was reached with low-finesse micro-pillar cavity and a NA= 0.6 collection lens [217]. In Ref. [218] quantum dots in electrically-tunable micro-pillar cavities are coupled with a single-mode collection efficiency of $\eta_c = 0.64(1)$. Under pulsed, resonant excitation this QD produces single photons with generation probability $\eta_g = 0.33$, purity $g^{(2)}(0) = 0.002(1)$ and indistinguishability $M = 0.995(5)$. Purity is, however, reduced when operating at saturation , $g^{(2)}(0) = 0.015(3)$. Although this single-photon source is an order of magnitude brighter than state-of-the-art SPDC in absolute

terms, the spectral brightness is lower at 4×10^4 phot MHz^{-1} due to the use of lower cavity finesse. Operating QDs in a cavity with finesse comparable to SPDC sources is an outstanding technical challenge.

Quantum dots are not grown deterministically, and the spectral properties vary from dot to dot such that their mutual interference is insufficient for use in quantum networks [219, 220]. Electrically tunable QD sources may be one avenue to improving parallel indistinguishability [221]. Electrically tuned quantum dots have achieved mutual indistinguishability $M = 0.82(3)$ which was sufficient to teleport a photonic frequency qubit from a QD source to a second QD spin [222]. This degree of indistinguishability was achieved with low-collection efficiency QDs in bulk and the necessary tunability is inconsistent with QD microcavity systems. Photons from optically excited QDs have very recently been made to interfere with mutual indistinguishability $M = 0.41(5)$ by actively stabilizing the frequency of each dot to an atomic resonance [223].

A single dot producing long streams of indistinguishable photons that can be demultiplexed across many spatial modes may still be useful for photonic computation [224]. Active demultiplexing schemes look to outperform passively demultiplexed photons and SPDC networks with feasible six-photon rates of ≈ 0.01 /s [225]. This technology is approaching the threshold for quantum advantage in (non-universal) photonic computing.

5.6.2 Diamond colour centres

Fluorescent crystal defects are solid-state qubits with coherence times that can be long even at room temperature. Nitrogen-vacancy (NV) and Silicon vacancy (SiV) defects in diamond have been well characterized as photon-sources, and Germanium vacancy centres in diamond are a promising new alternative. Like QDs, NV colour centres must operate at cryogenic temperatures or be coupled to high-finesse cavities to produce indistinguishable photons.

Photons from independent cold NV centres can interfere with HOM visibility $M = 0.66$ [226]. It is difficult to improve this indistinguishability further because the NV centre has a non-zero dipole moment that couples to material strains and charges that are not yet well-controlled. Nevertheless the mutual indistinguishability of NV centres is sufficiently good for spin-qubit teleportation [227] and loophole-free Bell tests [14]. SiV centres are better isolated, they benefit from an inversion symmetry, and have been shown to interfere with visibility $M = 0.72$ [228]. SiV centres have comparatively low quantum efficiency because of competing pathways to the zero-phonon emission line. SiV centres have been shown to be bright, but not spectrally bright [229]. Germanium vacancies are considered a likely candidate for simultaneously narrow and bright transitions.

Most photons emitted from colour centres in bulk diamond are trapped inside the high refractive index material by total internal reflection, and near the diamond surface, dipole emission still prefers the high index material. To efficiently collect photons from defect transitions the optical mode in the diamond must be engineered. Strategies include coupling to guided modes in pillar-like structures (which must in turn be out-coupled), collection by solid immersion lenses on the diamond surface, and embedding defects inside diamond micro-resonators (see the recent review [230]) and references therein). The best collection efficiency achieved by such methods is $\eta_c \approx 0.3$ [231] with a surface-etched immersion lens of NA = 1.5. It is believed that surface etching of this sort introduces crystal defects that degrade the transition spectrum.

Demonstrated colour-centre sources are noisy compared to QDs or trapped atoms. The

single-photon purity of colour centres in diamond is obscured by the collection of scattered background light, with few results better than $g^{(2)}(0) = 0.1$ [232].

Bibliography - Single photon sources

14. B. Henson, et al., Loophole-free Bell inequality violation using electron spins separated by 1.3 kilometres, *Nature* **526**, 682–686 (2015).

15. L. K. Shalm, et al., Strong loophole-free test of local realism, *Phys. Rev. Lett.* **115**, 250402 (2015).

16. M. Giustina, et al., Significant loophole-free test of Bell's theorem with entangled photons, *Phys. Rev. Lett.* **115**, 250401 (2015).

42. T. Monz, et al., Realization of a scalable Shor algorithm, *Science* **351** (2016).

44. E. Knill, R. Laflamme, and G. J. Milburn, A scheme for efficient quantum computation with linear optics., *Nature* **409**, 46–52 (2001).

57. C. Monroe, and J. Kim, Scaling the ion trap quantum processor, *Science* **339**, 1164–9 (2013).

111. R. Maiwald, et al., Collecting more than half the fluorescence photons from a single ion, *Phys. Rev. A* **86**, 043431 (2012).

116. E. W. Streed, et al., Imaging of trapped ions with a microfabricated optic for quantum information processing, *Phys. Rev. Lett.* **106**, 10502 (2011).

118. M. Sondermann, et al., Design of a mode converter for efficient light-atom coupling in free space, *Appl. Phys. B* **89**, 489–492 (2007).

133. G. Leuchs, and M. Sondermann, Light–matter interaction in free space, *J. Mod. Opt.* **60**, 1–7 (2013).

134. M. Planck, Zur Theorie des Gesetzes der Energieverteilung im Normalspectrum, *Verhandl. Dtsc. Phys. Ges.* **2**, 237 (1900).

135. A. Einstein, On a heuristic point of view concerning the creation and conversion of Light, *Ann. Phys.* **17**, 91 (1905).

136. B. Lounis, and M. Orrit, Single-photon sources, *Reports Prog. Phys.* **68**, 1129–1179 (2005).

137. M. D. Eisaman, et al., Invited review article: Single-photon sources and detectors., *Rev. Sci. Instrum.* **82**, 071101 (2011).

138. M. Grimau Puigibert, et al., Heralded single photons based on spectral multiplexing and feed-forward control, *Phys. Rev. Lett.* **119**, 083601 (2017).

139. A. Soujaeff, et al., Quantum key distribution at 1550 nm using a pulse heralded single photon source, *Opt. Express* **15**, 726 (2007).

140. M. Bock, et al., Highly efficient heralded single-photon source for telecom wavelengths based on a PPLN waveguide, *Opt. Express* **24**, 23992 (2016).

141. M. Rambach, et al., Sub-megahertz linewidth single photon source, *APL Photonics* **1**, 096101 (2016).

142. C.-S. Chuu, G. Y. Yin, and S. E. Harris, A miniature ultrabright source of temporally long, narrowband biphotons, *Appl. Phys. Lett.* **101**, 051108 (2012).

143. P.-J. Tsai, and Y.-C. Chen, Ultrabright, narrow-band photon-pair source for atomic quantum memories, *Quantum Sci. Technol.* (2017).

144. E. Waks, E. Diamanti, and Y. Yamamoto, Generation of photon number states, *New J. Phys.* **8**, 4–4 (2006).

145. S. Fasel, et al., High-quality asynchronous heralded single-photon source at telecom wavelength, *New J. Phys.* **6**, 163–163 (2004).

146. L. K. Shalm, et al., Three-photon energy–time entanglement, *Nat. Phys.* **9**, 19–22 (2012).

147. T. Guerreiro, et al., Nonlinear interaction between single photons, *Phys. Rev. Lett.* **113** (2014).

148. W. P. Grice, A. B. U'Ren, and I. A. Walmsley, Eliminating frequency and space-time correlations in multiphoton states, *Phys. Rev. A* **64**, 063815 (2001).

149. P. G. Evans, et al., Bright source of spectrally uncorrelated polarization-entangled photons with nearly single-mode emission, *Phys. Rev. Lett.* **105**, 253601 (2010).

150. K. F. Lee, et al., Generation of high-purity telecom-band entangled photon pairs in dispersion-shifted fiber, *Opt. Lett.* **31**, 1905 (2006).

151. B. J. Smith, et al., Photon pair generation in birefringent optical fibers, *Opt. Express* **17**, 23589 (2009).

152. A. Ling, et al., Mode expansion and Bragg filtering for a high-fidelity fiber-based photon-pair Source, *Opt. Express* **17**, 21302 (2009).

153. T. Jeong, et al., Quantum interference between autonomous single-photon sources from Doppler-broadened atomic ensembles, *Optica* **4**, 1167 (2017).

154. I. Aharonovich, D. Englund, and M. Toth, Solid-state single-photon emitters, *Nat. Photonics* **10**, 631–641 (2016).

155. R. Blatt, and C. F. Roos, Quantum simulations with trapped ions, *Nat. Phys.* **8**, 277–284 (2012).

156. A. Reiserer, and G. Rempe, Cavity-based quantum networks with single atoms and optical photons, *Rev. Mod. Phys.* **87**, 1379–1418 (2015).

157. L. Luo, et al., Protocols and techniques for a scalable atom-photon quantum network, *Quantum* **1152**, 1–19 (2009).

158. T. E. Northup, et al., An ion-cavity interface for quantum networks, *Proceedins SPIE* **961506**, 1–9 (2015).

159. A. Kuhn, M. Hennrich, and G. Rempe, Deterministic single-photon source for distributed quantum networking., *Phys. Rev. Lett.* **89**, 067901 (2002).

160. M. Hennrich, et al., Photon statistics of a non-stationary periodically driven single-photon source, *New J. Phys.* **6**, 86–86 (2004).

161. J. McKeever, et al., Deterministic generation of single photons from one atom trapped in a cavity., *Science* **303**, 1992–1994 (2004).

162. T. Wilk, et al., Polarization-controlled single photons, *Phys. Rev. Lett.* **98**, 063601 (2007).

163.   M. Keller, et al., Continuous generation of single photons with controlled waveform in an ion-trap cavity system, *Nature* **431**, 1075–1078 (2004).

164.   A. Kuhn, Cavity Induced Interfacing of Atoms and Light, in *Engineering the atom-photon interaction: Controlling fundamental processes with photons, atoms and solids*, edited by A. Predojević, and M. W. Mitchell, (Springer International Publishing, 2015).

165.   H. G. Barros, et al., Deterministic single-photon source from a single ion, *New J. Phys.* **11**, 103004 (2009).

166.   A. Stute, et al., Quantum-state transfer from an ion to a photon, *Nat. Photonics* **7**, 219–222 (2013).

167.   A. Stute, et al., Tunable ion-photon entanglement in an optical cavity, *Nature* **485**, 482–485 (2012).

168.   M. Mücke, et al., Generation of single photons from an atom-cavity system, *Phys. Rev. A* **87**, 063805 (2013).

169.   H. P. Specht, et al., A single-atom quantum memory., *Nature* **473**, 7 (2011).

170.   S. Ritter, et al., An elementary quantum network of single atoms in optical cavities, *Nature* **484**, 195–200 (2012).

171.   N. Kalb, et al., Heralded storage of a photonic quantum bit in a single atom, *Phys. Rev. Lett.* **114**, 220501 (2015).

172.   C. Nölleke, et al., Efficient teleportation between remote single-atom quantum memories, *Phys. Rev. Lett.* **110** (2013).

173.   A. Reiserer, et al., Ground-state cooling of a single atom at the center of an optical cavity, *Phys. Rev. Lett.* **110**, 223003 (2013).

174.   D. Hunger, et al., A fiber Fabry–Perot cavity with high finesse, *New J. Phys.* **12**, 065038 (2010).

175.   S. Kato, and T. Aoki, Strong coupling between a trapped single atom and an all-fiber cavity, *Phys. Rev. Lett.* **115**, 1–5 (2015).

176.   B. Dayan, et al., A photon turnstile dynamically regulated by one atom., *Science* **319**, 1062–5 (2008).

177.   T. Aoki, et al., Efficient routing of single photons by one atom and a microtoroidal cavity, *Phys. Rev. Lett.* **102**, 083601 (2009).

178.   J. D. Thompson, et al., Coupling a single trapped atom to a nanoscale optical cavity., *Science* **340**, 1202–5 (2013).

179.   M. Steiner, et al., Single ion coupled to an optical fiber cavity, *Phys. Rev. Lett.* **110**, 043003 (2013).

180.   B. Brandstätter, et al., Integrated fiber-mirror ion trap for strong ion-cavity coupling, *Rev. Sci. Instrum.* **84**, 123104 (2013).

181.   D. Pinotsi, and A. Imamoglu, Single photon absorption by a single quantum emitter, *Phys. Rev. Lett.* **100**, 93603 (2008).

182.   M. Stobińska, G. Alber, and G. Leuchs, Perfect excitation of a matter qubit by a single photon in free space, *Europhys. Lett.* **86**, 14007 (2009).

183. Y. Wang, et al., Quantum memory with a single two-level atom in a half cavity, *Phys. Rev. A* **85**, 1–8 (2012).

184. M. Sondermann, and G. Leuchs, The phase shift induced by a single atom in free space, *J. Eur. Opt. Soc. Rapid Publ.* **8**, 13052 (2013).

185. M. Sondermann, and G. Leuchs, Photon-atom coupling with parabolic mirrors, in *Engineering the atom-photon interaction: Controlling fundamental processes with photons, atoms and solids*, edited by A. Predojević, and M. W. Mitchell, (Springer International Publishing, 2015), pp. 1–18.

186. L. Slodička, et al., Free space interference experiments with single photons and single ions, in *Engineering the atom-photon interaction: Controlling fundamental processes with photons, atoms and solids*, edited by A. Predojević, and W. M. Mitchell, (Springer International Publishing, Cham, 2015), pp. 99–124.

187. M. K. Tey, et al., Strong interaction between light and a single trapped atom without the need for a cavity, *Nat. Phys.* **4**, 924–927 (2008).

188. S. A. Aljunid, et al., Interaction of light with a single atom in the strong focusing regime, *J. Mod. Opt.* **58**, 299–305 (2011).

189. N. Piro, et al., Heralded single-photon absorption by a single atom, *Nat. Phys.* **7**, 17–20 (2010).

190. L. Slodička, et al., Atom-atom entanglement by single-photon detection, *Phys. Rev. Lett.* **110**, 083603 (2013).

191. J. Wong-Campos, et al., High-resolution adaptive imaging of a single atom, *Nat. Phot.* **10**, 606–610 (2016).

192. D. Hucul, et al., Modular entanglement of atomic qubits using photons and phonons, *Nat. Phys.* **11**, 37–42 (2014).

193. D. Kielpinski, et al., Integrated optics architecture for trapped-ion quantum information processing, *Quantum Inf. Process.* **15**, 5315–5338 (2016).

194. A. Roy, A. B. S. Jing, and M. D. Barret, The trapping and detection of single atoms using a spherical mirror, *New J. Phys.* **14** (2012).

195. M. Fischer, et al., Shifting the phase of a coherent beam with a 174 Yb+ ion: influence of the scattering cross section, *Appl. Phys. B* **123**, 48 (2017).

196. G. Hétet, et al., Free-space read-out and control of single-ion dispersion using quantum interference, *Phys. Rev. A* **88**, 041804 (2013).

197. S. Aljunid, et al., Phase shift of a weak coherent beam induced by a single atom, *Phys. Rev. Lett.* **103**, 153601 (2009).

198. A. Jechow, et al., Controllable optical phase shift over one radian from a single isolated atom, *Phys. Rev. Lett.* **110**, 113605 (2013).

199. G. Wrigge, et al., Efficient coupling of photons to a single molecule and the observation of its resonance fluorescence, *Nat. Phys.* **4**, 60–66 (2008).

200. M. Pototschnig, et al., Controlling the phase of a light beam with a single molecule, *Phys. Rev. Lett.* **107**, 063001 (2011).

201. A. N. Vamivakas, et al., Strong extinction of a far-field laser beam by a single quantum dot, *Nano Lett.* **7** (2007).

202. L. Slodička, et al., Electromagnetically induced transparency from a single atom in free space, *Phys. Rev. Lett.* **105**, 4 (2010).

203. G. Hétet, et al., Single atom as a mirror of an optical cavity, *Phys. Rev. Lett.* **107**, 1–5 (2011).

204. S. A. Aljunid, et al., Excitation of a single atom with exponentially rising light pulses, *Phys. Rev. Lett.* **111**, 103001 (2013).

205. B. B. Blinov, et al., Observation of entanglement between a single trapped atom and a single photon., *Nature* **428**, 153–7 (2004).

206. D. L. Moehring, et al., Entanglement of single-atom quantum bits at a distance, *Nature* **449**, 68–71 (2007).

207. S. Olmschenk, et al., Quantum teleportation between distant matter qubits, *Science* **323**, 486–9 (2009).

208. J. Hofmann, et al., Heralded entanglement between widely separated atoms, *Science* **337**, 72–76 (2012).

209. C. Cabrillo, et al., Creation of entangled states of distant atoms by interference, *Phys. Rev. A* **59**, 1025–1033 (1999).

210. Z. Yuan, et al., Electrically driven single-photon source, *Science* **295** (2002).

211. A. V. Kuhlmann, et al., Charge noise and spin noise in a semiconductor quantum device, *Nat. Phys.* **9**, 570–575 (2013).

212. M. Wiesner, et al., Single-photon emission from electrically driven InP quantum dots epitaxially grown on CMOS-compatible Si(001), *Nanotechnology* **23**, 335201 (2012).

213. A. Kress, et al., Manipulation of the spontaneous emission dynamics of quantum dots in two-dimensional photonic crystals, *Phys. Rev. B* **71**, 241304 (2005).

214. D. Press, et al., Photon antibunching from a single quantum-dot-microcavity system in the strong coupling regime, *Phys. Rev. Lett.* **98**, 117402 (2007).

215. M. Förtsch, et al., A versatile source of single photons for quantum information processing., *Nat. Commun.* **4**, 1818 (2013).

216. X. Ding, et al., On-demand single photons with high extraction efficiency and near-unity indistinguishability from a resonantly driven quantum dot in a micropillar., *Phys. Rev. Lett.* **116**, 020401 (2016).

217. K. H. Madsen, et al., Efficient out-coupling of high-purity single photons from a coherent quantum dot in a photonic-crystal cavity, *Phys. Rev. B* **90** (2014).

218. N. Somaschi, et al., Near-optimal single-photon sources in the solid state, *Nat. Photonics* **10**, 340–345 (2016).

219. A. J. Shields, Semiconductor quantum light sources, *Nat. Photonics* **1**, 215–223 (2007).

220. S. Kako, et al., A gallium nitride single-photon source operating at 200K, *Nat. Mater.* **5**, 887–92 (2006).

221. R. B. Patel, et al., Two-photon interference of the emission from electrically tunable remote quantum dots, *Nat. Photonics* **4**, 632–635 (2010).

222. W. Gao, et al., Quantum teleportation from a propagating photon to a solid-state spin qubit, *Nat. Commun.* **4** (2013).

223. M. Zopf, et al., Frequency feedback for two-photon interference from separate quantum dots, *Arxiv Prepr. 1712.08158v1* (2017).

224. J. C. Loredo, et al., Scalable performance in solid-state single-photon sources, *Optica* **3**, 433 (2016).

225. F. Lenzini, et al., Active demultiplexing of single photons from a solid-state source, *Laser Photonics Rev.* **11**, 1600297 (2017).

226. A. Sipahigil, et al., Quantum interference of single photons from remote nitrogen-vacancy centers in diamond, *Phys. Rev. Lett.* **108**, 143601 (2012).

227. W. Pfaff, et al., Unconditional quantum teleportation between distant solid-state quantum bits, *Science* **345** (2014).

228. A. Sipahigil, et al., Indistinguishable photons from separated silicon-vacancy centers in diamond, *Phys. Rev. Lett.* **113**, 113602 (2014).

229. E. Neu, M. Agio, and C. Becher, Photophysics of single silicon vacancy centers in diamond: implications for single photon emission, *Opt. Express* **20**, 19956 (2012).

230. T. Schröder, et al., Quantum nanophotonics in diamond, *J. Opt. Soc. Am. B* **33**, B65 (2016).

231. L. Li, et al., Efficient photon collection from a nitrogen vacancy center in a circular bullseye grating, *Nano Lett.* **15**, 1493–1497 (2015).

232. T. Schröder, et al., Ultrabright and efficient single-photon generation based on nitrogen-vacancy centres in nanodiamonds on a solid immersion lens, *New J. Phys.* **13**, 1–9 (2011).

Trapped-ion apparatus

How did I escape? With difficulty. How did I plan this moment? With pleasure.
– Alexandre Dumas, The count of Monte Cristo (1844)

This part of the thesis contains experimental and theoretical results regarding the coupling of trapped atoms and travelling light fields with free-space optics. The atoms are trapped with oscillating electric fields in an ion trap. Trapped ions have many properties uniquely suited to the preparation and manipulation of non-classical atomic and optical states. They are well isolated mechanical systems and a very good approximation of the ideal harmonic oscillator. The ions can be well insulated from thermal effects such that the coherence time of their motional states is long. Furthermore, laser cooling techniques for preparing the ions in the lowest motional state of the trapping potential are well-established. For these reasons trapped ions are a well developed, albeit small-scale, platform for quantum computation.

In this chapter we provide an overview of the trapped-ion apparatus used in the experiments that follow in this part of the thesis. Its key components are a macroscopic Paul trap for trapping Barium ions, lasers for ionizing, cooling and manipulating the configuration of the trapped ions, and a pair of high-aperture lens objectives (HALOs) for coupling the atomic states to optical fields. The HALOs are configured with a remote mirror that may couple either two adjacent atoms to a common optical mode or a single atom with its own reflection.

6.1 The Barium ion

Alkaline earth metals like Barium are common in ion trapping experiments because singly-ionized alkaline earth metals have only a single valence electron and straightforward hydrogen-like electronic structure. Barium (atomic number 56) is the heaviest stable alkaline earth, considerably heavier than Calcium (atomic number 20) which is the ion of choice for trapped-ion quantum computers. Light atoms are desirable for trapped-ion processors that utilize shared motional modes as the basis of multi-qubit gates because the time required for each gate scales like $\sqrt{Nm}$ where m is the atomic mass and N is the number of ions in the trap. However, we prefer Barium for these experiments because, conversely, heavier atoms can be better localized for coupling to to optical fields. Other advanced ion trap quantum computers and simulators use singly ionized Ytterbium (atomic number 70) which is the penultimate lanthanide [43].

In the following experiments we use the most common of Barium's seven naturally occurring isotopes, ^{138}Ba. Since the nuclear spin of this isotope is zero, there is no hyperfine splitting in the atomic spectra. The electronic ground state of ^{138}Ba$^+$, [Xe] $6\,\mathrm{S}_{1/2}$ is shown
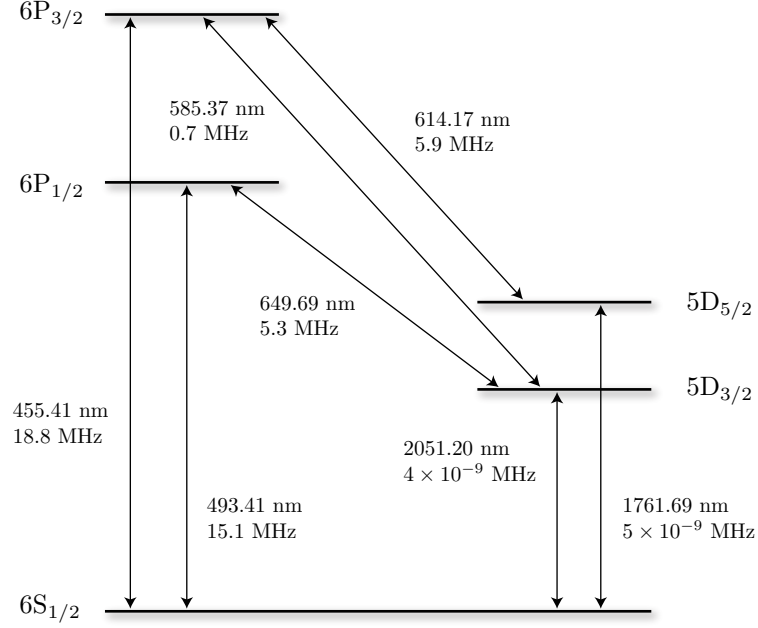
Figure 6.1: Electronic level structure of ^{138}Ba$^+$.

in Fig. 6.1 alongside the low-lying states we use in this thesis, and the corresponding wavelength and natural linewdith of each transition.

The 'blue'[1] dipole transition $6\,S_{1/2} \leftrightarrow 6\,P_{1/2}$ with transition wavelength $\lambda_b = 493.41$ nm and natural linewidth $\Gamma_b = 2\pi \times 15.1$ MHz is used for Doppler cooling, optical pumping, Raman scattering and state read-out. The excited state $6\,P_{1/2}$ decays with branching ratio $\approx 3{:}1$ to the long-lived metastable state $5\,D_{3/2}$. During cooling and pumping it is necessary to repump out of this long-lived state by driving the $6\,P_{1/2} \leftrightarrow 5\,D_{3/2}$ transition with an additional 'red' field at $\lambda_r = 649.69$ nm. The red transition linewidth is $\Gamma_r = 2\pi \times 5.3$ MHz.

In the experiments reported here we apply a weak magnetic field that determines the atomic quantization axis and lifts the degeneracy of the Zeeman sub-levels. It is necessary to impose a quantization axis in this way to optically drive σ transitions between the Zeeman states, otherwise continuous driving by the cooling and repump beams addresses only π transitions and simply pumps the atom into an extremal $5\,D_{3/2}$ state that is not cooled any further.

6.1.1   Qubits on the Barium ion

The Zeeman split ground states $6\,S_{1/2}, m_j = \pm\frac{1}{2}$ can be prepared in a decoherence-free subspace with long coherence times. Measurements taken as part of this thesis and reported in Ref. [5] show that dephasing of the Zeeman qubit is completely negligible over 4 ms. Coherence times many orders of magnitude larger than this are expected. For example, the coherence time of qubits in the comparable decoherence-free Zeeman sub-space of ^{40}Ca have been shown to be longer than 20 s [233]. These states compose a microwave-addressable qubit basis.

The other natural qubit states in ^{138}Ba$^+$ are the dipole-forbidden transitions between

---

[1]In terms of nomenclature, 493 nm is an inconvenient sort of cyan. To keep things simple we'll call this transition 'blue', but reasonable people can disagree as to whether 'green' is the better choice.

the $5\,\mathrm{D}$ and $6\,\mathrm{S}$ states. The lifetime of the metastable $5\,\mathrm{D}_{3/2}$ state is 80 s, amongst the longest radiative lifetime of any trapped ion transition [234]. The motional sidebands about these narrow quadrupole transitions are spectrally resolved, and can be addressed directly for sideband cooling.

6.2 Ion trapping 101

For the purpose of this thesis, we require stationary qubits that are well isolated from their environment, and localized sufficiently for optical control and coupling. A natural way to isolate and separate charged particles such as atomic ions is to trap them using electric fields. Unfortunately, no stationary electric field can confine a particle in all three directions, such a field would violate the condition $\nabla \cdot \mathbf{E} = 0$. However, charged particles can be confined in free space with oscillating electric fields. The trap-of-choice for trapped-ion quantum information experiments is the linear radio-frequency (RF) trap, which creates an oscillating planar quadrupole potential between two pairs of linear electrodes, one ground one RF at frequency Ω [235]. The quadrupole potential averaged over RF period $\frac{2\pi}{\Omega}$ gives a near-radial harmonic trap pseudo-potential. A pair of endcap electrodes provide a further axial static trapping potential. When the axial potential is weaker than the radial potential, cold trapped particles form a linear crystal along the axial 'trap' direction, separated by their mutual Coulomb repulsion. Typical linear trap depths range from 0.1 to 10 eV. At UHV background pressure a heavy ion can be kept trapped for months without cooling.

Following the comprehensive discussion of Paul traps in Ref. [53], the trapping potential can be decomposed into static and dynamic parts with quadratic form and respective amplitudes U and V

$$\phi = \frac{1}{2} \sum_{i=x,y,z} \left(U\alpha_i + V\cos\left(\Omega t\right)\gamma_i\right) x_i^2\,. \tag{6.1}$$

The ideal linear trap has geometric factors $\alpha_z = -(\alpha_x + \alpha_y)$, $\gamma_z = 0$ and $\gamma_y = -\gamma_x$. Because the potential terms are not coupled we can write independent equations of motion for each coordinate x_i

$$\frac{\mathrm{d}^2 x_i}{\mathrm{d}\xi^2} + \left[a_i - 2q_i \cos\left(2\xi\right)\right] x_i = 0\,, \tag{6.2}$$

which is the Mathieu differential equation with timescale $\xi = \Omega t/2$ and stability parameters

$$a_i = \frac{4|e|U\alpha_i}{m\Omega^2},\ q_i = \frac{2|e|V\gamma_i}{m\Omega^2} \tag{6.3}$$

for a unit positive charged particle. The stability diagram for two common ion trap configurations is reproduced from Ref. [53] in Figure 6.2. The region of stability is shown on the a_i, q_i plane alongside the characteristic exponent of classical motion in the driven potential β_i [53]. The trap is stable when $0 \leq \beta_i \leq 1\ \forall\, i \in x, y, z$. The Mathieu equation for the linear trap configuration allows stable solutions for $0 < a_i < 0.7$ and $q_i \leq \pm a_i^2/2$.

The stability diagrams of traps without this degree of symmetry are, in general, more complicated. Furthermore, the DC potential introduced by the linear trap to provide confinement along the trap axis has a radial defocussing effect that modifies the above stability diagram. The weak axial DC confinement changes not only the maximum stable trap q_i parameters, but also introduces an effective q_i minimum below which the trap is unstable. This effect is considerable when the axial and radial confinements are comparable
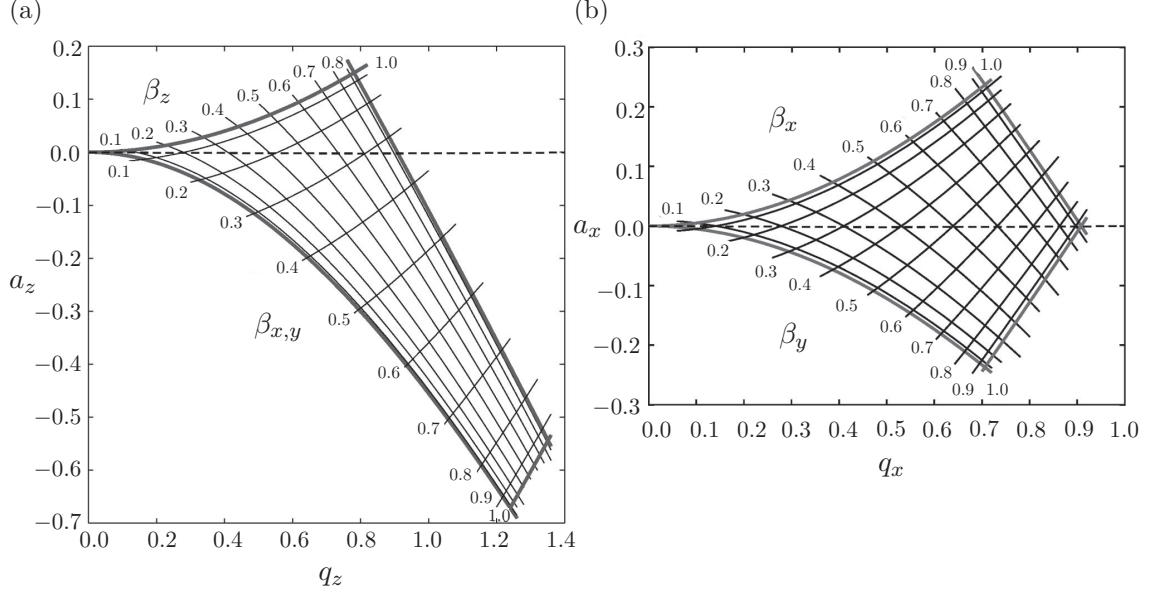
Figure 6.2: Stability diagrams of the lowest order stability regions for (a) a cylindrically symmetric 3D RF Paul trap ($\alpha_x = \alpha_y = -\alpha_z/2$, $\gamma_x = \gamma_y = -\gamma_z/2$) and (b) a linear RF Paul trap ($\alpha_x + \alpha_y = -\alpha_z$, $\gamma_x = -\gamma_y$, $\gamma_z = 0$) of the sort introduced in this chapter and used in Chaps. 7 to 9. Figure reproduced from Ref. [53]

[236]. In Chap. 11 we introduce the design of an ion trap for use with high-aperture optics that has a more complicated geometry. We will determine the stability regions of this trap by simulating ion trajectories numerically.

When $a_i, q_i \ll 1$ the particle motion is close to the lowest-order approximate solution

$$x_i(t) \propto \cos\left(\nu_i t\right) \left(1 - \frac{q_i}{2} \cos\left(\Omega t\right)\right) \tag{6.4}$$

consisting of two superimposed harmonic motions: so-called 'secular' motion with frequency $\nu_i = \frac{\Omega}{2}\sqrt{a_i + q_i^2/2}$ and 'micro' motion at the RF trap frequency Ω with amplitude smaller than the secular motion by a factor $q_i/2$.

When the mean position of a single trapped particle is the minimum of the RF pseudo-potential [53]

$$\tilde{\phi}_{\mathrm{RF}} = \frac{q|\nabla\phi_{\mathrm{RF}}|^2}{4m\Omega^2}, \tag{6.5}$$

the micromotion can be made vanishingly small, however it is impossible to remove micromotion completely when more than one particle is trapped in the same potential. The linear trap reduces the micromotion of trapped-ion crystals by aligning the linear crystal along a near-null pseudo-potential axis. In the secular approximation micromotion is neglected and the motion of the trapped particle is simply a three dimensional harmonic oscillator with oscillation frequencies ν_i.

6.3   Motional states of harmonically trapped atoms

The complete energy configuration of the atom includes not only the internal electronic configuration, but also the motional mode. The motional states of a trapped atom in a

harmonic potential are quantized with regularly spaced energy eigenstates

$$E_n = \hbar\nu \left(n + \tfrac{1}{2}\right) . \tag{6.6}$$

The eigenfunctions of the Schrödinger equation with a simple harmonic potential may be expressed in terms of the Hermite polynomials H_n

$$\psi_n(\rho) = \frac{1}{\sqrt{2^{n-1}(j-1)!\sqrt{\pi}}} H_{n-1}(\rho) e^{-\rho^2/2} , \tag{6.7}$$

where the dimensionless parameter ρ is related to the atomic displacement x according to $\rho = \sqrt{\frac{m\nu}{\hbar}}x$. The position and momentum operators of the trapped atom can be written in terms of ladder operators for the motional quanta

$$\begin{aligned}
\hat{x} &= \sqrt{\frac{\hbar}{m\nu}} \frac{1}{\sqrt{2}} \left(\hat{b} + \hat{b}^\dagger\right) , \\
\hat{p} &= i\sqrt{\frac{\hbar}{m\nu}} \frac{1}{\sqrt{2}} \left(\hat{b} - \hat{b}^\dagger\right) .
\end{aligned} \tag{6.8}$$

The combined motional and electronic eigenstates can be coupled with optical fields. The interaction Hamiltonian for transitions that conserve motional energy is just the semi-classical atom-light interaction derived in Eqn. 3.31. The interaction term for transitions that remove a phonon (red sideband) is the Jaynes-Cummings Hamiltonian [78]

$$\hat{H}_i = -i\eta\hbar \left(\Omega_0 \hat{b}\hat{\sigma}_+ + \Omega_0^* \hat{a}^\dagger \hat{\sigma}_-\right) , \tag{6.9}$$

where the electronic raising and lowering operators are coupled to creation and annihilation operators for the motional modes instead of photonic modes. Transitions that add a phonon (blue sideband) are similarly given by the anti-Jaynes-Cummings Hamiltonian. In contrast to the interaction term in Eqn. 3.21, the vacuum Rabi frequency for the sideband transition interaction is scaled by the Lamb-Dicke parameter[2]

$$\eta = k\cos\phi\sqrt{\frac{\hbar}{2m\nu}} \tag{6.10}$$

where k is the wavenumber of the optical transition, ϕ is the angle between the optical and trap axes and ν is the secular frequency along the relevant axis. The Lamb-Dicke parameter quantifies the coupling strength between internal and motional states of the atom. It is the overlap of the photon wavevector $\mathbf{k}$ with the ground-state root mean square displacement extent $z_0 = \sqrt{\frac{\hbar}{2m\nu}}$ and also the square root of the ratio between the photonic recoil and trap frequencies. The vacuum Rabi frequency of n-th sideband transitions scales like η^n. When $\eta \ll 1$, the probability of higher order phonon transitions is vanishingly small.

Coherent coupling between the internal atomic configuration and travelling photonic modes requires η to be very small. In such experiments the atomic motion is not measured, and acts instead as a reservoir that must be traced over. Interactions that leave a complete or partial record in the motional state are therefore a source of decoherence. Although motional states of trapped ions can be harnessed coherently for quantum information

---

[2]Not to be confused with the collection efficiency, also η. The meaning of this notation should be clear from context.

applications [54, 55, 155], and even prepared in exotic quantum states of fundamental interest [237–239], in this thesis atomic motion is merely a problem to be minimized as much as possible, and the ions will always be in a thermal motional state. The thermal state with mean phonon number $\langle n \rangle$ is a statistical mixture of phonons with probability distributed according to

$$P_n = \frac{\langle n \rangle^n}{(\langle n \rangle + 1)^{n+1}} \, . \tag{6.11}$$

Taking the weighted sum of position probability distributions Eqn. 6.7 with weightings Eqn. 6.11 gives a Gaussian position distribution for the thermal motional state.

6.4 Experiment configuration

6.4.1 The linear Barium trap

The linear trap used in these experiments has been in operation for some time. Daniel Rotter reports in detail the implementation of this linear trap in Ref. [240]. The design itself is common to many trapped-ion experiments, and was modified from the Calcium trap design of Stephan Gulde in Ref. [241]. The design of the trap is shown schematically in Fig. 6.3 with the salient dimensions. The trap consists of four blade-shaped electrodes spaced regularly around the trap axis. The tip of each blade is 0.7 mm from the trap centre. One opposing pair of electrodes are at radio frequency (RF) and the other pair are grounded. The trap operates with a radio frequency of $\Omega \approx 2\pi \times 15.1$ MHz and powers of 2-7 Watts. Two endcap electrodes with a static voltage of $U \approx 400 - 1000$ V lie on the trap axis 2.2 mm from the trap centre. Typical trap potentials and frequencies for trapping one or two ions are given in Tab. 6.1 .

The trap is loaded from a beam of thermal, neutral Barium atoms ejected from an oven inside the vacuum chamber. In contrast to shallow optical traps, which are typically only a few mK deep, ion traps do not need to be loaded with pre-cooled atoms. The neutral atoms are photo-ionized via a resonant two-photon process with a continuous 413 nm photo-ionization beam from a Toptica DL100 diode laser system. The photo-ionization beam co-propagates with cooling and repump beams to provide simultaneous ionization and cooling at the same location. A detailed analysis of the loading scheme and feasible loading rates is provided in Ref. [240].

6.4.2 Laser systems

In addition to the photo-ionization beam described above, four laser systems provide control over the electronic configuration shown in Fig. 6.1. The 493 nm beam addressing the $6\,\mathrm{S}_{1/2} \leftrightarrow 6\,\mathrm{P}_{1/2}$ transition used for cooling, pumping and excitation pulses is generated by frequency doubling 986 nm laser light from a Toptica DL Pro. The 986 nm source is Pound-Drever-Hall (PDH)[242, 243] locked to an external reference cavity with a finesse of 1200. This reference cavity is stabilized with respect to a Tellurium line by modulation-transfer spectroscopy in a Tellurium vapour cell with the frequency-doubled 493 nm output light [244]. The source is doubled in a $KNbO_3$ crystal inside a ring cavity. About 20 mW of 493 nm light with a linewidth of $\Delta\omega_b \approx 2\pi \times 100$ kHz is available at the output of the system. Details of this scheme are available in Ref. [244].

A 650 nm beam addressing the $6\,\mathrm{P}_{1/2} \leftrightarrow 5\,\mathrm{D}_{3/2}$ transition is used as a repump during cooling and pumping, and as an excitation beam. It is provided directly by a Toptica

(a)

(b)   Along detection axis   (c)   Along quadrupole beam
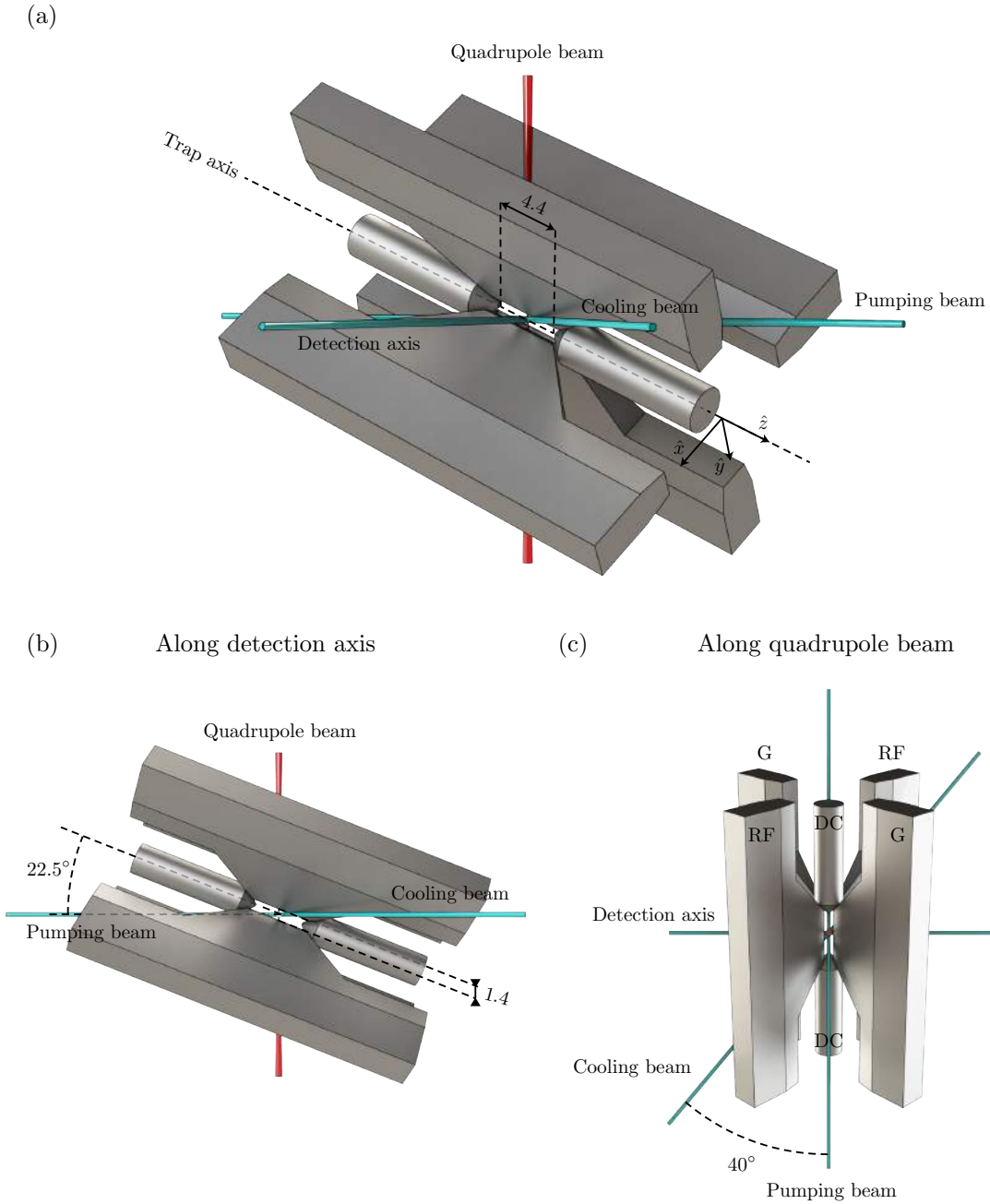
Figure 6.3: Schematic of the linear radio-frequency ion trap used in the following experiments, with the relevant cooling, pumping and quadrupole beams as well as the detection axis (also shown as a beam, although with reduced divergence). The trap dimensions are shown in mm. Angles between each beam and the trap axes $\hat{x}$, $\hat{y}$ and $\hat{z}$ are given in Tab. 6.1.

Parameter	Single ion			Ion pair		
DC potential, U (V)	1,000			400		
RF potential, V (V)	1,300			1,000		
	x	y	z	x	y	z
Secular frequency, ν (MHz)	1.81	1.84	0.97	1.45	1.47	0.49
Cooling angle ϕ_c (deg.)	75.69	48.56	44.95	75.69	48.56	44.95
Lamb-Dicke cooling, η_c	0.014	0.038	0.056	0.016	0.042	0.078
Pumping angle, ϕ_p (deg.)	74.30	74.30	22.50	74.3	74.3	22.50
Lamb-Dicke pumping, η_p	0.016	0.015	0.073	0.017	0.017	0.102
Detection angle, ϕ_d (deg.)	45.00	45.00	90.00	45.00	45.00	90.00
Lamb-Dicke detection, η_d	0.040	0.040	0.000	0.045	0.045	0.000
Quadrupole angle, ϕ_q (deg.)	49.21	49.21	67.50	49.21	49.21	67.50
Lamb-Dicke quadrupole, η_q	0.011	0.010	0.008	0.012	0.012	0.012

Table 6.1: Key parameters of the linear RF trap. Typical voltage configurations and corresponding trap frequencies are shown for trapping one or two ions. Beam angles and Lamb-Dicke parameters are listed for each beam and each trapping axis.

DL100 diode laser PDH locked to an external reference cavity. The reference cavity is not stabilized, and instead we monitor the frequency on a High Finesse, WS7 wavemeter. This system provides 8 mW of 650 nm light with a short term linewidth of $\Delta\omega_r \approx 2\pi \times 100$ kHz.

A quadrupole excitation beam addressing the $6\,P_{1/2} \leftrightarrow 5\,D_{5/2}$ transition at 1762 nm is derived from a 'Koheras Adjustik' Thulium doped fiber laser. This field can be used for sideband cooling, direct manipulation of the quadrupole qubit and shelving operations on the RF qubit. The laser frequency is stabilized to a high-finesse reference cavity as described in detail in Ref. [245]. This scheme produces 4 mW of power with a linewidth of $\Delta\omega_q \approx 2\pi \times 1$ kHz. The quadrupole transition addressed with this laser is therefore Zeeman and sideband resolved.

Because the quadrupole transition is so long-lived, it is sometimes necessary to pump the ion out of the $5\,D_{5/2}$ states with a 614 nm beam addressing the $6\,P_{3/2} \leftrightarrow 5\,D_{5/2}$ dipole transition. This beam is derived from a Toptica, DL-DFB diode laser at a wavelength of 1228 nm that is PDH locked to an external cavity and monitored on the wavemeter. The output of this laser drives a Toptica DL-SHG doubling cavity to produce the 614 nm quenching beam with an available power of 300 μW.

6.4.3   Magnetic field and pumping

The quantization axis $\hat{\mathbf{B}}$ is fixed by three orthogonal pairs of Helmholtz coils attached to the exterior of the vacuum chamber. In this configuration the coils are capable of compensating ambient static fields, such as the Earth's magnetic field, and fixing an arbitrary static field at the location of the trapped ions. The magnetic field shifts each level by an amount

$$\Delta E = m_J g_J \mu_{\mathrm{B}} |\mathbf{B}| \,, \tag{6.12}$$
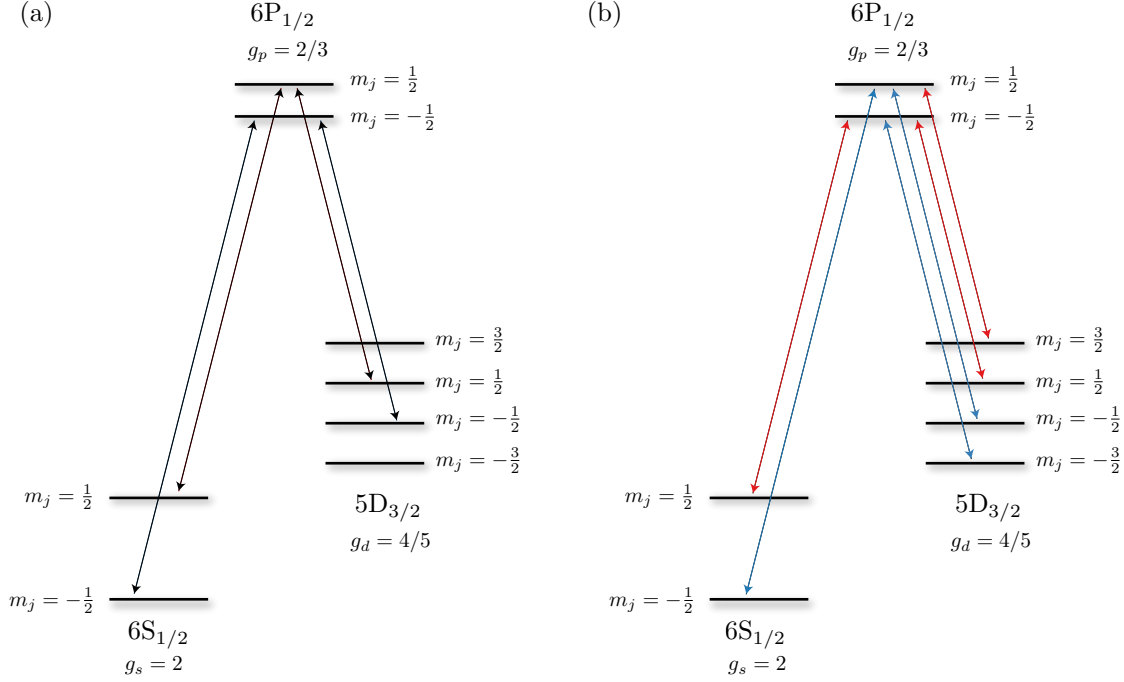
Figure 6.4: Zeeman splitting of the ^{138}Ba$^+$ cooling manifold showing (a) possible π transitions and (b) possible σ^+ (blue) and σ^- (red) transitions. Each level is shown with the corresponding Lande factor $g_{s,p,d}$.

where the Lande factors g_j are given by

$$g_j = \frac{J(J+1) + S(S+1) - L(L+1)}{2J(J+1)} \tag{6.13}$$

and S, L and J are the electron spin, orbital angular momentum and composite angular momentum numbers respectively and $\mu_B = e\hbar/(2m_e)$ is the Bohr magneton.

The experiments reported here are performed with a static field in the range of $B = 1$-5 G which produces a ground-state splitting of 2.8-14 MHz. The quantization axis will be chosen to lie on a plane containing the detection axis, cooling and repump beams that is 22.5° from the trap axis, see Fig. 6.3(b). For applications requiring pumping we will choose $\hat{\mathbf{B}}$ to lie along the projection of the trap axis onto this plane so that the detection and quantization axes are perpendicular. As shown in Fig. 6.3, the pump beam lies along the same axis and drives simultaneous $\sigma_{+,-}$ transitions in some proportion and with relative phase depending on the optical polarization. When circularly polarized, and used in combination with a repump beam (not necessarily co-propagating), the pumping beam prepares the ion in one of the Zeeman-split ground states.

The Zeeman-split ground state transition can be driven coherently by RF magnetic fields. For this purpose a 8.5 cm diameter, 1 mm thick, single-loop coil is arranged 6 cm below the trap and outside the vacuum chamber. The coil and trap capacitance form an LC circuit at a frequency of 11.5 MHz. Details of the driven RF qubit transition can be found in Ref. [245]

6.4.4 Doppler cooling

For strong optical coupling we must localize the trapped ions to within regions much smaller than the optical wavelength. In practice this means cooling the ions to within a score of motional quanta of the ground state. With laser cooling it is possible to prepare trapped atoms and ions at temperatures from milli- to micro-Kelvin, more than sufficient for this work. In the following experiments we will Doppler cool the trapped ions with a 493 nm cooling beam addressing the $6\,S_{1/2} \leftrightarrow 6\,P_{1/2}$ dipole transition and 650 nm repump beam addressing the $6\,P_{1/2} \leftrightarrow 5\,D_{3/2}$ dipole transition [246, 247]. The cooling and repump beams co-propagate along either the pumping or cooling axes, see Fig. 6.3, so that they overlap with each independent motional degree of freedom.

The cooling beam is red-detuned from the atomic transition by Δ, such that momentum-exchange in scattering from this transition produces a viscous force opposing the ion's oscillation and an associated cooling rate [248]. However, each photon scattering event consists of absorption followed by random scattering (usually into the dipole mode). Because the scattering is undirected, the associated photon recoil is diffusive with an associated heating rate. Doppler cooling reaches an equilibrium at the Doppler temperature limit T_{D} when the heating and cooling rates are identical. On a cyclic transition

$$T_{\mathrm{D}} = \frac{\hbar\left((1+s)\,\Gamma^2 + 4\Delta^2\right)(1+\epsilon)}{16\Delta k_{\mathrm{B}}}\,, \tag{6.14}$$

where s is the resonant saturation parameter $s = \Omega^2/\Gamma^2$ and ϵ is a geometry factor associated with the scattering mode ($\epsilon = 2/5$ for π-dipole radiation oriented away from the motional axis, $\epsilon = 1$ for uniform emission) [53]. At the optimal Doppler detuning

$$\Delta_{\mathrm{D}} = \tfrac{1}{2}\Gamma\sqrt{1+s}\,, \tag{6.15}$$

but random dipole orientation, and with low power $s \approx 0$, the limit becomes

$$T_{\mathrm{D}} = \frac{\hbar\Gamma(1+\epsilon)\sqrt{1+s}}{4k_{\mathrm{B}}}\,, \tag{6.16}$$

$$\approx \frac{1}{2}\frac{\hbar\Gamma}{k_{\mathrm{B}}}\,, \tag{6.17}$$

the same as for atoms in free-space. The micromotion of the trapped ion complicates this picture slightly, but for trapping parameters $a,q \ll 1$ the scalar potential approximation above holds well [249].

In our experiments the cooling transition is not cyclic and requires a repump. Ignoring Zeeman splitting for now, the cooling configuration is the Λ-atom of Sec. 3.4 and the scattering rate goes like the excited state population. The optimal final temperature is reached when both beams are configured to cool and approaches Eqn. 6.17 with $\Gamma = \Gamma_b + \Gamma_r = 2\pi * 20.4$ MHz which gives $T_{\mathrm{D}} = 489$ μK. Because each of the levels in this cooling manifold are Zeeman split, the actual system dynamics are more complicated, and in practice we often configure the repump for maximum fluorescence rather than optimal cooling, but the Doppler limit above remains a good rule of thumb for the temperature of our trapped ions. In Fig. 6.5(a) the standard deviation from the trap centre is shown as a function of temperature for the single-ion trap configuration from Tab. 6.1. The ion position probability distributions according to Eqn. 6.11 are shown in Fig. 6.5(b) at the Doppler limit temperature T_{D}. At this temperature the spatial extent along the trap axis

(a)

(b)
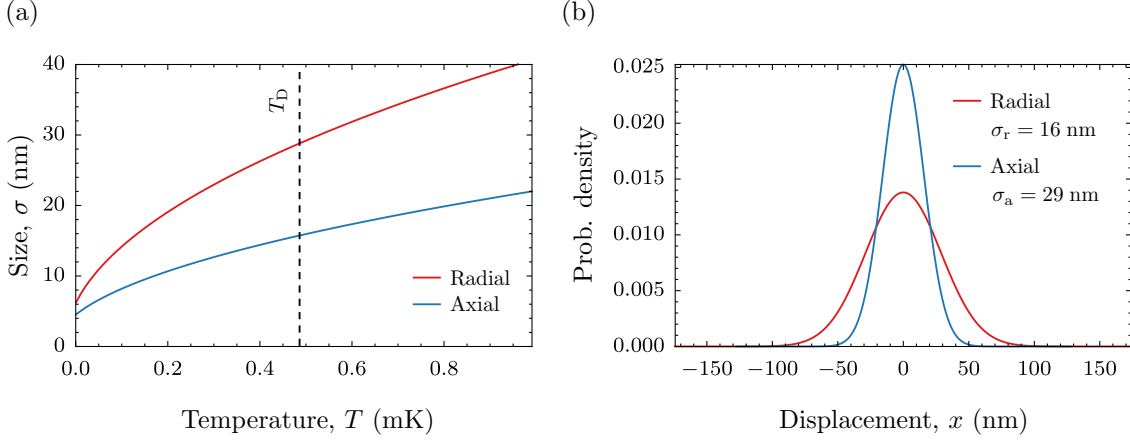
Figure 6.5: Typical atomic displacement distributions for Doppler-cooled ions in the linear trap. (a) Standard deviation from the centre of the trap as a function of temperature for the radial (blue) and axial (red) trap frequencies from the single-ion configuration of Tab. 6.1. The Doppler limit temperature T_D is shown by the dashed line. (b) Radial (blue) and axial (red) atomic probability distributions for the same trap configuration at temperature T_D.

and in the radial plane are about 29 nm and 16 nm respectively.

Initially, cooling on a fast transition is desirable because it yields a faster cooling rate. However, we've seen that the cooling temperature limit generally scales with the transition decay rate. Once the atom is sufficiently cool it is advantageous to continue cooling on a narrower transition. Cooling to the ground state would reduce the standard axial atomic displacement from 29 nm to 6 nm. In our experiment this is possible using the narrow quadrupole transition $6\,S_{1/2} \leftrightarrow 5\,D_{5/2}$ (see Sec. 6.4.2) for sideband cooling, but this process is too slow to apply in any of the experiments presented here. Sideband cooling with this quadrupole transition is capable of cooling a single trapped ion to a mean phonon number of $\langle n \rangle = 0.03$ (or ground state probability $P_0 = 0.97$) in 10 ms [245].

A faster alternative is EIT cooling. As described in Refs.[250–252], EIT cooling is a technique that tailors a narrow EIT window induced by a Λ-driven atom to favour red-sideband absorption. An EIT cooling stage following the Doppler cooling would improve many of the results shown here, and will be introduced to the apparatus in the near future.

6.4.5   Collection and Detection

Fluorescence is collected from the trapped ions by two high-aperture lens objectives (HA-LOs) positioned inside the vacuum chamber. The HALOs are identical three-lens objectives (Linos Halo 25/04) with a numerical aperture of 0.4, focal length 25.0 mm, and total peak-to-valley wavefront distortion below 50 nm [253]. The objectives $H_{1,2}$ are configured near-confocally along the detection axis shown in Fig. 6.3. H_1 is well focussed on the ion, and produces a collimated field from the atomic fluorescence. H_2 is configured with focal plane ≈ 0.4 mm short of the trapped ions such that atomic fluorescence is imaged at a plane 34 cm from the objective. Light collected by each HALO can be measured with either fibre-coupled avalanche photodiodes (Laser Components, COUNT blue) or an intensified CCD camera (Andor iXon). The APDs have a quantum efficiency of ≈ 0.7 and a photon echo at a delay of ≈ 100 ns which we remove by introducing a 100 ns dead-time following detection with counting electronics. The CCD quantum efficiency is ≈ 0.9. De-
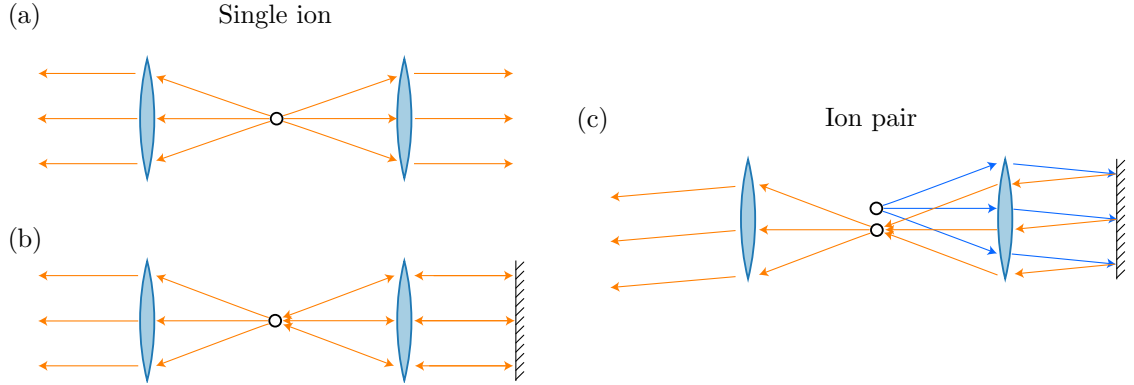
Figure 6.6: Detection configurations of the linear ion trap with one and two ions. Two high aperture lens objectives (HALOs, each objective shown here as a single lens) collect fluorescence from the trapped ions along one direction of the detection axis. (a) In the symmetric configuration each HALO collects one side of the ion fluorescence and both modes are measured. (b) In the reflected configuration one side of the ion fluorescence is returned by a distant mirror such that the ion is coupled to it's own reflection. The single combined mode is measured, interference is possible between the two combined fluorescence fields. (c) In the coupling configuration the remote mirror may be used to couple two different ions (adjacent or otherwise). The ions share a common fluorescence mode with relative phase determined by the mirror distance d. For clarity the forward and backwards travelling fluorescence are shown with different colours.

tection events at the APDs are time tagged using a photon counting module (Picoquant, PicoHarp 300) with a time resolution of 4 ps on detection channels and 1 ns on marker channels. The APDs have a specified dark count rate of 10 counts/s.

A remote mirror outside the vacuum chamber at a distance of 30 cm from the trapped ions can be used to return the collimated field through one lens. Single-ion detection may therefore be configured for 'symmetric' two-mode or 'reflected' single-mode detection, Fig. 6.6(a) and (b). The vacuum chamber viewport has been measured to distort the wavefront by less than 50 nm or $\lambda/10$ for the blue cooling transition. In the reflected configuration the ion fluorescence self-interferes with 90% visibility when sideband cooled to near the ground state [254] and 70% visibility when Doppler cooled to near T_D [255]. It is possible to lock the ion-mirror path length such that constructive interference enhances the detection efficiency [254]. With two or more trapped ions, the remote mirror may be used to couple selected atoms to a single mode as per Fig. 6.6(c).

As we derived in Sec. 4.3.1, two confocal spherical lenses with a NA of 0.4 are capable of collecting a proportion $\eta_I = 0.12$ of the fluorescence from an optimally oriented dipole, meaning a π (σ) transition quantized perpendicular (parallel) to the detection axis. This is why the detection and pumping axes are perpendicular in the configuration shown in Fig. 6.3. The fibre coupled photodiodes (APDs) are coupled with single-mode fibres to reduce the detection of stray light fields. In Sec. 4.7 we derived the optimal Gaussian mode fibre coupling efficiency for spherical lenses with NA = 0.4, $\eta_c = 0.81$. The maximum fluorescence photon detection efficiency in this experiment is therefore 10% with APDs and 12% on the CCD camera given optimally oriented transition dipoles.

6.5   Summary

We have described the details of the ion trap apparatus to be used in the following chapters, as well as the necessary ion-trapping theory. The required properties and optical transitions of $^{138}\text{Ba}^+$ are given, and we introduced the quadrupole and RF qubits available with such a system. The key trapping and cooling parameters of the linear RF trap we use were given, and typical motional states derived. We further detailed the laser systems and magnetic fields available for manipulating our trapped-atom qubits. In the next chapter we perform experiments to characterize the atom-field coupling with one or two ions trapped in this system.

Bibliography - Trapped-ion apparatus

5. G. Araneda, et al., Interference of single photons emitted by entangled atoms in free space, *Phys. Rev. Lett.* **120**, 193603–05 (2018).

43. S. Debnath, et al., Demonstration of a small programmable quantum computer with atomic qubits, *Nature* **536**, 63–66 (2016).

53. D. Leibfried, et al., Quantum dynamics of single trapped ions, *Rev. Mod. Phys.* **75**, 281–324 (2003).

54. J. I. Cirac, and P. Zoller, Quantum computations with cold trapped ions, *Phys. Rev. Lett.* **74**, 4091–4094 (1995).

55. A. Sørensen, and K. Mølmer, Quantum computation with ions in thermal motion, *Phys. Rev. Lett.* **82**, 1971–1974 (1999).

78. M. Orszag, *Quantum optics including noise reduction, trapped ions, quantum trajectories and decoherence* (Springer, Berlin, Heidelberg, New York, 2008).

155. R. Blatt, and C. F. Roos, Quantum simulations with trapped ions, *Nat. Phys.* **8**, 277–284 (2012).

233. H. Häffner, et al., Robust entanglement, *Appl. Phys. B* **81**, 151–153 (2005).

234. N. Yu, W. Nagourney, and H. Dehmelt, Radiative lifetime measurement of the Ba+ metastable D3/2 state, *Phys. Rev. Lett.* **78**, 4898–4901 (1997).

235. W. Paul, Electromagnetic traps for charged and neutral particles, *Rev. Mod. Phys.* **62**, 531–540 (1990).

236. M. Drewsen, and A. Brøner, Harmonic linear Paul trap: Stability diagram and effective potentials, *Phys. Rev. A* **62**, 045401 (2000).

237. D. M. Meekhof, et al., Generation of nonclassical motional states of a trapped atom, *Phys. Rev. Lett.* **76**, 1796–1799 (1996).

238. C. Monroe, et al., A "Schrodinger cat" superposition state of an atom, *Science* **272**, 1131–6 (1996).

239. D. Kienzler, et al., Observation of quantum interference between separated mechanical oscillator wave packets, *Phys. Rev. Lett.* **116**, 140402 (2016).

240. D. Rotter, Quantum feedback and quantum correlation measurements with a single Barium ion, PhD thesis (Leopold-Franzens-Universität Innsbruck, 2008).

241. S. Gulde, Experimental realization of quantum gates and the Deutsch-Jozsa algorithm with trapped 40Ca+ ions, PhD thesis (Leopold-Franzens-Universität Innsbruck, 2003).

242. R. W. P. Drever, et al., Laser phase and frequency stabilization using an optical resonator, *Appl. Phys. B* **31**, 97–105 (1983).

243. E. D. Black, An introduction to Pound–Drever–Hall laser frequency stabilization, *Am. J. Phys.* **69**, 79 (2001).

244. C. Raab, et al., Diode laser spectrometer at 493 nm for single trapped Ba+ ions, *Appl. Phys. B* **67**, 683–688 (1998).

245. L. Slodička, Single ion-single photon interactions in free space, PhD thesis (Leopold-Franzens-Universität Innsbruck, 2012).

246. W. Neuhauser, et al., Localized visible Ba+ mono-ion oscillator, *Phys. Rev. A* **22**, 1137–1140 (1980).

247. G. Janik, W. Nagourney, and H. Dehmelt, Doppler-free optical spectroscopy on the Ba+ mono-ion oscillator, *J. Opt. Soc. Am. B* **2**, 1251 (1985).

248. S. Stenholm, The semiclassical theory of laser cooling, *Rev. Mod. Phys.* **58**, 699–739 (1986).

249. J. I. Cirac, et al., Laser cooling of trapped ions: The influence of micromotion, *Phys. Rev. A* **49**, 421–432 (1994).

250. G. Morigi, J. Eschner, and C. H. Keitel, Ground state laser cooling using electromagnetically induced transparency, *Phys. Rev. Lett.* **85**, 4458–4461 (2000).

251. C. F. Roos, et al., Experimental demonstration of ground state laser cooling with electromagnetically induced transparency., *Phys. Rev. Lett.* **85**, 4 (2000).

252. R. Lechner, et al., Electromagnetically-induced-transparency ground-state cooling of long ion strings, *Phys. Rev. A* **93**, 1–10 (2016).

253. S. Gerber, et al., Quantum interference from remotely trapped ions, *New J. Phys.* **11**, 013032 (2009).

254. L. Slodička, et al., Interferometric thermometry of a single sub-Doppler-cooled atom, *Phys. Rev. A* **85**, 043401 (2012).

255. J. Eschner, et al., Light interference from single atoms and their mirror images, *Nature* **413**, 495–498 (2001).

Trapped-atom single-photon source

We never experiment with just one electron or atom or (small) molecule. In thought-experiments we sometimes assume that we do; this invariably entails ridiculous consequences... we are not experimenting with single particles, any more than we can raise Ichthyosauria in the zoo.

— Erwin Schrödinger, *Are there quantum jumps?* (1952)

Single atoms or atom-like emitters are the purest source of single photons; they are intrinsically incapable of multi-photon emission. To demonstrate this degree of photon number-state purity we have realized a single-photon source with a single atom coupled to travelling photon modes by free-space optics. The atomic and photonic states are coupled with a pair of high aperture lens objectives as described in Chap. 6. Despite the limited collection efficiency of this system, we're able to demonstrate several useful properties of the trapped-atom light source. In this chapter we develop and characterize two experimental schemes for the generation of low-noise single photons.

We produce a stream of single photons under pulsed excitation with either blue (493 nm) or red (650 nm) excitation beams. In each case we fit an eight-level Bloch model of the ^{138}Ba$^+$ cooling manifold dynamics to dark resonance spectra, and this model then accurately predicts both the arrival time distribution of pulsed photons and the $g^{(2)}(\tau)$ dynamics of photons produced by continuous excitation. This model captures features including Rabi-oscillations on the $6\,\mathrm{S}_{1/2} \leftrightarrow 6\,\mathrm{P}_{1/2}$ cooling transition and quantum beats caused by the interference of absorption pathways.

In the optimal configuration our trapped-ion source produces single-photon pulses with $g^2(0) = (1.9 \pm 0.2) \times 10^{-3}$ without any background subtraction. After subtracting detector dark counts the residual $g^2(0)$ is less than 3×10^{-4} (95% confidence interval). An analysis demonstrates that our source produces a single-photon light field with critically low noise sufficient for scalable networks or coupling between multiple qubit registers.

Parts of this chapter appear in part in the following publications

[2] "**Pure single photons from a trapped atom source** D. B. Higginbottom, L. Slodička, G. Araneda, L. Lachman, R. Filip, M. Hennrich, and R. Blatt. *New Journal of Physics.* **18**, 93038 (2016)."

[6] "**Wavelength-scale errors in optical localization due to spin-orbit coupling of light** G. Araneda, S. Walser, Y. Colombe, D. B. Higginbottom, J. Volz, R. Blatt, and A. Rauschenbeutel. *Nature Physics* (2018)."

As noted in Chap. 4, the outstanding challenge for trapped atom quantum information networks remains the efficient coupling of stationary atomic and travelling photonic qubits.

In Chaps. 10 and 11 we consider methods of improving the atom light coupling in such systems and develop the necessary optics.

7.1   Configuration

For these experiments a $^{138}Ba^+$ ion is trapped and cooled in a linear Paul trap at the common focus of two high aperture lens objectives (HALOs) in the reflected configuration as described in Chap. 6. The complete configuration used here is shown in Fig. 7.1. The ion is Doppler cooled to within the Lamb-Dicke regime using a 493 nm cooling beam and a repump beam at 650 nm to close the $6\,S_{1/2} \leftrightarrow 6\,P_{1/2} \leftrightarrow 6\,D_{3/2}$ cycle. The cooling and repump beams are combined on a beam splitter and co-propagate to the ion along the cooling axis with a common polarization. The quantization axis is configured perpendicular to the detection axis, such that photons from σ and π transitions can be separated near-perfectly by a waveplate-polarizing beamsplitter (PBS) pair in the detection path.

7.1.1   Transition isolation

In this configuration, photons from the π (σ) transitions are $\hat{\mathbf{H}}$ $(\hat{\mathbf{V}})$ polarized along the detection axis. However, as we saw in Chap. 4, the dipole image field is not isotropic over the entire aperture. As the collection aperture increases, the ability to separate transitions by filtering linear polarizations with a PBS decreases, but in our case the numeric aperture is small enough to provide substantial extinction. An ideal PBS that selects $\hat{\mathbf{V}}$ polarized photons (for example) paired with the NA = 0.4 objective used here removes 99.998% of photons from the π transitions and 2.7% of photons from the σ transitions. The ratio between transmitted σ and π photons is $\sim 10^{-4}$, more than sufficient to neglect contributions from the undesired transition.

7.1.2   Detection

The detectors are configured for a Hanbury Brown-Twiss (HBT) measurement per Sec. 2.5.3; two low-noise fibre-coupled APDs with quantum efficiencies of $\eta_d = 70\%$ and 73% on either arm of a 50/50 beamsplitter sample a single spatial and polarization mode of the ion fluorescence collected by one of the HALOs. A remote mirror returns one half of the collected fluorescence past the ion. Because of losses along the reflected path, the reflected field intensity is only $\eta_R = 66\%$ of the directly collected intensity. Depending on the mirror-ion distance $d \approx 30$ cm, the two fields may interfere constructively or destructively. When we require high-visibility interference it is necessary to align the collection such that the two components are balanced, essentially discarding some of directly collected photons. Given the measured visibility of our Doppler-cooled ion interference fringe, we could enhance the collection efficiency by a factor of ≈ 1.4 if the mirror position were locked constructively.

The cooling fluorescence signal isn't sufficient to lock the mirror position to an interference fringe at high single-photon repetition rates. Instead, the mirror-ion distance drifts freely and each measurement is an average over the interference fringe. An extended cooling stage would increase the fluorescence but slow the repetition rate, so although a cooling stage long enough to lock the fringe would increase the detection efficiency, it would lower the total collected photon rate. An independent interferometer would provide a means of stabilizing the atom-mirror distance at low flux. A partially mirrored trap surface is desirable so that one arm of the interferometer can be reflected from the blades of the trap.
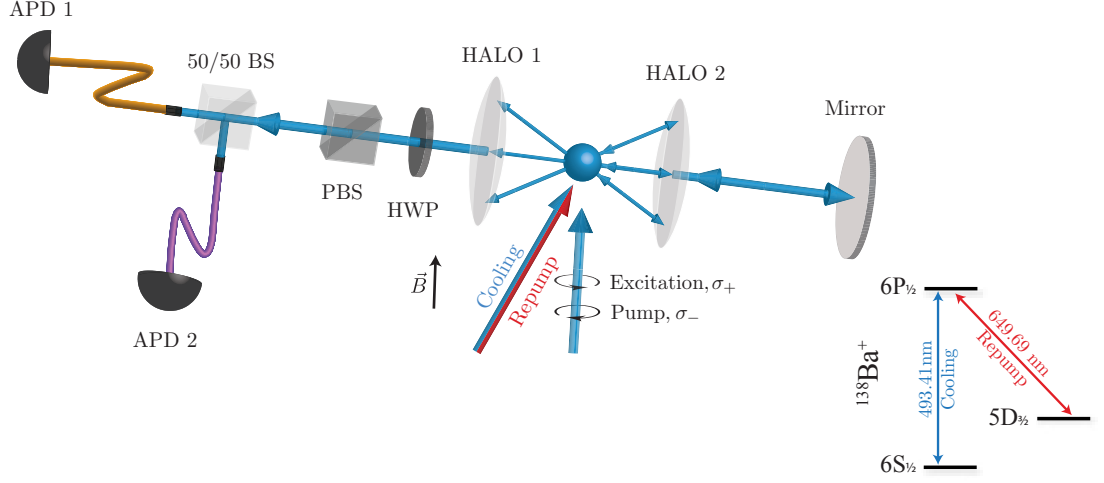
Figure 7.1: In this 'reflected' configuration one side of the ion fluorescence is collimated by a high aperture lens objective (HALO) and reflected from a distant mirror. The reflected light is focussed back past the ion into the same spatial mode as fluorescence collected by a second HALO. The combined fields are polarization filtered and split between two fibre-coupled APDs. (inset) Electronic level structure of ^{138}Ba$^+$.

We choose to collect photons along the perpendicular detection axis, and along this axis the probability of detecting photons from the π and σ transitions are

$$\eta^i = \eta_\mathrm{I}^i \eta_\mathrm{c}^i \eta_\mathrm{d} \left(1 + \eta_\mathrm{R}\right)/2 \tag{7.1}$$

where $i = \sigma, \pi$, η_I^i is the collection efficiency at angle $\delta = \frac{\pi}{2}$ from Eqns. 4.18 and 4.19, η_c^i is the corresponding coupling efficiency, η_d is the quantum efficiency of the APDs at 493 nm. From this we derive detection efficiencies

$$\eta^\pi = 0.058 \; , \; \eta^\sigma = 0.029 \, .$$

This is the maximum end-to-end efficiency of the scheme, not including absorption and scattering losses from optics along the detection path or sub-optimal fibre coupling. Compared to the π transition, photons are twice as likely to be scattered from the σ transition under continuous excitation, but half as likely to be detected because the collection angle is not optimal for these transitions, so that the measured fluorescence rate under continuous excitation is equal in each linear polarization.

7.2   Continuous fluorescence

Because a single atomic transition is incapable of multi-photon emission, the fluorescent field from a single atom[1] under continuous driving is antibunched. Antibunching in atomic fluorescence was first demonstrated with a neutral atomic beam [86] and later with trapped ions [256]. Similarly, the fluorescence field of our trapped atom under continuous excitation by the cooling beams shows a pronounced antibunching dip in the observed $g^{(2)}$ correlation function, see Fig. 7.2. $g^{(2)}(\tau)$ is near zero for τ smaller than the relaxation time of the atom, before rising to a re-emission peak. This is the most likely interval τ between consecutive

---

[1]In fact from any number of atoms, see Sec. 2.5.4
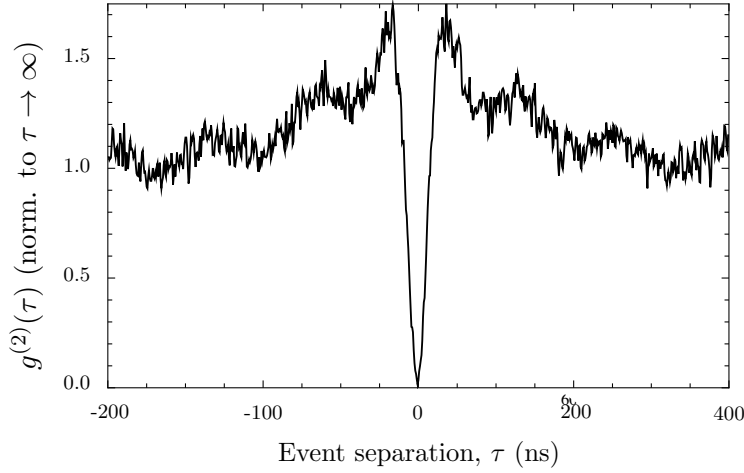
Figure 7.2: $g^{(2)}(\tau)$ of a single trapped atom under continuous excitation by the cooling and repump beams where τ is the event time separation of consecutively measured photons.

photon detection events. The correlation function is symmetric up to statistical noise, and is modulated by the trapping frequency due to residual micromotion. In the following sections we will model the finer details of correlation functions such as this using the eight-level Bloch equations.

7.3   Blue-triggered single photons

In addition to generating a continuous field of antibunched photons, the trapped atom can be operated to produce a stream of on-demand, single-photon pulses by a scheme similar to [257, 258]. First we shall consider photons scattered from the RF-qubit states $6\,\mathrm{S}_{1/2}, \mathrm{m_j} = \pm\frac{1}{2}$ by blue (493 nm) excitation pulses. In sec. 7.6 we describe an alternative scheme using the red (650 nm) 'repump' beam as an excitation pulse.

The experimental sequence is shown in Fig. 7.3. We begin with 10 μs of Doppler cooling by a vertically ($\hat{\mathbf{V}}$) polarized cooling beam that drives both blue $\sigma_{\pm}$ transitions, followed by 10 μs of pumping with either a $\hat{\mathbf{L}}$ or $\hat{\mathbf{R}}$ circularly polarized field along the quantization axis. The $\hat{\mathbf{V}}$ polarized repump beam along the cooling axis drives the four red $\sigma_{\pm}$ transitions and remains on during both cooling and pump stages, Fig. 7.4(a) and (b). With a $\hat{\mathbf{L}}$ ($\hat{\mathbf{R}}$) polarized pump, this sequence prepares the atom in the RF qubit state $6\,\mathrm{S}_{1/2}, \mathrm{m_j} = +\frac{1}{2}$ ($6\,\mathrm{S}_{1/2}, \mathrm{m_j} = -\frac{1}{2}$). A subsequent $\hat{\mathbf{R}}$ ($\hat{\mathbf{L}}$) polarized 493 nm 'excitation' pulse along the quantization axis transfers the atomic population to the opposite ground state, scattering at least one photon in the process.

During this process the excitation pulse may scatter several photons via the σ_{-} (σ_{+}) decay path, but no more or less than one single photon from the π transition, Fig. 7.4(c). After removing σ photons by polarization filtering, this scheme realizes an on-demand single photon source. Simultaneous with the excitation pulse, the APDs are gated and begin detecting for a window of 4.5 μs. A time tagging synchronization pulse is sent to the PicoHarp photon counter to mark the beginning of the detection window, and photon arrival times are recorded with respect to this marker.

Event	λ (nm)	Transitions	Time, t (μs)
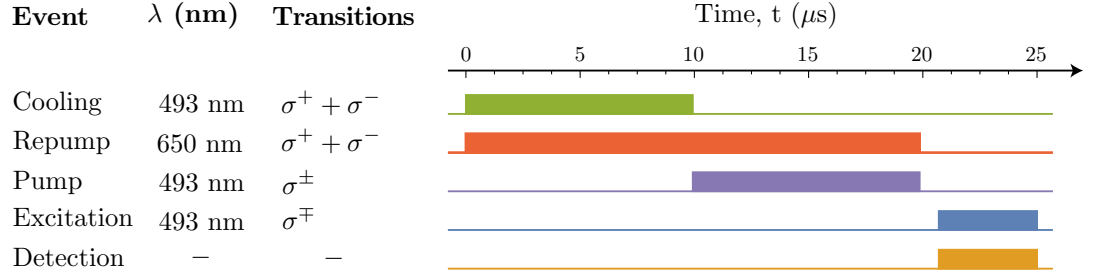
Figure 7.3: Experimental sequence for blue-triggered single photons showing the wavelength and transitions addressed by each excitation pulse.
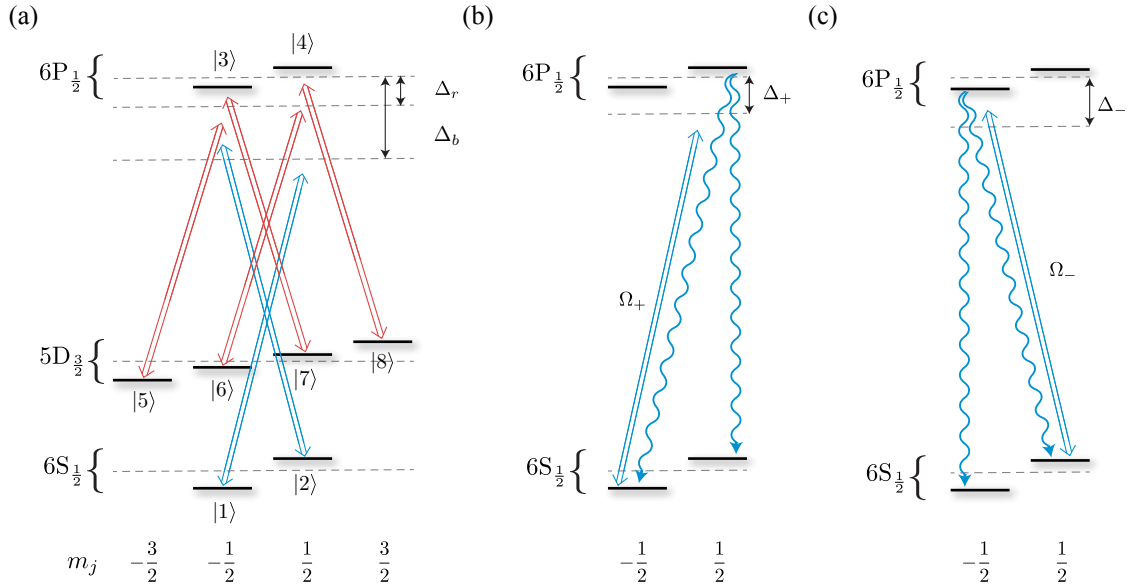
Figure 7.4: Level scheme for blue-triggered single photons. (a) Doppler cooling configuration. A single 493 nm cooling beam perpendicular to the quantization axis drives both blue σ transitions with equal Rabi frequency Ω_b and a single 650-nm repump beam perpendicular to the quantization axis drives four red σ transitions with equal Rabi frequencies Ω_r. A magnetic field splits each level into Zeeman states with magnetic quantum number m_j. Detunings $\Delta_{b,r}$ are defined with respect to the unsplit energy levels. (b) Pumping configuration. A σ_+ polarized pump beam with detuning Δ_+ and Rabi frequency Ω_+ and a 650 nm repump beam (not shown) prepare the atom in state $6\,\mathrm{S}_{1/2}, \mathrm{m_j} = \frac{1}{2}$. (c) Excitation configuration. A σ_- polarized excitation beam with detuning Δ_- and Rabi frequency Ω_- pumps the atom to state $6\,\mathrm{S}_{1/2}, \mathrm{m_j} = -\frac{1}{2}$ and scatters a single photon from the σ_+ transition.

7.3.1   Generation efficiency

Regrettably, this blue-triggered pulse scheme does not definitely produce photons from the selected transition. Because of the branching ratio between blue and red decay paths, there is a probability that the atom is pumped not to an RF-qubit state, but to one of the $\mathrm{D}_{3/2}$ levels, scattering a red photon in the process (that is subsequently filtered out).

The probability of generating photons from the π transition as desired is

$$\eta_{\mathrm{G}}^{\pi} = C_{\pi}^{2} \frac{\Gamma_{\mathrm{b}}}{\Gamma_{\mathrm{r}} + C_{\pi}^{2}\Gamma_{\mathrm{b}}} \tag{7.2}$$
$$= 0.49$$

where $C_{\pi} = \sqrt{1/3}$ is the Clebsch-Gordon coefficient for the blue π transitions and $\Gamma_{\mathrm{b,r}}$ are the free-space decay rates of the blue and red transitions.

We note here that the most efficient single-mode detection configuration is to collect photons from a σ transition along the quantization axis, which improves η^{σ} from Eqn. 7.1 by a factor of two. Because $\eta_{\mathrm{G}}^{\sigma} = 0.66$ (by an analogous expression to Eqn. 7.2), this configuration has slightly higher end-to-end efficiency than the scheme we've presented. In this case the excitation beam should be linearly polarized along the quantization axis to trigger single σ photons.

7.3.2 Photon-source dynamics

To completely characterize the photons produced by this scheme we need to understand the atomic dynamics during the cooling, pumping and excitation stages. For this purpose we take continuous excitation spectra. The resonance fluorescence under continuous driving is recorded as a function of one laser detuning, in this case we choose to scan Δ_{r}. The scan is slow enough that the fluorescence at any time is the steady-state fluorescence rate. Fig. 7.5(a) and (b) show the resonance fluorescence spectrum of a single trapped ion under continuous driving by (a) the cooling and repump beams and (b) the pump, excitation and repump beams.

We may also measure the $g^{(2)}(\tau)$ of the source by taking the auto-correlation of the photon arrival times measured by our HBT apparatus under continuous excitation in either configuration. The $g^{(2)}(\tau)$ of the source driven by the pump, excitation and repump beams is shown in Fig. 7.5(c). Finally, we can consider the photon arrival time histograms when the source is operated to produce pulsed photons from either the σ_{+} or σ_{-} transition by swapping the polarizations of the pump and excitation beams. Figure 7.5(d) shows the arrival time histograms recorded with the source configured for each polarization. Both photons triggered by the pump and excitation beams have wavepackets shorter than 500 ns, but this shouldn't be confused with the pumping time. Efficient pumping to a single ground state requires several decay and excitation cycles.

Although the $6\,\mathrm{S}_{1/2} \leftrightarrow 6\,\mathrm{P}_{1/2} \leftrightarrow 5\,\mathrm{D}_{3/2}$ cooling and repump transition forms a typical Λ system, each level is Zeeman split in the presence of the magnetic field **B**. The system dynamics of the trapped atom under excitation by cooling and repump beams are therefore given by a more complicated model taking each of the eight Zeeman levels and all possible dipole transitions into account. In the following section we develop such an eight-level master equation model and show how it predicts the observed behaviour.

7.4 Eight-level Bloch equations

We can extend the three level Λ-atom model we derived in Sec. 3.4 to describe the eight level $6\,\mathrm{S}_{1/2} \leftrightarrow 6\,\mathrm{P}_{1/2} \leftrightarrow 5\,\mathrm{D}_{3/2}$ cooling and repump manifold relevant to the blue-triggered single photon source. We begin by labelling the atomic eigenstates $|1\rangle$–$|8\rangle$ according to the scheme in Fig. 7.4(a). The Zeeman-split atomic Hamiltonian in this basis consists of
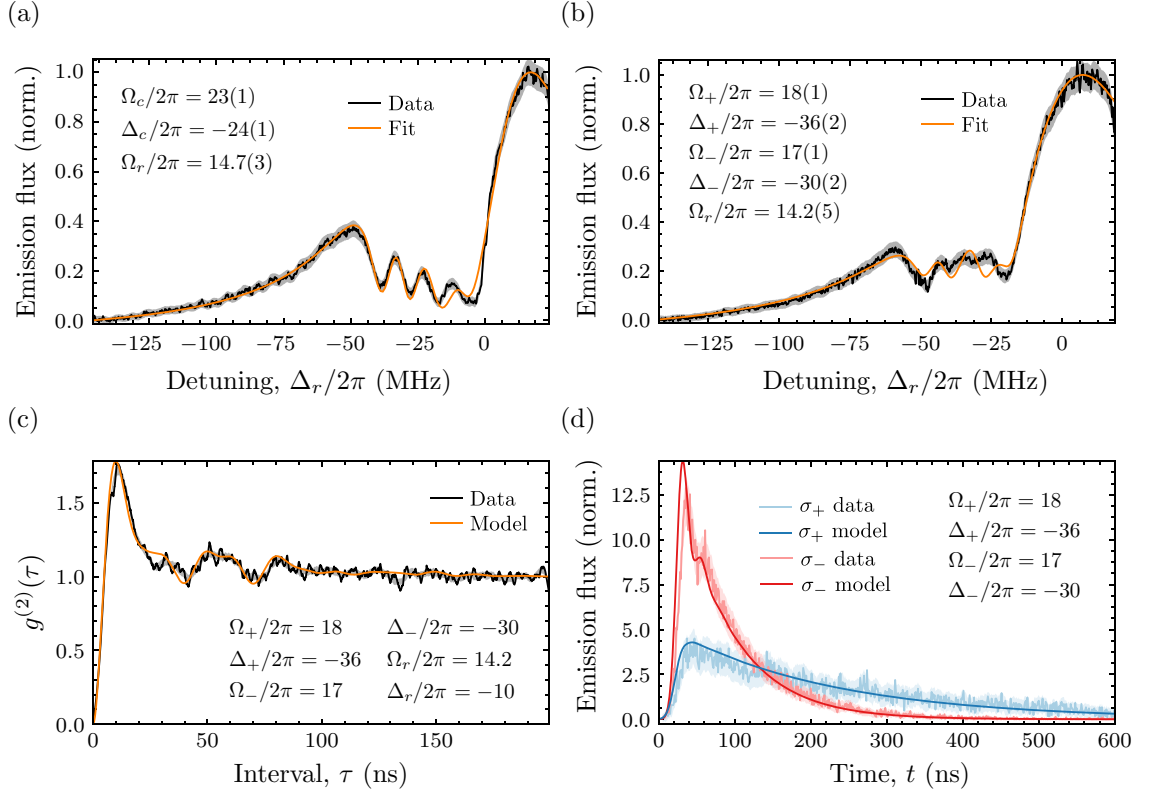
Figure 7.5: Blue-triggered $^{138}\text{Ba}^+$ single-photon source with corresponding Bloch model. (a) Dark-resonance spectrum of the trapped atom with cooling and repump beams (black) and fitted model (orange). (b) Dark resonance spectrum with the same repump beam and independent pump and excitation beams driving $\sigma_\pm$ transitions (black) and fitted model (orange). (c) $g^{(2)}(\tau)$ of the source driven continuously by the same $\sigma_\pm$ polarized pump beams (black) and model (orange) with parameters fixed from (c). (d) Single-photon arrival time histogram from the source pulsed according to Fig. 7.3 with the pump and excitation beams configured according to Fig. 7.4(b) and (c) (σ_- - red) and also with pump and excitation beams swapped (σ_+ - blue). The corresponding models are shown (solid lines) with parameters fixed from (c). The shaded region around each measurement indicates the 2-σ Poissonian uncertainty region. All parameters in MHz.

common optical detuning and Zeeman splitting terms. When we address only σ transitions, as in the cases above, we can write the atomic Hamiltonian

$$\hat{H}_a = \hbar \left(\Delta_+ \hat{\sigma}_{11} + \Delta_- \hat{\sigma}_{22} + \Delta_r \left(\hat{\sigma}_{55} + \hat{\sigma}_{66} + \hat{\sigma}_{77} + \hat{\sigma}_{88} \right) \right)$$
$$+ \hbar \mu_B |B| \left(-\hat{\sigma}_{11} + \hat{\sigma}_{22} - \tfrac{1}{3}\hat{\sigma}_{33} + \tfrac{1}{3}\hat{\sigma}_{44} - \tfrac{6}{5}\hat{\sigma}_{55} - \tfrac{2}{5}\hat{\sigma}_{66} + \tfrac{2}{5}\hat{\sigma}_{66} + \tfrac{6}{5}\hat{\sigma}_{88} \right) \quad (7.3)$$

where Δ_r is the repump detuning and $\Delta_\pm$ are the cooling/excitation detunings of the $\sigma^\pm$ transitions. As shown in Fig. 7.4, each detuning is defined with respect to the unsplit transition frequency.

The interaction Hamiltonian is the sum of repump, pump and excitation interaction

	Ω_c	Δ_c	Ω_r	Δ_r	Ω_+	Δ_+	Ω_-	Δ_-
Cool. spectrum	**23(1)**	**-24(1)**	**14.7(3)**					
Pumps spectrum			**14.2(5)**		**18(1)**	**-36(2)**	**17(1)**	**-30(2)**
Pumps $g^{(2)}(\tau)$			14.20	-10.0	18.0	-36.0	17.0	-30.0
Emm. flux σ_+					18.0	-36.0		
Emm. flux σ_-							17.0	-30.0

Table 7.1: Bloch model parameters of Fig. 7.5(a)-(d). The relevant parameters are shown for each measurement, with free parameters in bold. Parameters for the $g^{(2)}(\tau)$ and single photon emission flux measurements are fixed according the appropriate spectrum fit. All parameters are given in units of $2\pi \times$ MHz.

Hamiltonians

$$\hat{H}_r = \frac{\hbar\Omega_r}{\sqrt{2}} \left(C_{53}\hat{\sigma}_{53} + C_{73}\hat{\sigma}_{73} + C_{64}\hat{\sigma}_{64} + C_{84}\hat{\sigma}_{84} \right) + \text{H.c.}, \tag{7.4}$$

$$\hat{H}_+ = \hbar\Omega_+ C_{14}\hat{\sigma}_{14} + \text{H.c.}, \tag{7.5}$$

$$\hat{H}_- = \hbar\Omega_- C_{23}\hat{\sigma}_{23} + \text{H.c.}, \tag{7.6}$$

$$\tag{7.7}$$

where C_{ij} and $\hat{\sigma}_{ij}$ are Clebsch-Gordon coefficients and raising operators for the $|i\rangle \rightarrow |j\rangle$ transition, and $\Omega_{r,+,-}$ are the resonant Rabi frequencies associated with each beam. And the Liouvillian consists of collapse operators corresponding to decay by all ten transitions $|i\rangle \rightarrow |j\rangle$ shown in Fig. 6.4

$$\hat{C}_{ij} = \sqrt{\Gamma_{b,r}} C_{ij}\hat{\sigma}_{ij} \tag{7.8}$$

and decoherence terms

$$\hat{C}_{ii} = \sqrt{\Delta\omega_{b,r}} C_{ii}\hat{\sigma}_{ii} \tag{7.9}$$

corresponding to laser linewidths $\Delta\omega_{b,r}$ for each beam.

Solving the master equation from Eqn. 3.32 under the steady-state condition

$$\frac{\partial}{\partial t}\hat{\rho} = -\frac{i}{\hbar}\left[\hat{H}, \hat{\rho}\right] + \hat{\mathcal{L}}(\hat{\rho}) = 0, \tag{7.10}$$

gives the equilibrium density matrix $\hat{\rho}$. The π-polarized resonance fluorescence rate is proportional to the total excited state population $\hat{\rho}_{33} + \hat{\rho}_{44}$, therefore finding the equilibrium solution as a function of one detuning allows us to calculate an expected resonance fluorescence spectrum. Because the spectrum is sensitive to many parameters, fitting a resonance fluorescence model to the measured spectrum allows us to identify free parameters quite precisely. Having fixed these parameters by fitting the most sensitive measurement, we can use them predictively in the model.

We follow this process for the blue-triggered single-photon data presented in Fig. 7.5. Figure 7.5(a) shows the above model fitted to a resonance fluorescence taken under continuous excitation by the cooling and repump beams, while scanning the repump detuning Δ_r. This corresponds to the common blue beam case $\Omega_+ = \Omega_- = \Omega_c$, $\Delta_+ = \Delta_- = \Delta_c$. The magnetic field magnitude $|\mathbf{B}|$ is calibrated by spectroscopy of the quadrupole transition $6\,\text{S}_{1/2} \leftrightarrow 5\,\text{D}_{5/2}$ using the narrow-linewidth 1.7 μm laser, see Sec. 6.4.2. We scan the repump laser frequency by changing the reference cavity length. A portion of the re-

pump beam is sent to a wavemeter (High Finesse, WS7) to measure the repump frequency range. The fitted model has three free physical parameters: the cooling detuning Δ_c and the cooling and repump Rabi frequencies $\Omega_{c,r}$, all shown on the figure. Both the measured and modelled fluorescence are normalized such that the flux rate ranges from zero to one.

Figure 7.5(b) shows the model fitted by the same method to a spectrum taken with the same repump beam used during cooling, and excitation and pump beams with opposite circular polarizations. In this case the blue detunings and Rabi frequencies are independent for a total of six free parameters. Given that the spectra in Fig. 7.5(a) and (b) were taken with the same repump beam, we expect agreement between the fitted repump Rabi frequency Ω_r, and indeed the values agree to within the uncertainty of the fitting process.

The model shows close agreement with the measured spectra, matching the resonance width, and the location and width of the four dark resonance peaks, albeit with some discrepancies. Increasing the complexity of the fit by, for example, freeing the line width or magnetic field or including a small excitation of the red π transitions, removes these remaining differences. However, with any more free parameters the match to subsequent measurements deteriorates, presumably due to overfitting. By limiting the number of free parameters we reduce the closeness of the fit but improve the predictive power of the model. Sec. 7.4 demonstrates how the values from the spectrum fits are subsequently used in the $g^{(2)}(\tau)$ and single photon emission flux models.

The $g^{(2)}(\tau)$ correlation measurement in Fig. 7.5(c) was recorded with the pump and excitation beams from Fig. 7.5(b) and $\Delta_r = 10$ MHz chosen at the fluorescence peak. The correlation measurement was taken over 30 minutes. Resonance fluorescence spectra were taken immediately before and after to ensure limited parameter drift. Taking the steady state solution with parameters from the fit to Fig. 7.5(b), and time evolution given by the master equation, we can calculate the model correlation function between two-time detection operators for π polarized photons $(\hat{\sigma}_{31} + \hat{\sigma}_{42})/\sqrt{2}$. The measured and modelled correlation functions match well with parameters entirely fixed by the resonance fluorescence spectrum.

Finally, we can apply this model to predict blue-triggered photon arrival time histograms. Starting from the pure initial state $|1\rangle$ or $|2\rangle$ with only the pump or excitation interaction term $\hat{H}_+$ or $\hat{H}_-$ the master equation predicts single-mode fluorescence rates proportional to the single-photon detection probability density. Because the beams are switched by an AOM with rise time comparable to the excited state decay time, we must consider a time-dependent Hamiltonian

$$\hat{H} = \hat{H}_a + \sqrt{\frac{I(t)}{I_0}}\hat{H}_\pm \,, \tag{7.11}$$

where I_0 is the maximum beam intensity and $I(t)$ is the AOM intensity switching function. We measured an AOM switching function well approximated by an error function with time constant $\tau_r = 15$ ns. Again, taking the pump beam parameters from the resonance fluorescence fit in Fig. 7.5(b) and the measured rise time gives area-normalized photon arrival time distributions consistent with our measurement, including a weak Rabi-flop on $6\,S_{1/2} \leftrightarrow 6\,P_{1/2}$ by the strong excitation beam.

In summary, we have extended the Λ-atom model to an eight-level model for the $6\,S_{1/2} \leftrightarrow 6\,P_{1/2} \leftrightarrow 5\,D_{3/2}$ cooling and repump manifold excluding atomic motion. By fitting this model to observed resonance-fluorescence spectra under two driving conditions (but with a common repump beam) we identify cooling, repump, pump and excitation beam
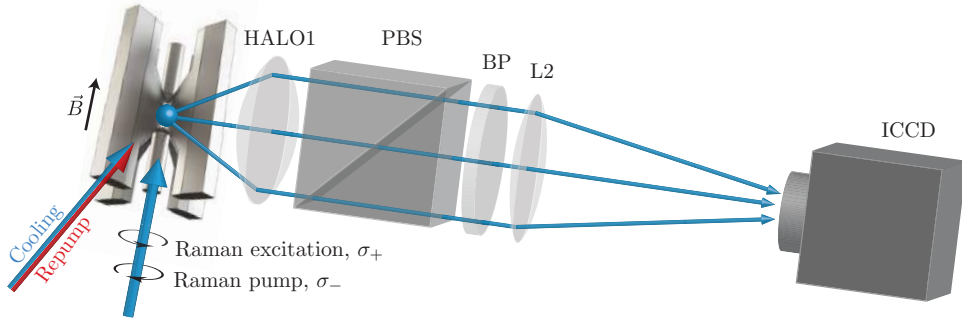
Figure 7.6: Experimental configuration for imaging a trapped ion. As before, the ion is Doppler cooled with off-axis cooling and repump beams. Photons are scattered from a blue-triggered Raman transition by alternating circularly polarized pump and excitation beams aligned with both the magnetic field **B** and the linear trap (x) axis according to the scheme of Figure 7.4 and collected about the optical (z) axis by HALO1. Repump photons are filtered using and optical bandpass filter. σ and π transitions are separated using a PBS. The photons are refocussed onto an ICCD using a second imaging lens L2.

Rabi frequencies and detunings. With parameters taken from these fits the model matches the $g^{(2)}(\tau)$ correlation function and single photon arrival time distributions taken under the same conditions without any further fitting. This model is a decent match for the observed dynamics, albeit with some discrepancies, under a variety of conditions, and accurately predicts the single-photon shape from our blue-triggered photon source. The strong agreement suggests our simulations are a realistic model of the complex atom-photon dynamics.

7.5 Imaging single photons

By replacing the APDs used above with an imaging system as shown in Figure 7.6, we can measure the dipole transition images we derived in Chap. 4. Photons generated by continuous excitation are imaged onto an intensified CCD camera (ICCD, Andor iStar A-DH334T-18H-63). Scattered repump photons and fluorescence on the 650 nm $6\,P_{1/2}$ $\leftrightarrow 5\,D_{3/2}$ transition are filtered using an optical bandpass filter with 97% transmittance at 493 nm and 20 nm bandwidth. The CCD pixel size is 13 μm, and we use a second imaging lens with a focal length of $f' = 150$ mm to provide a magnification of $M = 5.40 \pm 0.07$[2]. Due to misalignment of the in-vacuum optics and aberrations of the imaging lens, the dipole image is not diffraction-limited and has a $x(y)$-axis width of 15.6 ± 0.2 μm (14.2 ± 0.2 μm). This image an order of magnitude larger than the diffraction limit of the system $\sigma_d = \lambda/(2\mathrm{NA}) = 616$ nm and two orders of magnitude larger than the size of the atom's motional wavepacket $\sigma_a = 29$ nm (Figure 6.5).

Despite the size of the image, the dipole image centroid reaches a minimum uncertainty of only 3.3 ± 0.7 nm after 74 s of total accumulation time under continuous excitation, Fig. 7.7(a). This compares well to the best atom-position measurements [191, 259] and is, for example, better than the atom's localization at Doppler temperatures as derived in Sec. 6.4.4. For shorter times the uncertainty is dominated by shot noise, and for longer times the uncertainty is dominated by slow drifts of the imaging system—most likely due

---

[2]If the in-vacuum optics are perfectly focussed then the magnification should be $M = f'/f = 6.0$.
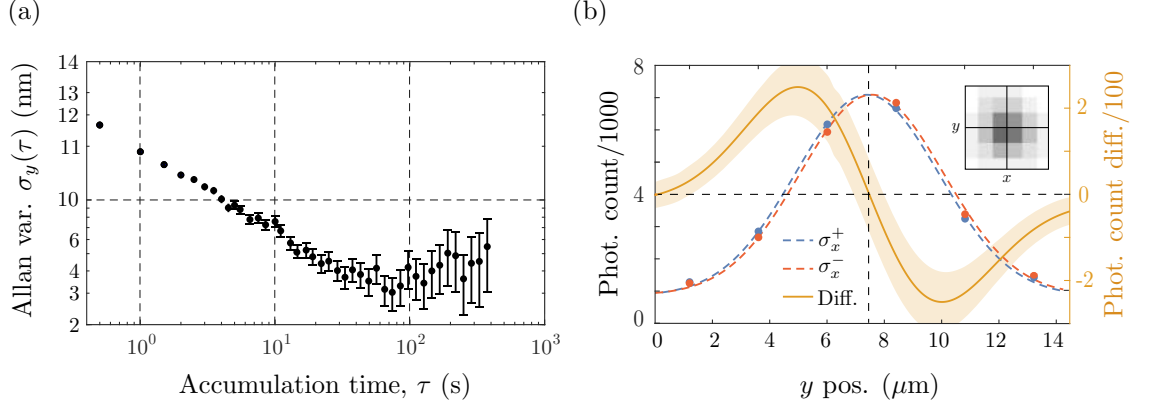
Figure 7.7: (a) Precision of vertical (y-axis) image centroid estimation as a function of accumulation time, as measured by the Allan variance. (b) Integrated y-axis intensity for images of the $\sigma_x^\pm$ atomic transitions (blue and red). Data points represent each row of pixels, and Gaussian fits to each distribution are shown with dashed lines. The difference between the fits (orange) is shown with an uncertainty region corresponding to the Poissonian uncertainty of the raw count data. Measurement and figure by Gabriel Araneda. (inset) Total accumulated image of the σ_x^+ photon field.

to temperature fluctuations, the same source as the interferometric instability we discussed in Sec. 7.1.

7.5.1   Chirally displaced photons

This precision is sufficient to measure small displacements of the image centroid caused by optical spin-orbit coupling in the photon field. As introduced in Sec. 4.2.3, the image of a circular dipole taken perpendicular to the quantization axis is displaced relative to the emitter's actual position by the circular dipole's spiral wavefront. We perform the first measurement of these displacements, and demonstrate that the effect has consequences for sub-wavelength optical microscopy with chiral fields. As we shall see, even small polarization imperfections can lead to large apparent displacements.

We generate single photons $\sigma_x^\pm$ from the blue $\sigma_\mp$ transitions, such that each photon carries angular momentum $\hat{J}_x |\sigma_x^\pm\rangle = \pm\hbar$ about the quantization (x) axis. Along the detection (z) axis this angular momentum manifests not as spin $\hat{s}_x$, but instead as orbital angular momentum $\hat{l}_x = \pm\hbar$. This, in turn, projects onto the perpendicular linear momentum $\hat{p}_y$ according to $\hat{\mathbf{l}} = \mathbf{r} \times \hat{\mathbf{p}}$. Finally, we have the operator for displacement in the image plane

$$\hat{y} = \frac{f'}{\hbar k}\hat{p}_y = \frac{f'}{f}\frac{1}{\hbar k}\hat{l}_x = \frac{M\lambda}{2\pi\hbar}\hat{l}_x\,. \tag{7.12}$$

This projection only holds along the detection axis, but remains a reasonable approximation in the small-aperture limit $\phi_a \ll \pi/2$. The aperture selects photons by their position in the Fourier plane, a weak position measurement, and therefore introduces uncertainty onto the image-plane position distribution according to the conjugate measurement rule. However, because $|\sigma^\pm\rangle$ are $\hat{p}_y$ eigenstates along the detection axis, the centroid (or mean) displacement is unaffected by the aperture and we are left with displacement

$$\Delta y = \langle\hat{y}\rangle = \frac{M\lambda}{2\pi\hbar}\left\langle\hat{l}_x\right\rangle = \mp\frac{M\lambda}{2\pi}\,, \tag{7.13}$$

in the small-aperture limit, consistent with the far-field image displacement of a rotating classical dipole as derived in Ref. [260] and the angular-momentum flux of single photons scattered with unit angular momentum as derived in Ref. [261].

To measure this displacement, blue-triggered single photons are produced according to the scheme of Sec. 7.3, with the PBS orientation chosen instead to filter out π photons. This means that we cannot guarantee to the same degree that each pulse contains only a single photon, but given weak excitation pulses and short detection times we attain once again the single-photon limit, albeit at the expense of generation efficiency. The photo-intensifier is gated electronically to suppress detection during the cooling and pump pulses. We can measure this displacement in the $\sigma_x^{\pm}$ single photon field because, as discussed in Sec. 7.1, the lens aperture is sufficiently small that polarization filtering allows us to collect only photons from the two $\sigma_{\mp}$ transitions with negligible distortion to the transition image.

The detection rate of blue-triggered single photons is considerably lower than the photon rate under continuous excitation, only ≈ 1600 phot./s. Because the imaging system drifts at the same rate, the pulsed-single photon centroid estimation is considerably lower. However, we measure relative displacements of the single photon field with comparable precision by alternating test and reference images. We alternate images of the $\sigma_x^{\pm}$ dipoles with a cooling fluorescence reference, exposing each image for 0.5 s and measuring the relative displacement between the two circular dipole images. The relative vertical (y-axis) displacement after three hours of measurement is $\Delta y / M = 158 \pm 4$ nm, consistent with the expected small-aperture image displacement $\Delta y / M = \lambda / \pi = 157.1$ nm. The measured distributions and their difference are shown in Fig. 7.7(b).

7.5.2 Displacement of elliptical dipoles

The σ_x dipoles are a special case of the general dipole

$$\mathbf{d} = \cos(\alpha)\mathbf{y} + I\sin(\alpha)\mathbf{z}, \tag{7.14}$$

corresponding to $\alpha = \pm\frac{1}{4}$, the dashed lines Fig. 7.8. Along with the linear dipoles $\mathbf{d}(\alpha = 0, \pm 1)$, these are the eigenstates of $\hat{l}_x$ in this subspace. In Fig. 7.8 the centre-of-mass displacement is calculated for images of the dipole $\mathbf{d}$ as a function of the mixing angle α for imaging systems with varying numeric aperture according to the method of truncated Hankel transforms developed in Sec. 4.4.2. The collimated and image fields of $\mathbf{d}(\alpha)$ are shown in Fig. 7.10.

Remarkably, although the eigenstate $|\sigma^{\pm}\rangle$ dipole fields are extremes of the angular momentum eigenspectrum, they are not the maximally displaced states. Dipoles near to $|\pi_z\rangle$, but with a small degree of ellipticity

$$|\psi\rangle = \frac{1 \pm \epsilon}{\sqrt{1 + \epsilon^2}} |\pi_z\rangle \mp \frac{\sqrt{2}\epsilon}{\sqrt{1 + \epsilon^2}} |\sigma_x^{\pm}\rangle, \tag{7.15}$$

where ellipticity $\epsilon = \arctan(\alpha)$, are displaced by considerably more than $\Delta_y = M\lambda/(2\pi)$ in the small-aperture limit, which is to say that Eqn. 7.13 doesn't hold in general. The measured displacement is, more strictly, the average over the aperture of the momentum per detected photon $p_y^{\mathbf{k}}$

$$\Delta y = \frac{M\lambda}{2\pi\hbar} \int_0^{\phi_a} \mathrm{d}\phi \int_0^{2\pi} \mathrm{d}\theta \, p_y^{\mathbf{k}(\theta,\phi)}, \tag{7.16}$$
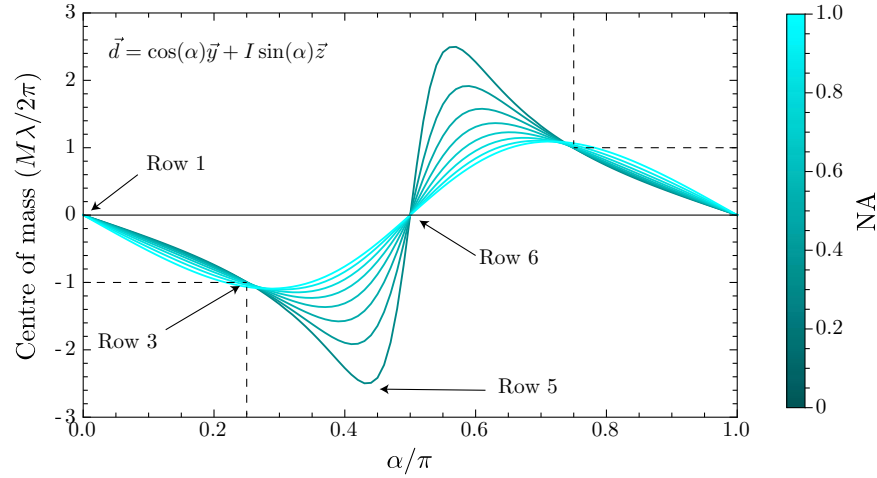
Figure 7.8: (a) Centre of mass of the dipole $\mathbf{d} = \cos(\alpha)\mathbf{y} + I\sin(\alpha)\mathbf{z}$ imaged by spherical lens with various numeric apertures. Elliptical dipoles like may be displaced by an amount Δy that is larger than the eigenmode spectrum and that scales inversely with the collected field proportion η_I according to the weak value amplification rule. This weak value amplification is an example of supermomentum in single-photon field. Several dipoles from Fig. 7.10 are labelled.

which we already defined for Eqn. 4.14

$$p_y^{\mathbf{k}} = \mathrm{Re}\, \frac{\langle \psi_{\mathbf{k}}|\hat{p}_y|\psi\rangle}{\langle\psi_{\mathbf{k}}|\psi\rangle} = \frac{p_y(\mathbf{k})}{I(\mathbf{k})}\, . \tag{7.17}$$

where ψ is the total photon mode and $\psi_{\mathbf{k}}$ is the plane wave mode with wavevector $\mathbf{k}$. The momentum per measured photon is the weak value of the momentum conditioned on emission angle. As such, it exhibits weak value amplification. States that are not angular momentum eigenstates violate Eqn. 7.13 and may be displaced by an amount inversely proportional to the collected portion of the dipole field, η_I from Eqn. 4.17, and take on values outside the eigenspectrum of the field.

In fact, the displacement can be arbitrarily large as the aperture vanishes. In other words, the orbital angular momentum components transverse to the optical axis result in a transverse linear momentum at the aperture that leads in turn to a displacement of the directed beam in the far field. The local angular momentum per photon can exceed $\pm\hbar$ where the field is weak. That is, each detected photon carries on average more angular momentum than either of the transitions from which the photon has originated. This 'super-momentum' is typical of symmetry-broken spin orbit systems [103, 106, 262, 263]. Unfortunately, generating such 'elliptical' single-photon states from a trapped atom requires an alternative level scheme, but coherent elliptical fields have been generated with gold nano-particles in a companion experiment in the group of Arno Rauschenbeutel published alongside these results in Ref. [6].

7.5.3   But is it quantum?

Imaging circular dipoles perpendicular to their axis of rotation has already been considered with both classical [260] and quantum [261] fields (with identical results). In our treatment above we defined the momentum per photon $p^{\mathbf{k}}$ in terms of the operators on the single photon field, giving rise to an expression for the observed momentum in terms of the
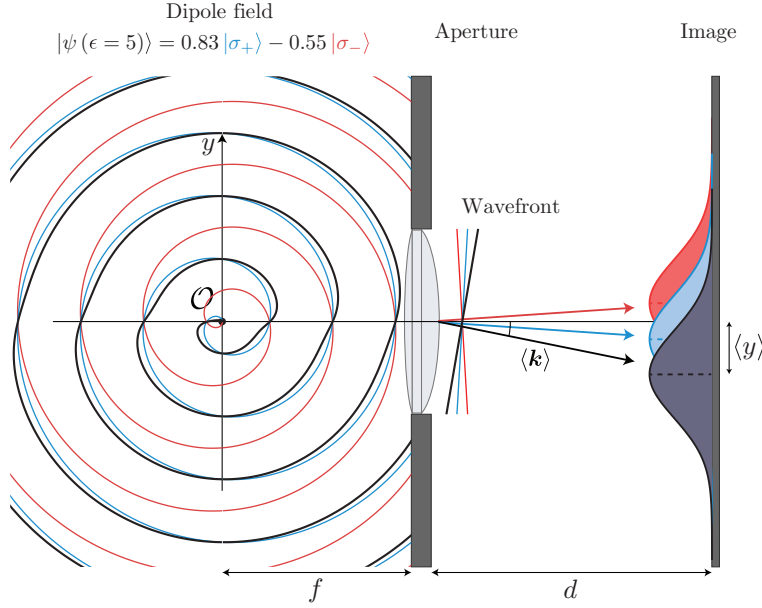
Figure 7.9: A $\sigma^\pm$ (blue/red) dipole at the origin emits spiral wavefronts that are collimated by a lens with focal length f. The wavefronts passing through the aperture are tilted at an angle with respect to the optical axis and the image of the dipole in the image plane appears displaced. Elliptical dipoles, such as $|\psi\rangle = 0.83|\sigma^+\rangle - 0.55|\sigma^-\rangle$ (black) can lead to complex wavefronts with, which yield bigger emitter apparent shifts. The wavefronts of $|\psi\rangle$ are kinky spirals, the kink along the optical axis corresponds to supermomentum in the orbital angular momentum of the field.

weak operator Eqn. 4.14. Like other weak values of quantum operators, this quantity exhibits unexpected behaviour, namely weak value amplification—the measured angular momentum can be arbitrarily large when the proportion of the field collected vanishes, even though the angular momentum of the source transitions is bounded.

To what extent is this surprising effect 'quantum'? Like optical spin-orbit coupling more generally, this displacement is due to conservation of momentum flux in the classical field mode. The super-momentum we have derived above is, for example, evident in the wavefronts of the classical dipole field as shown in Figure 7.9[3]. The wavefronts of the $\sigma^\pm$ dipoles (blue and red) are Archimedean spirals. In contrast, the wavefront of the elliptical dipole (black) is a kinky spiral, with the kink lying along the optical axis. The momentum in this plane is orthogonal to the wavefronts, and so the transverse component of the momentum of the elliptical dipole photon is larger than the circular dipole photons at this kinky angle. The average momentum remains larger for the elliptical dipole field so long as the aperture to integrate is sufficiently small.

What Fig. 7.9 doesn't show is the local intensity of the elliptical dipole field. The image-plane intensity distributions and centroid displacements in Fig. 7.8 are calculated by taking the Fourier transform of elliptical dipole fields according to the method of Sec. 4.3, which is also an entirely classical Fourier-optics operation. This more complete picture of the field shows that supermomentum is contingent on imaging a weak region of the field[4]. The centroid is the ensemble average of photon position at the image plane, as shown in

---

[3]The derivation of these wavefronts is provided as a digital appendix at https://github.com/dhigginbottom/thesis-appendices.git

[4] Figure 7.10 also shows that supermomentum is maximized when the elliptical dipole field's angular momentum vortex is just inside the collection aperture—a suggestive connection.
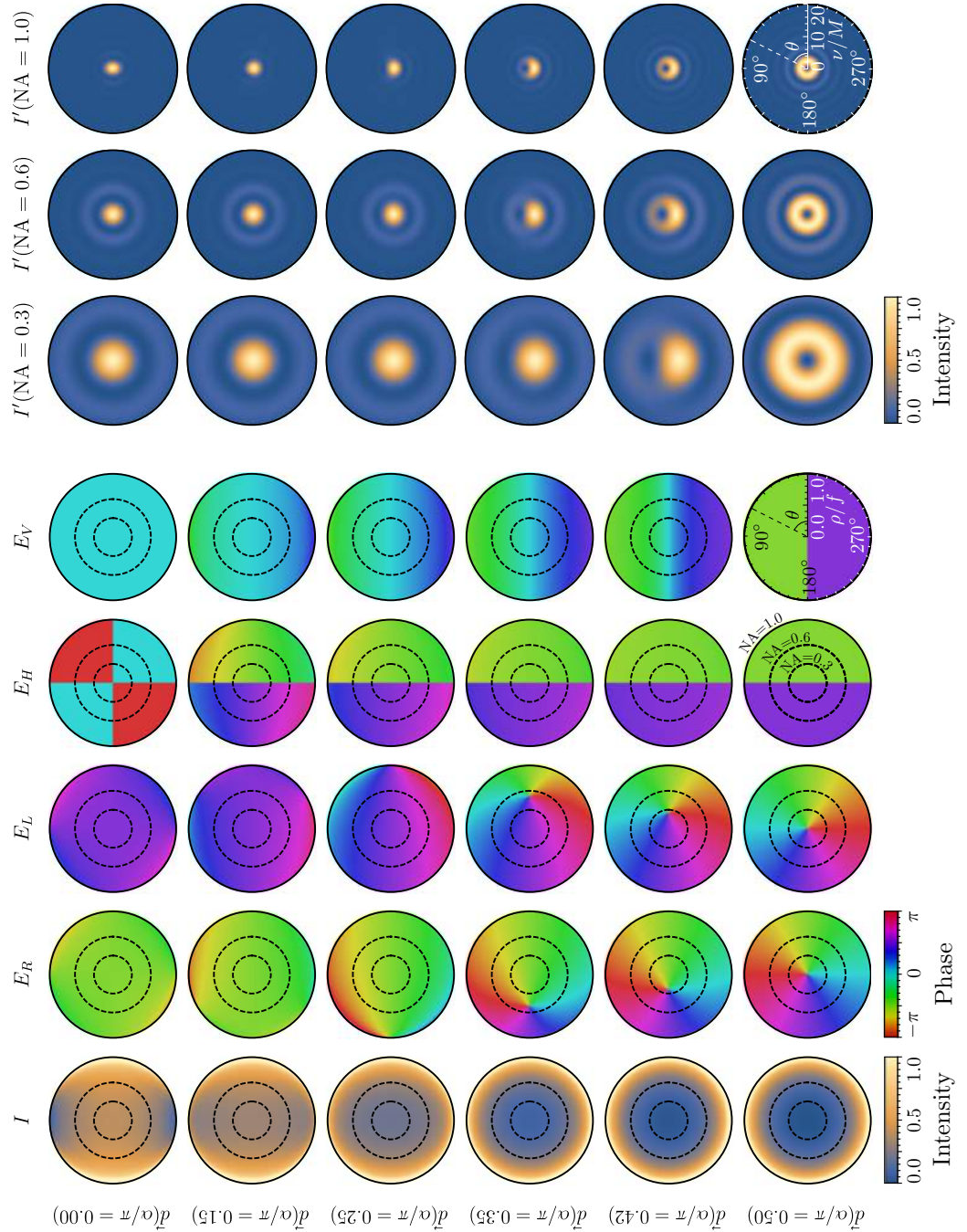
Figure 7.10: (Left five columns) Field intensity I and phase in the local linear (E_H, E_V) and local circular (E_R, E_L) polarization bases of the dipoles $\mathbf{d}(\alpha)$ by an apodized orthographic projection. This projection is identical to the field distribution as collimated by an ideal spherical lens, see Chap. 4. The fields are plotted in radial coordinates $\rho/f = \sin(\phi)$ to an aperture half-angle $\phi_a = \pi/2$. Dashed circles indicate NA= 0.3, 0.6. (Right three columns) Corresponding peak-normalized images I' calculated by full propagation of the optical dipole fields for NA= 0.3, 0.6 and 1. For NA< 1 the images are calculated by truncated Hankel transform according to the method of Chap. 4. I' is plotted in radial coordinates ν/M with units $\lambda/2\pi$. For $0.25 < \alpha < 0.5$ the circular components of the elliptical dipole fields have off-axis momentum-current vortices (phase singularities in the E_R and E_L fields). As α increases from 0.25 to 0.5, the phase singularities move in from the edges ($\rho/f = 1$) until reaching the optical axis ($\rho/f = 0$). The centroid is maximally displaced when the vortices are inside the imaging aperture. Rows four and five are the maximally displaced dipoles for NA= 0.6 and 0.3, respectively.

the rightmost three columns. Although we took this average over many distinct single photon states in our measurement above, it could just as easily be taken by measuring bright coherent or thermal states, so long as the spatial mode was the same. The image itself is a (somewhat surprising) consequence of purely classical optics.

The single-photon state measurement illustrates a startling consequence of this classical field transformation when the field itself is quantized: that the angular momentum per photon may, in general, be arbitrarily large (albeit in an area of the field that is vanishingly dim) [103]. Although the angular momentum flux is conserved, the indivisible quanta of action necessitates that the angular momentum per quanta can become arbitrarily large where the intensity is small. In this respect, the phenomena of supermomentum in elliptical photon states has a common origin with Heisenberg's microscope [264]. Like the diffraction-limited spot through Heisenberg's microscope, the measured image has a classical origin, but implies a startling property of the single photons that constitute the image. Through this thought-experiment (now realized in single-photon experiments like ours) Heisenberg argued that his uncertainty principle followed from complementary wave-particle pictures of the imaging process.

Regarding the 'quantum-ness' of such an effect: Your mileage may vary. Repeating the elliptical dipole measurement of Ref. [6] with single photons would certainly capture the remarkable presence of single-photon supermomentum in dipole emission more explicitly— a worthy extension of this work.

7.6   Red-triggered single photons

In the blue-triggered scheme, the excitation beam is the same frequency as the collected photons. This can lead to contamination between the photons from the source and excitation-beam photons scattered from the trap electrodes, vacuum chamber windows or other optics. We can reduce scattered-photon noise from our source by using an excitation beam that can be efficiently filtered from the desirable source photons. We produce red-triggered photons by pulsing the cooling and repump beams according to the scheme shown in Fig. 7.11, at an attempt rate of 2×10^5 s^{-1}.

Once again, the experimental sequence begins with Doppler cooling by both the cooling and repump beams, we have reduced the Doppler cooling time to 2 μs to improve the attempt rate and we have also removed the pumping stage. In this case the ion is prepared in a statistical mixture of the $D_{3/2}$ shelving states by 1 μs of driving with only the cooling beam. Both beams are off for 500 ns before the repump is switched back on to trigger the spontaneous emission of an unpolarized 493 nm photon.

The single-mode fibre coupling our APDs effectively removes any stray repump photons (which are more than 100 nm outside of the fibre bandwidth). An optical bandpass filter was also included in some measurements, but had no measurable impact on the dark count rate and was ultimately removed to reduce detection path losses.

7.6.1   Generation efficiency

The repump remains on throughout the detection window such that some photons are scattered after first decaying on the $6\,P_{1/2} \leftrightarrow 5\,D_{3/2}$ transition some number of times. The generation efficiency is therefore

$$\eta_{\mathrm{G}}^{\pi} = C_{\pi}^2 = 1/3 \,, \tag{7.18}$$

which is a little worse than in the blue-triggered scheme for a total end-to-end efficiency of $\eta_{\text{total}}^{\pi} \approx 0.019$ because the branching ratio between blue π and σ photons is worse than the branching ratio between blue π photons and all possible red transitions. The measured end-to-end efficiency is $\eta = 0.0054$, or 28% of the limit. The difference likely consists of absorption and scattering losses from the collection and filtering optics, which is not accounted for in Eqn. 7.1, and sub-optimal fibre coupling.

The initial state mixture produces frequency mixed photons with a corresponding increase in distinguishability proportional to $|\mathbf{B}|$. For applications requiring a high degree of indistinguishability it is necessary to prepare a well-defined state, but as we saw in Sec. 7.3.1 single photons scattered from the $6\,\mathrm{S}_{1/2} \leftrightarrow 6\,\mathrm{P}_{3/2}$ transition have competing decay channels that produce a mixed polarization even when the initial state was pure. A similar Raman scheme using the $6\,\mathrm{S}_{1/2} \leftrightarrow 6\,\mathrm{P}_{3/2} \leftrightarrow 5\,\mathrm{D}_{5/2}$ cycle (for example) would produce perfectly polarized photons at 455 nm if the ion were first prepared in a single extremal $5\,\mathrm{D}_{5/2}$ Zeeman state, because at the chosen wavelength only a single transition is possible (the Clebsch-Gordon coefficient is one). This alternative scheme would produce frequency and polarization pure photons from a σ transition, increasing the collection efficiency to $\eta_{\text{total}} = \eta_{\text{D}}/2 = 0.029$ in the current configuration, or by a factor of three to $\eta_{\text{total}} = \eta_{\text{D}} = 0.054$ in a configuration collecting σ photons along the quantization axis - limited only by the collection optics and detectors.

7.6.2   Photon-source dynamics

In Fig. 7.12(a) we show arrival time histograms of Raman scattered single photons as the repump power is steadily increased past the transition saturation point. As before, we can fit the eight-level Bloch model to measured resonance fluorescence spectra to infer the cooling and repump beam powers $\Omega_{\text{c,r}}$ and detuning Δ_{c}, see Fig. 7.12(b). The same parameters can then be used to calculate the dynamic single-photon scattering rate as a function of time after the repump is switched on under the driving scheme in Fig. 7.12(a), with repump beam parameters $(\Omega_{\text{r}}, \Delta_{\text{r}})$ inferred from the continuous-driving resonance fluorescence spectrum. This dynamic simulation takes into account the intensity profile of the repump beam as measured after the switching/shaping AOM, which is well-approximated by an error function with time constant of 50 ns. The initial state for this model is a mixed state with probabilities equally distributed between the four $5\mathrm{D}_{3/2}$ levels and with no coherences within that manifold.

The arrival time distribution features a distinctive oscillation at a frequency independent of the repump beam power. These quantum beats are caused by interference between $6\mathrm{P}_{1/2} \leftrightarrow 5\mathrm{D}_{3/2}$ absorption amplitudes that enhances and suppresses the emission of Raman-scattered $6\mathrm{S}_{1/2} \leftrightarrow 6\mathrm{P}_{1/2}$ photons in the detection mode with frequency determined by the D state energy splitting, as first observed in Ref. [265].

7.6.3   Photon-number purity

The second order intensity correlation function $g^{(2)}(\tau)$ of the red-triggered source is shown in Fig. 7.13. The source is pulsed according to the scheme of Fig. 7.11 but at one third of the trigger rate in order to collect a statistically significant amount of background events during an extended 20 μs detection window. Cooling fluorescence has been removed by gating the detectors during the cooling stage. The detection events, recorded separately by each detector, are sorted into time separation bins of 300 ns duration. Because photon emission is triggered by the excitation pulse, the observed intensity correlation forms a

Event	λ (nm)	Transitions					Time, t (μs)			
			0	1	2	3	4	5		
Cooling	493 nm	$\sigma^+ + \sigma^-$								
Repump	650 nm	$\sigma^+ + \sigma^-$								
Detection	$-$	$-$								
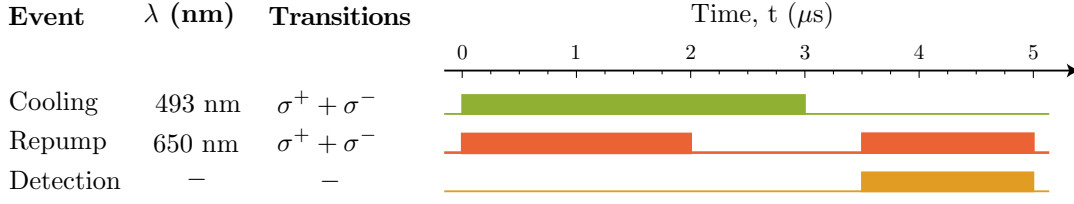
Figure 7.11: Experimental sequence for red-triggered single photons showing the wavelength and transitions addressed by each excitation pulse.

(a)

(b)
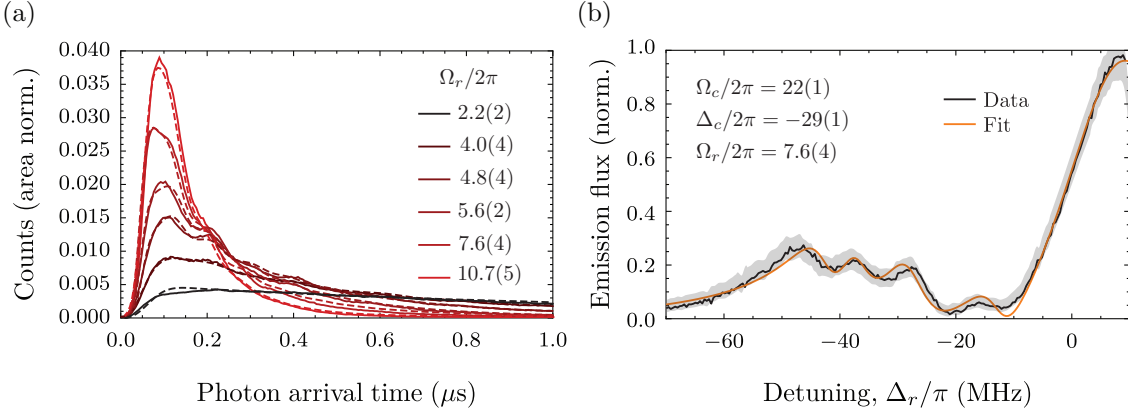
Figure 7.12: Red-triggered ^{138}Ba$^+$ single-photon source and corresponding Bloch model. (b) Area normalized histograms of red-triggered single-photon arrival times. The mean arrival time decreases as the repump beam power Ω_r is increased to the transition saturation point. The eight-level Bloch model of our system predicts corresponding single photon shapes shown by dashed lines. For each trace the model parameters are calibrated using a resonance fluorescence spectrum taken under the same driving conditions. The corresponding fitted repump power is shown in units of MHz. (b) A typical example of the resonance fluorescence spectrum with the measured fluorescence rate (black) and fit (orange).

sequence of spikes separated by the excitation pulse period with width determined by the pulse shape shown in Fig. 7.12. The peak at $\tau = 0$ contains only coincidence events.

We infer an anticorrelation parameter from these measurements according to eqn. 2.62 giving $\mathbb{A} = (1.9 \pm 0.2) \times 10^{-3}$, which violates the coherent state condition $\mathbb{A} \leq 1$ by 10^4 standard deviations. This is more than two orders of magnitude better than the $\mathbb{A}$ of blue-triggered photons generated in Sec. 7.3, which is limited by stray light scattered from the excitation pulse. This $\mathbb{A}$ is calculated without dark-count subtraction, and corresponds precisely to the stated and measured dark count rate of our two detectors, 10 ± 2 s^{-1} per detector. Subtracting the measured dark count rate from yields an intrinsic coincidence rate of our source below $\mathbb{A} = 3 \times 10^{-4}$ (95% confidence), amongst the lowest $\mathbb{A}$ measured.

In numerical models of discrete-variable quantum repeater networks the possible network size is critically bounded by the multi-photon component. In Ref. [266] the authors consider the entanglement-based QKD network of [267] and show that even a small multiple-pair probability can be extremely detrimental. An otherwise ideal network of efficient photon sources with $\eta = 0.9$ and $\mathbb{A} = 0.01$ becomes useless for QKD at any rate after only seven concatenated network links (even if the links are lossless). In contrast, an efficiently coupled trapped-atom photon source with the same $\mathbb{A}$ and dark noise-rate as our
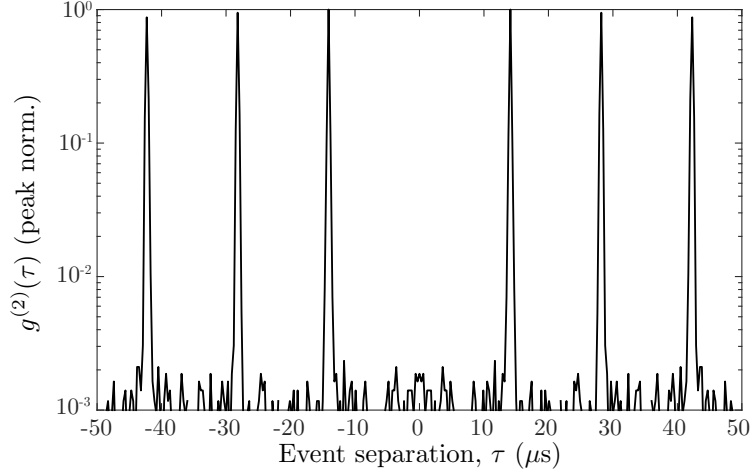
Figure 7.13: Intensity auto-correlation of the red-triggered single-photon operated at a rate of $7 \times 10^4 \ s^{-1}$. The data is presented without background subtraction and shows $g^2(0) = \mathbb{A} = (1.9 \pm 0.2) \times 10^{-3}$.

source may support high QKD rates over up to thirty network links. The same analysis applies to networks for computation. Because the information in a quantum network is stored between entangled nodes, the state space for networks of small quantum registers increases exponentially with the number of entangling links. Photon number purity is therefore also a critical parameter for scaling small quantum processors towards useful quantum information processing by optical links.

7.7   Summary

In this chapter we implemented and characterized two schemes for the operation of an on-demand ^{138}Ba$^+$ trapped-ion single-photon source. The blue-triggered scheme produces polarization and frequency mixed photons, even after pumping to a pure initial state. However, with polarization filtering we isolate photons from a single π transition, eliminating frequency mixing from competing transitions. However, the excitation pulse remains on throughout the detection window which increases generation probability by a factor of two, at the cost of power-broadening the scattered photons. The red-triggering scheme also produces frequency and polarization mixed photons, however we start from a mixed initial state and each polarization-filtered photon is scattered from one of two possible π transitions. The photons are therefore frequency mixed by the D-state splitting even after polarization filtering.

We introduced the eight-level Bloch model to describe the dynamics of the source, and by fitting this model to resonance fluorescence spectra we accurately predicted the intensity correlation function under continuous excitation and single-photon arrival time histograms of the photon-source. With the blue-triggered photon source we are able to observe a weak Rabi oscillation in the single-photon wave packet under strong excitation. We do not observe any evidence of Rabi flops in the red-triggered photon arrival times, but we do see a beat signal caused by absorption-path interference.

We measured chiral displacement of the blue triggered photons due to optical spin-orbit coupling with an imaging apparatus, and showed theoretically that the same effect gives rise to arbitrarily large displacements when the dipole source is elliptical and the

imaging aperture is small. Although this 'supermomentum' is an example of weak value amplification, it is strictly a property of the classical dipole field mode discussed extensively in Chap. 4. Because this effect is a property of dipole fields generally, it should be relevant to super-resolution microscopy whenever the excitation field or driven dipole are elliptical.

For a wide range of driving conditions, the red-triggered photon source produces a pulsed light field with coincidence rates indistinguishable from an ideal single-photon Fock state measured with our detectors. Single-atom photon sources of this sort are therefore sufficiently pure for applications in even large quantum networks, without the need for highly multimode quantum memories, photon number discriminating detectors or entanglement distillation [266, 268]. However, the efficiency of the source is limited by the collection proportion of the two HALOs, polarization mixing and filtering, APD detection efficiency, and fibre coupling efficiency so that the end-to-end efficiency is $\eta = 0.0054$ compared to an ideal efficiency limit of $\eta = 0.019$. The alternative level scheme for polarization and frequency pure photons from $^{138}\text{Ba}^+$ we discussed in Sec. 7.6.1 would increase the detection efficiency by (at most) a factor of 3, reaching the limit imposed by the collection proportion and fibre-mode coupling as discussed in Chap. 4. Efficient free-space atom-light coupling requires higher aperture coupling optics of the sort considered in Chap. 4. However, even with this imaging apparatus the single photons retain surprising higher-order quantum behaviour. In the following chapter we derive a new quantum-non Gaussian witness and apply the witness to photons from our trapped-ion source.

Bibliography - Trapped-atom single-photon source

2. D. B. Higginbottom, et al., Pure single photons from a trapped atom source, *New J. Phys.* **18**, 93038 (2016).

6. G. Araneda, et al., Wavelength-scale errors in optical localization due to spin-orbit coupling of light, *Nat. Phys.* **14**, 1–6 (2018).

86. H. Kimble, M. Dagenais, and L. Mandel, Photon antibunching in resonance fluorescence, *Phys. Rev. Lett.* **39**, 691–695 (1977).

103. M. V. Berry, Optical currents, *J. Opt. A* **11**, 094001 (2009).

106. K. Y. Bliokh, et al., Spin–orbit interactions of light, *Nat. Photonics* **9**, 796–808 (2015).

191. J. Wong-Campos, et al., High-resolution adaptive imaging of a single atom, *Nat. Phot.* **10**, 606–610 (2016).

256. F. Diedrich, and H. Walther, Nonclassical radiation of a single stored ion, *Phys. Rev. Lett.* **58**, 203–206 (1987).

257. M. Almendros, et al., Bandwidth-tunable single-photon source in an ion-trap quantum network, *Phys. Rev. Lett.* **103**, 213601 (2009).

258. H. Takahashi, et al., An integrated fiber trap for single-ion photonics, *New J. Phys.* **15**, 053011 (2013).

259. V. Blūms, et al., A single-atom 3D sub-attonewton force sensor, *arXiv Prepr. 1703.06561* (2017).

260. H. F. Arnoldus, X. Li, and J. Shu, Subwavelength displacement of the far-field image of a radiating dipole, *Opt. Lett.* **33**, 1446 (2008).

261. A. Dogariu, and C. Schwartz, Conservation of angular momentum of light in single scattering, *Opt. Express* **14**, 8425 (2006).

262. M. V. Berry, Lateral and transverse shifts in reflected dipole radiation, *Proc. Royal Soc. A* **467**, 2500–2519 (2011).

263. K. Y. Bliokh, and Y. P. Bliokh, Conservation of angular momentum, transverse shift, and spin Hall effect in reflection and refraction of an electromagnetic wave packet, *Phys. Rev. Lett.* **96**, 073903 (2006).

264. D. Bohm, and B. J. Hiley, *The undivided universe: An ontological interpretation of quantum theory* (Routledge, 1993).

265. M. Schug, et al., Quantum interference in the absorption and emission of single photons by a single ion, *Phys. Rev. A* **90**, 023829 (2014).

266. S. Guha, et al., Rate-loss analysis of an efficient quantum repeater architecture, *Phys. Rev. A* **92**, 022357 (2015).

267. N. Sinclair, et al., Spectral multiplexing for scalable quantum photonics using an atomic frequency comb quantum memory and feed-forward control, *Phys. Rev. Lett.* **113**, 053603 (2014).

268. H. Krovi, et al., Practical quantum repeaters with parametric down-conversion sources, *Appl. Phys. B* **122**, 52 (2016).

Quantum non-Gaussian photons

> *The quantum theory...has had only a fraction of the influence upon optics that optics has has historically had on quantum theory... To the extent that observations in optics have been confined to the measurement of ordinary light intensities, it is not surprising that classical theory has offered simple and essentially correct insights.*
>
> – Roy Glauber, *The quantum theory of optical coherence* (1963)

To meaningfully compare the performance of single-photon sources it is necessary to have a measure of quantum behaviour that captures the useful properties of the single photon field. Ideal single photons are the optimal carrier for DV-QKD, but how do we best measure the performance of realistic near-single photon states? The security of entanglement-based QKD protocols may be verified by checking the violation of Bell inequalities [73, 74], which is an essential requirement for device-independent QKD schemes. In contrast, conventional prepare-and-measure schemes are considerably simpler to implement because they do not require long-distance interference, but do require Alice and Bob to trust their state preparation and measurement devices. In these schemes security is verified by measuring a quantum signature of photons arriving at the receiver.

In the previous chapter we quantified the photon-number performance of our trapped-ion photon-source by the degree of photon anti-correlation. Anti-correlation is a non-classical witness and a ubiquitous metric for photon sources because in addition to being a noise source, multi-photon pulses are vulnerable to photon-number splitting attacks, which can be error-free (although decoy-pulse methods are able to improve the secret fraction achievable with a multi-photon source [269, 270]). Anti-correlation is a necessary criterion for single photon sources in quantum networks, even very weak coherent pulses (WCP) are insufficient for DV-QKD [68]. However anti-correlation alone is not sufficient to establish a secure, shared key. We will see that this is just the first in a hierarchy of more stringent quantum state witnesses that capture the performance of single photon sources in realistic QKD networks [271]. In particular, anti-correlation measurements neglect the vacuum component of the optical state, which determines the acceptable noise-threshold of and key rate over a secure channel [266]. SPDC sources (for example) can achieve arbitrarily high degrees of anti-correlation, but only by increasing the vacuum probability. To accurately judge such a trade-off and meaningfully compare sources we require a metric that considers both the multi-photon and vacuum components of the single-photon field.

In this chapter we will introduce the concept of quantum non-Gaussian (QNG) optical states, and how a statistical witness for QNG of the type first proposed in Ref. [272] can function as a superior single-photon source metric. In contrast to anti-correlated photon states, QNG states are known to be sufficient for secure QKD [273]. We derive such a
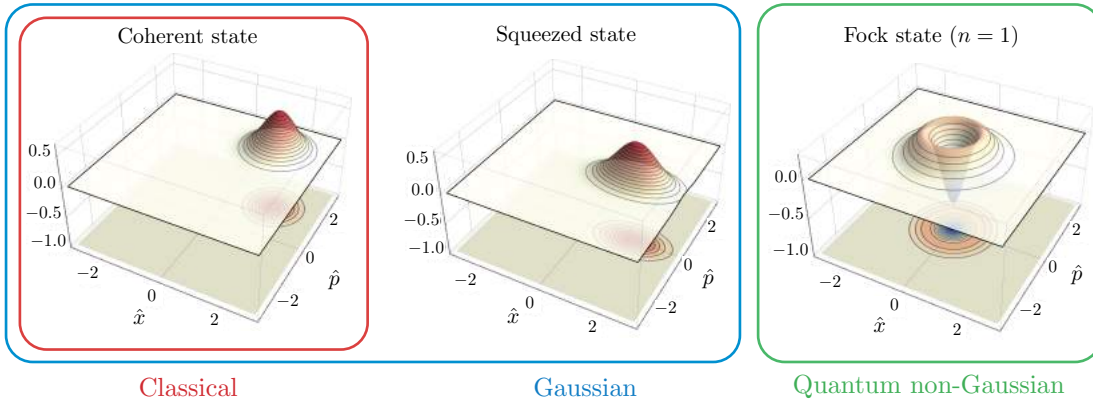
Figure 8.1: Illustrative states in the quantum hierarchy, as shown by their Wigner functions. The space of classical states consists of convex mixtures of pure coherent states that can be generated by a unitary linear bosonic Hamiltonian. The basic non-classical states are the squeezed states, which are generated by a unitary quadratic bosonic Hamiltonian. Convex mixtures of pure classical and squeezed states compose the space Gaussian states, named for their Wigner function distribution. Every state with a unitary generating Hamiltonian that is tertiary bosonic or higher, such as Fock states, is quantum non-Gaussian.

witness and measure the performance of our trapped-ion single-photon-source under this new metric. Our source surpasses the threshold even after 20 dB of attenuation. We briefly review the performance of single-photon-sources including SPDC and quantum dots under similar tests. This work is published in

[2] "**Pure single photons from a trapped atom source** D. B. Higginbottom, L. Slodička, G. Araneda, L. Lachman, R. Filip, M. Hennrich, and R. Blatt. *New Journal of Physics* **18**, 93038 (2016)."

8.1   Quantum non-Gaussian states

No convex mixture of coherent states can be photon anti-correlated. In this sense, anti-correlation is a non-classical witness: a signature of quantum behaviour that cannot be replicated by classical fields. However, we saw in Sec. 2.5.4 that for certain squeezing parameters R and displacements α, the number-squeezed state $|R, \alpha\rangle$ may be anti-correlated. Even Gaussian states with only a small degree of squeezing R are capable of arbitrarily high anti-bunching so long as the displacement α is small. To certify higher-order quantum behaviour, see Fig. 8.1, we need a similar witness that cannot be reproduced with any convex mixture of Gaussian states- a quantum non-Gaussian (QNG) witness. QNG is a sufficient criteria for security in realistic models of measure and prepare DV-QKD networks [273] and a necessary resource for quantum computation [274]. So how may we efficiently certify QNG states for use in quantum information networks?

8.1.1   Phase space QNG witnesses

Wigner function negativity is a distinguishing property of all pure QNG states [275], and a necessary quantum computational resource [274]. However, not all mixed QNG states are Wigner non-negative. A single photon field is QNG for any degree of attenuation, but the Wigner function is negative only for attenuation by less than 50%. For quantum

n	P_n^{max}	R	α	n	P_n^{max}	R	α
1	0.478	1.73	0.816	6	0.262	2.31	2.26
2	0.381	1.93	1.22	7	0.245	2.37	2.46
3	0.333	2.06	1.54	8	0.238	2.43	2.64
4	0.301	2.16	1.81	9	0.228	2.48	2.82
5	0.280	2.24	2.05	10	0.220	2.52	2.97

Table 8.1: The Gaussian state photon number probability P_n is bounded for $n > 0$. The maximum possible probability P_n^{max} is attained by a pure number squeezed state ($\phi = 0$) with squeezing parameter R and displacement α as shown. All numbers given to three significant figures.

networks we require a test to certify even QNG states that are mixed or very attenuated. Furthermore, reconstructing the complete Wigner function requires quantum-state tomography by measuring marginal distributions along multiple axes in quadrature phase space. Reconstructing single photon states to sufficient certainty by this method is a demanding process. A non-classical test does exist for single marginal distributions [276], and there is a QNG test that requires $W(x, p)$ at only four coordinates [277], but neither of tests are efficient for attenuated single-photon sources. To find an efficient an unambiguous QNG test for quantum networks we must turn to statistical (photon number) field measurements.

8.1.2   Statistical QNG witnesses

In Ref. [272] the authors proposed a novel class of QNG witnesses that requires only photon correlation measurements. In this picture the typical anti-correlation threshold is merely the first in a hierarchy of statistical quantum field tests [271]. Even in very simple configurations, these witnesses are an efficient means of quantifying useful higher-order quantum behaviour. Ideal single photon states, in particular, are robust QNG states by such measures and remain so for any degree of attenuation [278, 279].

Although the principle behind these witnesses is straightforward, the derivation of the witness we use in this chapter is a little involved. In order to guide readers that have not seen such QNG witness derivations before, we will first consider some illustrative examples that introduce the necessary concepts.

The probability P_n of finding a general, mixed Gaussian state with n photons is given by Eqn. 2.43. The single photon probability P_1 of pure squeezed states is bounded, as we can see from Fig. 2.4(b), and in fact P_n is bounded for all $n > 0$. We can maximize P_n over the Gaussian state free parameters R, α and ϕ to find photon number bounds P_n^{max} shown in Tab. 8.1.2. The boundary states are pure number-squeezed states ($\phi = 0$), with R and α increasing with n.

Any state with $P_n > P_n^{\mathrm{max}}$ is necessarily QNG. We might therefore perform a QNG test with an efficient photon-number resolving detector. Alternatively, HBT experiments are a means to make indirect photon-number measurements without number-resolving detectors. Without number-resolving detectors we must take into account the probability of 'false' single photon measurements in the HBT apparatus, in which two photons arrive simultaneously at the same detector. The success[1] and coincidence probabilities P_{s} and

---

[1]Single detection events are the only outcome consistent with a single-photon field. In this sense they are a 'success' in common jargon.

P_c in a HBT measurement are related to the photon number probabilities P_n by

$$P_\text{s} = \sum_{n=1}^{\infty} \frac{P_n}{2^{n-1}} \, , \tag{8.1}$$

$$P_\text{c} = \sum_{n=2}^{\infty} P_n \left(1 - \frac{1}{2^{n-1}} \right) . \tag{8.2}$$

The single photon component P_1 causes only success events, but with larger photon number n the coincidence probability increases and the success probability goes to zero.

Bright Gaussian fields cause almost no success events. Although P_c is unbounded on this set of optical states, we can bound the single photon event probability using the bounds P_n^max and Eqns. 8.1 and 8.2

$$P_\text{s}^\text{max} \quad \leq \quad \sum_{n=1}^{\infty} \frac{P_n^\text{max}}{2^{n-1}} \, , \tag{8.3}$$

$$\leq \quad 0.83 \, . \tag{8.4}$$

This illustrative bound shows how to apply the relationship between measured probabilities $P_{s,c}$ and the photon number probabilities P_n to derive a QNG test for the HBT apparatus, but it is very inefficient. A tighter bound can be found by maximizing P_s directly over the Gaussian state free parameters, which yields $P_\text{s} < 0.6$. This is an improvement, but a single-photon state attenuated by 41% will fail this test, even though it remains Wigner-function negative. To construct a statistical bound measurable with a HBT apparatus that is more efficient that Wigner-function negativity we must consider contingent probabilities.

The more beam-splitters you can concatenate in an expanded HBT scheme, the more information about the photon number distribution you can infer, and the more efficient the witness you can construct. With a concatenated HBT apparatus it is possible to construct QNG test for arbitrarily large ensembles of single-photon sources [280]. However, for single photon sources $\langle n \rangle < 1$, higher order correlations are negligible, and the typical HBT experiment is sufficient. In the following section we derive an efficient QNG witness that requires only a HBT apparatus.

8.2   Deriving an efficient QNG threshold

We saw above that the same HBT configuration as a typical $g^{(2)}(\tau)$ measurement is sufficient for estimating a QNG witness that distinguishes light fields from any convex mixture of coherent and squeezed states. More importantly, it is possible to perform an efficient QNG test with the same apparatus. In this section we derive a QNG witness according to the method of Refs. [272, 278]. In contrast to those works, this witness will be constructed in terms of the directly measured HBT probabilities $P_{s,c}$ to produce a tighter bound in the measurement space. It has since appeared in this form in Refs. [2, 273].

We will distinguish optical QNG states by the conditional success event probability P_s:P_c with a given coincidence probability. To derive the conditional QNG threshold for these HBT experiment probabilities we consider the linear functional

$$F(a) = P_\text{s} + aP_\text{c} \tag{8.5}$$

where a is a free parameter and $P_{s,c}$ are given by Eqns. 8.1 and 8.2. The Gaussian states that maximize this linear, unconstrained function are the border states forming the QNG threshold in the P_c, P_s parameter space. For a given P_c these states have the maximum or minimum possible P_s over the set of Gaussian states.

   The maxima and minima of the functional satisfy $\frac{\partial F}{\partial R} = 0$ and $\frac{\partial F}{\partial \alpha} = 0$ giving us

$$\frac{\partial P_s}{\partial R} = -a\frac{\partial P_c}{\partial R} \, , \tag{8.6}$$

$$-a\frac{\partial P_c}{\partial \alpha} = \frac{\partial P_s}{\partial \alpha} \, , \tag{8.7}$$

which can be combined to yield the condition

$$\frac{\partial P_s}{\partial R}\frac{\partial P_c}{\partial \alpha} = \frac{\partial P_s}{\partial \alpha}\frac{\partial P_c}{\partial R} \, . \tag{8.8}$$

It remains only to find the Gaussian states satisfying this condition. Like the maximum P_n Gaussian states of Tab. 8.1.2, the states that maximize P_s and P_c are pure. We can therefore take the pure squeezed state photon-number probabilities from Eqn. 2.46. In this equation the angle ϕ between the squeezing and displacement directions appears only in the argument of the cosine. P_s and P_c are positive weighted sums over P_n, so $F(a)$ is necessarily maximized by $\phi = 0$. The border states are, unsurprisingly, number-squeezed. We can therefore reduce the photon number probabilities P_n to

$$P_n = \frac{2^{1-n} R \left(\frac{R^2-1}{R^2+1}\right)^n e^{-\frac{2\alpha^2\left(R^4+R^2\right)}{(R^2+1)^2}} H_n\left(\frac{\sqrt{2}\alpha R^2}{\sqrt{R^4-1}}\right)^2}{R^2 n! + n!} \, . \tag{8.9}$$

With these probabilities the equivalence in Eqn. 8.8 is a rather involved relationship $\alpha(R)$ for the Gaussian boundary states in terms of products of infinite sums over n.

   To find closed-form solutions we will make a weak-field approximation with photon-number cut-off m. We can take the limit of this approximation as m increases, but even low-order approximations will provide an efficient QNG witness.

8.2.1   Weak-field approximation

We impose a photon-number threshold $m \geq 2$ and assume that photon-numbers above this threshold make a negligible contribution to the field, $P_n \approx 0 \; \forall \, n > m$. Given this approximation the m-th probability term must be

$$P_m \approx 1 - \sum_{n=0}^{m-1} P_n \tag{8.10}$$

so that the total probability sums to one. The HBT measurement probabilities are given by reduced versions of the sums in Eqns. 8.1 and 8.2 with only m terms

$$P_s \approx \sum_{n=1}^{m} \frac{P_n}{2^{n-1}} \, , \tag{8.11}$$

$$P_c \approx \sum_{n=2}^{m} P_n \left(1 - \frac{1}{2^{n-1}}\right) \, . \tag{8.12}$$
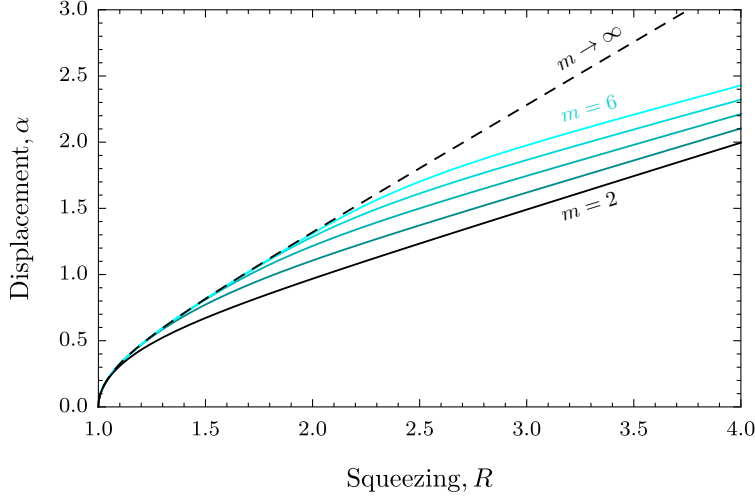
Figure 8.2: (a) Displacement of pure squeezed states on the Gaussian boundary as a function of squeezing. Multiple order solutions are shown and brightness indicates increasing photon-number threshold m. The solution approaches an approximate analytic function of R (dashed line) given in the text.

With the above measurement probabilities and P_n given by Eqn. 8.9, the condition Eqn. 8.8 gives $\alpha(R)$ as the root of an m-th order polynomial. Figure 8.2 shows the solutions $\alpha(R)$ for the lowest five orders of the weak-field approximation. Each approximation is valid to increasingly high R, and they converge to an approximate analytical function

$$\lim_{m\to\infty} \alpha \approx 0.94R - 0.54 - 0.4e^{-2.85(R-1)^{0.52}} \tag{8.13}$$

that is linear in the limit of large R. The lowest-order approximation gives the least efficient QNG bound, but because it may be written concisely we will expand on this particular case in the following section.

8.2.2   Lowest-order approximation

The lowest-order approximation, $m = 2$, treats all multi-photon fields P_{2+} as two-photon fields. Therefore, following Eqn. 8.10, we require only the single-photon and vacuum probabilities from Eqn. 2.40

$$P_0 = \frac{2R}{R^2 + 1} e^{-\alpha^2 \left(\frac{\left(R^2 - 1\right)\cos(2\phi)}{R^2 + 1} + 1 \right)}, \tag{8.14}$$

$$P_1 = P_0 \frac{2\alpha^2 \left(\left(R^4 - 1\right)\cos(2\phi) + R^4 + 1 \right)}{\left(R^2 + 1\right)^2}, \tag{8.15}$$

$$P_{2+} = 1 - P_0 - P_1, \tag{8.16}$$

and we have single and coincidence HBT measurement probabilities approximated from Eqns. 8.11 and 8.12

$$P_{\mathrm{s}} \approx P_1 + \left(P_{2+}/2\right), \tag{8.17}$$

$$P_{\mathrm{c}} \approx P_{2+}/2. \tag{8.18}$$
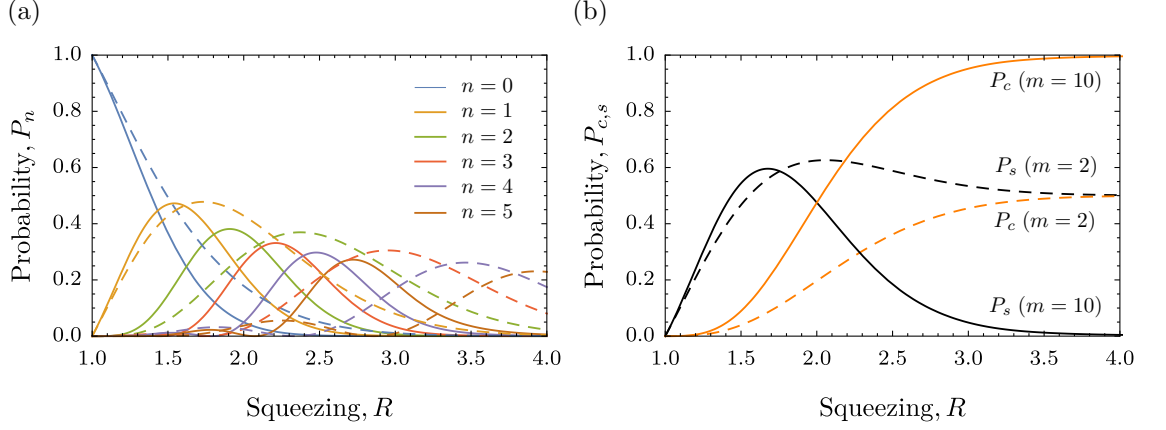
Figure 8.3: (a) Photon number probabilities P_n of the Gaussian boundary states as a function of squeezing parameter R according to the weak-field approximation with photon-number cutoffs $m = 2$ (dashed lines) and $m = 10$ (solid lines). (b) The corresponding success probability P_s (black) and coincidence probability P_c (orange) measured with a HBT apparatus with $m = 2$ (dashed lines) and $m = 10$ (solid lines). In the lowest-order ($m = 2$) approximation, P_c is always underestimated and P_s is overestimated for large R.

In this lowest-order approximation our pure squeezed state functional condition reduces to

$$\frac{e^{-\frac{4\alpha^2}{R^{-2}+1}}\left(R^{-4}+4\alpha^2 R^{-2}-1\right)}{\left(R^{-2}+1\right)^6} = 0 \tag{8.19}$$

which is satisfied when

$$\alpha = \frac{\pm\sqrt{R^4-1}}{2R}. \tag{8.20}$$

The positive root is the solid black line in Fig. 8.2.

The positive root of this lowest-order α-R relation gives the maximum threshold P_c, P_s values of the approximate pure Gaussian boundary states. These can be reduced to a pair of equations parametrized by R^2. The parametric equations for the approximate upper bound are

$$P_s = \frac{1}{2} + \frac{R\left(R^4-2R^2-1\right)e^{\frac{1}{2}(1-R^2)}}{\left(R^2+1\right)^2}, \tag{8.21}$$

$$P_c = \frac{1}{2} - \frac{R\left(R^4+1\right)e^{\frac{1}{2}(1-R^2)}}{\left(R^2+1\right)^2}. \tag{8.22}$$

Any state with conditional single photon probability P_s:P_c above this threshold is certifiably QNG within this lowest-order approximation. However, for the weak-field approximation of any order to yield an unambiguous witness we require that the approximate boundary is conservative. We shall see below that it is.
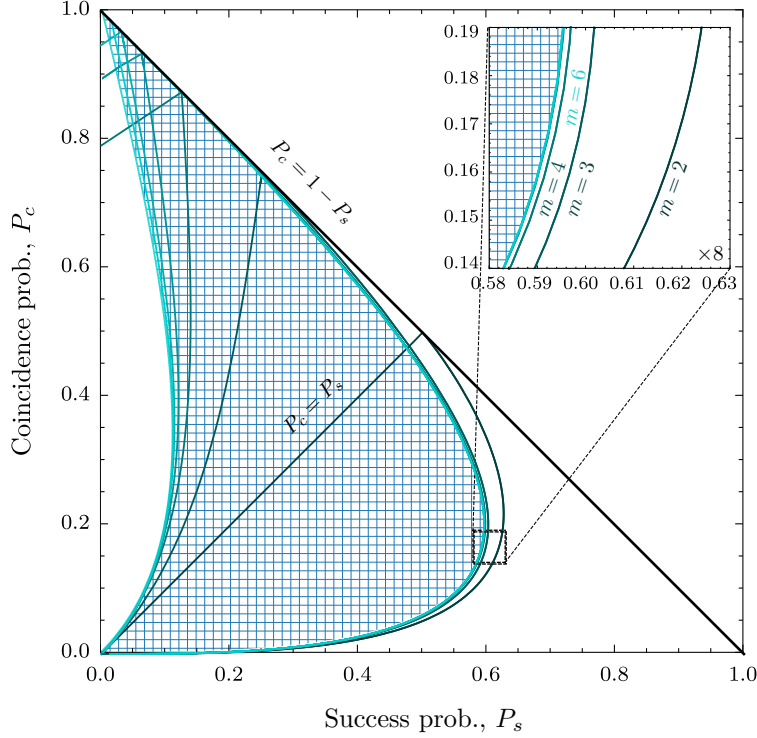
Figure 8.4: Pure Gaussian state boundaries calculated with photon-number threshold m. Brightness increases with m according to the same scheme as Fig. 8.2. All probabilities are bounded by $P_c < 1 - P_s$ (black line). The threshold states form upper and lower bounds on P_s for a given P_c. The lowest-order approximation overestimates P_s for bright fields and consequently bounds the Gaussian states by $P_s = P_c$. Both bounds decrease for higher m and converge to the true boundary (hatched region). In the region relevant to single-photon sources, $P_s \gg P_c$, only the upper bound is a QNG witness, and even the lowest order calculation is reasonably efficient.

8.2.3 Comparing bounds

Because the contribution to P_s by the n-photon term P_n only decreases with n, the weak-field approximation overestimates P_s for any given field and any cut-off m. However, $\alpha_m < \alpha_{m+1} \ \forall m$ and so the weak-field approximation underestimates P_1 for small squeezing. Figure 8.3(a) shows the probability terms P_n of the approximate upper threshold Gaussian states as a function of R for $m = 2$ (dashed) and $m = 10$ (solid) and Fig. 8.3(b) shows the corresponding HBT measurement probabilities $P_{s,c}$ for each approximation order. Where the weak-field approximation underestimates P_s, it underestimates P_c by a proportionally more. Therefore the conditional probability $P_s{:}P_c$ is always an overestimate. Taking this approximation therefore yields a conservative upper bound on $P_s{:}P_c$ for our QNG witness.

The negative root of Eqn. 8.20 gives an approximate lower bound on $P_s{:}P_c$ over the pure Gaussian states. In contrast to the upper bound, this lower bound is not conservative. We must take the limit of higher order approximations to find a meaningful lower bound on the Gaussian pure state statistics.

Upper and lower bounds are plotted in Fig. 8.4 for several approximation orders m. As

---

[2]This derivation is published in Ref. [2] with an alternative notation consistent with the broader body of work on statistical QNG witnesses [271–273, 278]. To save the interested reader some time: the parameters V and r in these works are related to our parameters R and α by $V = R^{-2} \in [0, 1]$ and $r = 4\alpha^2 \in [0, \infty]$.

we expect, the upper bound is a true conservative bound that gets tighter as the photon-number cut-off is raised, and the lower bound approaches a true bound only in the high m limit. Together these bounds define a quantum-Gaussian region of P_s:P_c combinations possible when measuring pure Gaussian states (blue hatched region). However, by mixing Gaussian states it is possible to decrease P_s:P_c further. In fact, there is no lower bound on P_s:P_c over the set of mixed Gaussian or coherent states. For example, although a bright coherent state mixed with vacuum has vanishing success probability P_s, it may have any desired coincidence probability P_c depending on the mixing ratio.

It is not possible to increase P_s:P_c by mixing Gaussian states, so the upper bound is a true bound over the set of mixed Gaussian states. The Gaussian state boundaries are shown alongside the classical state boundaries in Fig. 8.5(a). Any measurement of P_s above this boundary is a QNG witness. Importantly, the upper bound is the relevant QNG witness for single photon sources, which operate in the region $P_s \gg P_c$. For very attenuated fields (the operational region of our photon-source) the lowest-order QNG witness in Eqn. 8.21 may be reduced to

$$P_c \leq P_s^3/3\,,\tag{8.23}$$

or, taking the limit of higher-order approximations,

$$P_c \leq P_s^3/2\,.\tag{8.24}$$

The operational region of our source, where this approximation holds, is shown in Fig. 8.5(b). This reduced boundary is the efficient QNG witness we will use to characterize our trapped-ion photon-source in the next section.

8.3   QNG photons from a trapped-ion source

Because our trapped-ion photon-source is low noise, it beats the QNG threshold despite substantial attenuation. The performance of our red-triggered source (see Sec. 7.6) in a HBT experiment is compared to the classical and Gaussian boundaries in Fig. 8.5(b). The source is prepared in a mixture of $5D_{3/2}$ states so that 493 nm photons may be emitted by triggering with a 652 nm pulse. The magnetic field is oriented perpendicular to the detection axis, such that confocal lenses map the two $6P_{1/2} \rightarrow 6S_{1/2}$ π transitions to uniform $\hat{\mathbf{H}}$ polarized fields. The probabilities of success and coincidence events $P_{s,c}$ are determined in a 200 ns detection window from the beginning of the photon trigger. Data is shown for weak and bright trigger pulses, where trigger intensity increases efficiency at the cost of coherence. Each measurement is between 20 and 180 minutes of operation at 200 kHz repetition rate depending on the time required to collect a statistically significant number of coincidence events. P_c and P_s are conservative estimators of the true probabilities [281], given the measured probabilities and an effective beam splitter transmittance $T = 0.495(5)$ that includes all detection imbalances.

Red circles show the source measured in the reflected configuration, in which a distant mirror recombines the two collimated fields to a single polarization-filtered mode as described in Sec. 7.1. Even without interference enhancement, the trapped-ion source beats the QNG threshold by 6 standard deviations, Fig. 8.5(b)(red circles). Performance is limited solely by the overall single-photon collection efficiency and detector dark counts. A perfect, but attenuated, single-photon source measured with the same APDs and a

(a)

(b)
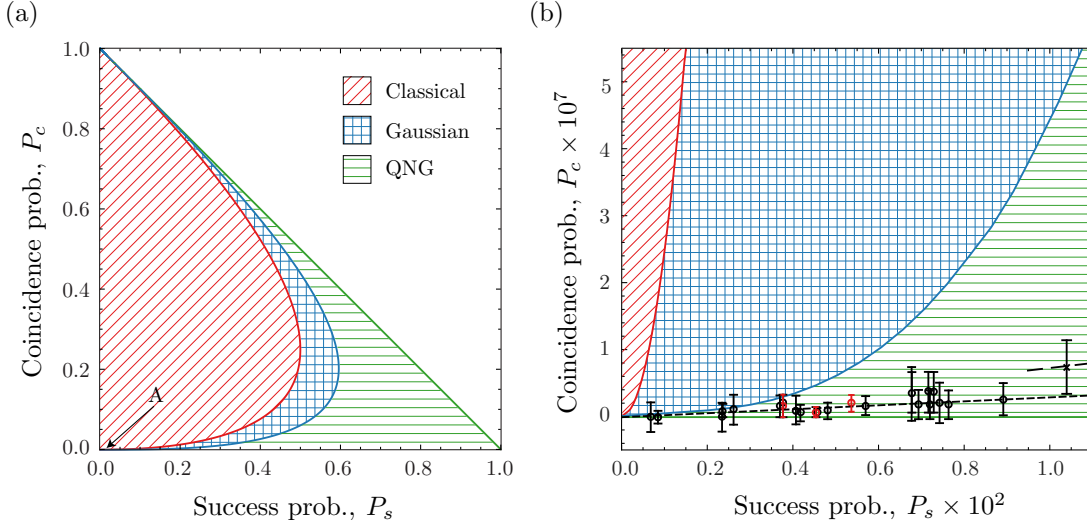
Figure 8.5: Coincidence probability P_c versus success probability P_s (a) over the complete probability space and (b) in the operational region of our source (arrow A). Classical light coincidence rates cannot be reduced below the NC threshold (red diagonal) and Gaussian light fields are similarly restricted to coincidence rates above the QNG threshold (blue hatched). Light fields with coincidence rates beyond this threshold (green horizontal) are unambiguously QNG. Circles correspond to measurements of our red-triggered single-photon source in the reflected (red) and symmetric (black) configuration with a 200 ns detection window. The black cross is a measurement under optimal conditions with a 500 ns detection window. Error bars indicate 95% confidence intervals. The performance of an ideal single-photon source measured with our APDs is shown for 200 ns (dotted line) and 500 ns (dashed line fragment) detection window.

200 ns detection window will perform according to the dotted line in Fig. 8.5(b), which is consistent with the measured data. This result confirms the single-photon purity of our trapped-ion photon-source. However, we must also be confident that we can maintain number-purity as the collection efficiency is improved.

The typical approach to improving collection efficiency from low-efficiency single photon emitters employs combinations of high numerical aperture optical elements [111, 116, 253, 282–284]. This corresponds to simultaneous emission of a light field into several spatial modes. Such a multi-mode source is useful so long as the purity of emitted single-photons is not compromised. Simultaneous enhancement of spurious background light collection, spatial restrictions on excitation beams, excitation beam scattering into the photon collection modes and other processes could make enhancing collection efficiency a source of additional photon-number noise. To estimate this effect, we measure the same QNG witness for a light state emitted coherently by a single-photon source into two spatial modes.

We apply this measure to our trapped-ion photon-source configured symmetrically according to Fig. 8.6. The fluorescence is detected in two spatial directions by fibre-coupled APDs positioned behind confocal HALOs. In the reflected configuration, the collected photons were combined into the same spatial mode prior to detection. In the symmetric setup they are emitted into two, in principle independent, directions. As demonstrated in [254, 255], ion fluorescence emitted in two opposite directions remains phase coherent and can be efficiently transferred into a single spatial mode, for example by recombination on
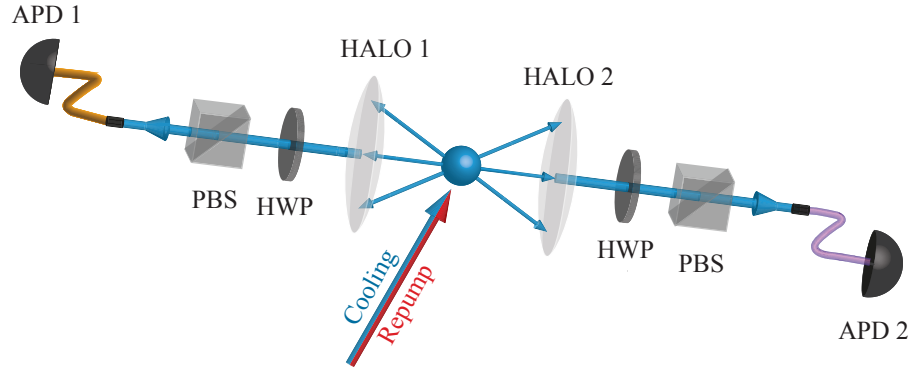
Figure 8.6: In the 'symmetric' configuration fiber-coupled APDs sample separate spatial and polarization modes from opposite sides of the ion simultaneously.

a beamsplitter. The single ion in the symmetric configuration thus comprises both the emitter and perfect unitary beamsplitter of the typical HBT measurement configuration. The QNG measurements presented for our source emitting into a single spatial mode can be compared to a two-mode coincidence measurement evaluated to yield the same measure.

Measurements made in the symmetric configuration with a detection window of 200 ns, Fig. 8.5 (black circles) suggest that fluorescence collected across two modes remains very close to an ideal single-photon Fock state, more than 20 s.d. from the QNG threshold. Optical losses are lower in this configuration and the fibre coupling is more efficient, improving end-to-end efficiency $\eta = 0.0089$. Increasing the detection window to 500 ns, Fig. 8.5 (black x), further improves the efficiency to $\eta = 0.0104$ compared to the expected end-to-end efficiency limit (see Sec. 7.6.1) of

$$\eta^\pi \quad = \eta_G^\pi \eta_I^\pi \eta_c^\pi \eta_d \tag{8.25}$$

$$= 0.023\,, \tag{8.26}$$

albeit with commensurate increase in coincidence rate. In combination these measurements suggest that the only noise source present is the detector dark count rate and that the field from our source is certifiably QNG for up to 24 dB of attenuation. This is the 'QNG depth' of our source.

8.4   Comparing QNG photon sources

Although most single-photon sources that we reviewed in Chap. 7 have not been explicitly compared to a QNG threshold, it is possible to infer QNG from the reported source efficiency. Several cutting-edge sources are plotted against the QNG threshold in Fig. 8.7. Of these the three photon sources in Ref. [279] merit specific comparison to our source (black circles). In this paper the authors optimize quantum dot and SPDC photon-sources for QNG depth, and test the performance under attenuation as we did above for the trapped-atom source. Fig. 8.7 includes the attenuation models (dashed lines) of these low-noise sources alongside the performance of our trapped-ion photon-source (dashed black line).

Although above-band excitation is too noisy to achieve substantial QNG depth with a quantum dot photon-source (green squares), resonantly driven quantum dots (purple squares) have narrowly beaten the QNG limit with a similar depth to our source. The
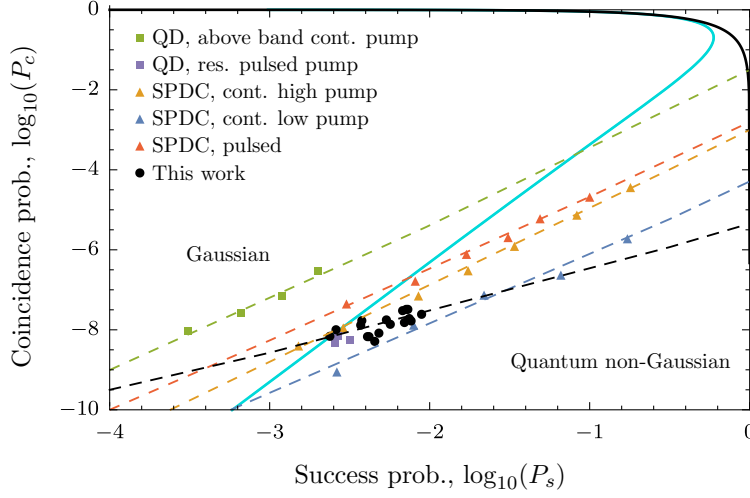
Figure 8.7: Success probability P_s and coincidence probability P_c of various photon sources compared to the QNG threshold (solid cyan line) on a log-log scale. Attenuation models (dashed lines) are shown where QNG depth tests have been performed for a given source. The boundary $P_s + P_c = 1$ is shown in black. All other sources from Ref. [279].

measurement was limited by a detector dark count rate that was large compared to the collection efficiency of the source [279, 285] and it was not possible to measure how the performance of the source scaled with attenuation. Attenuation tests performed with the above-band source show intrinsic noise that scales quadratically with P_s.

A clearer QNG state violation has been demonstrated for both pulsed and continuously driven spontaneous parametric down conversion (SPDC) sources. The SPDC source in Refs. [279, 281] is pumped continuously (cw) to produce photons probabilistically with herald efficiency P_s in a 2 ns detection window. At very low pump powers (blue triangles), the QNG depth is the largest yet reported for any source. As pump power is increased (yellow triangles) QNG depth decreases. A pulsed SPDC source in Ref. [286] (red triangles) is unable to outperform cw sources of the same heralding efficiency without multiplexing [287]. Compared to these SPDC sources, detector dark counts are two orders of magnitude higher at the bandwidth of our source and limit the measurable QNG depth. However, at any gain SPDC is intrinsically multi-photon. In the above measurements the coincidence rate P_c is substantially above the dark-count contribution, and P_c scales faster than proportionally with P_s.

8.5 Summary

We derived an efficient QNG witness for HBT experiments and applied this test to our trapped-atom photon-source. In both symmetric and reflected configurations, and for a wide range of trigger-pulse powers, the trapped-ion photon source produces a pulsed light field with coincidence rates indistinguishable from an ideal attenuated single-photon Fock state measured with our detectors, see Fig. 8.5(b - dashed line). Even the low efficiency source presented here is demonstrably QNG, the first such demonstration for a trapped-atom photon-source, and therefore sufficient for secure QKD [273]. Although trapped atoms are a spectrally bright source of indistinguishable photons and have already been used in rudimentary quantum networks [190, 207, 288] it remains to be seen whether they

can be coupled efficiently to network links. However, our work suggests that efficient collection is possible across multiple spatial modes without any detriment to the single-photon number state. Our source has a comparable QNG depth to resonant quantum-dot sources, and although it is surpassed by very low gain SPDC, it scales favourably with efficiency compared to both these single-photon sources.

Bibliography - Quantum non-Gaussian photons

2. D. B. Higginbottom, et al., Pure single photons from a trapped atom source, *New J. Phys.* **18**, 93038 (2016).

68. G. Brassard, et al., Limitations on practical quantum cryptography, *Phys. Rev. Lett.* **85**, 1330–1333 (2000).

73. A. K. Ekert, Quantum cryptography based on Bell's theorem, *Phys. Rev. Lett.* **67**, 661–663 (1991).

74. A. Acín, N. Gisin, and L. Masanes, From Bell's theorem to secure quantum key distribution, *Phys. Rev. Lett.* **97**, 120405 (2006).

111. R. Maiwald, et al., Collecting more than half the fluorescence photons from a single ion, *Phys. Rev. A* **86**, 043431 (2012).

116. E. W. Streed, et al., Imaging of trapped ions with a microfabricated optic for quantum information processing, *Phys. Rev. Lett.* **106**, 10502 (2011).

190. L. Slodička, et al., Atom-atom entanglement by single-photon detection, *Phys. Rev. Lett.* **110**, 083603 (2013).

207. S. Olmschenk, et al., Quantum teleportation between distant matter qubits, *Science* **323**, 486–9 (2009).

253. S. Gerber, et al., Quantum interference from remotely trapped ions, *New J. Phys.* **11**, 013032 (2009).

254. L. Slodička, et al., Interferometric thermometry of a single sub-Doppler-cooled atom, *Phys. Rev. A* **85**, 043401 (2012).

255. J. Eschner, et al., Light interference from single atoms and their mirror images, *Nature* **413**, 495–498 (2001).

266. S. Guha, et al., Rate-loss analysis of an efficient quantum repeater architecture, *Phys. Rev. A* **92**, 022357 (2015).

269. W.-Y. Hwang, Quantum key distribution with high loss: toward global secure communication, *Phys. Rev. Lett.* **91**, 057901 (2003).

270. Z. L. Yuan, A. W. Sharpe, and A. J. Shields, Unconditionally secure one-way quantum key distribution using decoy pulses, *Appl. Phys. Lett.* **90**, 011118 (2007).

271. R. Filip, and L. Lachman, Hierarchy of feasible nonclassicality criteria for sources of photons, *Phys. Rev. A* **88**, 043827 (2013).

272. R. Filip, and L. Mišta, Detecting quantum states with a positive Wigner function beyond mixtures of Gaussian states, *Phys. Rev. Lett.* **106**, 200401 (2011).

273. M. Lasota, R. Filip, and V. C. Usenko, Sufficiency of quantum non-Gaussianity for discrete-variable quantum key distribution over noisy channels, *Phys. Rev. A* **96**, 012301 (2017).

274. A. Mari, and J. Eisert, Positive wigner functions render classical simulation of quantum computation efficient, *Phys. Rev. Lett.* **109**, 230503 (2012).

275. A. Lvovsky, et al., Quantum state reconstruction of the single-photon Fock state, *Phys. Rev. Lett.* **87**, 050402 (2001).

276. J. Park, et al., Revealing nonclassicality beyond Gaussian states via a single marginal distribution., *Proc. Natl. Acad. Sci. USA* **114**, 891–896 (2017).

277. J. Park, et al., Testing nonclassicality and non-Gaussianity in phase space, *Phys. Rev. Lett.* **190402**, 1–5 (2015).

278. L. Lachman, and R. Filip, Robustness of quantum nonclassicality and non-Gaussianity of single-photon states in attenuating channels, *Phys. Rev. A* **88**, 063841 (2013).

279. I. Straka, et al., Quantum non-Gaussian depth of single-photon States, *Phys. Rev. Lett.* **113**, 223603 (2014).

280. L. Lachman, L. Slodička, and R. Filip, Nonclassical light from a large number of independent single-photon emitters, *Sci. Rep.* **6**, 19760 (2016).

281. M. Ježek, et al., Experimental test of the quantum non-Gaussian character of a heralded single-photon state, *Phys. Rev. Lett.* **107**, 213602 (2011).

282. C. Kurz, et al., Experimental protocol for high-fidelity heralded photon-to-atom quantum state transfer., *Nat. Commun.* **5**, 5527 (2014).

283. G. Shu, et al., Efficient fluorescence collection from trapped ions with an integrated spherical mirror, *Phys. Rev. A* **81**, 042321 (2010).

284. R. Noek, et al., High speed, high fidelity detection of an atomic hyperfine qubit, *Opt. Lett.* **38**, 4735 (2013).

285. A. Predojević, et al., Efficiency vs. multi-photon contribution test for quantum dots, *Opt. Express* **22**, 4789–98 (2014).

286. A. Predojević, S. Grabher, and G. Weihs, Pulsed Sagnac source of polarization entangled photon pairs, *Opt. Express* **20**, 25022 (2012).

287. M. A. Broome, et al., Reducing multi-photon rates in pulsed down-conversion by temporal multiplexing, *Opt. Express* **19**, 545–550 (2011).

288. D. L. Moehring, et al., Entanglement of single-atom quantum bits at a distance., *Nature* **449**, 68–71 (2007).

Two-atom, single-photon interference

In the usual treatment of spontaneous radiation by a gas, the radiation process is calculated as though the separate molecules radiate independently of each other... This simplified picture overlooks the fact that all the molecules are interacting with a common radiation field and hence cannot be treated as independent.
— Robert H. Dicke, *Coherence in spontaneous radiation processes* (1954)

By increasing the number of atoms in our trap, we can begin to explore the collective optical properties of ensembles in the few-atom limit. Part III of this thesis concerns the interaction of light and large ensembles of neutral atoms, containing up to 10 billion atoms. The total number of atoms in these ensembles fluctuates, and the state of individual atoms is not precisely controlled. However, with a chain of trapped ions we can realize small ensembles of definite atom number, and manipulate the state of each atom individually. The collective interaction of entangled emitters is particularly interesting for its application to quantum networks.

Optical interactions with few-atom ensembles have been made possible by advances in isolating, controlling and efficiently coupling atoms. Previous work has relied upon the interaction between the ensemble and a resonator mode. Ref. [289] demonstrated how the collective interaction of two atoms within an optical resonator enhances the efficiency of a quantum interface. Ref. [290] considered the same effect with two superconducting qubits decaying into a shared microwave resonator. In this chapter, we demonstrate the single-photon emission pattern of a two-atom entangled state in free space, which shifts continuously between constructive and destructive interference as a function of path-length difference. In doing so, we take our first step from coupling single atoms to coupling atomic ensembles.

This experiment was proposed and carried out with Gabriel Araneda, and will be covered in some greater detail in his thesis as well as in our publication

[5] "**Interference of single photons emitted by entangled atoms in free space** G. Araneda, D. B. Higginbottom, L. Slodička, Y. Colombe and R. Blatt. *Physical Review Letters* **120**, 193603 (2018)

9.1 Preparing atom-atom entanglement

To study the emission pattern of an entangled state, we must first trap two ions according to Chap. 6 and then prepare an entangled state. As we discussed in Sec. 1.4.1, atoms in a common trap can be entangled by laser-mediated motional gates [54, 55]. Atom-light couplers can also be used to establish entanglement between atoms, even when they are in
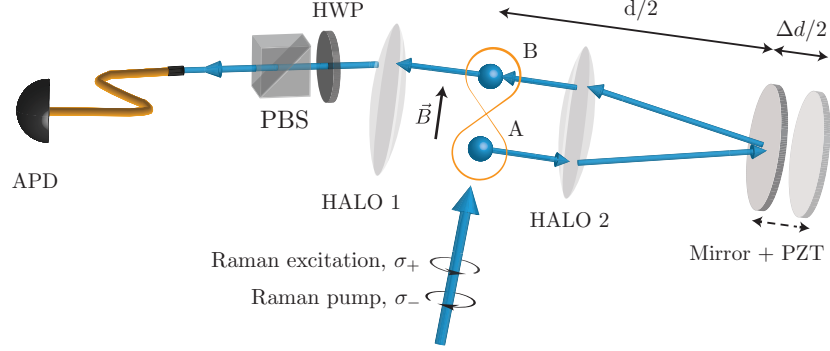
Figure 9.1: We couple two trapped ions via a shared optical mode. A high-aperture lens objective and remote mirror are aligned to superimpose the reflection of ion A over ion B. This common spatial mode is sampled by another high-aperture lens and an APD. The atoms are quantized perpendicular to the optical axis, and driven by orthogonal circularly polarized pump and excitation beams. The off-axis cooling and repump beams are not shown. Single-photon detection prepares the atoms in a bipartite entangled state. The mirror is mounted on a piezo so that the common-mode atom-atom distance d can be tuned between the entanglement operation and subsequent emission.

remote traps. Remote atoms have been entangled by the detection of coincident photons [288], and also by the detection of a single photon scattered into a common mode [190, 209].

Given that we already have the apparatus for coupling single photons out of our ion trap, we choose to entangle the two atoms by the scheme of Cabrillo [209], which was first demonstrated with this same apparatus [190]. The details of our entangling operation and verification are identical to this earlier work, so we provide only a cursory overview of these preliminary steps here.

Two atoms, A and B, are coupled indistinguishably to a common detection mode using the two high-aperture lens objectives (HALOs) and a remote mirror, as shown in Fig. 9.1. The atoms are first prepared in a ground state $|g\rangle$ by optical pumping, step one in Fig. 9.2. We then scatter a photon from the atoms by Raman excitation, exactly like operating the blue-triggered photon source in Sec. 7.3 and shown as step 2 in Fig. 9.2. We pump and excite with opposite circular beams at 493 nm and along the quantization axis and detect photons scattered into the common optical mode, which is perpendicular to the quantization axis and $\hat{\mathbf{H}}$ polarized. Photons in this mode are scattered almost entirely from π transitions (see Sec. 7.1). An atom that scatters a photon from the π transition is left in state $|s\rangle$ and goes dark. This is the origin of the photon-number purity in our blue-triggered single-atom single-photon source.

Now that we have a second atom in the trap, and coupled to the same spatial mode, detected photons could come from either atom. Detecting a single 'herald' photon from the two-atom system therefore projects the atom onto the entangled state[190]

$$|\psi\rangle = \frac{1}{\sqrt{2}} \left(|g,e\rangle + e^{i\phi} |e,g\rangle \right), \tag{9.1}$$

which is an equal superposition of every permutation of a single excitation over our two-
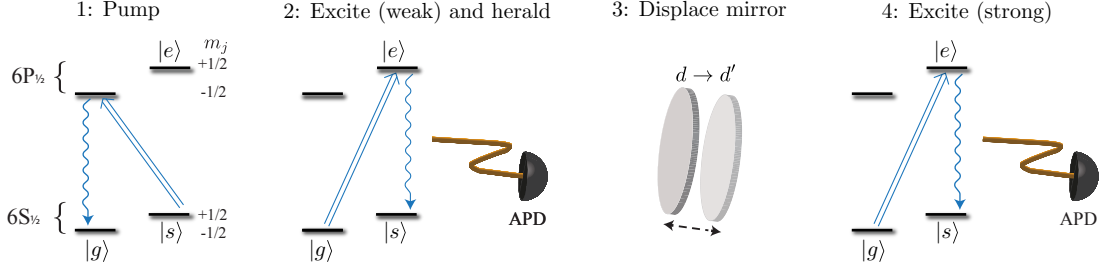
Figure 9.2: Sequence for generating bipartite entanglement. Description in text.

atom ensemble. This is the simplest ($N = 2$) case of the general N-atom Dicke state [291]. Because we collect each photon with low efficiency, the probability of heralding this entangled state is

$$p_\psi = 2p_e(1 - p_e)\eta \,, \tag{9.2}$$

where p_e is the single-atom transition probability for our excitation pulse ($p_e \approx 1$ for our single-photon source in Chap. 7) and η is the total collection efficiency. The state $|ss\rangle$ is prepared with probability

$$p_{|ss\rangle} = 2p_e^2\eta \,. \tag{9.3}$$

Heralding a pure entangled state requires $p_\psi/(p_\psi + p_{|ss\rangle}) = 1$. There is therefore a trade off between heralding probability and state purity when the detection efficiency is low.

The excitation probability is controlled by tuning the pulse length. We operate with $p_e = 0.06 \pm 0.01$ which corresponds to excitation pulses of 48 ns length and 95 nW mean power. We therefore expect the herald to prepare the state $|\psi\rangle$ with 94% probability, but the corresponding success probability yields a very low success rate. We measure only 5 herald photons per second.

Detector dark counts also produce a false herald that prepares the state $|gg\rangle$ with probability proportional to the herald detection window. We perform population measurements of the two-atom state prepared by our herald by measuring fluorescence on the $6\,\mathrm{S}_{1/2} \leftrightarrow 6\,\mathrm{P}_{1/2}$ transition following shelving π pulses addressed to the $6\,\mathrm{S}_{1/2}, \mathrm{m_j} = -\frac{1}{2}$ ($|g\rangle$) $\leftrightarrow 5\,\mathrm{D}_{5/2}, \mathrm{m_j} = -\frac{5}{2}$ transition with the narrow linewidth quadrupole transition laser (see Sec. 6.4.2). The fluorescence rate is measured over a 500 μs detection window. An example count distribution with discrimination thresholds is shown in Figure 9.3.

We measure 3% of the population in $|gg\rangle$, 6% of the population in $|ss\rangle$ and 91% of the population in $|\psi\rangle$.

The phase of the entangled state

$$\phi = (\phi_{L_B} - \phi_{L_A}) + (\phi_{D_B} - \phi_{D_A}) \tag{9.4}$$

has two components: the difference in excitation laser phase, and the difference in detection phase at the atom positions A and B. The detection path phase difference $\phi_{D_B} - \phi_{D_A} = kd$ where d is the path length difference from atoms A and B to the detector. We measure parity oscillations on the two atom state according to the method of Ref. [190] and estimate a fidelity $F = 0.65 \pm 0.02$ with state $|\psi\rangle$.

The fidelity is limited by the atom temperature. Photon scattering leaves a spatial phase on the position distribution of the atoms. The worse localized the atoms, the better we can distinguish the location of the scattering event (atom A or B). Once again,
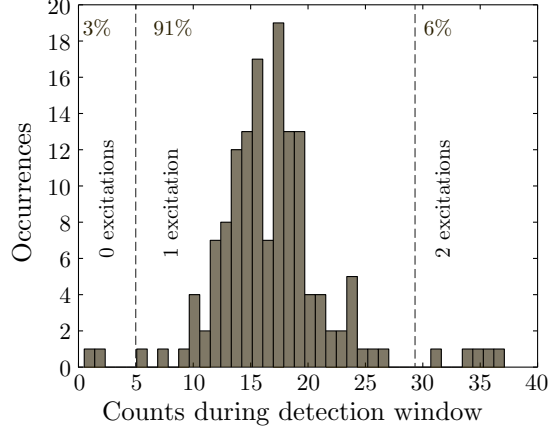
Figure 9.3: Measuring the number of excitations on the two-atom entangled state $|\psi\rangle$ by fluorescence rates. The ground state $|g\rangle$ is shelved outside of the cooling repump manifold with a narrowband π pulse (see text). The subsequent fluorescence rate under cooling and repump beams corresponds to the total number of excitations in state $|\psi\rangle$. The ideal $|\psi\rangle$ has only a single excitation.

ground-state cooling significantly reduces this effect, but sideband cooling reduces the source repetition rate by a factor of 100 and the repetition rate of our measurement drops commensurately.

9.2 Spatial interference

Now that we have prepared our entangled state, we may investigate its optical properties. We scatter a second photon from the entangled pair by a second excitation pulse, step 4 in Fig. 9.2. This time our excitation probability can high and we choose $p_e = 0.80 \pm 0.02$. After the second scattering event, the joint atom-photon system is

$$\left|\psi'\right\rangle = \frac{1}{\sqrt{2}} \left(|0,1\rangle + e^{i(\phi - \phi')} |1,0\rangle\right) \otimes |s,s\rangle \; , \tag{9.5}$$

where the photon states $|0,1\rangle$ and $|1,0\rangle$ correspond to a photon in the emission mode of atoms A and B, respectively, and ϕ' depends on the exciting laser phase and path length difference $\phi' = \left(\phi'_{L_B} - \phi'_{L_A}\right) + \left(\phi'_{D_B} - \phi'_{D_A}\right)$. Detecting a photon in a mode where atoms A and B are indistinguishable projects the state $|\psi'\rangle$ to

$$\left|\psi'_p\right\rangle = \frac{1}{\sqrt{2}} \left(1 + e^{i\phi - \phi'}\right) \otimes |s,s\rangle \; . \tag{9.6}$$

The photon detection probability is therefore

$$P \propto \left|\langle\psi'_p|\psi'_p\rangle\right|^2 = 1 + \cos\left(\phi - \phi'\right) \; . \tag{9.7}$$

The probability of detecting a photon scattered from $|\psi\rangle$ in a common mode depends on the entanglement phase ϕ and the observation phase ϕ'. At an observation point a distance $d \gg \lambda, \mathbf{r}_B - \mathbf{r}_A$ from the atom pair the spatial modes are indistinguishable. The atom-atom entanglement therefore causes a spatial interference pattern in the detection probability of photons scattered from $|\psi\rangle$, enhancing the detection probability when $\Delta\phi = \phi - \phi' = 0$
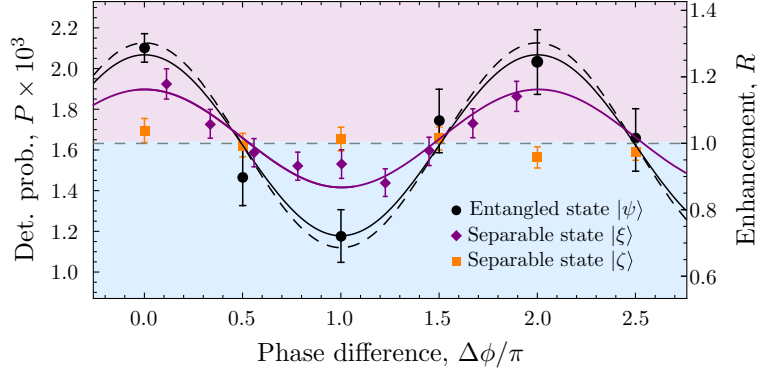
Figure 9.4: Interference fringe in the spatial mode of single photons scattered from the entangled state $|\psi\rangle$ (black), the single-excitation separable state $|\zeta\rangle$ (orange) and the maximum-interference separable state $|\xi\rangle$ (purple). $|\psi\rangle$ and $|\xi\rangle$ are shown with interference fringe fits (solid lines). The dashed grey line is the mean photon detection probability of $|\zeta\rangle$, and defines regions of enhanced (red) and suppressed (blue) emission. The dashed black line is the expected interference of $|\psi\rangle$ given the measured state preparation fidelity, and corresponds to the theoretical prediction $V = C$. Measurement by Gabriel Araneda.

and suppressing it when $\Delta\phi = \pi$. In particular the visibility of the interference fringes in radiation from a pair of two-level emitters with a single excitation should be equal to the concurrence of the bipartite quantum state [292, 293]. The concurrence is an entanglement monotone of the two-qubit state. Like the bipartite pure state entanglement

$$E(|\psi\rangle) = -\text{Tr}\rho \log_2 \rho \,, \tag{9.8}$$

where ρ is a partial trace over one of the subspaces, the concurrence is a measure of entanglement that varies from zero for a separable state to one for a perfectly entangled state.

This spatial interference pattern has not been measured before this work, the photon detection probability is simply too low to image the pattern directly. However, we can efficiently sample the same distribution with our near-confocal lens apparatus. By moving the mirror position as shown in Fig. 9.1 we tune the path length difference between atoms A and B in the common detection mode, equivalent to changing the position of detector in the spatial interference pattern.

Because the atom-mirror path length also appears in the Cabrillo entanglement phase ϕ, we must displace the mirror between the entangling and measurement steps, step 3 in Fig. 9.2. Assuming that the interatomic distance is fixed, the interference term is $\Delta\phi = k\Delta d$ where $\Delta d = d' - d$ is the path length change between entanglement and measurement. After receiving an entanglement herald we displace the mirror with a piezo in a time that depends on $\Delta\phi$. For $\Delta\phi/\pi = 2.5$ (the largest displacement we measure) the displacement time is $\tau = 220$ μs.

Figure 9.4 shows the detection probability P for several two-atom states as a function of the path length phase difference $\Delta\phi$. The maximum and minimum measured probabilities for the entangled state $|\psi\rangle$ are $P(\Delta\phi = 0) = (2.10 \pm 0.07) \times 10^{-3}$ and $P(\Delta\phi = \pi) = (1.17 \pm 0.12) \times 10^{-3}$. Fitting an interference fringe amplitude to the data gives a visibility of $V = 0.27 \pm 0.03$, consistent with the concurrence $C = 0.31 \pm 0.10$ calculated from our parity-reconstructed state and the prediction $V = C$ [292, 293].

For comparison, we measure the interference pattern of two separable states. These states are prepared by a combination of optical pumping, shelving to the $5\,\mathrm{D}_{5/2}, \mathrm{m_j} = -\frac{5}{2}$ Zeeman state with the 1.76 μm quadrupole transition beam, and global RF pulses on the $|g\rangle \leftrightarrow |s\rangle$ transition. The state $|\zeta\rangle = |e, g\rangle$ is the separable single-excitation state, corresponding to an excitation on a definite atom, A or B.

Scattering a photon under the same conditions used for $|\psi\rangle$ shows no dependence on the path length difference. The interference visibility is ≈ 0, consistent with the $C(|\zeta\rangle) = 0$ for a separable state. The single-photon detection probability $P(|\zeta\rangle)$ is used to define a relative detection probability $R = P/P(|\zeta\rangle)$, the right-side axis in Fig. 9.4. The constructive (destructive) interference enhancement (suppression) factor of the entangled state is $R_{\mathrm{sup}} = 1.29$ ($R_{\mathrm{sub}} = 0.72$). Because the states $|\psi\rangle$ and $|\zeta\rangle$ each contain a single excitation, we expect their mean detection probability over the entire emission mode to be equal, and indeed, the mean of the $R(|\psi\rangle)$ interference fringe is 0.99 ± 0.08.

Separable states with more than one excitation can also produce interference patterns. Single photons scattered from the most general bipartite state

$$|\beta\rangle = a\,|g, s\rangle + b\,|s, g\rangle + c\,|g, g\rangle + d\,|ss\rangle \ , \tag{9.9}$$

interfere with visibility

$$V_{|\beta\rangle} = \frac{2|ab|}{|a|^2 + |b|^2 + 2|c|^2} \ , \tag{9.10}$$

even though the state has concurrence $C_{|\beta\rangle} = 2|cd - ab|$. From Eqn. 9.10 we can see that even separable bipartite states with a mean excitation greater than one have an interference pattern; the rule $V = C$ holds only for $d = 0$. However the visibility of even general separable states is bounded by $V \leq 1/2$. We prepare the separable state

$$|\xi\rangle = \frac{1}{2}\left(|g\rangle + |s\rangle\right) \otimes \left(|g\rangle + |s\rangle\right) \qquad \left(a = b = c = d = \frac{1}{2}\right), \tag{9.11}$$

using global RF pulses. $|\xi\rangle$ maximizes the interference over the set of separable states. We observe an interference fringe visibility of $V_{|\xi\rangle} = 0.15 \pm 0.08$, also shown in Fig. 9.4. As expected, this is approximately half of $V_{|\psi\rangle}$.

9.3 Summary

We have demonstrated how interference between the entangled components of an atomic ensemble can selectively enhance or suppress single-photon emission into free-space modes. We prepared a bipartite entangled state by coupling two trapped ions to a common optical mode. The spatial interference pattern of our two-atom ensemble varies depending on the mean excitation, the degree of entanglement, and the path length difference between the two atoms and an observer. We detect photons from the ensemble with high aperture lens objectives and tune the path length difference using a remote, piezo-mounted mirror to measure the continuous interference pattern.

For bipartite states with a single excitation the interference visibility is equal to the concurrence. An interference measurement of this sort is therefore an entanglement witness for states with no $|ss\rangle$ component. In Part III we extend this theory to consider excitations that are distributed amongst many more than two atoms. As the number of atoms increases, emission from the entangled ensemble becomes increasingly directed [294]. In the many atom limit, such collective states are a means of efficiently and reversibly coupling

optical qubits into atoms, even without high aperture optics.

As with the previous chapters on our trapped-atom single-photon source, the success probabilities of both our photonic entanglement gate and second photon scattering event are limited dramatically by the collection efficiency of our high-aperture lens atom-light couplers. In the following chapters we turn our attention to a new strategy for efficiently coupling trapped atoms with single-pass optics and demonstrate some of the necessary components.

Bibliography - Two-atom, single-photon interference

5. G. Araneda, et al., Interference of single photons emitted by entangled atoms in free space, *Phys. Rev. Lett.* **120**, 193603–05 (2018).

54. J. I. Cirac, and P. Zoller, Quantum computations with cold trapped ions, *Phys. Rev. Lett.* **74**, 4091–4094 (1995).

55. A. Sørensen, and K. Mølmer, Quantum computation with ions in thermal motion, *Phys. Rev. Lett.* **82**, 1971–1974 (1999).

190. L. Slodička, et al., Atom-atom entanglement by single-photon detection, *Phys. Rev. Lett.* **110**, 083603 (2013).

209. C. Cabrillo, et al., Creation of entangled states of distant atoms by interference, *Phys. Rev. A* **59**, 1025–1033 (1999).

288. D. L. Moehring, et al., Entanglement of single-atom quantum bits at a distance., *Nature* **449**, 68–71 (2007).

289. B. Casabone, et al., Enhanced quantum interface with collective ion-cavity coupling, *Phys. Rev. Lett.* **114**, 023602 (2015).

290. J. A. Mlynek, et al., Observation of Dicke superradiance for two artificial atoms in a cavity with high decay rate, *Nat. Commun.* **5**, 5186 (2014).

291. R. H. Dicke, Coherence in spontaneous radiation processes, *Phys. Rev.* **93** (1954).

292. J. Suzuki, C. Miniatura, and K. Nemoto, Entanglement detection from interference fringes in atom-photon systems, *Phys. Rev. A* **81**, 062307 (2010).

293. T. Scholak, F. Mintert, and C. A. Müller, Entanglement witnesses from single-particle interference, *Europhys. Lett.* **83**, 60006 (2008).

294. M. O. Scully, and A. A. Svidzinsky, The super of superradiance., *Science* **325**, 1510–1 (2009).

Precise hemispheric mirrors

I am a plain, old-fashioned mirror from a bygone age, made of good white metal that stays clear without being polished... I am going to discuss serious matters now. Pay close attention, everyone.

$\qquad$ – Unknown, $\overline{O}$*kagami, the Great Mirror* (1119)

Useful quantum networks, be they large scale communication networks or distributed entanglement computing networks, require the efficient interaction of optical fields with material quantum systems. To reach the required efficiency, free-space atom-light couplers require optics with larger apertures than the lens objectives used in Chaps. 6 to 8. High precision, high numerical aperture mirrors are one means of mediating sufficiently strong atom-light coupling. In Chap. 4 we saw that the ideal mode converter for a point source emitting spherical waves is a deep parabolic mirror [118, 131]. This single-pass coupling approach requires high numerical aperture (NA) reflectors with sub-wavelength surface precision [111]. However the fabrication of high-NA mirrors with sufficient surface smoothness and form precision remains a technological challenge [295–297].

Whereas a parabolic mirror is the desired reflector for converting spherical waves into plane waves, a hemispheric mirror maximizes the self-interaction of a source by returning spherical waves from the source to their origin. The hemispheric mirror is an intriguing special case for high-NA atom-light couplers that bridges the gap between single-pass optics and cavity quantum electrodynamics. Like an optical resonator, a single hemispheric mirror may enhance atom-light interactions by shaping the vacuum mode density around an emitter, but unlike an optical resonator the hemisphere-mediated atom-light interaction is single-pass. It has been predicted [298] that the spontaneous emission rate of an atomic electron at the centre of curvature (CoC) of a spherical mirror may be suppressed or enhanced depending on the radius of the mirror, even when the mirror radius is much larger than the atomic wavelength. A previous attempt to measure such an effect with spherical optics measured emission rate fluctuations of 1% [255]. An ideal hemisphere that covers exactly half of the atomic emission solid angle will achieve the greatest possible modification, enhancing the spontaneous emission rate by a factor of two when the radius is $R = n\frac{\lambda}{2} + \frac{\lambda}{4}$ where n is a positive integer and λ is the transition wavelength, and completely suppressing spontaneous emission when the radius is $R = n\frac{\lambda}{2}$. Because deviations from an ideal hemisphere reduce the degree of suppression and enhancement, demonstrating this effect requires the fabrication of hemispheric mirrors with great surface precision.

The fabrication of ideal reference optics is also of interest to the broader optics community. The hemisphere retro-reflects an incoming spherical wavefront and could be used as a reference null for characterizing high-NA focusing optics [115]. Optical-reference microscopy requires reference surfaces considerably better than the surface to be measured.

The roundest manufactured objects are convex spheres made for NASA's Gravity Probe B rotors, which deviate by 17 nm from perfect spheres (peak to valley) [299, 300], closely followed by the Avogadro spheres, which are 89 nm from perfect [301, 302] [1]. Such outstandingly spherical spheres are produced by randomly rotating the sphere between two conical grinding/polishing tools for periods of several days. It is difficult to polish concave surfaces to comparable precision because no equivalent symmetric mounting process is possible, and there is an unmet demand for reference optics in this regime.

In this chapter we demonstrate the fabrication of highly-precise hemispheric mirrors. We diamond turn a nm-precise hemispheric mirror from an aluminium substrate and describe the challenges encountered when cutting such high NA concave optics. The mirror surface quality is verified by complementary measurements including single-shot optical interferometry with a reference sphere, multi-shot interferometry with a reference flat and contact probe measurements. We demonstrate the capacity to cut concave hemispheres that surpass the requirements for single-pass QED experiments, and characterize five consecutively manufactured mirrors as a test of consistency and reproducibility. The work in this chapter has been published as

[4] "**Fabrication of ultrahigh-precision hemispherical mirrors for quantum-optics applications** D. B. Higginbottom, G. T. Campbell, G. Araneda, F. Fang, Y. Colombe, B. C. Buchler, and P. K. Lam. Fabrication of ultrahigh-precision hemispherical mirrors for quantum-optics applications *Scientific Reports* **8**, 221 (2018)."

10.1 Diamond turning hemispheric mirrors

Single point diamond turning (SPDT) is an established tool for manufacturing ultra-fine optics with geometries accurate below optical wavelengths and smooth surface finishes. With SPDT it is possible to achieve both high material removal rates and low subsurface damage, making it an appealing technique for generating spheric and aspheric surfaces as well as rotationally asymmetric free-form elements for telescopes and head-up displays [296, 297, 303]. State-of-the-art diamond turning can produce low-NA optical surfaces 50 mm in diameter with peak-to-valley surface deviations of 150 nm [295] and local surface roughness below 0.4 nm [304]. This sub-wavelength precision has been utilized in quantum optics applications such as laser mode converters [305–307], monolithic microcavities [308], and other resonators [309].

We diamond turn hemispheres on a CNC nano-lathe, the Nanotech 250UPL from Moore Precision Tools, the configuration of which is shown in Fig. 10.1(a). The lathe has four precision controlled degrees of freedom: an aerostatic spindle that rotates the work-piece at 2,000 RPM around the spindle axis (C); two perpendicular linear axes (X and Z) for positioning the cutting tool and spindle on fully-constrained oil hydrostatic bearings; and an additional axis (B) that rotates the tool post on a groove-compensated air bearing. The final degree of freedom (Y) is the height of the cutting edge compared to the centre of the spindle, over which we have limited manual control. The X, Z, C and B axes are interferometrically stabilized with control resolution 1 nm (X, Z), 1 arc second (C, B) and feedback resolution 1 pm (X, Z), 0.01 arc seconds (C, B). The B axis rotates with radial and axial displacement error less than 50 nm over the full 360°, of which we require

---

[1]We understand from personal correspondence with the NMI and from the science media (see http://nautil.us/blog/the-most-symmetrical-objects-in-the-world) that the Avogadro project has since improved their spheres to within 25 nm (peak to valley) of perfect.
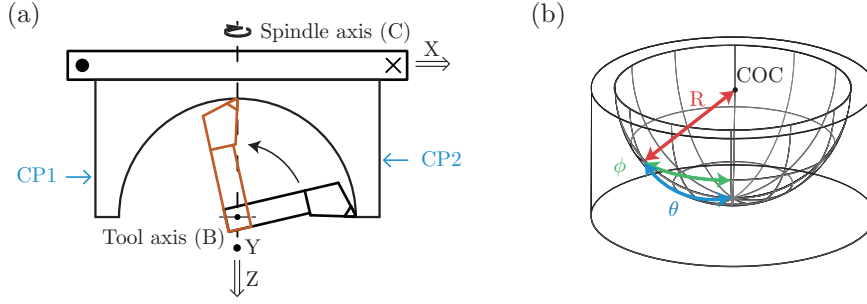
Figure 10.1: (a) Top view of the diamond turning lathe showing the two linear axes X and Z, two rotational axes B (tool) and C (spindle), and tool height axis Y (out of plane). The cutting tool is shown in its initial (black) and final (orange) position. Also shown are the counter-clockwise (CP1) and clockwise (CP2) contact points used for fine-calibrating the axes as described in the text. (b) Hemisphere with surface coordinate system: radial distance (r) from the centre of curvature (CoC), zenithal angle (θ) and azimuthal angle (ϕ).

90°. The Y axis is manually adjusted with μm resolution and not actively stabilized. The spherical coordinate system for the cut surface is shown in Fig. 10.1(b) with zenithal and azimuthal angles ϕ and θ related to the rotational axes B and C of the lathe respectively.

The hemispheres are cut from a cylindrical aluminium 6061 substrate with outside diameter 30 mm and height 13.5 mm. Because of their two-fold rotational symmetry, hemispheres may be cut by a single rotation of the B axis through 90° from the edge to the centre of the hemisphere, repeated at increasing depths by iterating the tool post towards the spindle along the Z axis. This technique uses a single point on the diamond tool edge to cut across the entire surface with two key consequences: the surface form is insensitive to the exact shape of the cutting tool edge, and the relative cutting force direction and magnitude is constant over the cut [310]. The mirror radius of curvature (RoC) is determined by the distance from the most remote point on the cutting tool edge to the B axis centre of rotation (R_c) and by the offset between the two rotating axes. We determine R_c by measuring the tool edge position as a function of B-axis angle with an optical microscope fixed above the lathe. In the limit of many measurements this approach should determine R_c to within 1 μm, although in practice we performed this calibration only to a measurement uncertainty of 10 μm.

10.1.1 Tool spiral

In contrast to the finely polished mirrors used for high-finesse cavities, SPDT produces a finished surface with a turning spiral that tracks the passage of the tool across the part. The groove spacing is $s = 2\pi \frac{\omega_B}{\omega_C} R_c$ where ω_B and ω_C are the rotational speed of the tool and spindle axes respectively. Assuming the mirror radius $R(\theta, \phi) \approx R_c$ is much larger than the tool edge radius r, the peak-valley height of the grooves h is $h = r - \sqrt{r^2 - (\frac{s}{2})^2}$. Together these parameters determine a minimum cut time

$$T_{min} = \frac{\pi R_c}{4\omega_C \sqrt{h_{\max}(2r - h_{\max})}} \tag{10.1}$$

for a surface with maximum groove height h_{max}. The time to cut a hemisphere with sub nm grooves in our case ($R_c = 12.4$ mm, $r = 0.6$ mm, $\omega_C = 2000$ rev/min) is 5 minutes.
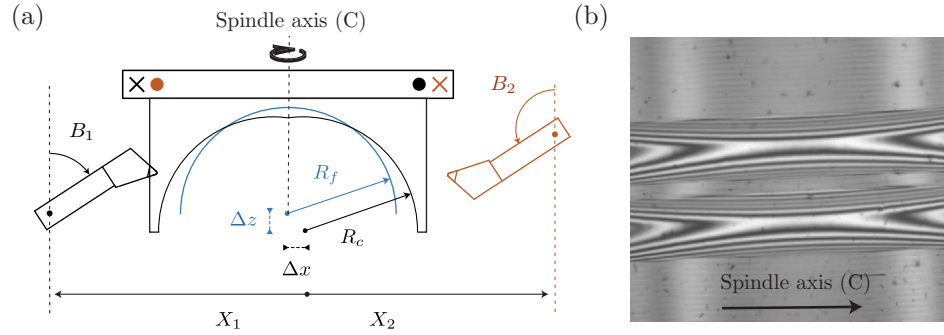
Figure 10.2: (a) Schematic of an exaggerated X-offset error profile and the corresponding calibration procedure as described in the text. The B-centre is offset from the C-centre by Δx and produces an aspheric surface (black). The spherical fit to this surface (blue) has RoC $R_f = R_c + \Delta R$ and CoC offset by Δz. To correct this X-offset we cut two grooves with the tool at positions $X_{1,2}, B_{1,2}$ where $X_2 = -X_1$ and $B_2 = 180° - B_1$. (b) A white-light interferogram showing two calibration grooves of equal depth.

It is feasible to cut mirrors larger than those demonstrated here (our lathe is capable of cutting mirrors with RoC up to 250 mm) so long as the temperature of the lathe environment is stable over the duration of the cut. Temperature variations of just 0.5 K are enough to significantly degrade form accuracy due to the thermal response of aluminium. At the other end of the scale, the mirror size cannot be made smaller than available diamond tool heads and so it would prove challenging to manufacture precise hemispheres with RoC < 1 mm by this technique.

10.2   Calibration error profiles

High-NA optics manufactured with SPDT are critically sensitive to the relative rest positions of the lathe axes. Any offset between the spindle rotation axis and the tool path symmetry axis causes a θ symmetric, ϕ dependent deviation that scales poorly with NA and quickly comes to dominate the error profile. When the X-axis is configured such that the rotational centres of the C and B axes are aligned, the B rotation cut describes a perfect circle with constant RoC. However when the C-axis centre is slightly past (before) the spindle centre C the tool will cut a slightly larger (smaller) radius and produce a distinctive radial error profile $r_e(\phi)$ with a single minimum (maximum) at the zenithal angle $\phi = 54.5°$.

10.2.1   X-offset error profile

During the cut the tool describes a near-perfect circle with radius R_c given by the distance from the cutting edge to the centre of rotation, limited by the radial and axial displacement of the lathe's B-axis over 90° rotation (both specified as less than 50 nm over 360°). However, the actual profile cut in the X-Z plane depends on the offset Δx between the tool rotation (B) axis and part rotation (C) axis (see Fig. 10.2a). In Cartesian coordinates the cut profile is

$$z_c = \sqrt{R_c^2 - (|x| - \Delta x)^2}\,. \tag{10.2}$$

We are interested in how closely this profile matches a circle with radius R_f and CoC displaced from the B-axis centre by distance Δz (the blue circle in Fig. 10.2(a)) given by

$$z_f = \sqrt{R_f^2 - x^2} + \Delta z \,. \tag{10.3}$$

To find the radial displacement between these two surfaces we transform the Cartesian curves z_c and z_f into radial profiles in spherical coordinates

$$r_c(\phi) = R_c \sqrt{1 - \frac{1}{2}\left(\frac{\Delta x}{R_c}\right)^2 (1 + \cos 2\phi)} + \Delta x \sin\phi \,, \tag{10.4}$$

$$r_f(\phi) = R_f \sqrt{1 - \frac{1}{2}\left(\frac{\Delta z}{R_f}\right)^2 (1 - \cos 2\phi)} + \Delta z \cos\phi \,. \tag{10.5}$$

In the limit $R_c, R_f \gg \Delta x, \Delta z$ the square-root terms approach one and the error profile, the difference between the cut and fit radial profiles, simplifies to

$$r_e(\phi) = r_f(\phi) - r_c(\phi) = \Delta R - \Delta z \cos\phi - \Delta x \sin\phi \,, \tag{10.6}$$

where $\Delta R = R_f - R_c$. We can integrate over the surface area of a sphere with $\mathrm{NA} = \sin\phi_a$ to find the RMS error

$$E_{\mathrm{RMS}} = \sqrt{\int_0^{\phi_a} r_e^2 \sin\phi \, d\phi / (1 - \cos\phi_a)} \,, \tag{10.7}$$

where the area element is weighted by $\sin\phi$ and the integral over θ yields a normalization factor $1 - \cos\phi_a$. For a complete hemisphere ($\mathrm{NA} = 1$, $\phi_a = \pi/2$) this reduces to

$$E_{\mathrm{RMS}} = \sqrt{\Delta R^2 + \frac{2}{3}\Delta x^2 + \frac{1}{3}\Delta z^2 + \frac{\pi}{2}\Delta x \Delta R + \Delta z \Delta R + \frac{2}{3}\Delta x \Delta z} \,. \tag{10.8}$$

The best-fit spherical surface is given by the parameters ΔR_{xfit} and Δz_{xfit} that minimize the RMS error for a given Δx

$$\Delta R_{\mathrm{xfit}}(\phi_a = \pi/2) = (\pi - 2)\Delta x \,, \tag{10.9}$$

$$\Delta z_{\mathrm{xfit}}(\phi_a = \pi/2) = \frac{1}{2}(3\pi - 8)\Delta x \,, \tag{10.10}$$

which are plotted in Fig. 10.3 (red and green lines) as a function of Δx. With these optimal parameters the radial error profile is

$$r_e = -\Delta x [(\frac{3\pi}{2} - 4)\cos\phi + \sin\phi + (2 - \pi)] \,. \tag{10.11}$$

This whole-hemisphere X-calibration error profile is plotted in Fig. 10.3(a) where the radial deviation from a perfect hemisphere is given as a function of the zenithal angle ϕ from the mirror centre. We will use this model to infer the residual offset of the finished hemispheres from their measured surface profile, and therefore the accuracy of our offset calibration technique.

We can calculate the RMS error and PV error from this profile (Fig. 10.3(b) black and
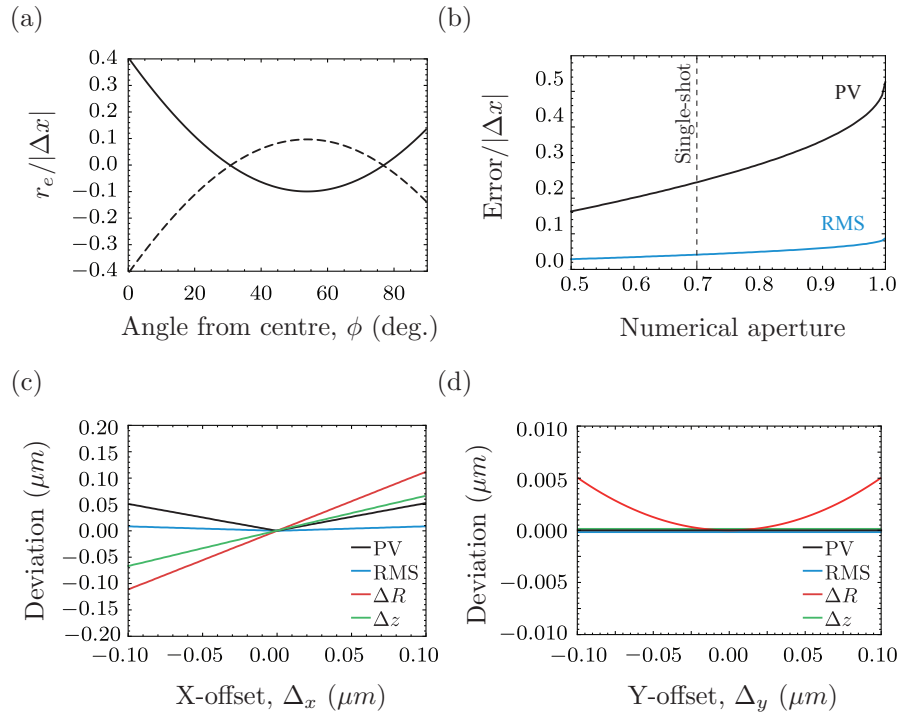
Figure 10.3: (a) Radial error r_e from a positive (solid) and negative (dashed) X-axis offset as a function of zenithal angle ϕ. (b) The PV (black) and RMS (blue) aggregate error of a surface with error profile r_e measured over a central region as a function of the aperture. (c and d) Form errors and fit parameters from an X-axis (c) and a Y-axis (d) offset. The PV error (black) and RMS error (blue) are proportional to the X-offset but insensitive to a Y-offset. In each case a spherical fit to the cut surface differs from the tool arc by a change in the RoC by ΔR (red) and CoC position shift Δz (green).

blue lines) to give an X-calibration error budget rule of thumb

$$E_{\mathrm{RMS}} = |\Delta x| \sqrt{\frac{3\pi(\pi - 4) - 8}{12}} \approx \frac{|\Delta x|}{11} \, , \tag{10.12}$$

$$E_{\mathrm{PV}} = \frac{|\Delta x|}{2}(8 - 3\pi + \sqrt{68 - 48\pi + 9\pi^2}) \approx \frac{|\Delta x|}{2} \, . \tag{10.13}$$

The above expressions are true for a complete hemisphere (NA = 1), but in general the best-fit sphere parameters ΔR_{xfit} and Δz_{xfit} depend on the numerical aperture of the surface section being measured. For a spherical surface with NA $= \sin \phi_a < 1$ the parameters ΔR and Δz that satisfy

$$\frac{\partial E_{\mathrm{RMS}}}{\partial \Delta R} = \frac{\partial E_{\mathrm{RMS}}}{\partial \Delta z} = 0 \tag{10.14}$$

are

$$\Delta R_{\mathrm{xfit}}(\phi_a) = \frac{\Delta x}{4} \csc^6 \left(\frac{\phi_a}{2} \right) \left(\frac{3\phi_a}{2} - \sin \phi_a + \sin 2\phi_a + \phi_a \cos \phi_a + \frac{\phi_a}{2} \cos 2\phi_a \right) , \tag{10.15}$$

$$\Delta z_{\mathrm{xfit}}(\phi_a) = \frac{\Delta x}{32} \csc^8 \left(\frac{\phi_a}{2} \right) \sin^2 \phi_a \Big(6\phi_a - 8 \sin \phi_a + \sin 2\phi_a \Big) , \tag{10.16}$$

which are very closely approximated by their first order Taylor expansions in ϕ_a about $\phi_a = 0$

$$\Delta R_{\mathrm{xfit}}(\phi_a) \approx \Delta x \left(\frac{8}{5\phi_a} + \frac{8}{105}\phi_a \right) , \tag{10.17}$$

$$\Delta z_{\mathrm{xfit}}(\phi_a) \approx \Delta x \left(\frac{8}{5\phi_a} - \frac{4}{21}\phi_a \right) . \tag{10.18}$$

By substituting these parameters into the general equation of the radial error profile, Eqn. 10.6, and integrating over the surface area as in Eqn. 10.7 we can find the aggregate errors over any measured NA as a function of the X-offset error profile. The RMS error and PV error as a function of the measured aperture are shown in Fig. 10.3(b). A partial measurement of the surface, such as the single-shot, high-NA interferometry measurements we perform, underestimates the total error. However, if the error is dominated by an X-offset, we may infer the total error from this model.

As a consequence of X-axis misalignment, the CoC position along the optical axis of the hemisphere is corrected to match the new best-fit RoC. Fig. 10.3c shows how the RoC, CoC, RMSE and PV error scale with the size of an X-axis offset.

10.2.2 Y-offset error profile

In contrast to the X-axis, the Y-axis lies outside of the plane of B-rotation, and makes no contribution to the final form of the mirror outside of a small central defect. A Y-axis offset Δy produces a circular defect at the centre of the mirror with corresponding radius Δy. This defect is either a cone or a pillar depending on the sign of Δy, and can be measured and corrected directly using the on-lathe white light interferometer. Example interferograms of Y-axis defects are shown in Fig. 10.4. Once the defect has been identified

(a)

Pillar

(b)

(c)

Cone

(d)

200 μm
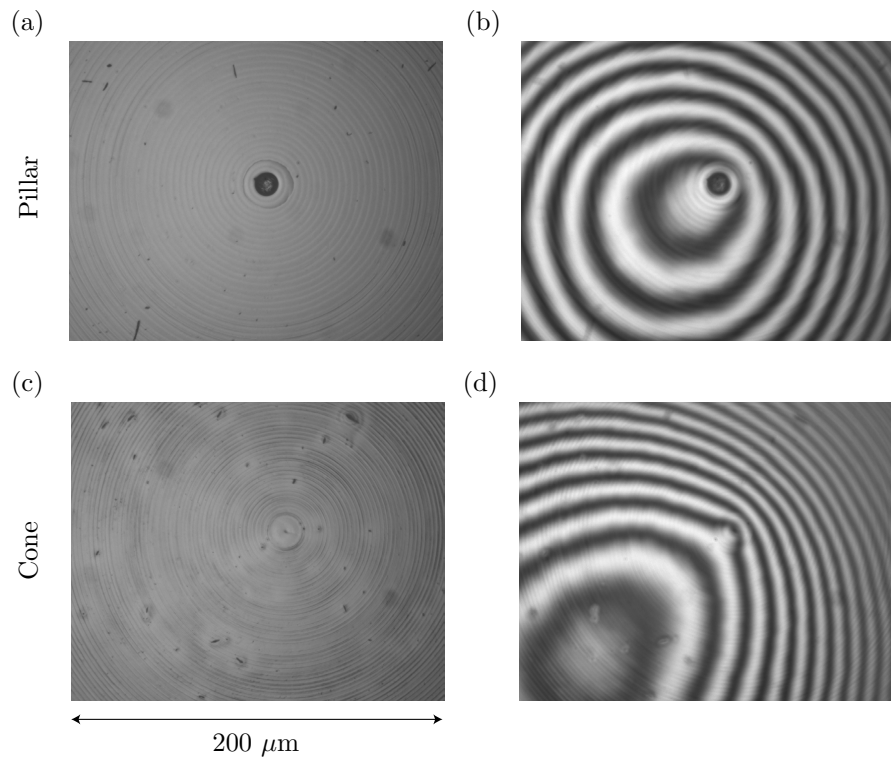
Figure 10.4: Central region of the hemisphere surface with Y-axis miscalibration defects. Tool below C-axis centre ($\Delta y < 0$) yields a pillar of uncut at aluminium with radius Δy and a jagged top, shown by (a) microscope image and (b) red-light interferogram. Tool above C-axis centre ($\Delta y > 0$) yields a cone with base radius Δy, shown by (c) microscope image and (d) red-light interferogram. The two interferograms show the curvature of the surface, which also contains a deep turning spiral.

and measured with the interferometer it can be corrected by an adjustment of the Y-axis. The small defect makes no contribution to the RMS error because it covers a negligible region of the surface.

Outside of the central defect, a Y-offset makes a small contribution to the final form by increasing the distance of the cutting edge to the centre of the C (part rotation) axis

$$r_c(\phi) = \sqrt{R_c^2 + \Delta y^2} \,. \tag{10.19}$$

In the limit $R_c \gg \Delta y$ this reduces to

$$r_c(\phi) = R_c + \frac{\Delta y^2}{2R_c} \,, \tag{10.20}$$

which is a spherical surface with RoC increased by

$$\Delta R_{\text{yfit}} = \frac{\Delta y^2}{2R_c} \,. \tag{10.21}$$

By the same logic we see that for a combination of X and Y offsets, and for any measurement aperture, the fit parameters from Eqn. 10.15 become simply

$$\Delta R_{\text{fit}}(\phi_a) = \Delta R_{\text{xfit}}(\phi_a) + \Delta R_{\text{yfit}}(\phi_a) \,, \tag{10.22}$$
$$\Delta z_{\text{fit}}(\phi_a) = \Delta R_{\text{xfit}}(\phi_a) \tag{10.23}$$

with no increase in the aggregate errors compared to an X-offset. This is illustrated in Fig.10.3(d) where a Y-offset results in a quadratic increase in the RoC but does not contribute to the aggregate error.

10.3 Interferometric calibration

To align the two rotational axes of the lathe, small calibration cuts are performed on the outer surface of the aluminium substrate. The cuts are performed on alternating sides of the the substrate, using alternating spindle rotation directions. Between each of the cuts, the B axis is rotated by 180° and, by measuring the depth of subsequent cuts, ΔX can be inferred.

The depth measurement is performed using a white-light interferometer that is mounted directly on the lathe. The instrument consists of a 20X Nikon Mirau interferometry objective mounted to a fixed-focal length video microscope with in-line white-light illumination. This in-situ surface metrology provides a depth resolution of 0.4 nm by fitting a complete interference fringe. To reduce the duration of the calibration procedure, however, we used a quick estimate of the relative cut depths by observing the fringe pattern while varying the position of the interferometer. This method provided a resolution of approximately 10 nm, which is sufficient to achieve our target form accuracy.

The offset Δx between the B and C axes centres is removed by an interferometric calibration process. Two 1 μm deep grooves are cut on the outer surface of the aluminum substrate with the tool at coordinates X_1, B_1 and X_2, B_2 shown in Fig. 10.2(a). The spindle rotation direction is reversed between the two positions. With coordinates $X_2 = -X_1$ and $B_2 = 180° - B_1$ the difference in depth between the two grooves is equal to $2\Delta x$. By measuring the depth difference we determine and correct the offset.

The depth of the grooves is measured with an in-situ white-light interferometer. The
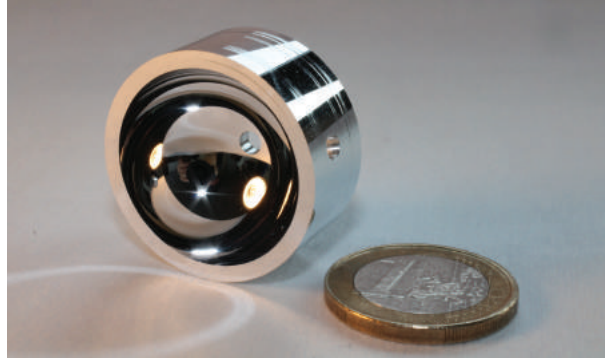
Figure 10.5: Hemispherical mirror, part E, with one Euro coin for scale. The mirror radius of curvature is 12.578(1) mm. This mirror was turned from a substrate with pre-drilled beam ports, which are visible in the photo. Also visible on the exterior surface of the mirror are shallow grooves cut during the lathe calibration process.

interferometer is fixed stably to the tool post in order to take advantage of the lathe axes' precise positioning control. Central-fringe identification provides a relative position measurement between the interferometer objective and the mirror surface. The X-axis displacement required to shift the central fringe from the bottom of one groove to the other is the depth difference between the two grooves. After shifting the centre position to $X_0' = X_0 + \Delta x$ the depth of two subsequent calibration cuts is equal. Fig. 10.2(b) shows an interferogram of two equal-depth calibration cuts made following an calibration step, the central maxima is simultaneously aligned with the bottom of both grooves.

Although the central-fringe maxima identifies the mirror surface position with sub-nm precision, and the lathe can be positioned with nm control precision, we infer from repeatability tests an alignment precision of 10 nm. This is consistent with the radial displacement error of the B-axis under rotation, which is specified as less than 50 nm. Furthermore, we expect additional uncertainty due to the difficulty of cutting under identical conditions at B_1 and B_2, from which we infer that the real radial uncertainty of B-rotation is less than 10 nm. This is the PV lower limit of hemispheres cut using this technique.

10.4   Surface interferometry

A finished hemisphere cut with the above technique is shown in Fig. 10.5. Two complementary interferometric measurements are used to verify the finished surface profile. The primary measurement is a large area surface profile by optical interferometry with a ZYGO interferometer. This measures the mirror surface against the optical wavefront produced by a reference sphere with PV error 20 nm. The size of the available reference sphere restricts these measurements to a NA of 0.7 (half angle 44.4°). To profile a complete mirror surface it is necessary to 'stitch' together separate scans that cover the entire surface, which requires at least eight scans of NA 0.7 [311]. However a single NA 0.7 interferogram taken at 45° to the optical axis of the hemisphere is sufficient on its own to measure the complete zenithal profile of an axially symmetric part, which is typically the largest component of the error profile of the hemispheres.

The partial profiles measured by reference-sphere interferometry are in agreement with stitched surface profiles taken by Meopta - optika. These complete surface profiles are

Part	Total form error		Zenithal form error		Azimuthal form error	
	PV	RMS	PV	RMS	PV	RMS
A	146.2	22.1	89.4	19.5	91.9	10.4
B	87.8	13.5	59.1	11.4	68.6	7.1
C	144.7	18.3	52.7	14.1	114.2	11.6
C*	215	27.4	47.5	14.2	207.7	23.4
D	317.3	51.2	219.4	44.7	193.2	23.0
E	116.5	18.1	76.2	15.8	73.8	8.7

Table 10.1: Comparison of five diamond-turned hemispheres, all quantities in nm. The total form error is the typical (RMS) and maximal (PV) radial deviation from an ideal hemisphere over the complete mirror surface. The zenithal profile (orange trace in Fig. 10.6) is used to separate the zenithal and azimuthal contributions to the form error.
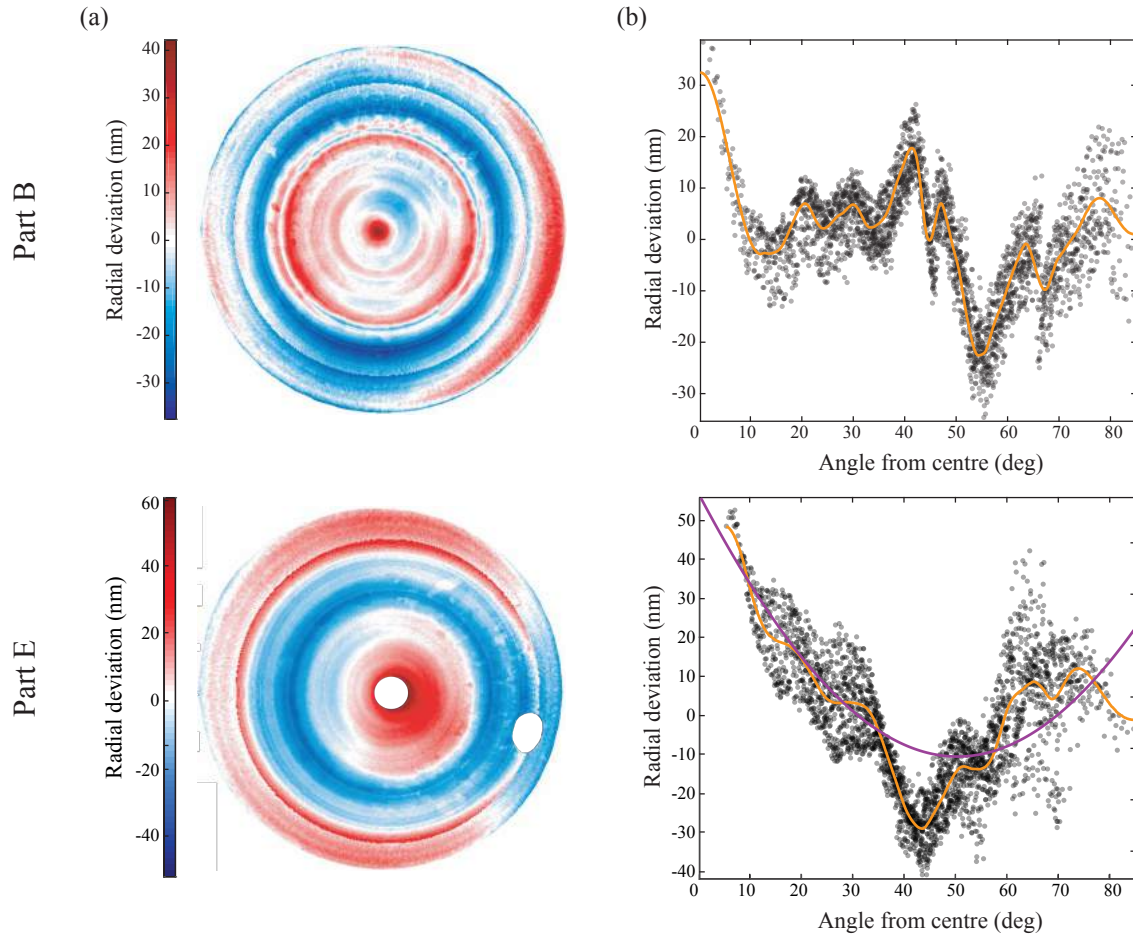
Figure 10.6: Surface detail of two hemispheric mirrors. (a) Radial error profile of part B as an azimuthal equidistant projection. The complete surface is reconstructed from stitched interferograms. (b) The radial error profile of part B as a function of zenithal angle (ϕ) with reduced resolution, every 40th pixel of the stitched interferogram is plotted. A Savitsky-Golay filter of the radial error (orange line) separates zenithal and azimuthal components. (c) Radial error profile of part E by the same method, the two beam ports are shown. (d) Radial error profile of part E as a function of zenithal angle including Savitsky-Golay filter (orange). The X-offset model e_r (purple) from Fig. 10.3(a) shows the contribution of an inferred residual X-offset $\Delta x = 150 \pm 10$ nm.

stitched from a hundred small interferograms taken against a reference flat. Two complete surface profiles are shown in Fig. 10.6(a) and (c). The circular density map is an azimuthal equidistant projection of the hemisphere onto the plane. Because the mirrors retain a degree of azimuthal symmetry it is illuminating to plot the same data as a function of zenithal angle ϕ to see the mean zenithal radius dependence, as shown in Fig. 10.6(b) and (d). For clarity these zenithal plots are shown with reduced resolution, every 40th pixel of the stitched interferograms is plotted. The scatter plot density scales with the value of the differential area element $dA/d\phi \approx \sin(\phi)$. A 3rd-order, 200 point Savitsky-Golay filter of the scatter plot separates the azimuthal and zenithal components of the form error. The zenithal radius function reconstructed in this way is consistent with contact probe measurements taken along an arc through the mirror centre.

10.5   Mirror surfaces

In Tab. 10.4 we compare five hemispheres. The results demonstrate the consistent fabrication of hemispheres with RMS error under 25 nm and as good as 14 nm. For each mirror the results are separated into zenithal and azimuthal components by the method described above. Parts A, B, C and D are consecutive attempts to cut the same hemisphere. Of these, part D is an outlier that is included for the sake of completeness. Its error profile indicates an abrupt and unusual shift in the position of the lathe during the cut that remains unexplained. Each profile features a peak at $0°$ as the cutting force vanishes towards the centre of the spindle that may be compensated by a progressive adjustment of the Z position over the final few degrees of the cut.

By fitting the X-offset model (Fig. 10.3(a)) to the measured surface profile we can infer the residual X-offset that remains after our on-lathe calibration technique. Part B, the best part yet measured, has a residual offset of 29 ± 3 nm, which accounts for only 20% of the total form error and which is largely spurious fitting to unrelated temperature fluctuations. However the typical residual offset is larger, as illustrated by the X-offset model fit to part E plotted in Fig. 10.6(d) which implies a residual offset of 150 ± 10 nm. Although this is the largest measured residual offset (excluding part D), the typical offset is considerably larger than the tolerance of the calibration process. The source of this shift, a gradual tilt due to a deflating vibration isolation airbag, has been identified and removed so that subsequent hemispheres should be more consistently similar to part B.

10.6   Experiment capability

In proposed QED experiments with hemispherical mirrors [298], a neutral or ionized atom would be confined to a region much smaller than the transition wavelength at the hemisphere CoC by either an optical or electromagnetic trap. In either case, UHV conditions are required to isolate the trapped atom from background collisions, and optical access from several directions is required for cooling. Two further measurements were made to test the suitability of these hemispheres for such experiments.

10.6.1   Bake-out test

Part C was measured before and after bake-out in vacuum as preparation for UHV experiments. As the temperature is increased and decreased, strains within the material substrate relax and produce volumetric changes that deform the spherical surface. These
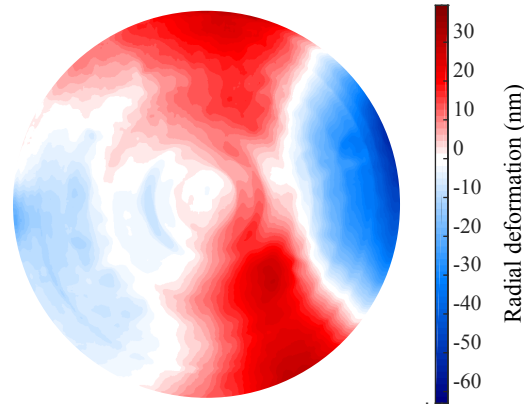
Figure 10.7: Deformation of part C during bake-out as an azimuthal equidistant projection.

strains may be due to the temper of the aluminium, or may be produced by the manufacturing process. To reduce this effect the mirror substrates are temperature cycled before the surface is turned on the nano-lathe, essentially undoing the material temper. All the parts presented here were cycled from room temperature to 300°C for one hour, three times before finishing.

The bake-out test was performed by heating part C to 200° C in vacuum for two hours. Table 10.4 and Fig. 10.7 compare the before and after measurements of the part. To produce Fig. 10.7 the after image is translated, rotated, and translated again until it has the maximum possible overlap with the before image. The residual difference is taken to be the distortion of the part. The final image is smoothed with a Gaussian filter (width 10 pixels) to remove artefacts of the fitting process. The bake-out induced deformation has distorted the surface by up to 60 nm, and the RMS error is correspondingly increased from 18.3 to 27.4 nm, an increase of 50%. This is a considerable distortion, although an order of magnitude smaller than the measured deformation of mirrors which were not temperature cycled before cutting.

10.6.2 Beam ports

Part E was cut to demonstrate the feasibility of diamond turning hemispheres from substrates with pre-drilled holes for beam ports. Proposed measurements with these hemispheres require on- and off-axis laser access to the mirror CoC through the mirror. Two beam ports with 3 mm diameter were drilled through the substrate of part E before the surface was lathed, one along the rotational axis and one at $\phi_{\text{port}} = 62°$ from the centre. The two ports are visible in the complete surface profile of part E in Fig. 10.6. The ports introduce cutting force variations visible at the zenithal angle of the port, and this degrades the form accuracy slightly as seen by comparing part E (RMS error 18 nm) to parts A, B and C (22, 14 and 18 nm).

10.7 QED experiments with spherical mirrors

10.7.1 Vacuum mode suppression

Part of our motivation for this work is to develop single-pass QED systems. Armed with detailed metrology of our surface quality we can now calculate how our mirror would

modify the emission of a dipole placed at the CoC. Following the plane-wave decomposition made in Ref. [298], the relative vacuum mode density ($\rho_r = \rho/\rho_0$) at position $\mathbf{r}$ is

$$\rho_r = \frac{1}{2\pi} \int \mathrm{d}\phi \, \sin(\phi) \int \mathrm{d}\theta \, (1 - \cos\left[2(kr_c(\theta,\phi) + \mathbf{k} \cdot \mathbf{r})\right]) \,, \qquad (10.24)$$

where $r_c(\theta, \phi)$ is the radial profile of the hemisphere. Fig. 10.8 shows how the relative vacuum mode density at the CoC ($\mathbf{r} = 0$) is altered by retro-reflection with spherical optics (dotted black line). The spontaneous emission rate of a dipole at the CoC is given by the same integral, weighted by the dipole emission profile as derived in Sec. 4.1. For a linear dipole perpendicular to the optical axis the relative spontaneous decay rate ($\gamma_r = \gamma/\gamma_0$) is

$$\gamma_r = \frac{3}{2\pi} \int \mathrm{d}\phi \, \sin(\phi) \int \mathrm{d}\theta \, \sin^2(\pi/2 - \phi) \, (1 - \cos(2kr_c(\theta,\phi))) \,. \qquad (10.25)$$

Whether this QED effect enhances or suppresses the vacuum mode density depends on the RoC. We do not, however, need to machine a hemisphere with an RoC calibrated to within a fraction of a wavelength. Like spheres, hemispheres expand uniformly about the centre of curvature. The coefficient of thermal expansion of aluminium 6061 at room temperature is 23.5×10^{-6} K^{-1} [312]. A temperature change of $0.42°$ K is enough to switch between enhancement and suppression of spontaneous emission at the focus of our mirror. So provided we achieve suitable form accuracy, the average radius can be actively tuned. The radius of the mirrors should be sufficiently tunable to scan over several spontaneous emission fringes. Resistively heating the mirror under the single-shot, white-light ZYGO interferometer shows tunability over the desired range, and no indication of surface distortion due to thermal expansion.

The key to a strong QED effect is maximizing the NA. The experiment of Ref. [255] used a multi-element lens and planar mirror combination with NA=0.4 (arrow a in Fig. 10.8). According to the model, the density of modes is reduced by 8% giving suppression of spontaneous emission by 24% at this NA. The highest NA lens one could realistically hope to use is about 0.7, limited by the geometry of the experiment. This point is shown by arrow b and reduces the density of modes by 30% and decay rate by by 65%. Our work has shown the machining of a spherical mirror with NA=0.996 (arrow c). The model allows us to include the reflectivity of aluminium (0.92 at $\lambda = 493$ nm [313, 314]) and the measured form error (Fig. 10.6) to predict the vacuum mode density dipole fluorescence enhancement, this is shown as a function of NA by solid lines in Fig. 10.8. Using the data for part B, we predict suppression of the density of modes and spontaneous emission rate of 88%. This figure is dominated by the reflectivity of the surface. A perfectly reflective surface with the same form error would give 96% suppression of mode density and emission. High-reflectivity surface coatings are one approach to improving reflectivity. Metallic coatings can improve on the reflectivity of aluminium at some wavelengths, and can be deposited over high-aperture surfaces without introducing substantial surface distortion. However, multi-layer dielectric coatings, which can be very close to perfectly reflective on low-aperture mirrors, require a higher degree of uniformity. Typical sputtering techniques are too directional to produce a high-reflectivity dielectric coating over a hemisphere.

10.7.2   Spatial mode shaping

In the above section we explored how ultra-precise hemispheric mirrors can be used to tune the overall mode density and spontaneous emission rate as proposed by Ref. [298].
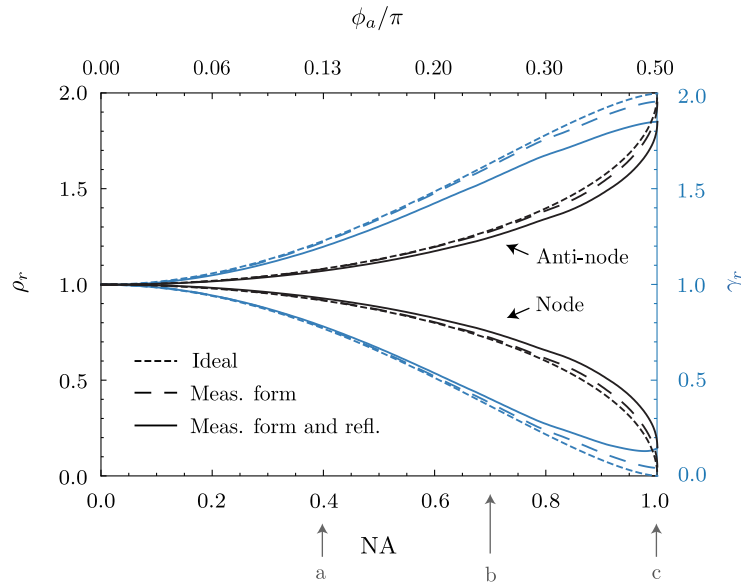
Figure 10.8: (black) Relative vacuum mode density ρ_r at the CoC of a spherical mirror as a function of NA (top axis shows the corresponding half-aperture in radians). The CoC is a node (anti-node) of the vacuum mode density at wavelength λ for $R = n\frac{\lambda}{2}$ ($R = n\frac{\lambda}{2} + \frac{\lambda}{4}$). (blue) The relative spontaneous emission rate γ_r of a linear dipole at the node/anti-node emitting at wavelength λ. Dotted lines are the result of an ideal spherical mirror [298], dashed lines are the result of a perfectly reflective sphere with the surface of part B (to a given NA), and solid lines are the same result including the known reflectivity of aluminium at λ=493 nm. Also shown are the NAs of (a) previous attempts to measure such an effect [255] (b) the best available diffraction-limited focusing optics and (c) this work. Considering its NA, reflectivity and form; part B is modelled to reduce or enhance both ρ and γ by 88%.
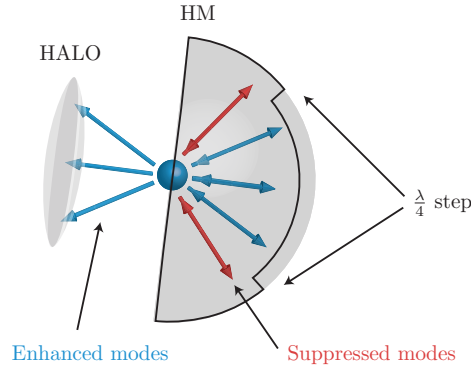
Figure 10.9: Illustration of the stepped-hemisphere mirror showing suppressed and enhanced modes.

We now turn to a novel extension of the same idea. Near-hemispheric mirrors may have an error profile r_e, by design, that preferentially enhances and suppresses some vacuum modes over others depending on the wave vector $\mathbf{k}(\theta, \phi)$. This, in turn, can be used to shape the spatial mode of an emitter at the mirror CoC, enhancing emission into chosen modes and suppressing others.

We shall consider first an illuminating example originated by Yves Colombe. An atom may be trapped at the CoC of a near-hemispheric mirror, and imaged by a lens with aperture half angle ϕ_a. The hemisphere differs from a perfect hemisphere, it has a $\lambda/4$ step at the same angle angle ϕ_a such that

$$r_c(\theta, \phi) = \begin{cases} \frac{n}{2}\lambda & \phi > \phi_a \\ \left(\frac{n}{2} + \frac{1}{4}\right)\lambda & \phi \le \phi_a \end{cases}. \tag{10.26}$$

As illustrated in Fig. 10.9, the step-hemispheric mirror surface suppresses emission into those modes outside of the collection angle of the lens, and enhances emission into the modes that are collected. In this way the mirror increases the collection efficiency beyond the covered solid angle, outperforming the dipole mode collection efficiencies derived in Sec. 4.3.1.

With only slightly more complexity, the near-hemispheric mirror surface can be tailored to produce a desirable optical mode in the imaging plane. Weighting the dipole mode (Eqn. 4.2) by the momentum distribution of the modified vacuum mode density (the integrand of Eqn. 10.24) and applying the spherical lens transformation (Eqn. 4.30) gives the image field distribution as imaged by a spherical lens. The spatial mode of a linear dipole at the mirror CoC, perpendicular to the optical axis, can be modified with the mirror profile shown in Fig. 10.10(a) to give a linearly polarized Gaussian mode that is smaller than readily available optics and can be efficiently manipulated and fibre-coupled. The asymmetric profile is shown along two cut sections at $\theta = 0, \pi$ where θ is the azimuthal angle from the dipole orientation.

As shown in Fig. 10.10(b), a large proportion of the natural emission must be suppressed to shape the dipole mode into a Gaussian mode. The free-space and modified mode intensities in the Fourier plane are shown along two cuts at $\theta = 0, \pi$ as a function of normalized radial distance ρ/f. The relative emission rate of the emitter in this configuration is only $\gamma_r = 0.22$. Any scheme that requires substantial suppression requires high
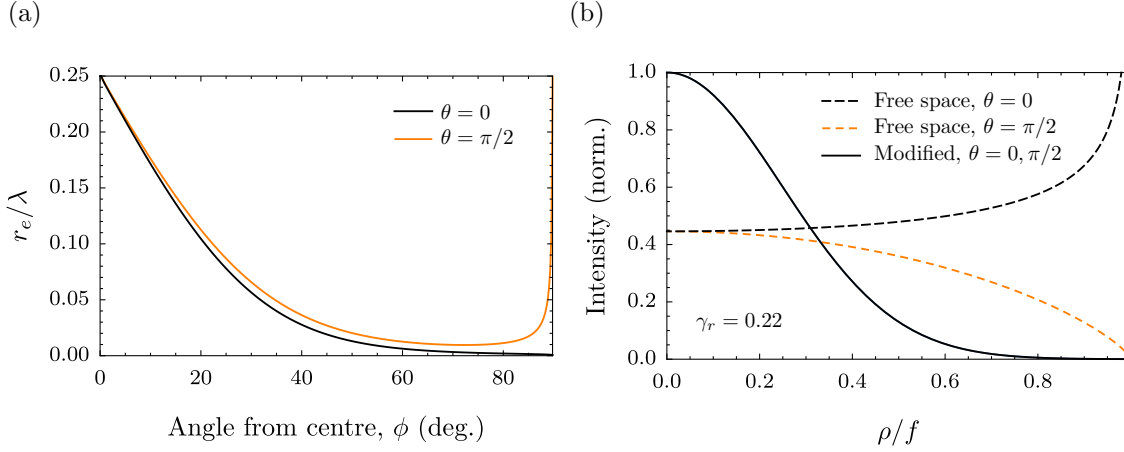
Figure 10.10: (a) The rotationally asymmetric mirror profile r_e yields a Gaussian mode from a linear dipole emitter at the CoC, oriented perpendicular to the optical axis. (b) Intensity profiles of the free-space and mirror-modified Fourier plane field distributions, as collimated by a spherical lens. The unmodified distribution is the same as the perpendicular linear dipole collimated by a spherical lens shown in Fig. 4.7(c). The intensity is shown along two cut sections at $\theta = 0$, π as a function of normalized radial displacement ρ/f. The modified profile is a Gaussian, and therefore rotationally symmetric. The mirror profile width has been chosen such that the Gaussian mode can be collected efficiently by realistic high-aperture lenses. The relative spontaneous emission rate of the modified dipole is $\gamma_r = 0.22$.

reflectivity surfaces, and will be sensitive to imperfections in the mirror profile. Given the demonstrated reflectivity and precision of the diamond turning technique developed in this chapter, if the same process were used to produce the mirror profile in Fig. 10.10(a), we could realistically expect the dipole to emit into the Gaussian mode with total two-sided, single-mode efficiency $\eta = 0.72$, substantially outperforming the single-mode collection efficiency of the NA = 0.7 spherical lens on its own (see Sec. 4.7) and in a more convenient spatial mode. With high-reflectivity mirrors it becomes feasible to efficiently couple emitters to even smaller Gaussian modes. In the extreme limit, this mode-shaping technique is an atom-light coupling approach that could efficiently couple trapped atoms to paraxial photons, what we might call 'paraxial atoms', without the need for deep parabolic mirrors or high-NA lenses.

10.8 Summary

We have demonstrated the fabrication of high-NA hemispheric optics for quantum optics experiments and metrology by single-point diamond turning. Our best sample achieves NA = 0.996, PV error 88 nm and RMS error 14 nm. These deviations from spherical are within a factor of five of the roundest manufactured spheres [300, 302], even without polishing. This accuracy meets the requirements for experiments that seek strong single-pass atom-light coupling. An ideal hemispheric mirror can reduce the vacuum mode density, and therefore the atomic fluorescence rate of an atom at the mirror CoC, to zero [298]. Our best mirror (part B) is close enough to spherical to reduce or enhance the vacuum mode density by 96%. With this degree of reservoir engineering it is possible to investigate QED effects with free space optical modes, and tune the emission spectra and spatial mode of emitters at the mirror CoC. We derived mirror profiles that enhance the

collection efficiency of a given lens, and shape the atomic dipole image into a Gaussian mode.

Four consecutively cut hemispheres demonstrate that this technique reliably produces surfaces with RMS error below 25 nm and further measurements show the suitability of these mirrors for proposed experiments, with the capacity to turn a comparable surface over a substrate with pre-drilled beam ports and minimal disturbance by bake-out for use in UHV. A crucial part of our setup was the development of an on-lathe white-light interferometer that was applied to measure a series of calibration cuts made immediately before the precision machining of a mirror. This calibration process has made possible the production of hemispheric reference surfaces with precision previously feasible only for reference flats and could be applied similarly for the diamond turning of high-NA parabolic and axially asymmetric reflectors and optics.

Bibliography - Precise hemispheric mirrors

4. D. B. Higginbottom, et al., Fabrication of ultrahigh-precision hemispherical mirrors for quantum-optics applications, *Sci. Rep.* **8**, 221 (2018).

111. R. Maiwald, et al., Collecting more than half the fluorescence photons from a single ion, *Phys. Rev. A* **86**, 043431 (2012).

115. S. Inoué, Characterizing high numerical aperture microscope objective lenses, in *Optical imaging and microscopy: Techniques and advanced systems*, edited by P. Török, and F.-J. Kao, (Springer Berlin Heidelberg, 2003).

118. M. Sondermann, et al., Design of a mode converter for efficient light-atom coupling in free space, *Appl. Phys. B* **89**, 489–492 (2007).

131. N. Lindlein, et al., A new 4π geometry optimized for focusing on an atom with a dipole-like radiation pattern, *Laser Phys.* **17**, 927–934 (2007).

255. J. Eschner, et al., Light interference from single atoms and their mirror images, *Nature* **413**, 495–498 (2001).

295. H.-S. Kim, et al., Fabrication of free-form surfaces using a long-stroke fast tool servo and corrective figuring with on-machine measurement, *Int. J. Mach. Tools Manuf.* **49**, 991–997 (2009).

296. H.-S. Kim, E.-J. Kim, and B.-S. Song, Diamond turning of large off-axis aspheric mirrors using a fast tool servo with on-machine measurement, *J. Mater. Process. Technol.* **146**, 349–355 (2004).

297. G. Leuchs, et al., Interferometric null test of a deep parabolic reflector generating a Hertzian dipole field, *Appl. Opt.* **47**, 5570 (2008).

298. G. Hétet, et al., QED with a spherical mirror, *Phys. Rev. A* **82**, 63812 (2010).

299. J. Turneaure, et al., The gravity-probe-B relativity gyroscope experiment: Development of the prototype flight instrument, *Adv. Sp. Res.* **9**, 29–38 (1989).

300. C. W. F. Everitt, et al., Gravity probe B: Final results of a space experiment to test general relativity, *Phys. Rev. Lett.* **106**, 221101 (2011).

301. A. Leistner, and W. Giardini, Fabrication and testing of precision spheres, *Metrologia* **28**, 503–506 (1991).

302. B. Andreas, et al., Determination of the Avogadro constant by counting the atoms in a Si28 crystal, *Phys. Rev. Lett.* **106**, 030801 (2011).

303. Jannick P. Rolland, and Kevin P. Thompson, Freeform optics: Evolution? No, revolution!, *SPIE Newsroom*, 1–3 (2012).

304. E. R. Marsh, et al., Predicting surface figure in diamond turned calcium fluoride using in-process force measurement, *J. Vac. Sci. Technol. B* **23**, 84 (2005).

305. C. G. Blough, et al., Single-point diamond turning and replication of visible and near-infrared diffractive optical elements, *Appl. Opt.* **36**, 4648 (1997).

306. Y. Shen, et al., Generation and interferometric analysis of high charge optical vortices, *J. Opt.* **15**, 044005 (2013).

307. S. R. Mishra, et al., Generation of hollow conic beams using a metal axicon mirror, *Opt. Eng.* **46**, 084002 (2007).

308. A. Brieussel, et al., Squeezed light from a diamond-turned monolithic cavity, *Opt. Express* **24**, 4042 (2016).

309. T. Klaassen, M. van Exter, and J. Woerdman, Characterization of a Fabry–Perot resonator with diamond-machined mirrors, *Opt. Commun.* **275**, 385–388 (2007).

310. J. Drescher, and T. Dow, Tool force model development for diamond turning, *Precis. Eng.* **12**, 29–35 (1990).

311. R. Kershner, The number of circles covering a set, *Am. J. Math.* **61**, 665–671 (1939).

312. G. E. Totten, and D. S. MacKenzie, *Handbook of aluminum* (CRC Press, Boca Raton, 2003).

313. L. F. Mondolfo, *Aluminum alloys: structure and properties* (Butterworths, 1979).

314. D. Smith, E. Shiles, and M. Inokuti, The optical properties of metallic aluminum, in *Handb. Opt. Constants Solids* (Elsevier, 1997), pp. 369–406.

A new ion trap for high aperture optics

Visibility is a trap.
      – Michel Foucault, *Discipline and Punish: The Birth of the Prison* (1975)

The typical linear ion trap of the sort described in Chap. 6 is incompatible with high aperture optics, the trap electrodes simply obstruct too much of the solid angle for the ion to emit freely over a large aperture. In fact, the high-aperture lens objectives (HALOs) that we used to collect atomic fluorescence in Chaps. 7 and 8 are already at the limit of the optical clearance between the trap electrodes. This poses a problem not only for atom-light networks, the primary interest of this thesis, but also for trapped-ion quantum processors. In these processors qubit state readout is performed by a fluorescence measurement to separate bright and dark atomic states, with readout speeds limited by the atomic fluorescence rate and collection/detection efficiency.

To improve free-space coupling with trapped ions therefore requires specialized trap designs featuring improved optical access, as close as possible to the complete 4π steradian solid angle access for efficient atom-light coupling. Noteworthy ion traps designed for this purpose include the 'stylus' trap consisting of staggered concentric cylinders [315] and the 'tack' trap comprising needle, hemispheric mirror, and ring electrodes [316]. Planar traps, in which the electrodes lie on (or very close to) a single surface, are also a path to improved collection efficiency, although typically only one hemisphere of the ion's fluorescence is unobstructed [317]. Planar traps are now operating with collection lenses up to NA = 0.8.

In this chapter we introduce a new design for an ion trap to be used in combination with the hemispherical mirrors produced in Chap. 10 to perform free-space QED experiments of the sort described in Ref. [298]. It has a simple structure and allows collection of 69% of trapped-atom dipole fluorescence. Like the linear ion trap described in Chap. 6 and those used as trapped-ion quantum processors [42], it traps ions along a linear string with trapping frequencies sufficient for ion-ion motional gates.

11.1 Trap design

Low profile, point-like ion traps can be made with electrodes wrapped about a narrow cylinder, this is the philosophy behind the stylus ion trap of Ref. [315] and the tack trap of Ref. [316]. The ion is trapped at some distance from the stylus and the entire solid angle outside of the small portion obstructed by the stylus may be collected. However, point-like ion traps are not well suited to motional gates of the sort used in linear-trap quantum computers. Weaker axial trapping encourages trapped ions to form linear crystals along the axis of a two dimensional trap, however when multiple ions are loaded into a point-like trap they form an asymmetric three-dimensional crystal. It is impossible to
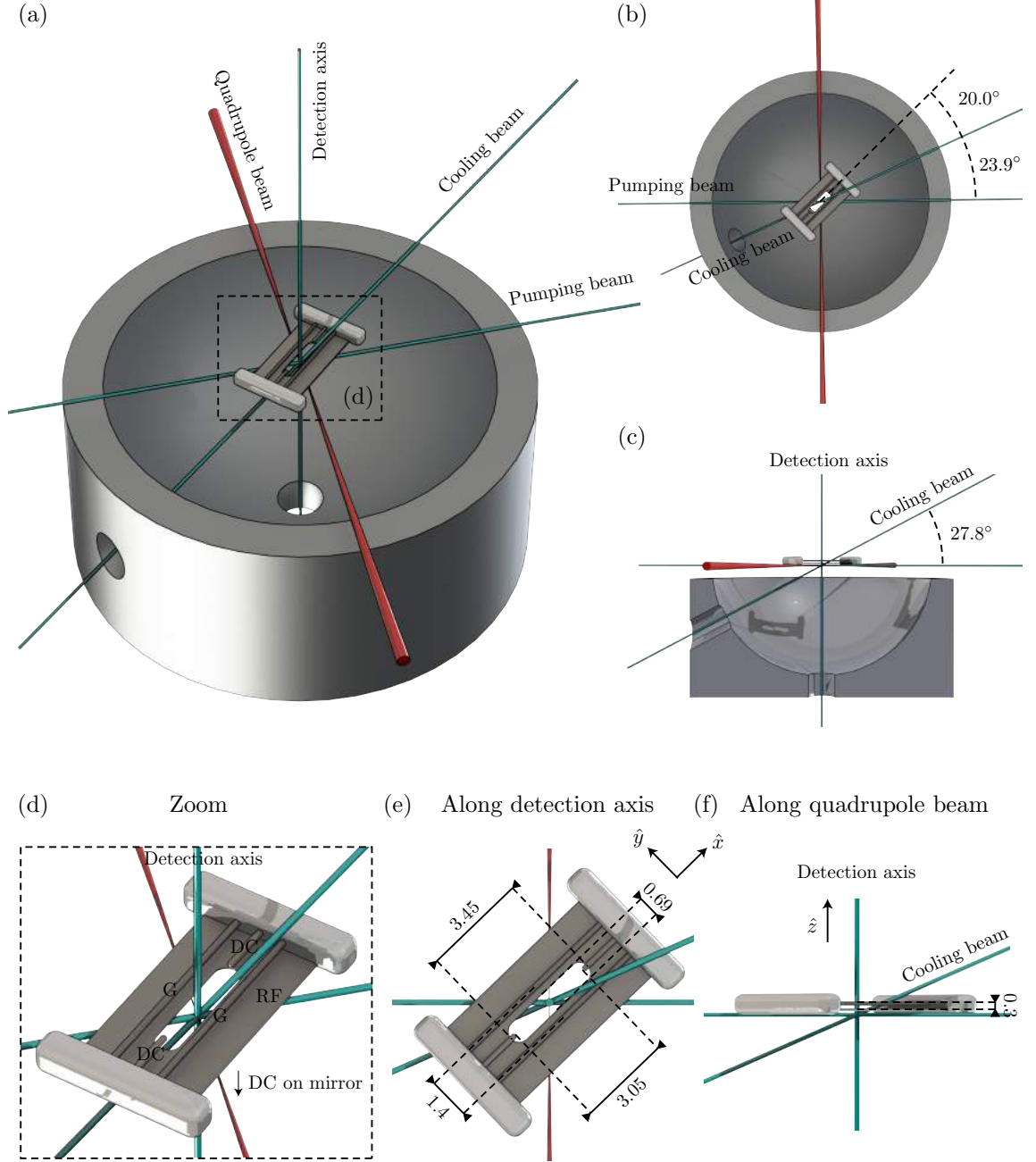
Figure 11.1: Schematic of the aperture-wire radio frequency ion-trap proposed for use with high aperture optics, in particular with a hemispheric mirror per Chap. 10. (a-c) Trap electrodes with hemispheric mirror. (d-f) detail of the trap electrodes. The relevant cooling, pumping and quadrupole beams and detection axis are shown. The cooling and pump beams have a 50 μm waist, the quadrupole beam has a 5 μm waist. All trap dimensions are in mm.

simultaneously compensate for the micromotion of all ions in such a trap. Although such traps aren't much use as motional-gate quantum processors, they are of interest for quantum simulations [318].

An alternative design strategy is to have the electrodes lie on a single plane. Although such planar traps obstruct too much of the reflected field to efficiently collect fluorescence with 4π steradian parabolas, they are well suited to two-sided collection by confocal optics so long as the trap electrodes have an aperture about the trap site. The most efficient coupling with such a scheme is achieved by quantizing the trapped atoms along an axis in the electrode plane such that fluorescence from π transitions can be collected efficiently. However, optically pumping the ions in this configuration requires a beam parallel to the electrode plane. For this reason the trap site must be displaced from the electrode plane, allowing a beam perpendicular to the electrode plane to intersect trapped ions without scattering off the electrodes themselves.

We consider an electrode geometry consisting of a planar RF electrode with an elongated circular aperture, as shown in Fig. 11.1, perpendicular to the optical (z) axis. This aperture electrode is analogous to the pair of radial RF electrodes in the typical linear trap (see Chap. 6). The role of the ground electrodes is played by a remote ground on one side of the aperture, and by two wire electrodes running parallel to the long (x) axis of the aperture on the other. The wire electrodes are displaced symmetrically about the long axis of the aperture (in the y direction) such that they do not obstruct collection from the aperture side of the trap centre. In Fig. 11.1 the remote ground is provided by a hemispherical mirror, but it could just as easily be a grounded mount for a second collection lens. The trap electrode cross section is shown in white in Fig. 11.2. The aperture is sufficiently long that the axial pseudo-potential is negligible, $\gamma_z \approx 0$. As in a typical two-dimensional trap, additional endcap electrodes on the same plane as the wires provide an axial DC trapping potential.

11.2   RF pseudo-potential

We simulate the trapping potential due to such a configuration using finite element methods provided by the COMSOL simulation package. As introduced in Sec. 6.2, the ion motion is close to that of ion in a pseudo-potential $\tilde{\phi}_{\mathrm{RF}}$ (eqn. 6.5) that is related to electric field norm of the static RF electrode potential by [53]

$$\tilde{\phi}_{\mathrm{RF}} = \frac{q|\nabla\phi_{\mathrm{RF}}|^2}{4m\Omega^2}\,, \tag{11.1}$$

where q and m are, respectively, the charge and mass of the trapped particle, and Ω is the trap drive frequency. The pseudo-potential due to the RF electrode of the aperture-wire trap configuration is shown in Fig. 11.2 as a cut plane perpendicular to the long (x) axis of the aperture.

As planned, the asymmetry between ground electrodes on either side of the aperture displaces the RF trap centre from the aperture plane towards the remote electrode (negative z). Complete optical access is available from this side, but fluorescence collection from the opposite ($+z$) side is restricted by the width of the aperture and the trap centre displacement d.

This aperture-wire electrode configuration produces two undesired trapping sites in addition to the central trapping site, as shown by the red contours in Fig. 11.2(a). These
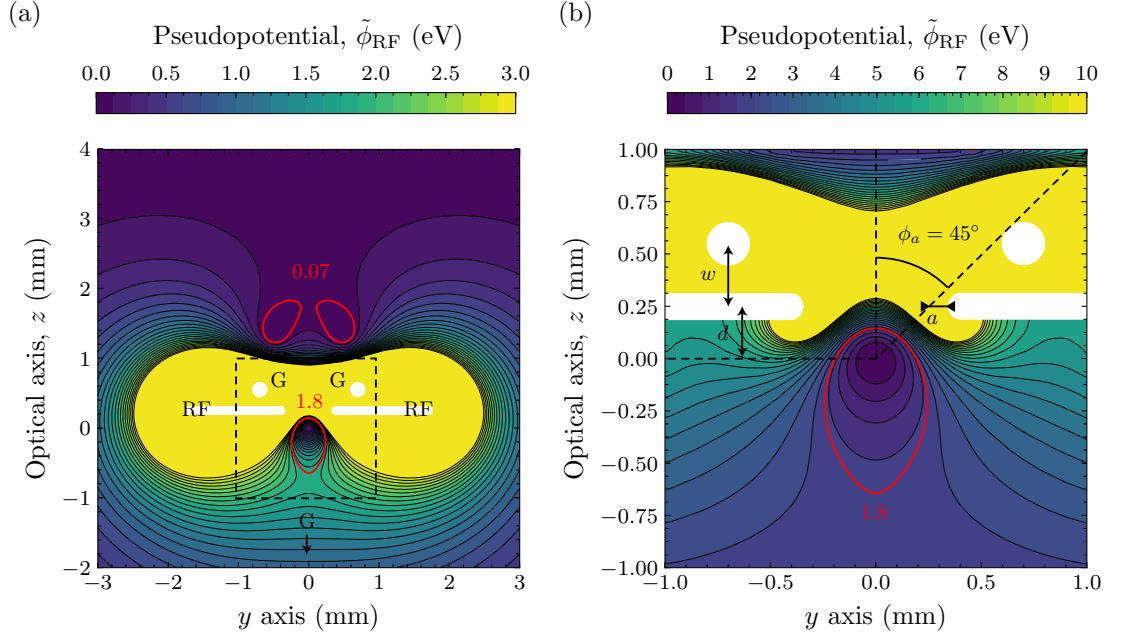
Figure 11.2: RF pseudo-potential about the aperture-wire trap in (a) the region around the electrodes and (b) in the proximity of the trapping site. The trap site is displaced from the aperture plane by a distance d. Also shown are design parameters $a = 70$ μm and $w = 300$ μm and the unobstructed collection angle $\phi_a = 45°$. This potential was calculated for ^{138}Ba$^+$ with RF potential amplitude $V = 1500$ V and frequency $\Omega = 16$ MHz. These are the RF parameters used in all subsequent simulations.

additional sites are substantially shallower than the central trap, and can be removed by an additional small negative potential at $+z$. We discuss this further in Sec. 11.3.

We may, somewhat arbitrarily, impose an unobstructed collection half-angle requirement of $\phi_a = 45°$ (or NA = 0.7). This corresponds to the diffraction-limited asphere we intend to use for collection in this new trap, provided by Asphericon, which has a working distance on 9.6 mm. We will see that ϕ_a may be increased, but only at the cost of relaxing other requirements. Having imposed that constraint, and apart from an overall scaling factor, the free parameters of this design are the additional aperture width a (additional in that this is further to our ϕ_a condition) and the aperture-wire distance w, both shown in Fig. 11.2(b). We'll now consider how the two dimensional RF trapping potential above changes with these design parameters.

In Fig. 11.3 we compare two key trap parameters as a function of the design parameters w and a. Fig. 11.3(a) shows the ion-aperture displacement and Fig. 11.3(b) shows the secular motion frequency along the optical axis. The larger the displacement the easier it is to address the ion with beams parallel to the aperture plane. However, as the ion moves further from the aperture, the aperture must also be wider to allow the desired optical access. This, in turn, lowers the trap frequency. Fig. 11.3 shows this design trade-off. Shifting the ion from the plane of the aperture is largely opposed to increasing the trap frequency. However, some optimization can be achieved by reducing w and a as much as possible within manufacturing constraints. The dashed lines in Fig. 11.3 show the parameter pair used in Fig. 11.2 and for further simulations.

Until now we have neglected the length l of the aperture along the x axis. We can

(a) Ion-aperture displacement, d (μm)

(b) Trap frequency, ν_z (MHz)
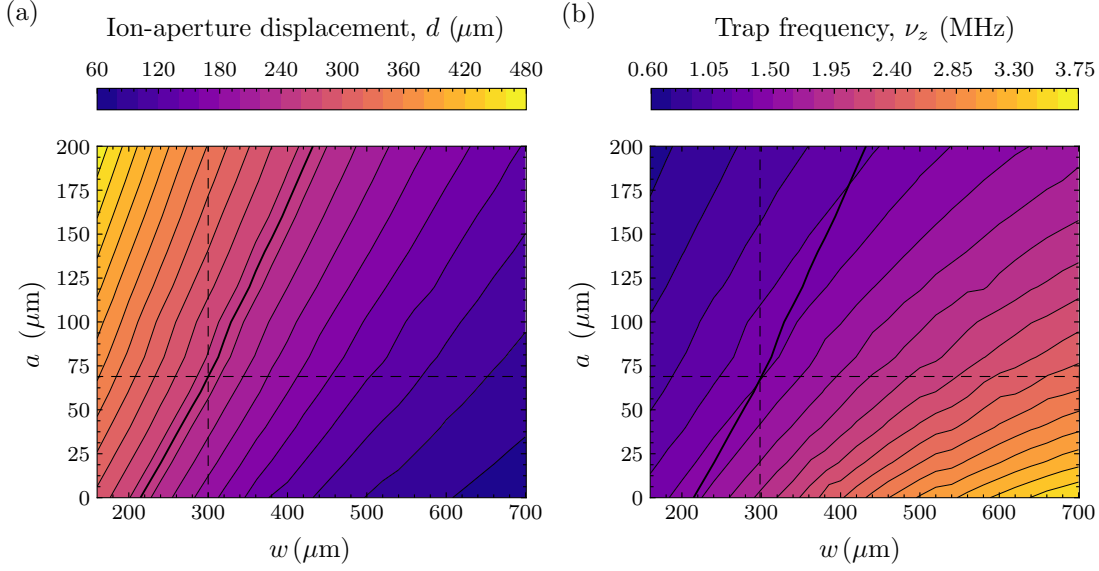
Figure 11.3: Design constraints of the aperture-wire ion trap. (a) Displacement of the ion from the aperture plane d as a function of wire-aperture displacement w and additional aperture width a as defined in Fig. 11.2. (b) The trap frequency ν_z as a function of the same parameters. The black line on each plot shows the 250 μm ion-aperture displacement contour, and dashed lines show the parameter values taken for Fig. 11.2 and further simulations.
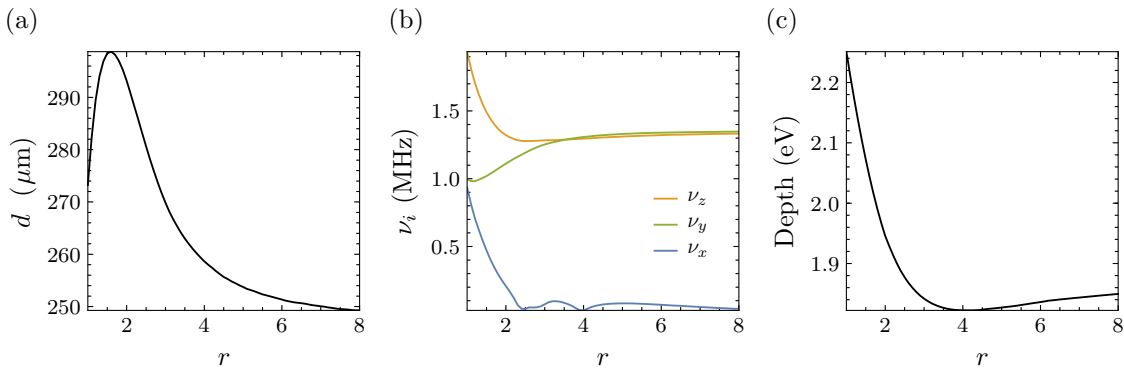
Figure 11.4: RF pseudo-potential trap parameters as a function of aperture aspect ratio. (a) Displacement of trap centre from the aperture plane, d. (b) Trap frequencies $\nu_{x,y,z}$. (c) Trap depth in eV.

consider the length as given by the aperture length/width aspect ratio r. The key trap parameters are plotted as a function of r in Fig. 11.4. Figure 11.4(a) shows the displacement of the trap centre from the aperture plane, d. Starting from $r = 1$ (circular aperture) the trap centre displacement first increases, before decreasing again after $r = 1.6$ until it reaches the limit $d = 250$ μm as $r \to \infty$. Figure 11.4(b) shows the trap frequencies along each of the primary axes (x,y,z) as a function of r. At $r = 1$ ν_x and ν_y are near-degenerate, this is the three-dimensional trap limit. As r increases ν_x drops rapidly, and ν_y and ν_z converge until reaching the two-dimensional trap regime at $r \approx 4$. Finally, Fig. 11.4(c) shows the trap depth as a function of r. As $r \to \infty$ the trap depth approaches 1.8 eV. For the following simulations we take $r = 6$. The degeneracy between ν_y and ν_z will be lifted by the DC fields.

11.3   DC potentials

To complete the trap potential we apply DC potentials to two endcap electrodes. The DC endcap electrodes in this design lie in the same plane as the wire electrodes, aligned along the long axis of the aperture and displaced symmetrically from the trap site along the x axis such that they protrude only 200 μm past the edge of the aperture. Because the ion is displaced from the wire and endcap electrode plane, we also require a compensating potential on the mirror to keep the RF pseudo-potential and total potential minima coincident. In combination, these DC potentials increase ν_x and ν_z, and reduce the ν_y ending the ν_z, ν_y degeneracy of the RF pseudo-potential. The potential configuration and trap frequencies are given by the table below.

Electrode potential (V)							Secular frequency (MHz)		
Cap 1	Cap 2	Wire 1	Wire 2	Mirror	Lens		ν_x	ν_y	ν_z
500	500	0	0	15.13	-50		0.43	1.20	1.45

Table 11.1: DC potential configuration used in trap simulations and resultant trap frequencies. These are the DC potentials used in all subsequent simulations.

The complete time averaged potential $\tilde{\phi} = \phi_{\mathrm{DC}} + \tilde{\phi}_{\mathrm{RF}}$ for this configuration is plotted in Fig. 11.5. The two undesired trapping sites on the $+z$ side of the wire electrodes have been pushed outwards by the endcap potential, and then removed by a remote negative potential at $+z$. This potential can be applied, for example, to the imaging lens mount. This is the 'lens' voltage listed in Table 11.1.

Examining the trapping region, we can explore how closely the total potential approximates the ideal quadratic potential well from Eqn. 6.1. Figure 11.5(a) shows the potential along each trap axis in a region 50 μm about the trap centre. Along the x and y axes the potential is near perfectly quadratic, but the z-axis asymmetry yields an additional component linear in z. Figure 11.5(b) shows how the $\tilde{\phi}$ minimum shifts as a function of a potential offset applied to particular electrodes in the configuration of Table 11.1. Each potential offset induces a shift along only one of the primary axes. Such shifts can be used to neutralize disturbances from stray charges or misalignment, and to compensate for micromotion by aligning the static and oscillating potential minima as shown in Figure 11.6.

Despite the z-axis trap potential asymmetry, the trap is stable for a wide range of driving conditions. We verify the stability by numerically integrating the trajectory of
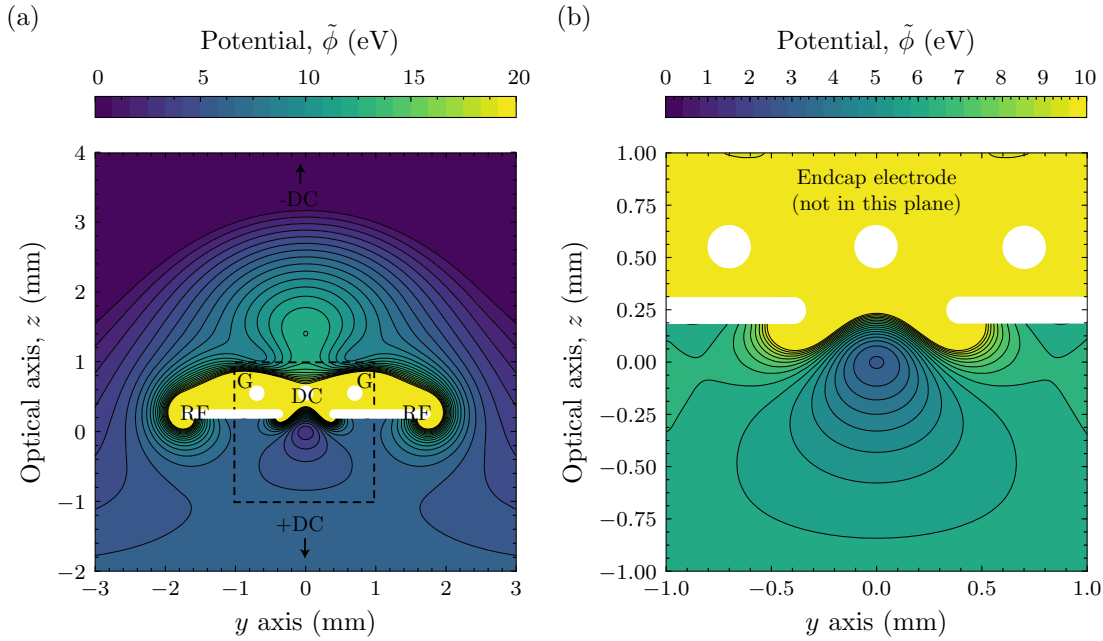
Figure 11.5: Total potential about the aperture-wire trap in (a) the region around the electrodes and (b) in the proximity of the trapping site. The position of the endcap electrodes is shown, although they do not intersect the plane. The unwanted trapping sites on the $+z$ side of the wire electrodes are removed with a remote negative potential (not shown). This potential was calculated for a $^{138}\text{Ba}^+$ with RF potential maximum $V = 1500$ V and frequency $\Omega = 16$ MHz and DC voltages according to Table 11.1.
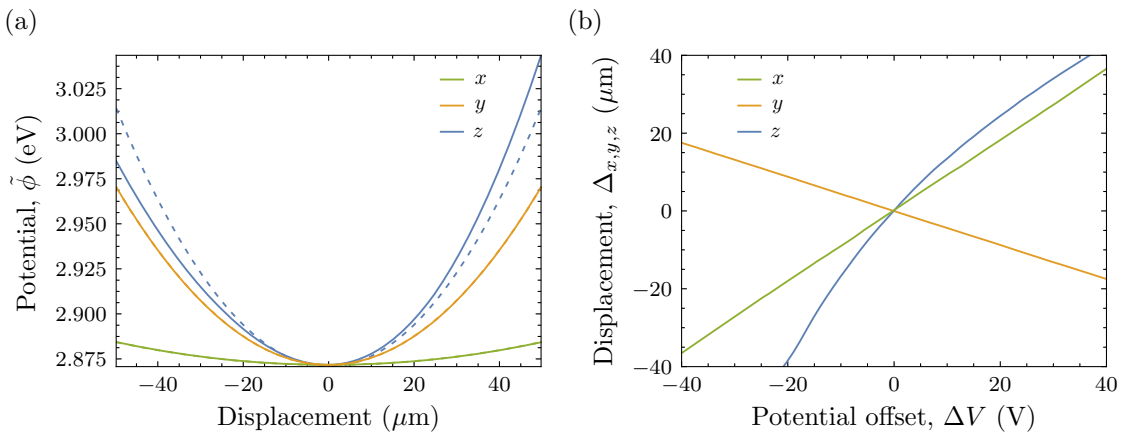
Figure 11.6: (a) Potential along each of the trap axes 50 μm about the trap centre (solid) with quadratic fits (dashed). The z axis asymmetry leads to a component linear in z. (b) Shifting the potential null with electrode voltage offsets. The null is shifted in the y direction by, respectively, adding and subtracting an offset ΔV from each wire electrode, in the x direction by adding and subtracting ΔV from each endcap electrode, and in the z direction by adding ΔV to the remote DC at $-z$.
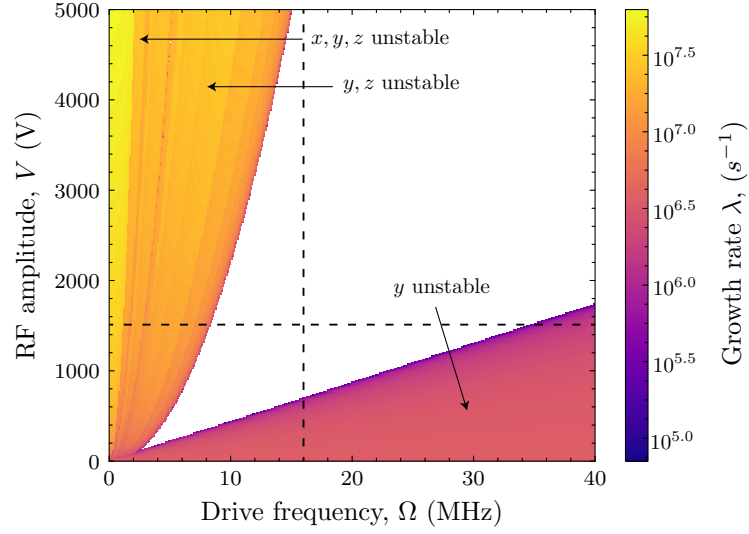
Figure 11.7: Stability of the aperture-wire trap for RF amplitude V and drive frequency Ω showing the displacement growth rate where the trap is unstable.

Parameter	x	y	z
Cooling angle ϕ_c (deg.)	33.80	72.39	62.17
Lamb-Dicke cooling, η_c	0.248	0.054	0.076
Pumping angle, ϕ_p (deg.)	43.90	46.10	90.00
Lamb-Dicke pumping, η_p	0.215	0.124	0.000
Detection angle, ϕ_d (deg.)	90.00	90.00	0.000
Lamb-Dicke detection, η_d	0.000	0.000	0.163
Quadrupole angle, ϕ_q (deg.)	46.10	43.90	90.00
Lamb-Dicke quadrupole, η_q	0.058	0.036	0.000

Table 11.2: Optical parameters of the aperture-wire radio frequency ion trap. Beam angles and Lamb-Dicke parameters are listed for each beam and each trapping axis.

trapped particles given the total time varying potential $\phi(t)$. The static, DC potential is produced by the voltage configuration in Table 11.1, and the time-varying RF potential oscillates with amplitude V and drive frequency Ω. Each potential is calculated separately according to finite-element simulations of the trap design in COMSOL, and the particle motion along each axis is integrated in the combined potential independently. Stable driving conditions V, Ω are shown by the white region in Fig. 11.7. Where the trap is unstable, we have indicated the growth rate λ defined by

$$|\mathbf{x}(t)| = |\mathbf{x}(0)|e^{\lambda t} \tag{11.2}$$

according to the colourbar. The RF parameters used in Fig. 11.2 and subsequent calculations, $\Omega = 16$ MHz and $V = 1500$ V, are shown with dashed lines.
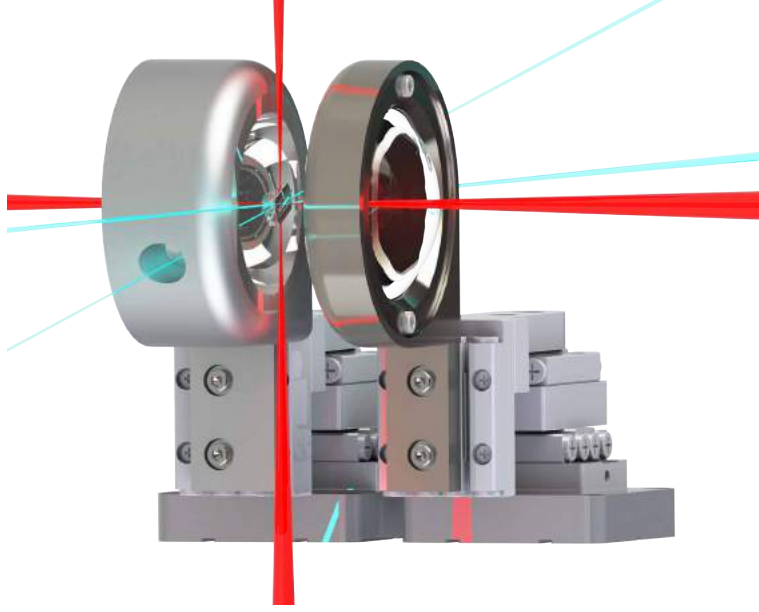
Figure 11.8: The aperture-wire trap operating with a hemisphere and NA = 0.7 collection asphere. The hemisphere and lens are mounted on positioning stages for alignment.

11.4 Summary

We have introduced an aperture-wire ion trap design with optical access sufficient for performing QED experiments with hemispheric mirrors as proposed in Ref. [298] and Sec. 10.7.2. The trap is designed to be used with the hemispheric mirrors produced in Chap. 10. Compared to noteworthy traps with near 4π steradian access, such as the stylus [315] and tack traps [316], the trapping potential is deeper, the trap frequencies are higher, and (because this is a two-dimensional trap) multiple ions may be trapped in a linear crystal along the RF potential symmetry axis. Feasible trap frequencies, see Table 11.1, are comparable to the linear trap of Chap. 6, and sufficient for ion-ion motional gates used by ion-trap quantum processors. In this respect the trap is most like planar or surface ion traps, with an aperture to allow optical access from two hemispheres.

The primary design trade-off is between, on one hand, the ion-aperture distance d that is required for pumping perpendicular to the detection axis, and, on the other hand, higher secular frequencies $\nu_{x,y,z}$ and a larger unobstructed angle ϕ_a. The presented design is a compromise predicated on the condition that $d \geq 250$ μm is required for pumping, and that the available collection optic has only $\phi_a = 45°$, or NA = 0.7. As shown in Fig. 11.3, reducing the wire-aperture distance w improves the trap frequencies slightly. This suggests a two-layer segmented electrode design as a promising alternative to the wire-trap design.

The ion-aperture displacement $d = 250$ μm reduces the fluorescence collection efficiency to 69% of the total dipole emission, substantially worse than the tack and stylus traps, but suitable for hemisphere-based QED experiments because one hemisphere of the ion's emission remains completely unobstructed. The proposed experimental configuration is shown in Fig. 11.8. According to Sec. 10.7.2, it will therefore be possible to improve collection efficiency from the aperture-wire trap to near unity by shaping the spatial emission mode of a chosen transition to favour collection.

The optical beam access is designed to be consistent with beams perpendicular to the ports of the Kimball 8" extended spherical octagon vacuum chamber (MCF800-ExtOct-

G2C8A16), allowing for cooling, pump, and quadrupole beams as well as detection along the primary optical axis. Lamb-Dicke parameters for each beam are listed in Table 11.2, given the secular frequencies we derived from the simulated trap, see Table 11.1. Each beam has 150 μm of clearance from the electrodes and (indicative) mount shown in Fig. 11.1. In contrast to the linear trap we used earlier, the quadrupole beam is perpendicular to the detection axis. A plausible alternative, if quadrupole-detection beam overlap is required, is to use the high-NA collection lens off-axis and in combination with a corrective lens to provide another quadrupole beam direction. Because the quadrupole beam diverges rapidly, any quadrupole beam that is tightly focussed and overlaps with the detection axis will impinge on the mirror, and light scattered from the mirror will be detrimental to quadrupole operations. These considerations aside, the design presented here is a feasible means of performing QED experiments with a hemispheric mirror and either one or a string of many trapped ions.

Bibliography - A new ion trap for high aperture optics

42. T. Monz, et al., Realization of a scalable Shor algorithm, *Science* **351** (2016).

53. D. Leibfried, et al., Quantum dynamics of single trapped ions, *Rev. Mod. Phys.* **75**, 281–324 (2003).

298. G. Hétet, et al., QED with a spherical mirror, *Phys. Rev. A* **82**, 63812 (2010).

315. R. Maiwald, et al., Stylus ion trap for enhanced access and sensing, *Nat. Phys.* **5**, 551–554 (2009).

316. G. Shu, et al., Efficient fluorescence collection and ion imaging with the "tack" ion trap, *J. Opt. Soc. Am. B* **28**, 2865 (2011).

317. S. Seidelin, et al., Microfabricated surface-electrode ion trap for scalable quantum information processing, *Phys. Rev. Lett.* **96**, 1–4 (2006).

318. K. Kim, et al., Quantum simulation of frustrated Ising spins with trapped ions, *Nature* **465**, 590–593 (2010).

Free-space couplers: Conclusions and outlook

From hence your eye takes in a wider expanse of snow; here tossed into ridges resembling breakers just about to plunge; there sunk in mazy furrows; there smooth slopes and level plains of exquisite purity.

– Walter White, *On Foot Through Tyrol* (1855)

We have demonstrated atom-light couplers for trapped-ion qubits using high-aperture lenses as free-space couplers. Free-space couplers are single pass, the interaction time bandwidth is limited by the atomic transition and not a cavity bandwidth. Nevertheless they can approach unit interaction efficiency in the limit of high apertures. We derived the images of atomic dipole fields for spherical lens, thin lens and parabolic mirror couplers and calculated their fibre-coupling efficiency depending on the dipole orientation.

The free-space coupled trapped ion is a source of exceptionally pure single photons. We demonstrated alternative methods of operating the photon source, and characterized the photon-emission behaviour. We showed that an eight-level Bloch model fitted to the dark-resonance spectrum of the ion successfully predicts the single-photon arrival time distribution and correlation function. We also showed that spin-orbit coupling in the single-photon spatial mode produces wavelength scale displacements in the single-photon image. This is fundamental to the atomic dipole mode, and will only become more consequential as free-space atom-light couplers approach high apertures and unit collection efficiency. However, even for inefficient collection, spin-orbit coupling in the field of dipoles that aren't angular momentum eigenstates can produce arbitrarily large displacements.

Although the lens-based atom-light couplers we use are inefficient, the single photon field is sufficiently pure that its higher-order quantum character persists. We derived an efficient witness for quantum-non Gaussian states and demonstrated that our single-photon source beats the witness under a wide range of conditions. The source is therefore sufficiently pure to operate a large quantum network, or equivalently to network a large number of quantum computer registers. However, improving the efficiency of our free-space couplers is necessary to provide a useful, spectrally bright photon source for networks or trapped-atom quantum computers.

We entangled a pair of trapped ions by single-photon detection, and then measured path-dependent spatial interference patterns in the emission mode of the two-atom entangled state. This is the small ensemble limit of Dicke enhancement, which will prove fundamentally important to ensemble-based atom-light couplers in Part III. The interference fringe visibility was limited by the entangled state fidelity, which is in turn limited by

the temperature of our atoms. The atoms could be ground-state cooled without a great time penalty by EIT cooling [252, 319].

We proposed a new method of efficient coupling with high aperture optics that combines the QED engineering typical of optical resonators in a single-pass configuration. Perfect hemispheric mirrors can enhance, or entirely suppress, the spontaneous emission of an atom trapped at the centre of curvature. Like all high-aperture, diffraction limited optics, making hemispheres sufficient for this task is a considerable challenge. We manufacture hemispheres with typical surface deviations as low 14 nm. To our knowledge the roundest concave surfaces ever produced, and within a factor of five of the roundest manufactured objects. Such round mirrors can reduce or enhance the vacuum mode density by 96%. By a slight modification, we could make near-hemispheric mirrors that enhance the emission of an atom into a high aperture lens, and suppress the emission outside of the collection angle. By shaping the dipole mode in this way, an atom can be efficiently coupled to a travelling photon mode without 4π optics. A calculation based on the mirrors we manufactured and our trapped ions shows feasible coupling efficiencies higher than the best existing free-space couplers.

Part III

Many atoms

Ensemble-light interactions

If I had the misfortune to know the laws of these phenomena, I could not succeed except by inextricable calculations, and I should have to give up the attempt to answer you; but since I am fortunate enough to be ignorant of them, I will give you an answer at once. And, what is more extraordinary still, my answer will be right.

– Henri Poincaré, *Science and Method* (1908)

At the outset of this thesis we described three broad strategies for efficiently coupling qubits from travelling photons to stationary atomic systems: increasing the interaction time using resonators, decreasing the mode volume with focussing optics, and increasing the number of atoms interacting with the field. Atom-light couplers typically employ some combination of these approaches, for example the coupling of ensembles to resonator modes. So far we have explored only the first two, which concern the coupling of optical qubits to single-atom qubits, like the atomic qubits in a linear ion-trap quantum processor, but now we will turn our attention to the third, ensemble, method. Although the free-space interaction of atoms and photons is weak, ensembles of identical atoms have a collective interaction strength that can be very large.

It is obvious that the optical depth of N atoms should be N times larger than a single atom, but quantum couplers with ensembles require N atoms that cooperate coherently. In his seminal paper, Ref. [291], Dicke identified that emissions from the individual atoms in an ensemble are correlated by their common radiation fields. Even spontaneous decay from an excited ensemble can initiate directed coherent emission, so-called 'collective spontaneous emission'. Under the right conditions, the dipole moments of spatially separated atoms in an uncorrelated, population-inverted ensemble may spontaneously correlate over the course of an emission process to produce a coherent field [320]. The correlated emission rate is faster than the natural spontaneous emission rate by a factor N. Additionally, the shape of the ensemble determines a preferred emission direction; an elongated cylindrical ensemble emits preferentially into the on-axis mode. The ensemble fundamentally enhances and directs the atom-light interaction.

The 'Dicke superradiance' discussed above is a transient coherent process that arises spontaneously, but we can engineer coherent ensemble-photon interactions by imposing the same phase coherence externally. In fact, we have already done this with a (very small) atom ensemble. The spatial interference pattern of the bipartite entangled states we prepared in Chap. 9 is an example of how the collective atomic state can enhance the atom-light interaction in particular modes. In order to understand these techniques with larger ensembles, we will expand the theory of atom-light interactions developed in Chap. 3 beyond isolated atoms to the coherent interaction of light with atomic ensembles.

Atoms are the subject of the experimental work in this thesis, and we'll continue to discuss atoms exclusively in the following chapter, although, once again, what is true of atoms is true of emitters more broadly, and the same ensemble techniques can be performed with the 'artificial atoms' we covered in Sec. 5.6.

We will introduce techniques for reversibly mapping quantum light fields to and from atomic ensembles, the essential capability of an optical quantum memory. In particular we introduce the 'gradient echo memory' scheme, which we employ to great effect in Chaps. 16 and 17 using clouds of cold, trapped Rb atoms. We will also show how the optical field can be trapped inside an ensemble to create strong, stationary light fields that may be a mechanism for ensemble-mediated photon-photon gates. This last work is part of the theory that appears in

[9] "**Dynamical observations of self-stabilizing stationary light** J. L. Everett, G. T. Campbell, Y.-W. Cho, P. Vernaz-Gris, D. B. Higginbottom, O. Pinel, N. P. Robins, P. K. Lam, and B. C. Buchler. *Nature Physics* **13** 68-73 (2017).

13.1   Ensemble states

In the ideal case, a single photon coherently absorbed into an ensemble of identical emitters creates an entangled Dicke state: a single excitation delocalized and distributed equally amongst each emitter in the ensemble [321]. Each excitation has a position-dependent phase so that the total ensemble state is

$$\psi_{\text{Dicke}} = \frac{1}{\sqrt{N}} \sum_{j=0}^{N} e^{i\mathbf{k}_0 \cdot \mathbf{r}_j} \hat{\sigma}_+^j \ket{G} \, , \tag{13.1}$$

where $\ket{G}$ is the ensemble ground state $\ket{G} = \bigotimes_{j=1}^{N} \ket{g}_j$, σ_+^j is the raising operator for the j-th atom, $\mathbf{r}_j$ is the position of the j-th atom, and $\mathbf{k}_0$ is the wave vector of the input photon field. The factor of $\sqrt{N}$ appears due to the N permutations of a single excitation amongst N atoms. The two-atom entangled states we produced by single-photon detection in Chap. 9 are the limiting case of a Dicke state as the ensemble shrinks to $N \to 2$. In that case, we observed spatial interference in the single-photon field of the two-atom Dicke state as the two superposition components combine constructively or destructively. As N increases the interference pattern focusses along the direction of the exciting photon $\mathbf{k}_0$. In the limit of very large N, the photon is emitted such that $\mathbf{k} = \mathbf{k}_0$. In the rotating reference frame of the exciting wave this lowest-order Dicke state is the N-atom W state. Compared to other multi-atom entangled states the entanglement of the W state is robust, retaining entanglement after atom-loss. In this way such distributed states can be the basis of robust quantum memories, indeed the operation of a quantum memory can be construed as a multi-atom entanglement witness [322].

The interaction Hamiltonian of the ensemble-light system is simply the sum of interaction Hamiltonians for each constituent atom. Following Eqn. 3.19 we have

$$\hat{H}_{\text{int}} = \hbar g \sum_{j=1}^{N} \hat{\sigma}_+^j \hat{a}_{\mathbf{k}_0} e^{i\mathbf{k}_0 \cdot \mathbf{r}_j} e^{-i(\omega_j - \omega_0)} + h.c. \, , \tag{13.2}$$

where we have allowed the detuning $\Delta_j = \omega_j - \omega_0$ to vary from atom to atom. The interaction Hamiltonian comprises the bare-state basis elements $\bra{\psi_{\text{Dicke}}} \hat{H}_i \ket{\psi_{\text{Dicke}}} = \bra{G} \hat{H}_i \ket{G} =$

0 and $\langle\psi_{\text{Dicke}}|\hat{H}_{\text{i}}|G\rangle = \hbar g\sqrt{N}$, which is equivalent to the single-atom Jaynes-Cummings interaction Hamiltonian Eqn. 3.21 with $g \to g\sqrt{N}$ [323]. The role of an N-atom ensemble in this sort of coherent absorption and remission process is therefore to enhance the interaction strength by a factor of $\sqrt{N}$. With this evidence alone, we can see that interactions between optical fields and large atomic ensembles is a promising means of efficiently coupling travelling photonic and stationary atomic qubits, although the atomic qubit is no longer localized in a single atom, but distributed amongst many atoms. To conveniently describe such distributed excitations we must introduce collective operators.

13.1.1 Collective operators

Until now we have considered only a single excitation in the ensemble, which allowed us to write the state as a straightforward permutation. To describe a more general state, containing any number of excitations, we will introduce collective operators [92]. In the limit of large N the ensemble can be approximated as a continuous distribution of atoms. We may therefore divide the interaction region into non intersecting volumes of size V_i[1] about points $\mathbf{r}_i$ sufficiently small that the detuning Δ_j is constant $\forall j \mid \mathbf{r}_j \in V_i$ but large enough to contain a macroscopic quantity of atoms $N_i = V_i n_i$, where $n_i = n(\mathbf{r}_i)$ is the local density at point $\mathbf{r}_i$. We'll limit ourselves to describing only ensembles of uniform density $n_i = n$, although this is not strictly true in the cold atom systems we experiment with.

We define locally average operators on the volume V_i according to

$$\hat{A}_i = \frac{1}{N} \sum_{j|\mathbf{r}_j \in V_i} \hat{A}_j \,, \tag{13.3}$$

which approach the continuous operators $\hat{A}(\mathbf{r})$ in the continuum limit. By applying this averaging to the atomic operators $\hat{\sigma}_\pm$ we subsume the sum from Eqn. 13.2 into the definition of the new collective atomic operators themselves[2]. The Heisenberg-Langevin equations for the atom-light interaction are linear, which means that the local collective atom-ensemble Hamiltonian is identical to the Jaynes Cummings atom-light Hamiltonian of Eqn. 3.21, but with the ensemble interaction Hamiltonian

$$\hat{H}_{\text{int}}^{\text{ens}} = \sum_i V_i n_i (H_{\text{int}})_i(\mathbf{r}_i)\,. \tag{13.4}$$

In the continuous limit this becomes

$$\hat{H}_{\text{int}}^{\text{ens}} = \int \mathrm{d}V \; n(\mathbf{r})\hat{H}_{\text{int}}(\mathbf{r})\,. \tag{13.5}$$

13.1.2 Field propagation

For the first time in this thesis we have an atom-light interaction that is spatially distributed, and so we need to describe how the light field propagates through the atom ensemble. Classically, this is the Maxwell equation for an electric field pulse propagating

---

[1]Here we use the index j for a sum over atoms, and the index i for a sum over volumes.

[2]We are not going to draw any notational distinction between single-atom and collective operators, since we will be almost exclusively concerned with collective atomic operators from this point forward.

in a dielectric medium [77]

$$\nabla^2 \mathbf{E} - \frac{1}{c^2}\frac{\partial^2 \mathbf{E}}{\partial t^2} = \mu_0 \frac{\partial^2 \mathbf{P}}{\partial t^2}, \tag{13.6}$$

where $\mathbf{P}$ is the polarization of the dielectric. For slowly varying ($\omega_{\mathbf{k}} \approx \omega_0$), paraxial ($|\mathbf{k}| \approx k_z = \omega_0/c$) envelopes $\mathcal{E}$ and $\mathcal{P}$ of uniform polarization $\mathbf{e}$

$$\mathbf{E}(\mathbf{r}, t) = \mathbf{e}\mathcal{E}(z, t)e^{i(kz - \omega t)} + h.c., \tag{13.7}$$

$$\mathbf{P}(\mathbf{r}, t) = \mathbf{e}\mathcal{P}(z, t)e^{i(kz - \omega t)} + h.c., \tag{13.8}$$

Eqn. 13.6 reduces to the first order differential equation

$$(\partial_t + c\partial_z)\,\mathcal{E} = i\frac{\omega}{2\epsilon_0}\mathcal{P}, \tag{13.9}$$

where the paraxial approximation has simplified the spatial derivative to a single propagation direction that we take to be $\hat{\mathbf{z}}$.

To find an analogous equation for the quantum field from Eqn. 2.1, we first define slowly varying and paraxial envelopes for an $\mathbf{e}$-polarized quantum field pulse in terms of the positive frequency operator

$$\hat{\mathbf{E}}^+ = \frac{1}{(2\pi)^3}\sqrt{\frac{\hbar\omega_0 V}{2\epsilon_0}}\int \mathrm{d}^3\mathbf{k}\,\sqrt{\frac{\omega_{\mathbf{k}}}{\omega_0}}\hat{a}_{\mathbf{k}}e^{i(\mathbf{k}\cdot\mathbf{r} - \omega_{\mathbf{k}}t)}. \tag{13.10}$$

$$= \epsilon_\omega \hat{\mathcal{E}}\mathbf{e}. \tag{13.11}$$

The Heisenberg equation of motion for the wave packet operator is

$$\frac{\mathrm{d}}{\mathrm{d}t}\hat{\mathcal{E}} = -\frac{i}{\hbar}\left[\hat{H}, \hat{\mathcal{E}}\right] + \partial_z\hat{\mathcal{E}}. \tag{13.12}$$

By calculating the partial derivatives of $\hat{\mathcal{E}}$, making paraxial and slowly-varying approximations, substituting the collective Jaynes-Cummings dipole interaction Hamiltonian from Eqn. 3.21, and rearranging (see, for example, Ref. [324]) we arrive at the propagation equation for the envelope operator

$$(\partial_t + c\partial_z)\,\hat{\mathcal{E}} = -\frac{i}{\hbar}\left[\hat{H}_i, \hat{\mathcal{E}}\right]. \tag{13.13}$$

Substituting collective operators for $\hat{\sigma}_\pm$ in Eqn. 3.21 and taking the ensemble interaction Hamiltonian from Eqn. 13.5 gives us the propagation of $\hat{\mathcal{E}}$ in terms of the collective excitation operator for a resonant transition, $\hat{\sigma}_+$,

$$(\partial_t + c\partial_z)\,\hat{\mathcal{E}} = igN\hat{\sigma}_+. \tag{13.14}$$

where g is the interaction strength between each photon and atom in the interaction region and N is the total number of atoms in the interaction region. This is equivalent to the classical expression Eqn. 13.9, where the polarizability $\mathbf{P}$ has been replaced by the the collective bulk polarization operator

$$\hat{\mathcal{P}} = N\,(\mathbf{d} \cdot \mathbf{e})\,\hat{\sigma}_+, \tag{13.15}$$
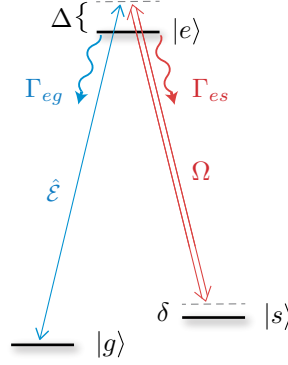
Figure 13.1: Level scheme for the Λ-atom ensemble used in the following chapters. We work exclusively in the weak-probe limit $g\hat{\mathcal{E}} \ll \Omega$ and typically with branching rate $\frac{1}{2}$, such that $\Gamma_{eg} = \Gamma_{es} = \Gamma/2$.

$\hat{\mathcal{E}}$ has been scaled by ϵ_ω and we assume that the dipole moment **d** and polarization **e** are aligned.

13.1.3   Bloch equations for Λ ensembles

The atom-ensemble experiments in this part of the thesis will concern ensembles of Λ-atoms that are driven by a weak field $\hat{\mathcal{E}}$ addressing the transition $|g\rangle \rightarrow |e\rangle$ and a strong control field with Rabi frequency Ω that drives a transition between the excited state $|e\rangle$ and a further, metastable ground state $|s\rangle$, as shown in Fig. 13.1. The equation of motion for the collective atomic density matrix ρ is given by the Λ-atom Hamiltonian (Eqn. 3.40) [92]

$$\partial_t \hat{\rho} = -\frac{i}{\hbar}\left[\hat{H}_i, \hat{\rho}\right] + \hat{\mathcal{L}}(\hat{\rho})\,, \tag{13.16}$$

where the Liouvillian contains three components in Linblad form: the spontaneous decay and dephasing terms with collapse operators as introduced in Sec. 3.3

$$\hat{C}_{\text{spon}} = \sqrt{\Gamma_{\text{spon}}}\left(\hat{\sigma}_{eg} + \hat{\sigma}_{es}\right)\,, \tag{13.17}$$

$$\hat{C}_{\text{deph}} = \sqrt{\Gamma_{\text{deph}}}\left(\hat{\sigma}_{gg} + \hat{\sigma}_{ss}\right)\,, \tag{13.18}$$

and an additional population exchange term corresponding to, for example, population exchange in inelastic collisions, with collapse operator

$$\hat{C}_{\text{coll}} = \sqrt{\Gamma_{\text{coll}}}\left(\hat{\sigma}_{gs} + \hat{\sigma}_{sg}\right)\,. \tag{13.19}$$

and corresponding collision rate Γ_{coll}. We will consider a Λ-ensemble with equal decay rates $\Gamma_{ge} = \Gamma_{se} = \Gamma/2$ where Γ is the excited state linewidth.

We write the evolution of $\hat{\rho}$ in terms of six coupled differential equations for the local

collective atomic operators $\hat{\sigma}_{ij}$

$$\partial_t\hat{\sigma}_{gg} = -ig\mathcal{E}\hat{\sigma}_{eg} + ig\mathcal{E}^\dagger\hat{\sigma}_{ge} + \frac{\Gamma}{2}\hat{\sigma}_{ee} + \Gamma_{\text{coll}}\left(\hat{\sigma}_{ss} - \hat{\sigma}_{gg}\right), \tag{13.20}$$

$$\partial_t\hat{\sigma}_{ss} = -i\Omega\hat{\sigma}_{es} + i\Omega^*\hat{\sigma}_{se} + \frac{\Gamma}{2}\hat{\sigma}_{ee} + \Gamma_{\text{coll}}\left(\hat{\sigma}_{gg} - \hat{\sigma}_{ss}\right), \tag{13.21}$$

$$\partial_t\hat{\sigma}_{ee} = ig\mathcal{E}\hat{\sigma}_{eg} + i\Omega\hat{\sigma}_{es} - ig\mathcal{E}^\dagger\hat{\sigma}_{ge} - i\Omega^*\hat{\sigma}_{se} - \Gamma\hat{\sigma}_{ee}, \tag{13.22}$$

$$\partial_t\hat{\sigma}_{es} = i\Omega^*\left(\hat{\sigma}_{ee} - \hat{\sigma}_{ss}\right) + ig\mathcal{E}^\dagger\hat{\sigma}_{gs} - \left(\gamma_{es} - i(\Delta - \delta)\right)\hat{\sigma}_{es}, \tag{13.23}$$

$$\partial_t\hat{\sigma}_{ge} = ig\mathcal{E}\left(\hat{\sigma}_{gg} - \hat{\sigma}_{ee}\right) + i\Omega\hat{\sigma}_{gs} - \left(\gamma_{ge} + i\Delta\right)\hat{\sigma}_{ge}, \tag{13.24}$$

$$\partial_t\hat{\sigma}_{gs} = i\Omega^*\hat{\sigma}_{ge} - ig\mathcal{E}\hat{\sigma}_{es} - \left(\gamma_{gs} + i\delta\right)\hat{\sigma}_{gs}, \tag{13.25}$$

where the polarization and spin coherence terms relax at rates

$$\gamma_{ge} = \gamma_{se} = \frac{\Gamma}{2} + \Gamma_{\text{deph}} + \Gamma_{\text{coll}}, \tag{13.26}$$

$$\gamma_{gs} = \Gamma_{\text{deph}} + \Gamma_{\text{coll}}. \tag{13.27}$$

It is worth noting that the collective atomic state is the ensemble average over many atomic states, so we may properly associate the expectation value of the collective operator with the ensemble state.

13.1.4   Weak-field limit

Fortunately, we can eliminate most of these equations in the weak-field limit $g\mathcal{E} \ll \Omega$ where the steady state population is almost entirely in the ground state [92]

$$\hat{\sigma}_{gg} \approx 1, \qquad \hat{\sigma}_{ee} \approx 0, \qquad \hat{\sigma}_{ss} \approx 0, \qquad \hat{\sigma}_{es} \approx 0. \tag{13.28}$$

Only two equations for the atomic state remain: one for the atomic polarization $\hat{\sigma}_{ge}$ and one for the atomic coherence $\hat{\sigma}_{gs}$,

$$\partial_t\hat{\sigma}_{ge} = ig\mathcal{E} + i\Omega\hat{\sigma}_{gs} - \left(\gamma_{ge} + i\Delta\right)\hat{\sigma}_{ge}, \tag{13.29}$$

$$\partial_t\hat{\sigma}_{gs} = i\Omega^*\hat{\sigma}_{ge} - \left(\gamma_{gs} + i\delta\right)\hat{\sigma}_{gs}. \tag{13.30}$$

Finally, the bright control field induces an AC Stark shift on the transition $|e\rangle\leftrightarrow|s\rangle$, changing the resonant frequency of the two-photon transition by an amount

$$\Delta_{\text{Stark}} = \frac{\Delta|\Omega|^2}{\Gamma^2 + \Delta^2}. \tag{13.31}$$

In practice, however, we are concerned only with the detuning about the true, shifted, resonance, and never with the unshifted resonance. We therefore redefine our two-photon detuning $\delta \to \delta - \Delta_{\text{Stark}}$ to compensate for the AC Stark shift and give Stark-independent equations of motion.

13.1.5   Λ-ensemble Maxwell-Bloch equations

Including the field propagation equation Eqn. 13.40, we have three coupled differential equations for the combined light field and Λ-ensemble system under the rotating wave,

pure state and slowly-varying envelope approximations

$$\partial_t \hat{\sigma}_{ge} = ig\mathcal{E} + i\Omega\hat{\sigma}_{gs} - (\gamma_{ge} + i\Delta)\,\hat{\sigma}_{ge}\,, \tag{13.32}$$

$$\partial_t \hat{\sigma}_{gs} = i\Omega^*\hat{\sigma}_{ge} - (\gamma_{gs} + i\delta - i\Delta_{\text{Stark}})\,\hat{\sigma}_{gs}\,, \tag{13.33}$$

$$(\partial_t + c\partial_z)\,\hat{\mathcal{E}} = igN\hat{\sigma}_+\,. \tag{13.34}$$

By moving into a reference frame travelling at the speed of light we further reduce Eqn. 13.34 to a first order differential equation in space alone

$$\tau = t - z/c \tag{13.35}$$

$$\partial_z \hat{\mathcal{E}}(z, \tau) = igN\hat{\sigma}_+(z, \tau)\,. \tag{13.36}$$

13.1.6 Optical depth

The interaction strength g and atom number N depend on the field mode $u(\mathbf{r})$ and ensemble density distribution $n(\mathbf{r})$, which are not straightforward to determine precisely in experiments. We will therefore make some transformations in order to arrive at simplified equations of motion in terms of directly measurable experimental parameters. We introduce the on-resonance optical depth for a collimated beam with cross section A travelling through a uniform density ensemble of length L [92]

$$d = \frac{d_{eg}^2 N\omega}{2c\hbar\epsilon_0 A\Gamma} = \frac{g^2 NL}{\Gamma c}\,. \tag{13.37}$$

where N is the number of interacting atoms, and we assume that the ensemble is larger than the probe beam so that the attenuation is even over the spatial extent of the beam.

The intensity of a weak on-resonance field will be attenuated by a factor e^{-d} on passing through the ensemble. In contrast to the interaction volume V and atomic density $n(\mathbf{r})$, the optical depth is directly observable by a probe attenuation measurement (although it may be necessary to make such a measurement off-resonance when the optical depth is very high). Writing the equations in terms of d will give us an experimentally verifiable equation of motion.

We first replace z with the dimensionless 'depth proportion'

$$\xi(z) = \frac{1}{N}\int \mathrm{d}x \int \mathrm{d}y \int_0^L \mathrm{d}z\, n(\mathbf{r})\,, \tag{13.38}$$

that ranges from 0 to 1 along the length L of the ensemble along the propagation direction. For an ensemble of uniform density n, cross section A, and length L, the propagation equation may be written terms of this transformed spatial coordinate

$$\xi = z/L\,, \tag{13.39}$$

$$\partial_\xi \hat{\mathcal{E}}'(\xi, \tau) = i\sqrt{d}\hat{\mathcal{P}}'(\xi, \tau)\,, \tag{13.40}$$

where $\hat{\mathcal{E}}'$ is $\hat{\mathcal{E}}$ with a dimensionless scaling

$$\hat{\mathcal{E}}' = \sqrt{\frac{c}{\Gamma L}}\hat{\mathcal{E}}\,, \tag{13.41}$$

and we have introduced scaled envelope operators for the polarization and spin coherences

$$\hat{\mathcal{P}}' = \sqrt{N}\hat{\sigma}_+\,, \qquad \hat{\mathcal{S}}' = \sqrt{N}\hat{\sigma}_-\,. \tag{13.42}$$

Applying these transformations and making these substitutions to Eqns. 13.32, 13.33 and 13.36 we arrive at the transformed equations of motion

$$\partial_\tau \hat{\mathcal{P}}' = i\sqrt{d\Gamma}\hat{\mathcal{E}}' + i\Omega\hat{\mathcal{S}}' - (\gamma_{ge} + i\Delta)\,\hat{\mathcal{P}}'\,, \tag{13.43}$$

$$\partial_\tau \hat{\mathcal{S}}' = i\Omega^*\hat{\mathcal{P}}' - (\gamma_{gs} + i\delta - i\Delta_{\mathrm{Stark}})\,\hat{\mathcal{S}}'\,, \tag{13.44}$$

$$\partial_\xi \hat{\mathcal{E}}' = i\sqrt{d}\hat{\mathcal{P}}'\,. \tag{13.45}$$

Compared to Eqns. 13.32, 13.33 and 13.36, these equations of motion have the advantage of being written in terms of the directly measurable optical depth d. From this point on we will work with these transformed equations and make the direct notational substitutions $\hat{\mathcal{E}}' \to \hat{\mathcal{E}}$, $\hat{\mathcal{P}}' \to \hat{\mathcal{P}}$, $\hat{\mathcal{S}}' \to \hat{\mathcal{S}}$ in order to save on apostrophes. These are the essential equations describing atom-light interactions in a Λ ensemble, and we will return to them many times in the following chapters.

However, there remain two further levels of approximation that we will make when appropriate: the adiabatic and far-detuned (Raman limit) approximations.

13.1.7 Adiabatic approximation

We may adiabatically eliminate the polarization in order to reduce Eqns. 13.43 to 13.45 to only two differential equations. When the single-photon detuning is considerably larger than the two photon detuning $\Delta \gg \delta$, the polarization envelope $\hat{\mathcal{P}}$ develops only slowly compared to the electric field and spin envelopes. We adiabatically eliminate $\hat{\mathcal{P}}$ by taking $\partial_t \hat{\mathcal{P}} \approx 0$, after which equation Eqn. 13.43 gives

$$\hat{\mathcal{P}} = \frac{\sqrt{d\Gamma}\hat{\mathcal{E}} + \Omega\hat{\mathcal{S}}}{\Delta - i\gamma_{ge}}\,. \tag{13.46}$$

By substitution back into the remaining Maxwell-Bloch equations we have the two adiabatic approximation equations of motion

$$\partial_\tau \hat{\mathcal{S}}' = \frac{\Omega^*\sqrt{d\Gamma}}{\gamma_{ge} - i\Delta}\hat{\mathcal{E}} - (\gamma_{gs} + \gamma_{\mathrm{scat}} + i\delta)\,\hat{\mathcal{S}}\,, \tag{13.47}$$

$$\partial_\xi \hat{\mathcal{E}} = \frac{d\Gamma}{\gamma_{ge} - i\Delta}\hat{\mathcal{E}} + \frac{\sqrt{d}\Omega}{\gamma_{ge} - i\Delta}\hat{\mathcal{S}}\,. \tag{13.48}$$

These are the equations that we will use most frequently to model our system. The AC stark shift that we subtracted from δ in Eqn. 13.33 has cancelled out of Eqn. 13.47 as we intended. The coherence relaxation rate is increased by the control field scattering

$$\gamma_{\mathrm{scat}} = \frac{\gamma_{ge}\Omega^2}{\gamma_{ge}^2 + \Delta^2}\,, \tag{13.49}$$

due to power broadening of the excited state. This is the mechanism by which the control field relaxes the spin coherence, and is important to understanding the operation of

gradient echo memories, with which we will soon be concerned. In Eqn. 13.47, the term

$$\frac{d\Gamma}{\gamma_{ge} - i\Delta}\hat{\mathcal{E}} \tag{13.50}$$

comprises real and imaginary parts corresponding to, respectively, absorption and dispersion caused by the excited state.

13.1.8 Raman limit

In the far-detuned (Raman) limit we have $\Delta \gg \gamma_{ge}$, and therefore the polarization becomes real

$$\hat{\mathcal{P}} \approx \frac{\Omega}{\Delta}\hat{\mathcal{S}} + \frac{\sqrt{d\Gamma}}{\Delta}\hat{\mathcal{E}}, \tag{13.51}$$

which further reduces the Maxwell-Bloch equations to

$$\partial_\tau \hat{\mathcal{S}} = i\frac{\Omega^*\sqrt{d\Gamma}}{\Delta}\hat{\mathcal{E}} - (\gamma_{gs} + \gamma_{\text{scat}} + i\delta)\hat{\mathcal{S}}, \tag{13.52}$$

$$\partial_\xi \hat{\mathcal{E}} = i\frac{d\Gamma}{\Delta}\hat{\mathcal{E}} + i\sqrt{d}\frac{\Omega}{\Delta}\hat{\mathcal{S}}. \tag{13.53}$$

In this far detuned limit, off resonant absorption is zero. The dispersion is also negligible, so long as $\Delta \gg g\hat{\mathcal{E}}$. In any case, we can incorporate dispersion into the envelope mode so that the Raman limit equations become simply

$$\partial_\tau \hat{\mathcal{S}} = i\frac{\Omega^*\sqrt{d\Gamma}}{\Delta}\hat{\mathcal{E}} - (\gamma_{gs} + \gamma_{\text{scat}} + i\delta)\hat{\mathcal{S}}, \tag{13.54}$$

$$\partial_\xi \hat{\mathcal{E}} = i\sqrt{d}\frac{\Omega}{\Delta}\hat{\mathcal{S}}. \tag{13.55}$$

These Raman-limit equations are identical to the equations of motion for two-level atoms, with effective two-photon coupling strength, optical depth and decoherence rate

$$g_{\text{eff}} = \frac{g\Omega}{\Delta}, \qquad d_{\text{eff}} = \frac{g^2 N}{c\Gamma}\left(\frac{\Omega}{\Delta}\right)^2, \qquad \gamma_{\text{eff}} = \gamma_{ge} + \gamma_{\text{scat}}. \tag{13.56}$$

In the remaining chapters of the thesis we will be dealing with two-photon transitions of this sort almost exclusively. Consequently, when we discuss the optical depth and coupling strength of our ensemble quantum memory we will mean the effective optical depth d_{eff} and effective coupling strength g_{eff} at some Δ, Ω combination, usually corresponding to the experimental configuration.

As we've seen, the Raman limit neglects some important physics, and we will not always be able to take it. Dispersion, in particular, will play an important role when the field strength is large, as it will be when we consider stationary light fields in Sec. 13.3. For this reason we will usually work with the adiabatic, and not Raman limit, Maxwell-Bloch equations of motion.

In the remainder of this chapter we illustrate first the operation of a gradient echo memory and second the generation of stationary light fields in the ensemble. Generating stationary light requires including counterpropagating fields in this model, to which we will turn in time. In Chap. 16 we further extend the model to describe two frequency separated, copropagating field modes such that the ensemble can be operated as a dual-rail memory

for frequency qubits.

13.1.9 Numerical modelling

We simulate the propagation of light in atomic ensembles by solving the above equations of motion numerically with the open-source numeric and stochastic partial differential equation solver XMDS2 (the eXtensible Multi-Dimensional Simulator)[325, 326]. XMDS2 compiles C++ code to solve systems of ordinary differential equations, like our equations of motion for the ensemble. The solver is compiled according to an XML document that dictates the dimensions and boundary conditions of the problem, along with the numerical integration algorithm to be used. XMDS and XMDS2 were developed jointly at the University of Queensland and the Australian National University by G. Dennis, G. Collecutt, P. D. Drummond M. Johnsson and J. Hope.

For the problems in this thesis, we will use only simple solvers. By assuming an ensemble of uniform cross section and density we have reduced to equations of motion to two first-order differential equations in ξ for the polarization and ground-state coherence envelopes, and a single first-order differential equation in τ for the electric field envelope. We can therefore solve this problem on a two dimensional τ-ξ (or t-z) grid. The input fields are specified by a boundary condition applied at one end of the grid and the local ODEs are solved by a method-of-lines approach. The spatial equation Eqn. 13.45 is integrated with a non-adaptive 4th-order Runge-Kutta algorithm, and the temporal equations Eqns. 13.43 and 13.44 are integrated by an adaptive 4th-order Runge-Kutta algorithm.

13.2 Gradient echo memory

Gradient echo memory (GEM) is a technique for reversibly storing and recalling quantum optical fields inside an ensemble of emitters [327–329]. It is an instance of the broader category of memories that operate by controlled reversible inhomogeneous broadening (CRIB) [330, 331]. GEM is a promising candidate for real-world optical quantum memories, as we demonstrated in Chaps. 16 and 17 with cold atomic vapours. In this section we consider the relevant theory of operation, using the Maxwell-Bloch equations developed above. The operation of a GEM may be described analytically in the appropriate limits, and this problem has been considered extensively over the last decade [329]. A great deal of this detail lies outside the scope of this thesis, and interested readers should see, for example, the thesis of Geoff Campbell, Ref. [332].

In a GEM the resonant transition of an atomic ensemble is broadened by the application of external fields such that the resonant frequency, and therefore the signal detuning $\Delta(\xi)$, varies across the ensemble (where we are using the scaled length $\xi = z/L$). Each spectral component of the signal is resonant with a separate section of the ensemble. Once absorbed, the optical pulse is mapped to a spatial coherence that evolves according to the local resonant frequency. GEM, like other CRIB memories [330, 331], works by reversing this evolution such that the ensemble reconstitutes its original polarization under excitation. Once returned to this state, the ensemble spontaneously and coherently emits back into the exciting mode. Because the Maxwell-Bloch equations are linear under weak excitation, this operation maps the complete quantum state of the field- be it a coherent state, single-photon state, or any other exotic quantum state- onto the collective polarization coherence, and then maps it back again. Under ideal conditions this operation reconstitutes the original state exactly.

The time evolution of the coherence is reversed by switching the applied fields such that the local detuning inverts across the ensemble, $\Delta(\xi) \to -\Delta(\xi)$. This neatly avoids the need for rotations by π-pulses, on which photon-echo (the photonic analogue of spin echo [333]) and some CRIB memories rely [334, 335]. To operate efficiently, it is necessary that reemission occurs without any subsequent reabsorption. This is ensured so long as the the detuning function $\Delta(\xi)$ is monotonic along the propagation direction ξ. Because the ensemble at each position ξ is resonant with only one frequency component, the GEM operation maps the spectrum of the excitation pulse to a spatial distribution. When the detuning varies linearly along the direction of propagation, $\Delta(\xi) = \delta_\xi \xi$, the stored coherence in ξ is exactly the Fourier transform of the input field in τ. This makes GEM a natural platform for spectral operations with quantum fields [336, 337].

13.2.1   Λ-GEM

Although GEM is possible with a two-level ensemble, the storage lifetime will be limited by the relaxation rate $\gamma_{ge} \propto \Gamma$ of the polarization coherence $\hat{\mathcal{P}}$. In the Λ-GEM scheme, a strong coupling field forms an off-resonant Raman transition between the ground and metastable states $|g\rangle \leftrightarrow |s\rangle$. The signal pulse is stored not in the polarization $\hat{\mathcal{P}}$, but in the spin wave $\hat{\mathcal{S}}$. The linewidth of the Raman transition is not limited by the excited state lifetime, approaching the spin decoherence rate γ_{gs} in the far-detuned limit, as shown by Eqn. 13.54. γ_{gs} depends only in the elastic dephasing and inelastic depopulating terms according to Eqn. 13.27. The coherence time of the spin wave $\hat{\mathcal{S}}$ can therefore be much longer than the coherence time of the polarization $\hat{\mathcal{P}}$ so long as these Γ_{coll} and Γ_{deph} are small. For an ideal ensemble of stationary atoms addressed with narrow linewidth lasers, both terms are zero. Unfortunately such a perfect ensemble is hard to engineer, but in Chap. 17 we will get quite close with a free-falling cloud of cold rubidium atoms.

From Eqn. 13.56, the effective optical depth decreases with Δ according to $d_{\text{eff}} \propto \left(\frac{\Omega}{\Delta}\right)$. Therefore in order to operate with a large detuning, the resonant optical depth of the ensemble must be very large. In practice, the optical depth is constrained by the size and density of the ensemble in an experiment. Simultaneously achieving high optical depths and long coherence times is challenging. Real experiments usually operate with a control field that produces control field scattering at rate $\gamma_{\text{scat}} \propto \Gamma \left(|\Omega|/\Delta\right)^2$ such that $\hat{\mathcal{S}}$ relaxes at rate $\gamma_{gs} + \gamma_{\text{scat}}$ that is not negligible.

Applying a field gradient further broadens the two-photon resonance. For successful operation GEM requires $\delta_\xi > \gamma_{gs} + \gamma_{\text{scat}}$. This further reduces the optical depth $d_{\text{eff}} \propto \delta_\xi^{-1}$. From this relationship we can see that the required resonant optical depth is proportional to the bandwidth of pulses to be stored. GEM is usually, but not necessarily, operated with a broadened linewidth that is still small compared to the excited state linewidth, $\delta_\xi < \Gamma$.

13.2.2   The ensemble polariton

The signal field enters the ensemble and drives a spin wave, but is not itself absorbed completely. The system is a superposition of $\hat{\mathcal{E}}$ and $\hat{\mathcal{S}}$ that we call a 'polariton'. The polariton is best described, in the spatial Fourier domain. Transforming the spatial differential of the Raman-limit equations of motion Eqn. 13.55 with the assumption gives us

$$k\hat{\mathcal{E}} = \sqrt{d_{\text{eff}}}\hat{\mathcal{S}}\,. \tag{13.57}$$

We can define bright and dark modes of the combined system in the adiabatic limit

$$\hat{B} = \sin\theta\hat{\mathcal{E}} + \cos\theta\hat{\mathcal{S}}\,, \qquad \hat{D} = \cos\theta\hat{\mathcal{E}} - \sin\theta\hat{\mathcal{S}}\,, \tag{13.58}$$

where the mixing angle $\theta = \arctan\left(k/\sqrt{d_{\text{eff}}}\right)$. The polariton adiabatically follows the dark state $\hat{D}$, therefore the evolution of the polariton has two key characteristics. Firstly, the spatial momentum of the polariton k increases while the gradient is on, and decreases when the gradient is reversed according to

$$k(t) = k_0 + \delta_\xi(t)t\,, \tag{13.59}$$

where the initial spin wave momentum depends on the difference of the probe and control fields $k_0 = k_p - k_c$. The spatial phase coils and uncoils during storage and retrieval. Second, the larger the momentum the lower the proportion of the polariton that is contained in the optical field. Until the gradient is reversed, the polariton momentum k grows and the optical field amplitude drops.

In general, storage and recall by GEM may distort the phase front of $\hat{\mathcal{E}}$, particularly when the signal and memory bandwidths are comparable. Switching δ_z reverses the evolution of the $\hat{S}$ but not $\hat{E}$, and the evolution is therefore not perfectly symmetric [338]. Integrating the equations of motion Eqn. 13.57 yields a transfer function for the recalled pulse that incorporates phase and frequency distortion [332].

In many GEM experiments, including the ones in Chaps. 16 and 17, the atoms in the ensemble are not stationary. They may be warm atoms diffusing through a vapour cell, or cold atoms expanding ballistically out of a magneto-optical trap, but however the atoms move they will carry their local coherence with them, breaking the field reversal symmetry of $\delta_\xi \to -\delta_\xi$. This has the effect of washing out the phase of $\hat{S}$ over a characteristic distance D that increases with time. When the ratio D/k is large, the proportion of the polariton that can be recalled coherently is low.

13.2.3   GEM operation example

Figure 13.2 shows the theoretical operation of a Λ-GEM in an ideal atomic ensemble. Figure 13.2(a) and (b) show, respectively, the propagation of $\hat{\mathcal{E}}$ and $\hat{S}$. $\hat{\mathcal{P}}$ is not plotted. The fields are shown by phase-intensity figures, in which the opacity and hue represent, respectively, the intensity and phase of the field[3]. In Fig. 13.2(a) we see a Gaussian envelope $\hat{\mathcal{E}}$ enter at $\xi = 0$ and propagate through the ensemble, simultaneously increasing k and losing amplitude as the optical component of the polariton drops. Meanwhile, the spin wave $\hat{S}$ shown in Fig. 13.2(b) increases both k (visible as a coiling of the spatial phase- the wavefronts in ξ become closer) and amplitude. The spatial coherence in ξ is the Fourier transform of $\hat{\mathcal{E}}$ in τ, which in this case is simply another Gaussian. The dashed line in Fig. 13.2(b) indicates the point at which the gradient δ_ξ is reversed, and the coherence begins unwinding. As k decreases again, the proportion of the polariton in the optical field increases until the original wave packet is reconstituted and exits the ensemble at $\xi = 1$. Just like the Dicke state in Eqn. 13.1, the ensemble spontaneously and coherently emits a field when the coherence is phase-matched to the optical mode, in this case a two-photon Raman transition between the control Ω and probe $\hat{\mathcal{E}}$.

Figure 13.2(c) shows the input and output pulse intensities as a function of time. No dephasing or depopulating terms are included in this simulation, so loss during storage is

---

[3]This is the same method we used to plot dipole field images in Figs. 4.7 and 4.8.
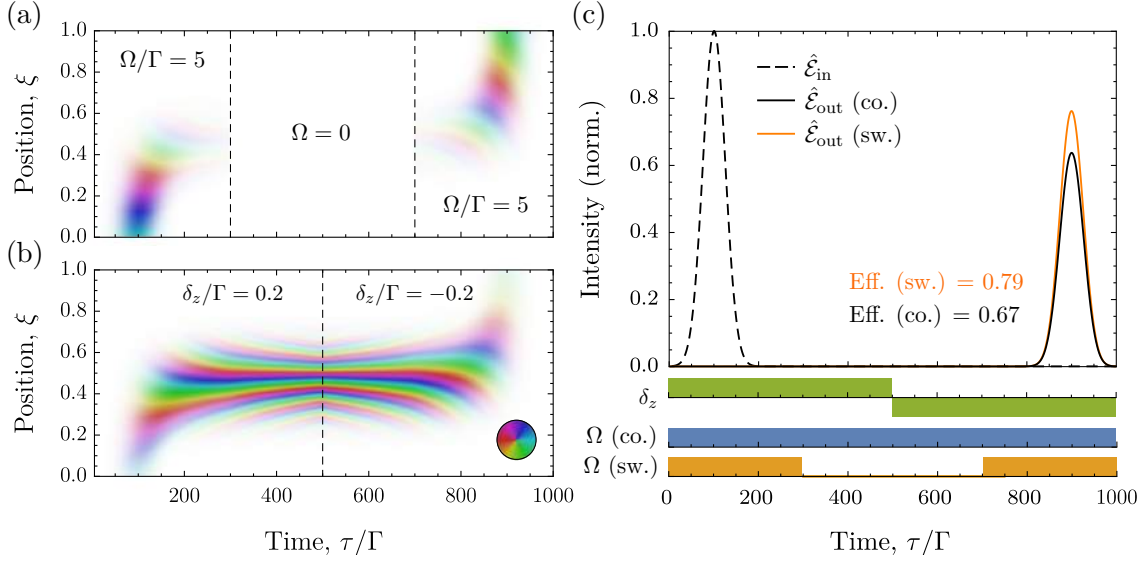
Figure 13.2: Storage and recall by Λ-GEM. Propagation of (a) the electric field envelope $\hat{\mathcal{E}}$ and (b) the spin wave $\hat{S}$ through the ensemble. The fields are plotted with hue $\angle\hat{\mathcal{E}}$ according to the colour wheel (inset) and opacity $\left|\hat{\mathcal{E}}\right|^2$. (c) Field intensity at the input (dashed) and output (solid) of the ensemble for two operation methods: continuous (black) and switched (orange) control. In either case the detuning gradient δ_ξ reverses at time $\tau_s = 500/\Gamma$. The pulse scheme for δ_ξ both continuous and switched Ω are shown at bottom. These simulations are performed with $d = 1000$.

entirely due to control field scattering. Two output pulses are shown, corresponding to storage performed with a constant control field $\Omega(\tau) = \Omega_c$ and storage performed with $\Omega_c = 0$ when the polariton is mostly spin wave. Switching off the control field during this part of the storage reduces total control field scattering and increases the memory efficiency from 0.67 to 0.79. The envelopes $\hat{\mathcal{E}}$ and $\hat{\mathcal{E}}$ shown in Fig. 13.2(a) and (b) are actually the envelopes under switched-control GEM. The dashed lines in Fig. 13.2(a) indicate the switching points according to

$$\Omega(\tau) = \begin{cases} \Omega & \tau/\Gamma < 300 \\ 0 & 300 < \tau/\Gamma < 700 \\ \Omega_c & 700 < \tau/\Gamma \end{cases} . \tag{13.60}$$

When γ_{scat} is not negligible, it is advantageous to switch the control field off during storage, but control field scattering during the read and write stages can only be limited by simultaneously increasing d and Δ. The switch sequences for δ_ξ and Ω are included at the bottom of Fig. 13.2(c). When $\Omega = 0$, $|D\rangle = \hat{S}$. Removing the control field instantaneously immediately suppresses the optical component of the polariton. This process is not adiabatic, and may produce further changes to the phase and frequency of the output pulse. This is visible in Fig. 13.2(a) as a slight angle to the output phase front that is not present without control field switching.

This simulation is performed without including any atomic motion. With atomic motion, it is advantageous to keep the polariton at low k. This may be achieved simply by turning the field gradient off after the signal is absorbed. Like the control field, the gradient is only necessary during read and write operations. Following Eqn. 13.57, the
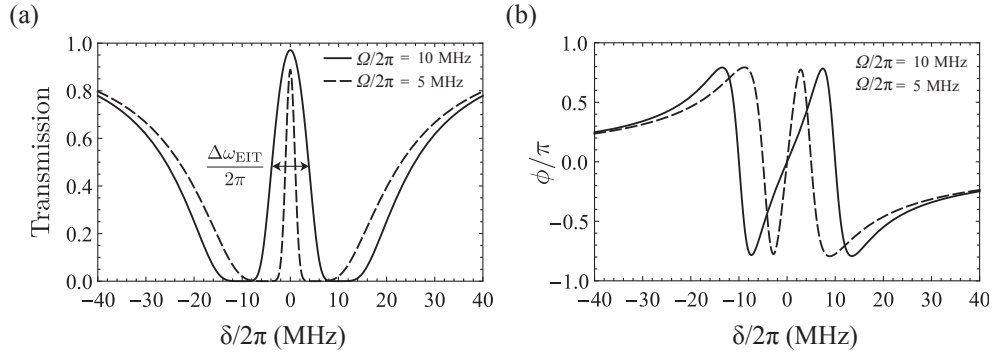
Figure 13.3: Electromagnetically induced transparency. A weak probe, $\hat{\mathcal{E}}$, copropagates with a bright control field Ω which opens a narrow transparency window for the probe about the two-photon resonance $\delta = 0$. (a) Probe transmission and (b) phase shift, ϕ through an ensemble of Λ-type atoms as a function of two-photon detuning δ. The width of the EIT window, $\Delta\omega_{\text{EIT}}$, increases with control field power (dashed: lower power, solid: higher power).

spatial evolution freezes while $\delta_\xi = 0$.

We will often choose to use a control field at a slight angle θ to the probe beam, this makes it easier to separate the beams after the memory. However, the angle increases the initial spin wave momentum k_0. This spatial frequency causes accelerated decoherence in the presence of atomic motion. Ideally the momentum k should be kept low by limiting both δ_ξ and θ.

13.3 Stationary light

Atom ensembles are a non-linear optical medium. In addition to storing and recalling light fields, they may also be used to generate an interaction between light fields that are stored or travelling in the ensemble. Interactions of this sort are the basis of ensemble-mediated two-qubit optical phase gates [339]. The total phase shift is the product of the interaction strength and time, and so nonlinear optics usually involves high intensity fields. For photonic qubit gates it is necessary to show a large phase shift for fields down to the single photon level. The key to a large optical nonlinearity with low-light fields is therefore to localize two fields within a small region of an ensemble such that the electric field per photon ϵ_ω is large, and then to hold the fields inside that region for long enough to produce a conditional phase shift. The optical component of the polariton is inversely proportional to its velocity under normal GEM operation. As a result, GEM cannot (on its own) enhance the non-linear interaction between optical qubits.

An older optical quantum memory protocol (see sec. 14.2) is based on the phenomena of electromagnetically induced transparency (EIT), which exists in Λ-ensembles configured identically toFig. 13.1 in the limit of $\Delta \to 0$ [340–342]. The bright control field opens a narrow transparency for a weak probe $\hat{\mathcal{E}}$ in an ensemble that would otherwise be opaque, as shown in Fig. 13.3(a). At this two-photon resonance the probe and control excitations interfere such that the resonant probe is unable to drive the excited state $|e\rangle$. The two-photon transparency window reduces the group velocity of the probe in proportion to its linewidth, which is determined by the control field Rabi frequency Ω as shown in Fig. 13.3(b). The slow light exists as a polariton superposition per sec. 13.2.2 [343]. A resonant probe field may be slowed and then stopped inside the ensemble by adiabatically

reducing the control field power to zero once the probe has been absorbed. However, once again, the optical field intensity is in inverse proportion to its velocity such that the possible interaction between EIT slowed light fields is normally weak.

However, an alternative scheme has been proposed to generate large stationary fields by the addition of a counter-propagating control field [344]. In this scheme, which was quickly realized in experiments[345, 346], counter-propagating control fields drive a non-zero optical field that is not just slow, but completely stationary. The control fields simultaneously propel the polariton in opposite directions, and it becomes unable to propagate. This approach was used to demonstrate the first interaction of two stopped light pulses in an atomic medium [347].

In this section we introduce a new technique for the generation of bright, stationary fields inside a Λ-ensemble by an extension of GEM that includes counterpropagating control fields. The atomic coherences that drive these stationary light fields have been directly and dynamically imaged [348], confirming the theory presented here. In contrast to previous work with stationary light in EIT, the spin wave and optical field need not coincide. This opens the possibility of engineering more exotic stationary light distributions. This theoretical work is published in Ref. [9].

13.3.1   Counter-propagating fields

To describe our stationary light effect, we first introduce counter propagating fields and revisit the Maxwell-Bloch propagation equations, Eqns. 13.47 and 13.48. Many of the assumptions we made to arrive at these equations don't strictly hold with two counter-propagating reference frames, however we will derive equivalent expressions and state the conditions under which they are valid. We follow the same method as Ref. [323] and write the Jaynes-Cummings interaction Hamiltonian for counterpropagating probe fields $\hat{a}^{\pm}$ and control fields $\Omega^{\pm}$ with the spatial dependence of each field separated explicitly from the operators such that we have

$$
\hat{H}_{\text{int}} = \hbar \sum_{i=1}^{N} \Big[\left(\Omega^{+} e^{-i\omega_c^{+}(t-z_i/c)} + \Omega^{-} e^{-i\omega_c^{+}(t+z_i/c)} \right) \hat{\sigma}_{se}
$$
$$
+ g \left(\sqrt{\frac{L}{2\pi c}} \right) \left(\int_{\omega_p^{+}} d\omega \, \hat{a}_\omega e^{i\omega z/c} + \int_{\omega_p^{-}} d\omega \, e^{-i\omega z/c} \right) \hat{\sigma}_{ge} \Big] . \quad (13.61)
$$

The control fields are at definite frequencies ω_c^{+} and ω_c^{-}, so we may separate both the time and space dependence of the control fields. The control field frequencies $\omega_c^{\pm}$ are not necessarily equal.

We define positive frequency forward and backward propagating envelopes with frequencies $\omega_p^{\pm}$ within a narrow bandwidth about ω_p. This is similar to Sec. 13.1.2, incorporating the temporal (but not spatial) dependence

$$
\hat{\mathcal{E}}_p^{\pm} = \sqrt{\frac{L}{2\pi c}} e^{i\omega_p^{+}(t \mp z/c)} \int_{\omega_p^{\pm}} d\omega \, \hat{a}_\omega e^{i \pm \omega z/c} , \quad (13.62)
$$

We now, once again, define slowly-varying envelope operators at position z for the local atomic state, but this time we define two envelope operators for each atomic transition operator, one in each of the forward and backward propagating frames of the addressing

field

$$\hat{\sigma}_{eg}^{\pm} = \frac{1}{N_z} \sum_{i}^{N_z} \hat{\sigma}_{eg} e^{-i\omega_p^{\pm}(t \mp z/c)} \,, \tag{13.63}$$

$$\hat{\sigma}_{es}^{\pm} = \frac{1}{N_z} \sum_{i}^{N_z} \hat{\sigma}_{es} e^{-i\omega_c^{\pm}(t \mp z/c)} \,, \tag{13.64}$$

$$\hat{\sigma}_{sg}^{\pm} = \frac{1}{N_z} \sum_{i}^{N_z} \hat{\sigma}_{sg} e^{-i(\omega_p^{\pm} - \omega_c^{\pm})(t \mp z/c)} \,, \tag{13.65}$$

$$\tag{13.66}$$

where N_z is the number of atoms in the slice at position z. The definition of our ground state population envelope operators is unchanged,

$$\hat{\sigma}_{gg} = \frac{1}{N_z} \sum_{i}^{N_z} \hat{\sigma}_{gg} \,, \qquad \hat{\sigma}_{ss} = \frac{1}{N_z} \sum_{i}^{N_z} \hat{\sigma}_{ss} \,, \tag{13.67}$$

but we define separate excited state operators

$$\hat{\sigma}_{ee}^{\pm} = \frac{1}{N_z} \sum_{i}^{N_z} \hat{\sigma}_{ee} e^{-i\omega_p^{\pm}t} \,, \tag{13.68}$$

in the reference frame of each probe field.

Substituting these envelope operators in to the interaction Hamiltonian yields cross-terms of the form $\Omega^{\pm}\hat{\sigma}_{eg}^{\mp}$ with spatial dependence $e^{-i[\omega_c^{\pm}(t-z/c) - \omega_c^{\mp}(t+z/c)]}$ and $\hat{\mathcal{E}}^{\pm}\hat{\sigma}_{eg}^{\mp}$ with spatial dependence $e^{-i[\omega_p(t-z/c) - \omega_p(t+z/c)]}$. These beat-note terms have large spatial frequencies and cause, respectively, a rapid AC Stark shift oscillation and high spatial frequency coherences. For $\Delta \gg \Delta\omega_p^{\pm}$, these fast spatial terms average to zero and so we neglect them here.

This interaction drives two spin waves $\hat{\sigma}_{gs}^{\pm}$ with momentum $\mathbf{k}_s^{\pm} = \mathbf{k}_p^{\pm} - \mathbf{k}_s^{\pm}$. So long as the control fields are phase matched, we have $\mathbf{k}_s^{+} = \mathbf{k}_s^{-}$ and we can take $\hat{\sigma}_{gs}^{+} = \hat{\sigma}_{gs}^{-} = \hat{\sigma}_{gs}$. Phase matching can be achieved with counterpropagating control fields of equal detuning, but unfortunately we're about to see that the more useful case concerns control fields of equal and opposite detuning $\Delta^{+} = -\Delta^{-} = \Delta$. Phase matching may still be achieved with this two-colour control field by introducing equal and opposite angles θ^{+} and θ^{-} between each control and its corresponding probe field. For the purpose of this derivation, we're going to assume that the phase matching condition is met. The forward and backward propagating fields therefore drive a common spin wave $\hat{\sigma}_{gs}$.

Making the usual weak-probe approximation, we're left with the following equations for counter-propagating probe and control fields

$$\partial_t \hat{\sigma}_{ge}^{\pm} = ig\hat{\mathcal{E}}^{\pm} + i\Omega^{\pm}\hat{\sigma}_{gs} - (\gamma_{ge} + i\Delta^{\pm}) \tag{13.69}$$

$$\partial_t \hat{\sigma}_{gs} = i\Omega^{+*}\hat{\sigma}_{ge}^{+} + i\Omega^{-*}\hat{\sigma}_{ge}^{-} - (\gamma_{gs} + i\delta - i\Delta_{\text{Stark}}) \tag{13.70}$$

$$(\partial_t \pm c\partial_z)\hat{\mathcal{E}}^{\pm} = igN\hat{\sigma}_{ge}^{\pm} \,, \tag{13.71}$$

where Δ_{Stark} contains contributions from both control fields.

Again, because we have two fields $\hat{\mathcal{E}}^{\pm}$ travelling in opposite directions, we cannot
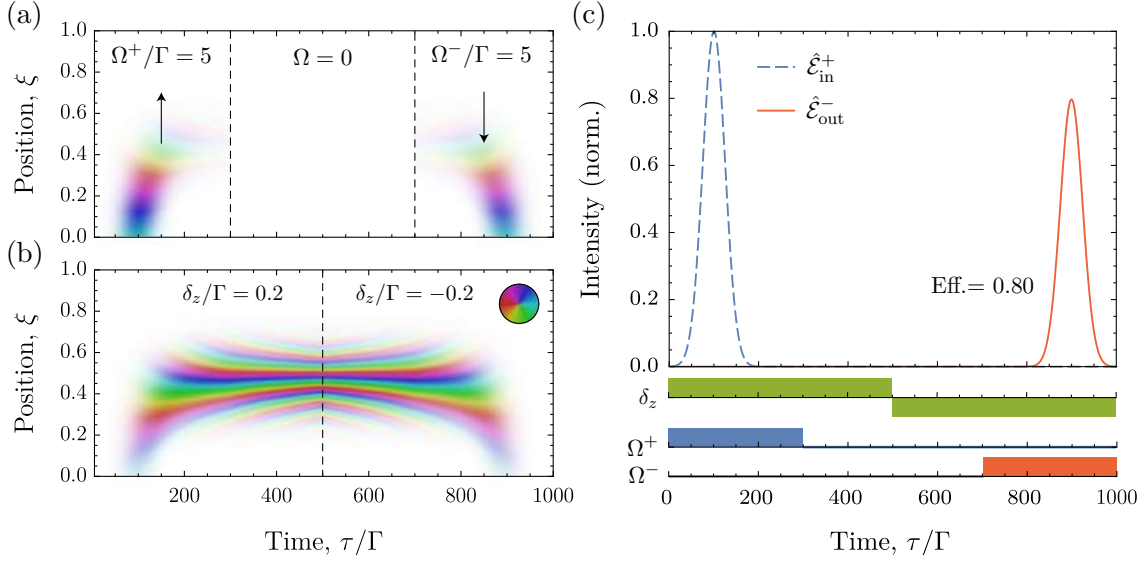
Figure 13.4: Storage and reverse recall by Λ-GEM. Propagation of (a) the electric field envelope $\hat{\mathcal{E}}$ and (b) the spin wave $\hat{S}$ through the ensemble. The fields are plotted with hue $\angle\hat{\mathcal{E}}$ according to the colour wheel (inset) and opacity $\left|\hat{\mathcal{E}}\right|^2$. (c) Field intensity at the input (dashed) and output (solid) of the ensemble for forward (blue) and backward (red) propagating fields. The field is recalled into the backward propagating field by recalling with the backward propagating control according to the pulse scheme at bottom. These simulations are performed with $d = 1000$.

move the equations into a single frame travelling at the speed of light. However, so long as $L/c \ll \Omega, \Delta, \Gamma$, the time derivative in Eqn. 13.71 is negligible. We may discard this term without changing frames under reasonable experimental conditions.

Making the same 'optical depth' transformations as in Sec. 13.1.6 and the adiabatic approximation as in Sec. 13.1.7 we have

$$\partial_t \hat{S} = \frac{\Omega^{+*}\sqrt{d}\Gamma}{\gamma_{ge} - i\Delta^+}\hat{\mathcal{E}}^+ + \frac{\Omega^{-*}\sqrt{d}\Gamma}{\gamma_{ge} - i\Delta^-}\hat{\mathcal{E}}^- - (\gamma_{gs} + \gamma_{\text{scat}} + i\delta)\hat{S}, \qquad (13.72)$$

$$\partial_\xi \hat{\mathcal{E}}^\pm = \pm\left(\frac{d\Gamma}{\gamma_{ge} - i\Delta^\pm}\hat{\mathcal{E}}^\pm + \frac{\sqrt{d}}{\gamma_{ge} - i\Delta^\pm}\hat{S}\right), \qquad (13.73)$$

where γ_{scat} now contains contributions from both the control fields.

13.3.2   Reverse-recall GEM

Armed with these equations of motion for counter-propagating fields we can simulate the operation of a GEM with forwards and backward control fields with equal detuning $\Delta^+ = \Delta^- = \Delta$. For example, by recalling a forward-stored pulse with a backward-propagating control field we may restore the quantum light field in the backwards mode, as shown in Fig. 13.4. This reverse-recall GEM has complete time reversal symmetry, and introduces less phase distortion than the typical operation.
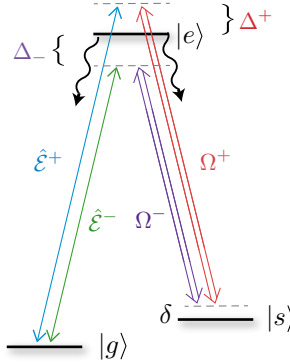
Figure 13.5: Level scheme for generating stationary light fields in a Λ-atom ensemble with GEM. Counter-propagating probe and control fields couple to a common spin coherence. The forward and backward propagating fields have equal and opposite single-photon detuning $\Delta^+ = -\Delta^- = \Delta$. Phase matching is achieved by introducing equal and opposite angles between each control field $\Omega^\pm$ and weak probe fields $\hat{\mathcal{E}}^\pm$.

13.3.3 Stationary light simulations

The imaginary part of the the first term in Eqn. 13.73 is the dispersion. Stationary light requires that these dispersion terms are symmetric in $\hat{\mathcal{E}}^\pm$, which is true for $\Delta^+ = -\Delta^- = \Delta$ (as we signposted earlier). Under this two-colour control configuration, shown in Fig. 13.5, the equations of motion are symmetric in $\hat{\mathcal{E}}^\pm$ up to the assumptions we made above.

Because of this symmetry, simultaneous two-colour control of a probe pulse stored by GEM may amplify the optical component of the polariton, without pushing the polariton out of the ensemble. Integrating Eqn. 13.73 over ξ in the Raman limit and substituting into Eqn. 13.72, we see that the spin wave is static under two-colour control so long as the spatial integral of the spin wave is zero. If $\int d\xi\, \hat{\mathcal{S}} \neq 0$ then $\hat{\mathcal{E}}^\pm(\xi = 0, 1) \neq 0$ and the probe fields evolve, and perhaps leak from the ensemble, until the spinwave reaches an equilibrium state with zero mean. At equilibrium $\hat{\mathcal{E}}^\pm$ circulate in the centre of the ensemble, the divided spin wave having reached a relative phase such that $\hat{\mathcal{E}}^\pm$ interfere destructively to arrest any further evolution.

We'll consider two examples of this two-colour stationary light field: first, the effect of the control on a typical Gaussian pulse stored by GEM, Fig. 13.6(a–d), and second the effect on a coherence that has been chosen to produce stable stationary light fields, Fig. 13.6(e–h).

In Fig. 13.6(a–d) a Gaussian pulse is stored in the ensemble by GEM. The second stage in this stationary light sequence (high k) is the application of two-colour control fields to the stored polariton. The counter-propagating control fields drive counter-propagating probe fields that inherit the momentum of the polariton and circulate back and forth over the coherence. For $k \gg 1$, $\int d\xi\, \hat{\mathcal{S}} \approx 0$ zero, and the light fields are stationary. However, control field scattering increases alongside the optical field amplification. Including this effect, the control fields required to generate a large field at high k quickly reduce the coherence (and the field it drives) to zero.

The third stage ($k \to 0$) of the sequence in Fig. 13.6(a-d) is the evolution of $\hat{\mathcal{E}}^+$ and $\hat{\mathcal{S}}$ under two-colour control fields as $k \to 0$. The control fields drive counter-propagating probe fields in proportion to $\Omega^\pm$, and inversely with k. Even with lower control power, the probe fields are much brighter than they were at high k. However, the unmodified spin

wave is unstable. As $\mathbf{k} \to 0$ the mean of $\hat{\mathcal{S}}$ becomes non-zero and the counter-propagating probe fields split $\hat{\mathcal{S}}$ and push each half towards the edge of the ensemble until the fields escape at the edge as shown by the leakage in Fig. 13.6(d). At each time τ the remaining spin wave is an equilibrium state satisfying $\int d\xi \hat{\mathcal{S}} = 0$, and the remainder may be recalled as usual.

Reaching stationary light equilibrium by the absorption of a Gaussian pulse, as in Fig. 13.6(a-d), without leakage requires very high d_{eff} so that the coherence is displaced without reaching the edge. However, we can manufacture the equilibrium spin wave by absorption of a modulated pulse. This is the second scheme, shown in Fig. 13.6(e-h). The input pulse is modulated such that

$$\hat{\mathcal{E}}_{\text{in}}^{+} = \left(e^{i\omega_m t} + e^{-i\omega_m t + \phi} \right) e^{t^2/\sigma^2} \tag{13.74}$$

where σ is the pulse width, ω_m is the modulation frequency and ϕ is an arbitrary phase. GEM creates a spin wave that is the Fourier transform of the input pulse. In this case the side bands of the pulse create a spatially divided spin wave. It so happens that the chosen modulation produces a temporal shape that looks like two divided pulses, but this is only a coincidence. The modulation frequency could well be higher than the initial pulse bandwidth, in which case the pulse would clearly show a fast modulation of a Gaussian envelope.

We may choose the phase ϕ such that $\int d\xi \hat{\mathcal{S}} = 0$ and the divided spin wave is stable under simultaneous two-colour control fields. In this simulation the stationary light fields are brighter than the input pulse even with only $\Omega^{\pm} = 5\Gamma$ and the control field scattering (not shown) is not considerable. The remaining leakage is due to off-resonant absorption, and vanishes in the Raman limit.

In contrast to all previous stationary lights schemes, the stationary light fields in this scheme do not need to coincide with the coherences. In the implementation explored here, and performed experimentally by my colleagues in Ref. [348], the stationary light field is strongest where the coherence is near zero. This approach is therefore a more flexible means of optical-qubit XPM with stationary light than the EIT-based schemes which had been demonstrated prior.

13.3.4   Summary

We have now considered the third of our three broad strategies for engineering strong atom-light interactions. Ensembles with sufficiently stationary atoms, and also sufficiently long coherence times, may host long-lived, collective excitations or coherences in a generalization of the single excitation Dicke state. These many-atom entangled states can be generated by absorption of quantum fields, and also made to reconstitute the exciting field on demand. The spatial distribution of the collective excitation or coherence may cause coherent emission in a mode that is very different to the natural atomic dipole mode. We derived the equations of motion for quantum light fields propagating in an atomic ensemble, and from the Bloch equations for Λ atoms we derived the equations of motion for atomic polarization and spin coherences in the limit of large detuning.

With these optical Bloch equations for atom ensembles we demonstrated the operational theory of gradient echo memories (GEMs). GEM is one of the most accomplished quantum memory schemes, and in Chaps. 16 and 17 we will demonstrate the capabilities of a GEM in a cold-atom ensemble.
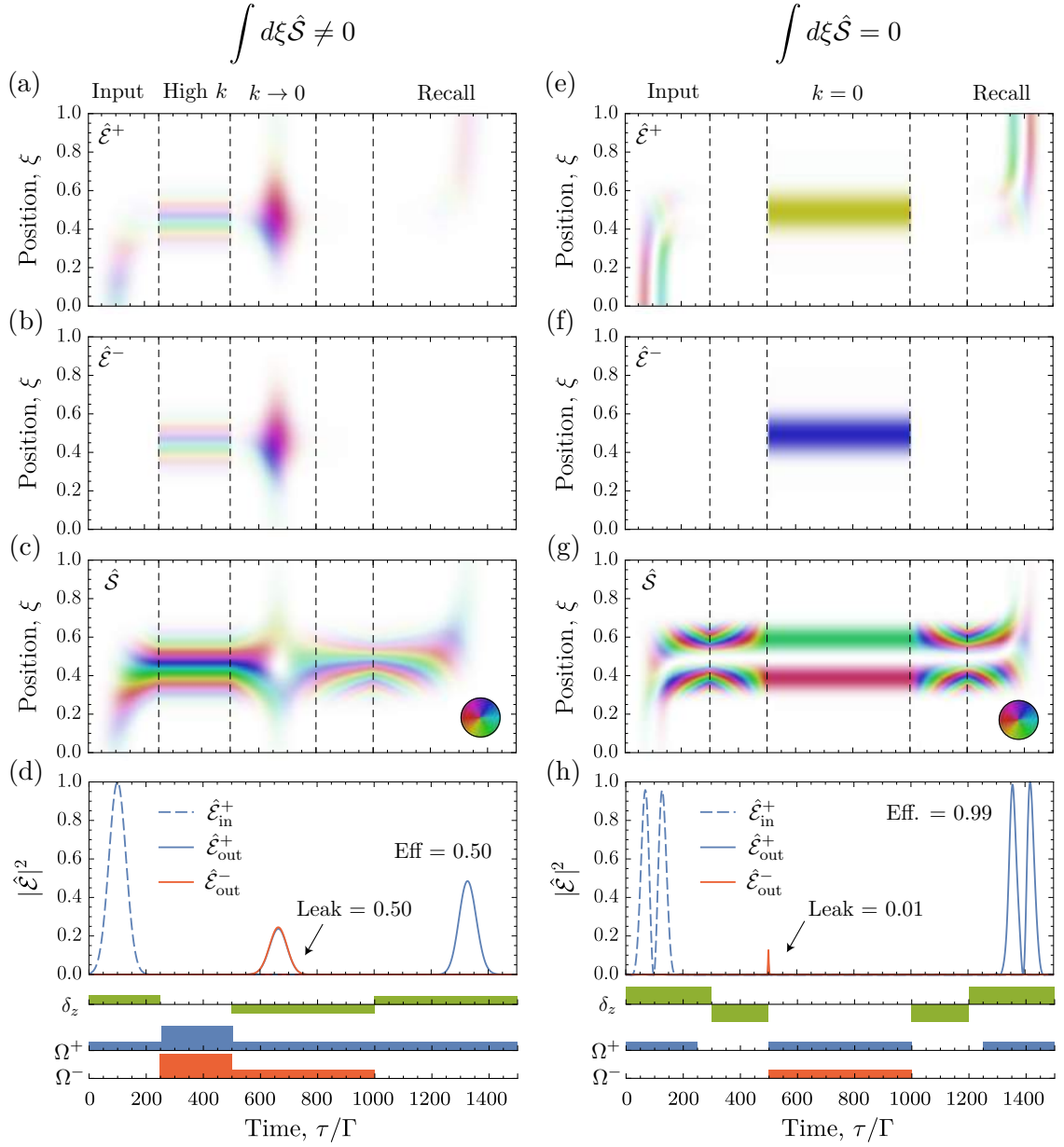
Figure 13.6: Stationary light prepared by GEM. Propagation of the (a, e) forward propagating probe $\hat{\mathcal{E}}^+$, (b, f) backward propagating probe $\hat{\mathcal{E}}^-$, (c, g) spin wave $\hat{S}$ through the ensemble under the two pulse schemes at bottom. Fields are plotted with hue $\angle\hat{\mathcal{E}}$ according to the colour wheel (inset) and opacity $\left|\hat{\mathcal{E}}\right|^2$. (d, h) Forward (blue) and backward (red) probe intensity at the input (dashed) and output (solid) of the ensemble. Simulations performed with $d = 1000$, maximum detuning gradient $\delta_\xi = 0.4\Gamma$, maximum control field amplitude $\Omega = 15\Gamma$. The stationary light fields are stable when $\int d\xi\hat{S} = 0$. Control field scattering has been suppressed for the purpose of these simulations.

Further to the operation of GEM as an optical quantum memory, we showed theoretically that a modified system with counter-propagating control fields produces a new type of stationary light field. The most interesting property of this stationary light is that the light field and spin wave may be spatially separated. Theoretical calculations by Jesse Everett and published in Ref. [348] show that stationary light in the apparatus of Chap. 17 should be capable of producing a cross-phase modulation of 1 mrad between two single-photon pulses.

In the following chapter we consider the leading quantum memory schemes and platforms, in order to provide some context for our work with gradient echo memories.

Bibliography - Ensemble-light interactions

9. J. L. Everett, et al., Dynamical observations of self-stabilizing stationary light, *Nat. Phys.* **13**, 68–73 (2017).

77. P. Lambropoulos, and D. Petrosyan, *Fundamentals of quantum optics and quantum information* (Springer, Heidelberg, 2007).

92. D. A. Steck, *Quantum and atom optics* (2007).

291. R. H. Dicke, Coherence in spontaneous radiation processes, *Phys. Rev.* **93** (1954).

320. A. V. Andreev, V. I. Emel'yanov, and Y. A. Il'inskiĭ, Collective spontaneous emission (Dicke superradiance), *Sov. Phys. Uspekhi* **23**, 493–514 (1980).

321. M. O. Scully, et al., Directed spontaneous emission from an extended ensemble of N atoms: Timing is everything, *Phys. Rev. Lett.* **96**, 10501 (2006).

322. P. Zarkeshian, et al., Entanglement between more than two hundred macroscopic atomic ensembles in a solid, *Nat. Commun.* **8**, 906 (2017).

323. A. V. Gorshkov, et al., Photon storage in Λ-type optically dense atomic media. II. Free-space model, *Phys. Rev. A* **76**, 33805 (2007).

324. D. B. Higginbottom, Spatial multimode storage in a gradient echo memory, Honours thesis (The Australian National University, 2011).

325. P. T. Cochrane, et al., *XMDS : eXtensible Multi Dimensional Simulator*, 2008.

326. G. R. Dennis, J. J. Hope, and M. T. Johnsson, XMDS2: Fast, scalable simulation of coupled stochastic partial differential equations, *Comput. Phys. Commun.* **184**, 201–208 (2013).

327. A. L. Alexander, et al., Photon echoes produced by switching electric fields, *Phys. Rev. Lett.* **96**, 1–4 (2006).

328. G. Hétet, et al., Photon echoes generated by reversing magnetic field gradients in a rubidium vapor, *Opt. Lett.* **33**, 2323–5 (2008).

329. J. J. Longdell, et al., Analytic treatment of controlled reversible inhomogeneous broadening quantum memories for light using two-level atoms, *Phys. Rev. A* **78**, 032337 (2008).

330. B. Kraus, et al., Quantum memory for non-stationary light fields based on controlled reversible inhomogeneous broadening, *Phys. Rev. A* **73**, 4 (2006).

331. N. Sangouard, et al., Analysis of a quantum memory for photons based on controlled reversible inhomogeneous broadening, *Phys. Rev. A* **75**, 9 (2007).

332. G. Campbell, Quantum memories and monolithic resonators, PhD thesis (The Australian National University, 2015).

333. E. L. Hahn, Spin echoes, *Phys. Rev.* **80**, 580–594 (1950).

334. N. A. Kurnit, I. D. Abella, and S. R. Hartmann, Observation of a photon echo, *Phys. Rev. Lett.* **13**, 567–568 (1964).

335. U. Kopvil'em, and V. Nagibarov, Fizika metallov i metallovedenie, *Fiz. Met. i Metalloved.* **2**, 313 (1963).

336. B. C. Buchler, et al., Precision spectral manipulation of optical pulses using a coherent photon echo memory, *Opt. Lett.* **35**, 1091–1093 (2010).

337. B. Sparkes, et al., Precision spectral manipulation: A demonstration using a coherent optical memory, *Phys. Rev. X* **2**, 021011 (2012).

338. S. A. Moiseev, and J.-L. Le Gouët, Rephasing processes and quantum memory for light: Reversibility issues and how to fix them, *J. Phys. B* **45**, 124003 (2012).

339. N. Matsuda, et al., Observation of optical-fibre Kerr nonlinearity at the single-photon level, *Nat. Photonics* **3**, 95–98 (2009).

340. S. E. Harris, J. E. Field, and A. Imamoğlu, Nonlinear optical processes using electromagnetically induced transparency, *Phys. Rev. Lett.* **64**, 1107–1110 (1990).

341. K.-J. Boller, A. Imamoğlu, and S. E. Harris, Observation of electromagnetically induced transparency, *Phys. Rev. Lett.* **66**, 2593–2596 (1991).

342. M. Fleischhauer, A. Imamoglu, and J. Marangos, Electromagnetically induced transparency: Optics in coherent media, *Rev. Mod. Phys.* **77**, 633–673 (2005).

343. M. Fleischhauer, and M. D. Lukin, Dark-state polaritons in electromagnetically induced transparency, *Phys. Rev. Lett.* **84**, 5094–5097 (2000).

344. A. André, and M. Lukin, Manipulating light pulses via dynamically controlled photonic band gap, *Phys. Rev. Lett.* **89**, 143602 (2002).

345. M. Bajcsy, A. S. Zibrov, and M. D. Lukin, Stationary pulses of light in an atomic medium., *Nature* **426**, 638–41 (2003).

346. Y.-W. Lin, et al., Stationary light pulses in cold atomic media and without Bragg gratings, *Phys. Rev. Lett.* **102**, 213601 (2009).

347. Y.-H. Chen, et al., Demonstration of the interaction between two stopped light pulses, *Phys. Rev. Lett.* **108**, 173603 (2012).

348. J. L. Everett, et al., Dynamical observations of self-stabilizing stationary light, *Nat. Phys.* **1** (2016).

Ensemble quantum memories: a review

Do you guys put the word quantum in front of everything?
— Scott Lang, Ant-man and the Wasp (2018)

A universal optical quantum memory is a device for coherently storing and recalling unknown quantum states of light, ideally on demand. We've already discussed how such a memory may be used to convert a photon source from probabilistic to deterministic in Sec. 5.2. More generally, optical quantum memories are desirable for two applications in quantum information: as repeaters for long-distance QKD and for synchronizing operations in optical quantum computers [349]. Each of these applications imposes its own unique challenges.

Long-distance quantum communication networks based on optical fibres are a means of guaranteeing cryptographic security, as we've seen, and perhaps also enhancing the capabilities of distributed quantum processors [350]. However, long distance communication through fibres is lossy. Even in the 1.5 μm telecommunications band losses are still no better than 0.2 dB/km [69]. In contrast to classical signals, quantum states cannot be amplified deterministically without adding noise that results in decoherence, a consequence of the no-cloning theorem. Repeater protocols have been proposed that create long-distance entanglement from short-distance entanglement by entanglement swapping [351]. These repeater protocols require quantum memories capable of storing and recalling entangled photonic qubits at nodes distributed along a communication link. The memories in repeaters must have storage times longer than the optical travel time of the total link distance: about 1 ms for a 200 km fibre link.

Quantum memories may also be used for synchronizing operations in optical quantum computers, buffering probabilistic entanglement operations between the photonic register in much the same way that memories may be used for buffering entanglement swapping operations between repeater nodes. Linear optical quantum computing (LOQC) requires operation synchronization to scale beyond tens of qubits and tens of gates [45]. Memories for optical quantum computers require a high bandwidth because this defines the clock time of any memory-based processor.

Incredible progress has been made towards the goal of engineering useful quantum memories across a wide range of platforms, and using several protocols. Important landmarks include the storage and retrieval of entangled qubits[352–359] and squeezed light fields [360–362], and the entanglement of remote ensembles [363, 364]. In this chapter we review the state of ensemble-based quantum memory research and the capabilities and deficiencies of existing quantum memory devices. We divide this research by protocol to emphasize the operational physics of ensemble-based memories. The key protocols are electromagnetically induced transparency, off-resonant Raman, atomic frequency comb

and gradient echo. The most promising platforms to date are cold-atom vapours[1] like the one we present in Chap. 17, hot atomic vapours and rare-earth ion doped crystals (REICs). Beyond storage, quantum memories have demonstrated capabilities for the manipulation and interaction of qubits. For more detailed reviews of the same subject, see Refs. [351, 365–367].

14.1 Quantum memory performance criteria

The ultimate performance metric for a quantum repeater network is the secure key rate. Similarly, a memory-based LOQC will be judged by the number of consecutive operations it can perform beyond the required fault tolerance. Each of these is a complicated function of many parameters, only some of which are depend on the memory. We must break these goals down to some important fundamental performance criteria for quantum memories.

- **Efficiency -** The entanglement rate of a repeater network increases exponentially with the storage and recall efficiency

$$\eta = \eta_{\rm s}\eta_{\rm r} = \frac{I_{\rm in}}{I_{\rm out}} \ . \tag{14.1}$$

An important efficiency benchmark is $\eta > 0.5$. This is the threshold at which a quantum memory without post-selection outperforms prepare and measure schemes [368]. Below this threshold no degree of entanglement can be distilled from pure entangled states stored in the memory. Efficiencies greater than 90% are required before repeater networks have any advantage over direct transmission at all [351].

- **On-demand readout -** In this thesis we draw a distinction between quantum memories and quantum delay lines. A true quantum memory can recall stored states on demand. A length of optical fibre is a good quantum optical delay line, but cannot (on its own) operate as a quantum memory. A delay line is, for example, no use for converting single-photon sources from probabilistic to deterministic.

- **Fidelity -** An ideal quantum memory returns the exact input field, perfectly reconstructed. In practice, the operation of storing and recalling the quantum state introduces noise from various sources. The overlap fidelity for a given state $\hat{\rho}_{\rm in}$ is

$$F(\hat{\rho}_{\rm in}) = {\rm Tr}\left[\sqrt{\hat{\rho}_{\rm out}}\hat{\rho}_{\rm in}\sqrt{\hat{\rho}_{\rm out}}\right] \ . \tag{14.2}$$

Fidelity is contextual, it depends on the input state. The memory may be for single-photon qubits, in which case the fidelity depends on how the qubit is encoded (photon number, time, polarization, frequency, spatial mode) and also the set of qubits to be stored. A typical demonstration of an optical memory for qubits consists of storing and recalling the four two-qubit Bell states, and the reported memory fidelity is the minimum of F over this set.

An essential threshold for quantum memories (for any application) is that the storage fidelity outperforms an ideal classical prepare and measure scheme. Simply measuring one qubit projectively and preparing another based on the result already has

---

[1]It is not unusual in the literature to see cold-atom vapours of this sort described as 'atom clouds'. Here we have avoided this (admittedly poetic) phrase lest we wrongly suggest that these cold-atom vapours, like clouds, consist of droplets.

$F = 2/3$[369], this is the performance limit of a classical memory. More stringently, single qubit storage with $F > 0.854$ is required to maintain entanglement when one half of an entangled pair is stored in the memory [366].

In contrast to single emitter memories, ensemble quantum memories can store not only single-photon qubits, but also more general quantum states with correlated continuous degrees of freedom. In this respect ensemble quantum memories are universal. The state may be, for example, a two-mode squeezed state or a superposition of weak coherent states of opposite phase. Again, the fidelity is contingent on the set of relevant states. Generalizations of the prepare-and-measure and entanglement-preserving bounds exist for continuous variable quantum states as well [370].

- **Storage time -** The recall efficiency and fidelity of real-world memories are functions of the storage time. Typically, the storage efficiency of ensemble schemes like those below decays exponentially with a storage lifetime τ_s that is limited by the decoherence rate of the atomic ensemble, but other relaxation mechanisms can lead to alternative decay profiles. Another important benchmark is the time at which the efficiency drops below 50%. Beyond this storage time the memory no longer outperforms prepare and measure schemes without post-selection [368].

- **Bandwidth -** The repetition rate of the network is limited by the bandwidth of the memory $\Delta\omega$. The higher the bandwidth the faster the network.

- **Time-bandwidth product -** Uniting the above two criteria, we arrive at the time-bandwidth product (TBP) $\tau_s\Delta\omega$. This is the limit of simultaneously stored pulses, or the number of network operations that can be carried out during the storage time. This metric is most useful for comparing memories operating at different timescales; a memory with $\tau_s = 1$ s is not terribly useful if $\Delta\omega < 1Hz$.

- **Multimode capacity -** The multimode capacity N is the number of optical modes (be they spatial, temporal or spectral) that can be stored in the memory simultaneously. Each mode may carry an independent qubit, and those modes may be selectively recalled and multiplexed to increase the success rate of probabilistic operations. Multiplexing increases the bit rate of repeater networks dramatically [371, 372]. For spectral modes the multimode capacity is the bandwidth. In this review we mean multimode capacity excluding spectral modes, given that we already consider the bandwidth independently.

- **Wavelength -** A useful memory must operate at an appropriate wavelength for its application. For repeater networks, that means memories that either operate in the low loss telecommunications band at about $1,550$ nm, or at a wavelength that can be converted coherently and efficiently to $1,550$ nm.

14.2   EIT

Slowing light fields by electromagnetically induced transparency (EIT) [341], which we introduced in Sec. 13.3, can be the operating mechanism of a quantum memory. The narrow transparency window opened at the two-photon resonance by a control field applied to a Λ-ensemble correspondingly reduces the group velocity of the signal light field. A signal pulse traversing the ensemble is delayed, and this delay can be tuned by the brightness

of the control. As the control power drops, the transparency window at the two photon resonance narrows and the pulse is slowed. EIT has been used to reduce the speed of light in atomic ensembles by up to seven orders of magnitude [373, 374].

When the control field drops to zero, the transparency vanishes and the slow light polariton is stopped and transferred to the distributed atomic state. This process is coherent, and can be reversed by restoring the original control field. This initial observation that light could be stopped and restored by EIT has since prompted a great deal of research into EIT quantum memories [375]. In order to operate an EIT memory with $\eta = 1$ the optical depth must be sufficiently large that the pulse delay is longer than the pulse width, in this regime the pulse may be contained entirely within the ensemble [376].

EIT storage and recall efficiency has reached 78% with cold atomic vapours [377]. EIT lifetimes are limited by decoherence, atomic motion and inhomogeneous broadening of the atomic resonance. Atomic vapours have naturally narrow linewidths sufficient for EIT, but solid-state ensembles such as rare-earth ion doped crystals are typically too inhomogeneous. Although inhomogeneous broadening may be overcome by spectral hole burning, the useful optical depth after this process is a small fraction of the total. Nevertheless, spectral hole burning techniques have been used to store pulses with $\tau_\mathrm{s} = 40$ s in rare-earth ion doped crystals by EIT [378]. The bandwidth depends on the control field power, at high powers the effect transitions smoothly between two distinct phenomena: EIT and Autler-Townes splitting [379, 380], although both can be used as a memory. In general the time-bandwidth product of EIT memories is poor. EIT with a TBP of 3.7 was used to store two pulses simultaneously with 50% efficiency in the course of this doctorate [8].

Entangled polarization qubits have been stored by EIT in warm [354, 355] and cold [356–359] atomic vapour ensembles with efficiencies up to $\eta = 0.68$[381]. Squeezed light fields have also been stored and recalled by EIT [360–362].

14.3 Raman memory

Off-resonant Raman memory is similar to EIT in that a bright control field is used to couple a weak probe onto a spin coherence but, unlike EIT, the control field is far detuned from the excited state and opens a two-photon Raman absorption line instead of a transparency window. Raman memory does not rely on a slow light, but instead scatters the signal onto a spin coherence directly by a two-photon transition.

In order to absorb a broad spectrum signal, the control field itself must be broad spectrum. The key to Raman memory is therefore to shape the control field temporally in a way that is matched to the signal pulse. Reversing this process with a second control pulse at a later time recalls the stored field from the spin wave [382, 383]. Typically the control field is a pulse train with a comb-like spectrum that opens a coherent comb of two-photon Raman resonances. The Raman condition with an ensemble is $\Delta \gg d\Gamma$ rather than $\Delta \gg \Gamma$[323]. Operating with such large detuning allows bandwidths in the range 1 - 1000 GHz with Raman memories in warm atomic vapours [383, 384]. To date, Raman memories are most suited to synchronizing LOQC, for which these enormous bandwidths are necessary.

Raman memories are most efficient when recall happens in the opposite direction, restoring a perfect time symmetry. They do work in with forward recall, albeit in a reduced fashion. Four-wave mixing is an important noise source for both EIT and Raman memories. Raman memories in leaky, birefringent cavities are able to suppress FWM noise substantially [385]. Entangled polarization qubits have been stored and recalled by

Raman memory with $F = 0.97$ [386].

14.4   AFC

Atomic frequency comb (AFC) is a memory protocol that begins with the preparation of a comb-like absorption profile in an inhomogeneously broadened atomic ensemble. An optical field is absorbed by the comb, and the atoms in each tooth dephase at integer multiples of the comb spacing Δ. At time $t = 2\pi/\Delta$ the teeth are once again in phase and spontaneously emit a coherent, directed echo of the input field. This process is similar to the controlled rephasing that we described as part of the operation of a gradient echo memory in Sec. 13.2.

AFC is an appealing memory protocol for use with rare-earth ion crystals because it can utilize the entire inhomogeneously broadened ensemble linewidth. The frequency comb is prepared by spectral hole burning, and because the comb uses more of the ensemble than the single resonance that must be prepared for EIT, the available optical depth is much larger. Moreover, large inhomogeneous linewidths can provide exceptionally large bandwidths for AFC memories [352, 387]. AFC memories typically operate with a bandwidth of $\Delta\omega \approx 2\pi \times 1$ GHz.

The absorption comb itself provides only an optical delay line; recall occurs at a time predetermined by the absorption spectrum. To operate on demand the excitation must be transferred to and from a long lived spin state $|s\rangle$ using adiabatic control pulses on a Λ-ensemble [388]. This control must be carefully crafted to form a π-pulse for the entire inhomogeneously broadened resonance. Even with such a pulse, the available bandwidth for storage is typically much narrower than the bandwidth for delay. The memory bandwidth cannot be larger than the spacing between $|s\rangle$ and adjacent levels, else the inhomogeneously broadened excitation will be scattered to different spin coherences. To date, AFC quantum memories have much lower time-bandwidth products than delay line AFCs.

AFC delay line with a rare-earth ion crystal in a resonant cavity has achieved efficiency $\eta = 0.56$ [389]. The maximum storage time achieved with AFC delay line is 5 μs [390]. An AFC memory has been demonstrated with a similar rare-earth ion crystal and cavity apparatus [391, 392]. This memory operated with $\eta = 0.12$ and storage lifetime $\tau_{\mathrm{s}} = 500$ μs, but a bandwidth of only 5 MHz. Entangled time-bin qubits have been stored in a REIC AFC memory with fidelities as high as $F = 0.97$ [352, 393], and entangled polarization qubits have been delayed with $F = 0.995$ [353].

14.5   GEM

The experimental work with ensemble memories in this thesis will focus on the operation of a gradient echo memory (GEM) [327–329], first extending the GEM protocol to store frequency-encoded qubits and then demonstrating a GEM in a cold atom ensemble with $\eta = 0.87 \pm 0.02$ and $\tau_{\mathrm{s}} = 1$ ms. We already considered the operational theory of a gradient echo memory in some detail in Sec. 13.2.1, in this section we will review the capabilities and potential of existing GEMs.

A key advantage of GEM compared to some other CRIB or Raman memory schemes is that GEM doesn't require optical π-pulses to control the atomic dynamics. Control fields in GEM are switched, but not pulsed, and coherent control is provided by magnetic field or AC Stark gradients, which is considerably simpler. Unlike Raman memories, forward

recall is not a great detriment to the memory efficiency. Also, where EIT is a first-in, first-out memory protocol, simple GEM is a first-in, last-out process. Repeatedly changing the control field gradient allows GEM to recall pulses from a train selectively [394].

GEM was first realized with an electric field gradient applied to a rare-earth ion doped crystal with efficiency less than 1% [327]. With a magnetic field gradient and a hot atomic vapour the efficiency was improved to $\eta = 0.87$, and this is still the highest demonstrated quantum memory efficiency [395]—although now tied with the cold-vapour memory we present in Chap. 17. Storage of coherent fields in hot-vapour GEM was shown to be not only efficient, but essentially noiseless, with $F = 0.98$ such that the memory unambiguously beats the no-cloning limit [396]. However coherence times in hot vapours are limited by atomic motion: diffusion as well as collisions between atoms and with the cell walls. Coherence times in cold vapours are considerably longer. Before the work of this thesis, the best demonstrated efficiency and storage time for GEM in a cold atomic vapour was $\eta = 0.80$ and $\tau_{\rm s} = 200$ μs [397]. We improve the storage lifetime to $\tau_{\rm s} = 1$ ms in Chap. 17. A two-level GEM in rare-earth ion crystal achieved $\eta = 0.69$ and $\tau_{\rm s} = 5$ μs. Λ-GEM in solid state could conceivably have very long storage times, but requires a crystal with low inhomogeneous broadening in order to combine high coherence time and optical depth (just like EIT with REIC). This remains an area of active research.

In contrast to AFC, GEM stores the frequency components of the signal in a spatially structured way. As we saw in Sec. 13.2.1, a linear detuning gradient leads to a polarization or spin coherence that is the Fourier transform in ξ of the input pulse in τ. GEM therefore lends itself to spectral processing by spatial control [337, 394]. Recalled pulses can be stretched or compressed with respect to the input, and spectral components of the signal can be stored and recalled independently.

GEMs also support spatial-multimode storage [398], which means that GEM is compatible with spatially encoded qubits [399]. In this thesis we further extend GEM to to achieve simultaneous dual-rail storage, so that GEM becomes a memory for frequency encoded qubits as well.

Unlike AFC and EIT memories, entangled qubits have not yet been stored and recalled by a GEM. The primary challenge is engineering single-photon sources compatible with the narrow linewidth of existing GEMs and at an appropriate wavelength. As we saw in Chap. 5, this is a challenge has been surmounted very recently, and entanglement storage by GEM is likely to be achieved in the coming years. Similarly, squeezed light has yet to be stored and recalled by GEM.

14.6 Summary

Quantum memory devices have come a long way in the last decade. We're now approaching laboratory devices that meet several of the requirements for repeater-based quantum networks, including efficiencies near 90% [395, 402], bandwidths of several GHz [403], and storage times approaching 1 m [378]. These achievements are summarized in Table 14.1. At present, no single device achieves these benchmarks simultaneously, but they are getting closer.

One of the most challenging outstanding requirements for repeater networks is a memory that operates near the telecommunications band. One of the leading candidates for a telecommunications compatible memory is Er^{3+}, which has a transition at $1,538$ nm, and recently demonstrated coherence times of 1.3 s in a REIC [404].

Moving beyond proof-of-principle laboratory experiments, quantum memories have yet

	η	F	τ_s	$\Delta\omega$	Multimode
Benchmark	0.9 [351]	0.9 [366]	1 ms	1-10 GHz [400]	High
Protocol					
EIT	0.78 [377]	0.99 [381]	40 s [378]	100 MHz	Low
Raman	0.30 [401]	0.97 [386]	10 μs	1 THz [384]	Low
AFC delay	0.56 [389]	-	5 μs [390]	1 GHz [389]	High
AFC storage	0.12 [391]	0.95 [387]	1 ms [392]	5 MHz [392]	Moderate
GEM	$0.87^\dagger$ [3, 395]	0.98 [396]	1 ms† [3]	1 MHz	Moderate

Table 14.1: Summary of ensemble quantum memory results (this work: †). Reported fidelities depend on the chosen state, and comparisons should be made cautiously. For example, the fidelity listed for GEM is the fidelity of weak-coherent storage. The fidelities listed for AFC and EIT are for entangled two-qubit single-photon states, postselected on successful reemission.

to be made robust, small or simple enough for real-world applications. Cold-atom vapours are one of the most successful laboratory platforms, but no practical quantum memory will involve the apparatus necessary for magneto-optical atom trapping. Hot atomic vapours may prove more promising, improving coherence times in hot-atom vapours is a problem of restricting atomic motion and collisions. Anti-relaxation coated microcells are a plausible avenue towards sufficiently coherent memories and remain simpler than existing cold-atom experiments.

Solid-state memories are preferred over vapours of either sort for robust and integrated memories, and rare-earth ion doped crystals have shown enormous progress towards our quantum memory benchmarks [405]. Most of the existing REIC memories use variants of AFC and, unfortunately, AFC storage does not necessarily inherit the bandwidth of AFC delay. For this reason, inhomogeneous broadening is still a barrier to REIC memories, and must be overcome by crystal engineering- perhaps by moving to stoichiometric REICs. More fundamentally, REIC memories operate at cryogenic temperatures $\approx$ 3 K. For integration with other cryogenic quantum information devices this poses no additional challenge, but for repeater networks it is a substantial overhead.

Finally, miniaturization is an important goal for scalable memories. In many cases, miniaturization requires increasing the optical depth of a small ensemble by resonator or waveguide enhancement, combining two of our broad strategies for efficient atom-light interactions.

Bibliography - Ensemble quantum memories

3. Y.-W. Cho, et al., Highly efficient optical quantum memory with long coherence time in cold atoms, *Optica* **3**, 100 (2016).

8. J. Geng, et al., Electromagnetically induced transparency and four-wave mixing in a cold atomic ensemble with large optical depth, *New J. Phys.* **16**, 113053 (2014).

45. P. Kok, et al., Linear optical quantum computing with photonic qubits, *Rev. Mod. Phys.* **79**, 135–174 (2007).

69. G. P. Agrawal, *Optical fibers* (John Wiley & Sons, Inc., Hoboken, 2011).

323. A. V. Gorshkov, et al., Photon storage in Λ-type optically dense atomic media. II. Free-space model, *Phys. Rev. A* **76**, 33805 (2007).

327. A. L. Alexander, et al., Photon echoes produced by switching electric fields, *Phys. Rev. Lett.* **96**, 1–4 (2006).

328. G. Hétet, et al., Photon echoes generated by reversing magnetic field gradients in a rubidium vapor, *Opt. Lett.* **33**, 2323–5 (2008).

329. J. J. Longdell, et al., Analytic treatment of controlled reversible inhomogeneous broadening quantum memories for light using two-level atoms, *Phys. Rev. A* **78**, 032337 (2008).

337. B. Sparkes, et al., Precision spectral manipulation: A demonstration using a coherent optical memory, *Phys. Rev. X* **2**, 021011 (2012).

341. K.-J. Boller, A. Imamoğlu, and S. E. Harris, Observation of electromagnetically induced transparency, *Phys. Rev. Lett.* **66**, 2593–2596 (1991).

349. A. I. Lvovsky, B. C. Sanders, and W. Tittel, Optical quantum memory, *Nat. Photonics* **3**, 706–714 (2009).

350. H. J. Kimble, The quantum internet, *Nature* **453**, 1023–30 (2008).

351. N. Sangouard, et al., Quantum repeaters based on atomic ensembles and linear optics, *Rev. Mod. Phys.* **83**, 33–34 (2011).

352. E. Saglamyurek, et al., Quantum storage of entangled telecom-wavelength photons in an erbium-doped optical fibre, *Nat. Photonics* **9**, 83–87 (2015).

353. Z.-Q. Zhou, et al., Realization of reliable solid-state quantum memory for photonic polarization qubit, *Phys. Rev. Lett.* **108**, 190505 (2012).

354. Y.-W. Cho, and Y.-H. Kim, Atomic vapor quantum memory for a photonic polarization qubit, *Opt. Express* **18**, 25786–93 (2010).

355. C. Kupchak, et al., Room-temperature single-photon level memory for polarization states, *Sci. Rep.* **5**, 7658 (2015).

356. K. S. Choi, et al., Mapping photonic entanglement into and out of a quantum memory., *Nature* **452**, 67–71 (2008).

357. S. Riedl, et al., Bose-Einstein condensate as a quantum memory for a photonic polarization qubit, *Phys. Rev. A* **85**, 22318 (2012).

358. H. Zhang, et al., Preparation and storage of frequency-uncorrelated entangled photons from cavity-enhanced spontaneous parametric downconversion, *Nat. Photonics* **5**, 628–632 (2011).

359. Z. Xu, et al., Long lifetime and high-fidelity quantum memory of photonic polarization qubit by lifting zeeman degeneracy, *Phys. Rev. Lett.* **111**, 240503 (2013).

360. D. Akamatsu, K. Akiba, and M. Kozuma, Electromagnetically induced transparency with squeezed vacuum., *Phys. Rev. Lett.* **92**, 203602 (2004).

361. J. Appel, et al., Quantum memory for squeezed light, *Phys. Rev. Lett.* **100**, 093602 (2008).

362. K. Honda, et al., Storage and retrieval of a squeezed vacuum., *Phys. Rev. Lett.* **100**, 4 (2008).

363. I. Usmani, et al., Heralded quantum entanglement between two crystals, *Nat. Photonics* **6**, 234–237 (2012).

364. N. Maring, et al., Photonic quantum state transfer between a cold atomic gas and a crystal, *Nature* **551**, 485–488 (2017).

365. C. Simon, et al., Quantum memories, *Eur. Phys. J. D* **58**, 1–22 (2010).

366. F. Bussières, et al., Prospective applications of optical quantum memories, *J. Mod. Opt.* **60**, 1519–1537 (2013).

367. T. Chanelière, G. Hétet, and N. Sangouard, Quantum optical memory protocols in atomic ensembles, in *Adv. At. Mol. Opt. Phys.* (2018), pp. 77–150.

368. F. Grosshans, and P. Grangier, Quantum cloning and teleportation criteria for continuous quantum variables, *Phys. Rev. A* **64**, 010301 (2001).

369. S. Massar, and S. Popescu, Optimal extraction of information from finite quantum ensembles, *Phys. Rev. Lett.* **74**, 1259–1263 (1995).

370. S. L. Braunstein, and P. van Loock, Quantum information with continuous variables, *Rev. Mod. Phys.* **77**, 513–577 (2005).

371. O. A. Collins, et al., Multiplexed memory-insensitive quantum repeaters, *Phys. Rev. Lett.* **98**, 060502 (2007).

372. C. Simon, et al., Quantum repeaters with photon pair sources and multimode memories, *Phys. Rev. Lett.* **98**, 190503 (2007).

373. D. Budker, et al., Nonlinear magneto-optics and reduced group velocity of light in atomic vapor with slow ground state relaxation, *Phys. Rev. Lett.* **83**, 1767–1770 (1999).

374. L. V. Hau, et al., Light speed reduction to 17 metres per second in an ultracold atomic gas, *Nature* **397**, 594–598 (1999).

375. M. Fleischhauer, S. Yelin, and M. Lukin, How to trap photons? Storing single-photon quantum states in collective atomic excitations, *Opt. Commun.* **179**, 395–410 (2000).

376. A. V. Gorshkov, et al., Photon storage in Λ-type optically dense atomic media. II. Free-space model, *Phys. Rev. A* **76** (2007).

377. Y.-H. Chen, et al., Coherent optical memory with high storage efficiency and large fractional delay, *Phys. Rev. Lett.* **110**, 083601 (2013).

378. G. Heinze, C. Hubrich, and T. Halfmann, Stopped light and image storage by electromagnetically induced transparency up to the regime of one minute, *Phys. Rev. Lett.* **111**, 033601 (2013).

379. P. M. Anisimov, J. P. Dowling, and B. C. Sanders, Objectively discerning Autler-Townes splitting from electromagnetically induced transparency, *Phys. Rev. Lett.* **107**, 163604 (2011).

380. L. Giner, et al., Experimental investigation of the transition between Autler-Townes splitting and electromagnetically-induced-transparency models, *Phys. Rev. A* **87**, 013823 (2013).

381. P. Vernaz-Gris, et al., Highly-efficient quantum memory for polarization qubits in a spatially-multiplexed cold atomic ensemble, *Nat. Commun.* **9**, 363 (2018).

382. J. Nunn, et al., Mapping broadband single-photon wave packets into an atomic memory, *Phys. Rev. A* **75**, 011401 (2007).

383. P. S. Michelberger, et al., Interfacing GHz-bandwidth heralded single photons with a warm vapour Raman memory, *New J. Phys.* **17**, 043006 (2015).

384. P. J. Bustard, et al., Toward quantum processing in molecules: A THz-bandwidth coherent memory for light, *Phys. Rev. Lett.* **111**, 083901 (2013).

385. D. J. Saunders, et al., Cavity-enhanced room-temperature broadband Raman memory, *Phys. Rev. Lett.* **116**, 090501 (2016).

386. D. G. England, et al., High-fidelity polarization storage in a gigahertz bandwidth quantum memory, *J. Phys. B* **45**, 124008 (2012).

387. E. Saglamyurek, et al., Broadband waveguide quantum memory for entangled photons, *Nature* **469**, 512–5 (2011).

388. M. Afzelius, et al., Demonstration of atomic frequency comb memory for light with spin-wave storage, *Phys. Rev. Lett.* **104**, 40503 (2010).

389. M. Sabooni, et al., Efficient quantum memory using a weakly absorbing sample, *Phys. Rev. Lett.* **110**, 133604 (2013).

390. N. Maring, et al., Storage of up-converted telecom photons in a doped crystal, *New J. Phys.* **16**, 113021 (2014).

391. P. Jobez, et al., Cavity-enhanced storage in an optical spin-wave memory, *New J. Phys.* **16**, 083005 (2014).

392. P. Jobez, et al., Coherent spin control at the quantum level in an ensemble-based optical memory, *Phys. Rev. Lett.* **114**, 230502 (2015).

393. M. Gündoğan, et al., Solid state spin-wave quantum memory for time-bin qubits, *Phys. Rev. Lett.* **114**, 230501 (2015).

394. M. Hosseini, et al., Coherent optical pulse sequencer for quantum applications., *Nature* **461**, 241–5 (2009).

395. M. Hosseini, et al., High efficiency coherent optical memory with warm rubidium vapour, *Nat. Commun.* **2**, 174 (2011).

396. M. Hosseini, et al., Unconditional room-temperature quantum memory, *Nat. Phys.* **7**, 794–798 (2011).

397. B. M. Sparkes, et al., Gradient echo memory in an ultra-high optical depth cold atomic ensemble, *New J. Phys.* **15**, 085027 (2013).

398. D. B. Higginbottom, et al., Spatial-mode storage in a gradient-echo memory, *Phys. Rev. A* **86**, 1–10 (2012).

399. K. Wagner, et al., Entangling the spatial properties of laser beams., *Science* **321**, 541–3 (2008).

400. N. Gisin, and R. Thew, Quantum communication, *Nat. Photonics* **1**, 165–171 (2007).

401. K. F. Reim, et al., Single-photon-level quantum memory at room temperature, *Phys. Rev. Lett.* **107**, 7 (2011).

402. B. M. Sparkes, Storage and manipulation of optical information using gradient echo memory in warm vapours and cold ensembles, PhD thesis (The Australian National University, 2013).

403. M. Bonarota, J.-L. Le Gouët, and T. Chanelière, Highly multimode storage in a crystal, *New J. Phys.* **13**, 013013 (2011).

404. M. Rančić, et al., Coherence time of over a second in a telecom-compatible quantum memory storage material, *Nat. Phys.* **14**, 50–54 (2017).

405. M. Zhong, et al., Optically addressable nuclear spins in a solid with a six-hour coherence time, *Nature* **517**, 177–180 (2015).

Cold atomic vapour apparatus

There are no two-level atoms and [Rubidium] is not one of them.
    – Bill Phillips, *Laser cooling and trapping of neutral atoms* (1998)

The neutral atoms in an atomic vapour barely interact apart from atomic collisions, which are a source of elastic decoherence and inelastic relaxation, and are therefore an appealing ensemble of well-isolated emitters. Although the density of vapours is not naturally high, it improves with increasing temperature. Hot vapours are one means of achieving an optically deep atomic ensemble. Increasing temperature does, however, simultaneously increase the collision and diffusion rates along with the atomic density. The storage lifetime of quantum memories in hot vapours is ultimately limited by atomic motion.

Cold atomic vapours can also be made very dense, so long as they are confined in a trapping potential somewhat like the trapping potential at the centre of our ion trap in Chap. 6. Magneto-optical traps are a means of trapping neutral atoms [406], without the RF electric fields we used to trap charged ions. Laser cooling lowers the vapour temperature, and the density may be reduced down to the Bose-Einstein condensate limit, although not in this instance. Laser-cooled atomic vapours are one of the most advanced platforms for coherent ensemble-light interactions because they can combine high optical depths and long coherence times. In this chapter we describe the magneto-optical trap (MOT) apparatus that we use for preparing cold atomic vapour quantum memories in Chaps. 16 and 17.

This cold-vapour apparatus was first built by Ben Sparkes, Julien Bernu and Nick Robins and details of that work are available in Refs. [397, 402]. In the sections below we give a brief overview of the apparatus to provide context for the new experiments. Noteworthy changes since the previous works include new, lower noise laser systems, a mains-line trigger, an additional polarization gradient cooling stage, and lifting the vacuum chamber from the optical bench to reduce eddy currents from magnetic field switching. The combined effect of these changes has been to improve the optical depth and coherence time of the ensemble considerably, making the results of Chap. 17 possible.

15.1 The Rubidium atom

The experiments in these chapters are performed with a laser-cooled rubidium atom vapour. Neutral alkali metals such as rubidium are appealing for quantum information experiments because, like singly ionized alkaline Earths, they have a single valence electron with a simple hydrogen-like energy level structure. However, in contrast to $^{138}\text{Ba}^+$, with

which we've worked up until this point (see Sec. 6.1), almost all stable or long-lived alkali metals have nuclear spin, and therefore a hyperfine electronic level structure.

Of the alkali metals, we choose to work with rubidium because it has optical transitions between low-lying states with accessible wavelengths, low angular momentum ground states, and high vapour pressures at low temperatures. In addition to the cold rubidium vapour, we'll use rubidium vapour cells extensively as frequency references. Rubidium has two naturally occurring isotopes: ^{85}Rb (which is stable) and ^{87}Rb (which is a long-lived radio-isotope), and both can be used for quantum information experiments. The rubidium dispensers in our apparatus contain a natural mixture of rubidium: 72% ^{85}Rb and 28% ^{87}Rb. Our magneto-optical trap can be configured to cool and confine either isotope, but in the experiments presented here we work exclusively with ^{87}Rb. Of the two isotopes ^{87}Rb has the lower ground-state angular momentum, with nuclear spin 3/2, which simplifies the hyperfine structure.

The level structure of ^{87}Rb is shown in Fig. 15.1. The transitions that concern us are the the two lowest energy optical transitions, the D$_1$ and D$_2$ lines, with central wavelengths and linewidths shown. The spin relaxation time of the two ground states can be more than one second in all-optical traps [407]. This spin coherence is therefore sufficiently long-lived for use in quantum memories. Once again, we apply a weak magnetic field that determines the atomic quantization axis and lifts the degeneracy of the Zeeman sub-levels m_F. It is necessary to impose a quantization axis in this way to optically drive σ transitions between the Zeeman states and prepare the ensemble in an extremal m_F state. Modifying equation Eqn. 6.12 for the hyperfine levels, the Zeeman splitting is

$$\Delta E = m_F g_F \mu_{\mathrm{B}} |\mathbf{B}| \tag{15.1}$$

where the Lande factors g_F are shown in Fig. 15.1.

We use hyperfine and Zeeman split levels of the D$_1$ transition to form a Λ transition for our quantum memories. We identify one of the magnetically sensitive $F = 1$ Zeeman levels as our ground state $|g\rangle$. Either of the $m_F = \pm 1$ levels are adequate, but for single-rail memory we choose $m_F = 1$. In Chap. 16 we use the $m_F = \pm 1$ levels simultaneously to form parallel Λ schemes for probes at separate frequencies. This is the basis of our dual-rail memory for frequency qubits.

The corresponding metastable state $|s\rangle$ is the $F = 2$ state with matching Zeeman number $m_F = 1$ so that the combined two-photon transition has $\Delta m = 0$. As indicated in Fig. 13.1, we choose the probe and control field to be blue-detuned, in which case the preferred excited state is in the $F' = 2$ manifold. The probe and control fields are aligned with the quantization axis and drive only σ transitions. In the simplest configuration, shown in Fig. 15.2(a), the $\hat{\sigma}_{gs}$ coherence is driven via a single excited state $m_F' = 2$ by probe and control beams with same-circular polarizations. This is the configuration we use in Chap. 17.

Alternatively, we can choose probe and control with orthogonal linear polarizations and drive the coherence by a combination of Λ transitions via both of the excited states $m_F' = 2$ and $m_F' = 0$ as shown in Fig. 15.2(b). This configuration is less straightforward, and can rotate the polarization of the probe as described by the model we derive in Sec. 16.2. However, in the orthogonal-linear configuration we can combine and separate the beams by PBS. In Chap. 16 we use an orthogonal-linear configuration in order to balance the optical depth of the $m_F = \pm 1$ transitions.
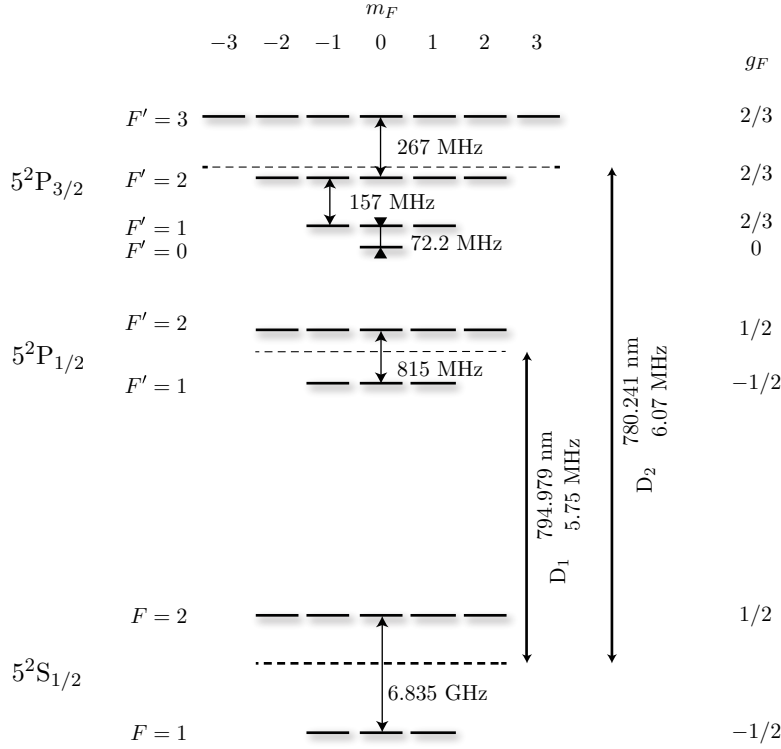
Figure 15.1: Electronic level structure of ^{87}Rb. All values from Ref. [408].

15.2 Magneto-optical trapping

Magneto-optical traps (MOTs) combine laser cooling and magnetic field gradients to both cool and trap neutral atoms. The techniques of magneto-optical trapping are well known, and so we provide only a brief description here. The first trapping mechanism at work in a MOT is a variation of the Doppler cooling we presented in Sec. 6.4.4 called 'optical molasses'. Atoms travelling at the intersection of three orthogonal counter-propagating pairs of red-detuned optical fields preferentially absorb photons from the field opposing their direction of travel, which is Doppler shifted closer to resonance compared to its counter-propagating partner. The net effect of many absorption and scattering cycles is to cause a force opposing the direction of motion, an effective viscosity. The excited state linewidth of the ^{87}Rb D$_2$ line is $\Gamma = 2\pi \times 6.07$ MHz [408], about 1/4 the excited state linewidth of ^{138}Ba$^+$ on the cooling transition and the Doppler temperature limit for our ^{87}Rb vapour, defined in Eqn. 6.14, is commensurately lower: $T_{\mathrm{D}} = 146$ μK.

Although this molasses cools thermal atoms within a small capture velocity range, it doesn't provide any restoring force equivalent to the time-averaged electric fields in our ion traps of Chaps. 6 and 11. An additional effect is required to form a trap for our atomic vapour.

Introducing a quadrupole magnetic field about the beam intersection point provides a restoring force [92, 409]. The trapping site is the magnetic field zero, and atoms experience a Zeeman shift relative to the trap centre that depends on their displacement. The counter-propagating trapping fields have the same circular polarization, such that they drive opposite $\sigma_\pm$ transitions. The beams address transitions with opposite Zeeman shifts and therefore atoms displaced from the centre preferentially absorb photons from one of
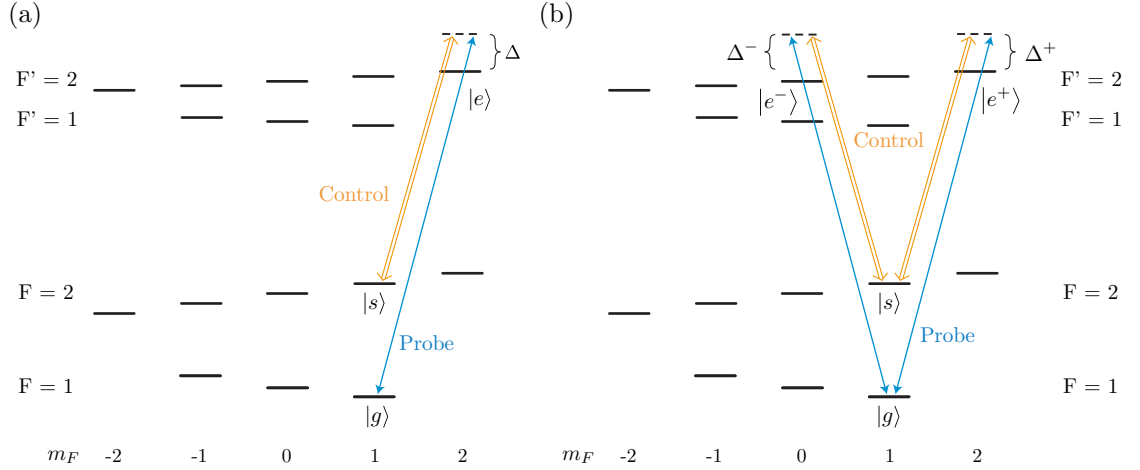
Figure 15.2: The Zeeman-split ^{87}Rb D$_1$ line and the Λ schemes we use for gradient echo memory. The Zeeman levels are split by a static magnetic field **B** such that the Zeeman transitions are spectrally resolved. (a) The same-circular configuration used in Chap. 17. (b) The orthogonal-linear configuration used in Chap. 16. The coherence $\hat{\sigma}_{gs}$ is driven simultaneously by two Raman transitions, one for each of the circularly polarized probe and control components. Interference between the two Raman transitions defines orthogonal 'coupled' and 'uncoupled' probe polarizations, see Sec. 16.2.

the two counter-propagating beams. Correctly choosing the polarization of the beams, this preferential absorption favours the beam travelling inwards and produces a restoring force towards the centre of the trap. In contrast to the molasses, this restoring force is proportional to the atom displacement and not to the velocity, and therefore compresses the atomic vapour about the trap site until this trapping force is balanced by the vapour pressure of the ensemble.

This trapping configuration has been shown to prepare vapours with temperatures below the Doppler limit by an effect called polarization gradient cooling [409, 410]. The combined effect of the counter-propagating circular fields and atomic motion is to produce a population difference among the Zeeman sublevels in the standing wave and, consequently, a large motion-sensitive radiation pressure imbalance from the two fields. A slightly different mechanism effect exists for sub-Doppler cooling with counter-propagating orthogonal linear fields. In principle, the temperature of the vapour under polarization gradient cooling can approach the recoil-limit temperature [411]

$$T_{\mathrm{R}} = \frac{\hbar^2 k^2}{k_{\mathrm{B}} m} \,, \tag{15.2}$$

where k_{B} is the Boltzmann constant and m is the atomic mass. $T_{\mathrm{R}} = 0.36$ μK for ^{87}Rb on the D$_2$ transition.

Because the transition we use for trapping is not cyclic, the atom may decay to the unaddressed hyperfine ground state after each excitation. To trap and cool continuously therefore requires a repump beam to return the atoms to the cooling-trapping manifold, much as the repump beam facilitated continuous Doppler cooling for our trapped ion in Chap. 6.

15.3   Atomic motion

Memory experiments must be performed with the MOT fields off; the near-resonant trapping fields cause too much decoherence for a functional memory and the magnetic trapping field gradients are 10 G cm^{-1}. During memory operations the vapour is no longer trapped, and both falls under gravity and expands ballistically. The gravitational displacement is only 5 μm in 1 ms, and common to every atom in the MOT, so we can safely neglect it. However, the ballistic motion will prove to be very important, and we must consider its impact on storage time. In contrast to a hot atomic vapour, the collision rate is sufficiently low that redirecting collisions are negligible. Rather than diffusing, each atom in our vapour expands essentially unimpeded in a direction and at a rate determined by its velocity.

Assuming thermal equilibrium, the velocity of atoms in our vapour is Maxwell-Boltzmann distributed everywhere. Given an initial atom density distribution n_0, the distribution at time t later is given by convolution with the displacement function for each coordinate

$$n(t) = n_0 * D_x(t) * D_y(t) * D_t(t) \tag{15.3}$$

$$D_x(t) = \sqrt{\frac{m}{2\pi m k_{\mathrm{B}} T}} \frac{1}{t} e^{-\frac{m}{2k_{\mathrm{B}}}\left(\frac{x}{t}\right)^2} , \tag{15.4}$$

where T is the ensemble temperature. We can apply the same convolution operation to the collective atomic operators $\hat{S}$ and $\hat{P}$ to give their evolution under atomic motion so long as the operators are otherwise static. Radial and longitudinal motion impact the GEM spin wave in distinct ways.

Radial motion distorts the memory by increasing the radial size of the coherence with respect to the input signal. Eventually atoms may leave the interaction region altogether. If the initial coherence is Gaussian in x and y with waist w_0 given by the beam waist of the signal beam, then the overlap between the recalled and signal modes is the overlap between a Gaussian with width w_0 and a Gaussian with width $w_0 + \langle v \rangle t$ where $\langle v \rangle = \sqrt{k_{\mathrm{B}}T/m}$. The characteristic time of this Gaussian overlap decay is $\tau_{\mathrm{r}} = w_0/\langle v \rangle$. The decoherence of spin waves with transverse structure is faster, this was considered under diffusive motion in Ref. [324].

Longitudinal motion washes out the phase fringes of the spin wave. For a static spin wave with spatial wavelength k the coherence is mostly lost when $\langle D_z(t) \rangle > \tau_{\mathrm{l}}$ where $\tau_{\mathrm{l}} = 1/(k\langle v \rangle)$ is the characteristic time for longitudinal diffusion over a static spin wave [412]. The decoherence of a static spin wave under longitudinal diffusion is exponential in t.

Combining the equations for Gaussian radial and exponential longitudinal decays we arrive at the recall efficiency of a static spin wave [412]

$$\eta(t) = \eta_0 \frac{1}{1 + (t/\tau_{\mathrm{r}})^2} \exp\left[\frac{-(t/\tau_{\mathrm{l}})^2}{1 + (t/\tau_{\mathrm{r}})^2}\right] , \tag{15.5}$$

where η_0 is the recall efficiency at zero and includes losses due to control field scattering.

However, we saw in Sec. 13.2 that the GEM polariton spatial frequency is not fixed, but instead increases and then decreases during storage and recall. The trajectory of the polariton may be quite complicated depending on the magnetic field switch scheme. The decoherence of this dynamic spin wave under longitudinal diffusion was considered analytically for several operation schemes in Ref. [413]. To describe the same process in

a cold-atom vapour it is only necessary to replace the diffusion distribution in Ref. [413] with the ballistic distribution from Eqn. 15.3. We can incorporate the diffusion numerically in our XMDS2 scripts by adding differential ballistic convolution at every time step, or equivalently by multiplying the Fourier components by the convolution function. Nevertheless, Eqn. 15.5 is a reasonable approximation of cold-atom GEM efficiency when the spin wave is kept stationary during storage and the storage is long compared to the read and write stages. In this case we define the typical spin wave momentum

$$k = \delta_z t/2 + (k_\mathrm{p} - k_\mathrm{c})\,, \tag{15.6}$$

where $\delta_z = \delta_\xi/L$ is the spatial magnetic field gradient and t is the total time the polariton evolves under δ_z.

Generally, to operate a GEM with atomic motion it is optimal to freeze the polariton evolution at low k for as long as possible, and to use co-propagating control and probe beams so that $\theta = 0$ and the initial spin wave momentum $k_0 = k_p - k_c$ is small.

15.4   MOT apparatus

15.4.1   Rubidium sources

Our rubidium vapour is held in a rectangular glass cell connected to a vacuum system maintained at 10^{-10} Torr by continuous ion pumping. The vapour is produced by heating dispensers containing rubidium salts. The initial dispensers in our apparatus, manufactured by SAES, expired during the course of Chap. 16, and we briefly replaced them with rubidium alloy based dispensers from Alvatec before returning to SAES dispensers for Chap. 17, due to contamination problems with the Alvatec sources.

A large MOT requires a high background vapour pressure to trap from, however if the background pressure is too high then collisions with thermal atoms will limit the size of the MOT. We optimize the dispenser current, and all trapping parameters, for the preparation of high optical depths.

15.4.2   Trap and repump lasers

The trapping and repump fields are generated by temperature-stabilized MOGlabs cateye diode lasers (CEL v001) and amplified. The cateye diode lasers were chosen for their excellent stability and wide mode-hop-free scan range of ≈ 15 GHz. Tapered amplifiers increase the laser field power from ≈ 10 mW to up to 1 W.

The trapping and repump lasers are frequency locked to one of the ^{87}Rb D$_2$ hyperfine transitions by Doppler-free saturated absorption spectroscopy. A bright circularly polarized pump and a weak circularly polarized probe derived from the same beam counterpropagate through the Doppler-broadened ensemble. Only atoms moving perpendicularly to the direction of propagation are simultaneously resonant with both beams. The pump therefore opens a transparency window in the centre of the Doppler broadened absorption feature of each hyperfine transition [414]. In the limit of weak probe fields, this transparency window is limited by the natural linewidth of the transition. The laser is locked to this feature by modulating the magnetic field about vapour cell (Zeeman modulation). The absorption signal is demodulated in a process similar to Pound-Drever-Hall locking [242]. An acousto-optic modulator (AOM) is used to shift the locking beams so that the

trap and repump lasers can be locked anywhere within 220 MHz of any of the hyperfine lines.

Locking an external cavity diode laser to an atomic transition in this way can reduce the linewidth of the source to 80 kHz [415]. In our case, using Zeeman modulation and a vapour cell without magnetic shielding, the lasers operate with linewidth < 300 kHz, which is more than sufficient for trapping and repumping the atoms in our MOT.

15.4.3   MOT coils

Ultimately we want our cold rubidium vapour to provide an efficient gradient-echo memory platform. As we discussed in Sec. 13.2, Λ-GEM only approaches unit efficiency in the Raman limit. The effective optical depth (Eqn. 13.56) decreases in proportion to the single-photon detuning Δ, and although we may compensate by increasing the control field power, this in turn reduces the memory efficiency by control field scattering (Eqn. 13.49). An efficient GEM therefore requires a very high resonant optical depth to start with, which we achieve by compressing our vapour into an elongated cigar shape.

The optical depth (from Eqn. 13.37) is

$$d = \frac{g^2 N L}{\Gamma c} \,. \tag{15.7}$$

Since $g \propto 1/\sqrt{V}$, we have $d \propto 1/A$ for a collimated beam and fixed atom number N. We can therefore optimize the depth by compressing as many atoms as possible into a narrow region along the optical axis of a narrow, but still collimated, beam.

Our magneto-optical trap is designed to prepare a cold atomic vapour with an elongated cigar shape, pictured in Figure 15.3. This provides a high optical depth for the signal beam along the direction of propagation. The 2D radial magnetic quadrupole field is produced by an anti-Helmholtz pair of rectangular coils. The vapour cloud is trapped radially and concentrates along the long axis, this type of MOT was first pioneered by Y. Lin in Ref. [416]. We also have capping coils that provide axial confinement near the edges of the ensemble. The resulting cloud contains $\approx 10^{10}$ atoms and has a length of 5 cm. Three further pairs of coils mounted around the optical table are used to compensate static ambient magnetic fields.

GEM must be performed with the MOT magnetic coils switched off, but switching the MOT coils causes eddy-currents in neighbouring conductors. These eddy-currents produce, in turn, magnetic field variations that decohere the stored spin wave. We lifted the vapour cell and vacuum chamber by ≈ 50 cm from the optical table to reduce fields due to eddy currents.

15.4.4   Preparing the ensemble

The cold atomic vapour is assembled during a 170 ms 'loading' phase. During this stage, the trap and repump fields continuously trap and cool thermal rubidium atoms from the dispensers until the vapour in the trap reaches an equilibrium temperature, size and density. During the loading phase, the trapping laser is red detuned by 35 MHz from the D_2 $F = 2 \leftrightarrow F' = 3$ transition and the repump laser is resonant with the D_2 $F = 1 \leftrightarrow F' = 2$ transition.

After loading we further increase the MOT density with a radial compression phase. We increase the 2D MOT coils current smoothly over a period of 20 ms to ramp up the
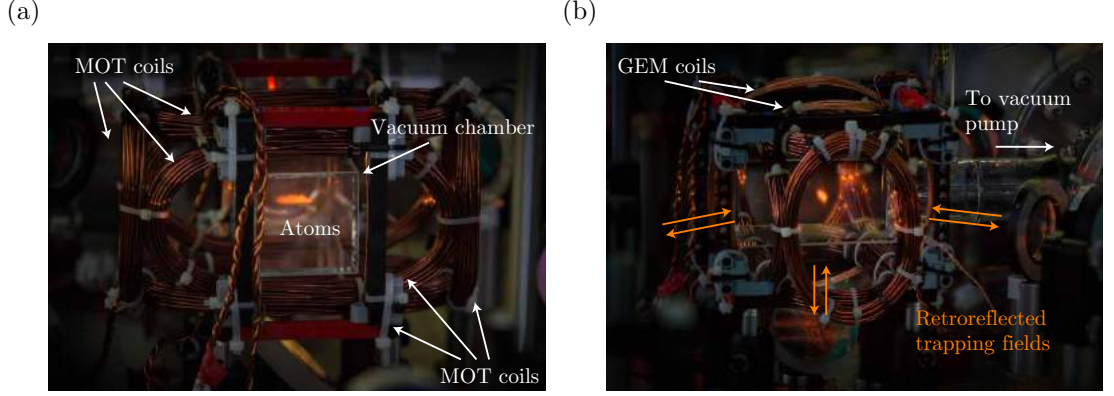
Figure 15.3: The MOT apparatus shown with a trapped cold-atom vapour from (a) side and (b) along the propagation axis. The atoms are pictured after loading but before the compression stage of our ensemble preparation, and are still diffuse. They fluoresce under the continuous trapping and repump fields. The retroreflected optical fields and elongated magnetic field coils produce the magneto-optic trapping potential. The anti-Helmholtz gradient coils and bias coils (not pictured) produce the gradient field we use for memory operations. Over the course of this thesis the Lego coil holders pictured were replaced with purpose machined coil mounts and the atom-cloud density was improved considerably.

radial magnetic field gradient. At the same time, we ramp up the red detuning of the repump laser by $\Delta = 25$ MHz. This type of compression phase has been shown to achieve transient increases in atomic density of up to an order of magnitude [417].

The MOT coils are then switched off in order to conduct the memory experiment, at which point the vapour begins falling under gravity and expanding ballistically. Recording the optical depth of the vapour over time, we estimate that the equilibrium temperature is $T = 95\ \mu$K, slightly under the Doppler temperature limit. The corresponding mean velocity is $\langle v \rangle = 0.095$ m/s. Ideally, we should operate the memory immediately after the trap is dropped, before ballistic expansion has a chance to reduce the density too dramatically. Unfortunately, we first need to wait for stray magnetic fields due to the trap coils to stabilize.

The decay of the magnetic trapping fields and eddy currents induced in nearby metallic objects was found to have a time constant of ≈ 0.7 ms. We wait for 1–2 ms before performing any measurements. During this drop time the trapping lasers remain on, and we detune the trapping field by a further 63 MHz to further cool the falling vapour by polarization gradient cooling and limit the ballistic expansion. If we desire the ensemble to be prepared in a single extremal Zeeman state then we apply a circularly polarized pump beam along the optical axis on the $D_1\ F = 1 \leftrightarrow F' = 2$ transition for 0.5 ms after this final cooling stage. This pump beam is accompanied by a linearly polarized repump beam on the $D_1\ F = 2 \leftrightarrow F' = 2$ transition.

Once the eddy currents have died down and all optical and magnetic MOT fields are switched off we are prepared to perform a memory experiment. We measure the OD at this point in the cycle by absorption measurements with an off-resonance probe. The highest resonant OD we inferred on the $D_1\ F = 1 \leftrightarrow F' = 2$ probe transition was $d \approx 600$, with which we took the high efficiency GEM data for Chap. 17. After each experiment we bring the trapping fields back up and recapture the falling atoms in the next loading phase.

15.5   GEM apparatus

15.5.1   Probe and control lasers

The probe and control fields at 795 nm are derived from a single, continuous-wave Ti:Sapphire laser with a scanning external reference cavity, the M^2 'SolsTiS 2000'. The SolsTiS is pumped at 532 nm by a frequency doubled 1064 nm DPSS source. The SolsTiS provides a maximum of 2.4 W of power with a linewidth of ≈ 50 kHz, which can be further narrowed to 1 Hz with the use of an ultra-stable, high-finesse reference cavity of the sort we employed in Sec. 6.4.2, however the experiments in this section will be carried out with atomic dipole transitions alone and the 50 kHz linewidth of the scanning reference cavity will be sufficient. There is a limited range of commercial continuous-wave Ti:Sapphire lasers, of these options the SolsTiS was chosen for its narrow linewidth and compact construction.

The probe and control fields need to be separated by the ground-state splitting $\approx$ 6.8 GHz. As the control requires the most power, we lock the source laser to a cavity reference ≈ 200–300 MHz blue detuned from the D_1 $F = 2 \leftrightarrow F' = 2$ transition, and produce the probe field by modulation. A fibre EOM modulates one arm of the source at ≈ 6.8 GHz and one of the sidebands is selected using a mode-cleaning cavity, PDH locked with another modulator.

The probe field is focused into the centre of the ensemble with a beam waist of $w_0^{\mathrm{p}} = 110$–200 μm. The control field is collimated and telescoped up to $w_0^{\mathrm{c}} = 7$ mm so that it illuminates the ensemble uniformly. The probe and control beams are combined on a 50:50 beam splitter at a slight angle θ so that they can be separated after the ensemble. However, the angle θ imprints a longitudinal phase onto the ensemble spin wave. The larger the angle, the more rapidly the spin wave dephases under atomic motion. We operate with $\theta = 0$ for long storage times.

The polarization, fine-detuning and amplitude of the probe and control beams are set independently with waveplates and AOMs. Depending on the Λ-scheme to be used, we choose the probe and control to have either same circular or orthogonal linear polarizations.

15.5.2   Detection

The control field is orders of magnitude brighter than the probe, and so we require substantial filtering to suppress control light at the detectors. This filtering is achieved by a combination of methods. First, a knife edge takes advantage of the propagation angle θ to remove most of the control after the ensemble. Second, the probe is focussed through a 100 μm pinhole which removes any remaining or scattered control. This spatial filtering suppresses the control field by 50 dB and the probe field by only 0.9 dB.

The input and output probe pulses are measured with either a balanced heterodyne detector, photodiode or APD. Input amplitude reference pulses are measured in the absence of a MOT, and every signal pulse is preceded by a phase reference pulse that passes through the MOT without a control field.

15.5.3   GEM coils

A pair of axial Helmholtz coils generate a magnetic field gradient along the direction of propagation for operating a gradient echo memory. Independent current sources powered by Apex Power PA107 op-amps drive the coils, providing 5 A and 100 V with a rise-time of less than 1 μs. This is the limit of the the gradient switch time.

The magnetic field is nearly, but not perfectly, linear between the two coils. The common current determines the uniform magnetic field bias B_0 and the current difference determines the magnetic field gradient δB. The field gradient is switched by reversing the current difference. In gradient echo memory experiments with hot vapours we have used cylindrical coils with a winding density gradient to produce more homogeneous magnetic field gradients. Unfortunately, such coils obstruct too much of the optical access for use with a MOT. Magnetic field inhomogeneity is one of the remaining decoherence sources in our memory.

15.6   Summary

We have described the relevant details of the magneto-optical trap apparatus for cooling and trapping cold rubidium vapours. The electrical configuration and optical transitions of ^{87}Rb were given, and we described how the hyperfine-split ground-state spin coherence can be used for storing qubits in the ensemble. We detailed the laser systems and magnetic field coils available for trapping and manipulating our cold rubidium vapour, and the experimental sequence we use for preparing a cold, dense ensemble as a platform for gradient echo memory. We also detailed the laser systems and magnetic field coils used to operate our GEM. In the following two chapters we report results with this quantum memory, first by extending GEM to support frequency-encoded qubits, and then by pushing the efficiency and coherence time of our memory into a regime that outperforms, for the first time, a fibre delay line in the no-cloning regime.

Bibliography - Cold atomic vapour apparatus

92. D. A. Steck, *Quantum and atom optics* (2007).

242. R. W. P. Drever, et al., Laser phase and frequency stabilization using an optical resonator, *Appl. Phys. B* **31**, 97–105 (1983).

324. D. B. Higginbottom, Spatial multimode storage in a gradient echo memory, Honours thesis (The Australian National University, 2011).

397. B. M. Sparkes, et al., Gradient echo memory in an ultra-high optical depth cold atomic ensemble, *New J. Phys.* **15**, 085027 (2013).

402. B. M. Sparkes, Storage and manipulation of optical information using gradient echo memory in warm vapours and cold ensembles, PhD thesis (The Australian National University, 2013).

406. W. D. Phillips, Nobel Lecture: Laser cooling and trapping of neutral atoms, *Rev. Mod. Phys.* **70**, 721–741 (1998).

407. L. Khaykovich, et al., Ultrasensitive two-photon spectroscopy based on long spin-relaxation time in a dark optical trap, *Europhys. Lett.* **50**, 454–459 (2000).

408. D. A. Steck, Rubidium 87 D line data, 1–29 (2001).

409. J. Dalibard, and C. Cohen-Tannoudji, Laser cooling below the Doppler limit by polarization gradients: Simple theoretical models, *J. Opt. Soc. Am. B* (1989).

410. A. M. Steane, and C. J. Foot, Laser cooling below the Doppler limit in a magneto-optical trap, *Europhys. Lett.* **14**, 231–236 (1991).

411. C. Salomon, et al., Laser cooling of cesium atoms below 3 μK, *Europhys. Lett.* **12**, 683–688 (1990).

412. S. D. Jenkins, T. Zhang, and T. A. B. Kennedy, Motional dephasing of atomic clock spin waves in an optical lattice, *J. Phys. B* **45**, 124005 (2012).

413. X. W. Luo, et al., Diffusion effects in gradient echo memory, *Phys. Rev. A* **87** (2013).

414. C. J. Foot, *Atomic physics* (Oxford University Press, 2005).

415. S. D. Saliba, and R. E. Scholten, Linewidths below 100 kHz with external cavity diode lasers, *Appl. Opt.* **48**, 6961 (2009).

416. Y.-W. Lin, et al., Using a pair of rectangular coils in the MOT for the production of cold atom clouds with large optical density, *Opt. Express* **16**, 3753 (2008).

417. W. Petrich, et al., Behavior of atoms in a compressed magneto-optical trap, *J. Opt. Soc. Am. B* **11**, 1332 (1994).

Dual-rail optical gradient echo memory

*I am at one with my duality.*

– G. K. Chesterton

In this chapter we introduce a scheme for the parallel storage of frequency separated signals in an optical quantum memory and demonstrate that this dual-rail storage is a suitable memory for high fidelity frequency qubits. The two signals are stored simultaneously in the Zeeman-split Raman absorption lines of a cold atom ensemble using gradient echo memory techniques. Analysis of the split-Zeeman storage shows that the memory can be configured to preserve the relative amplitude and phase of the frequency separated signals. In an experimental demonstration dual-frequency pulses are recalled with 35% efficiency, 82% interference fringe visibility, and 6° phase stability. The fidelity of the frequency-qubit memory is limited by frequency-dependent polarization rotation, our analysis describes how these can be addressed in an alternative configuration. This work has been published in full as

[1] "**Dual-rail optical gradient echo memory** D. B. Higginbottom, J. Geng, G. T. Campbell, M. Hosseini, M. T. Cao, B. M. Sparkes, J. Bernu, N. P. Robins, P. K. Lam, and B. C. Buchler. *Optics Express* **23**, 24937 (2015). "

16.1 Frequency qubits

The performance of a practical quantum memory for qubits is contingent on the way those qubits are encoded in the single-photon field. Any linear, single-mode memory is capable of storing photon number qubits, however inefficiency and loss in the memory or other network elements will decrease output state fidelity. For this reason an alternate encoding is often used, such as the polarization, orbital angular momentum, path, or arrival time (time-bin) of a single photon. Memories for polarization qubits have been demonstrated using electromagnetically induced transparency (EIT) [354, 355, 357], atomic frequency comb (AFC) [418] memories, and Raman absorption [386]. EIT has also been used to store orbital angular momentum qubits with high fidelity [419]. Temporally multimode memories, such as AFC [387] and gradient echo memories (GEM) [394], are also suitable for time-bin qubits.

Here we present work based on the three-level GEM protocol [327–329] towards a quantum memory for frequency qubits [420, 421]. We extend the GEM protocol to make use of Zeeman sub-levels to store and recall two frequency channels, this provides a basis to store frequency qubits with a high fidelity. These split Zeeman levels have previously been used to store matched pulses with EIT [422].
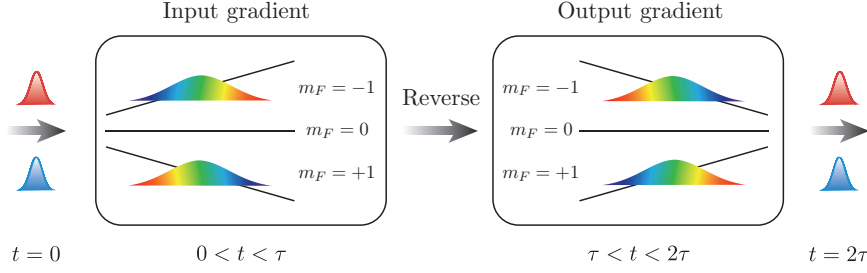
Figure 16.1: A simplified energy diagram of atomic levels $m_F = -1, 0, 1$ under constant uniform bias field B_0 and reversible gradient field B_z illustrating the operation of the dual-rail gradient echo memory.

As per the gradient echo memory protocol from Sec. 13.2, the atomic resonances in our Λ-atom ensemble are prepared by applying a tailored magnetic field along the optical propagation axis. A bias magnetic field B_0 lifts the degeneracy of the Zeeman sub-levels by introducing a Zeeman shift given by $\Delta E = m_F g_F \mu_B B_0/h$, where m_F is the Zeeman level number, g_F is the Landé factor for hyperfine state F, μ_B is the Bohr magneton and h is the Planck constant. For the D1 line of ^{87}Rb atoms the Landé factors are respectively $g_1 = -1/2$ and $g_2 = 1/2$. A single coupling field detuned from the $F = 2 \leftrightarrow F' = 2$ transition will produce three Raman absorption lines for a weak signal field on the $F = 1 \leftrightarrow F' = 2$ transition, corresponding to signal field detunings of 0 (insensitive line) and $\pm\delta_0$ relative to the unsplit Raman transition, where δ_0 is given by

$$\delta_0 = \frac{\mu_B}{\hbar} B_0 \simeq 2\pi \times 1.4\,\text{MHz/G} \times B_0\,. \tag{16.1}$$

A reversible magnetic field gradient $B_z(z)$ is applied along the ensemble in addition to the uniform bias field B_0 to broaden the two magnetically sensitive lines around $\pm\delta_0$ for light storage using the GEM protocol, as illustrated in Fig 16.1. Our GEM in Chap. 17, and all previous GEM experiments, used only one of these two magnetically sensitive lines to store and recall pulses. In this chapter we show that the sub-levels responsible for the two absorption lines can be utilized to store pulses of light at frequencies $\pm\delta_0$ in parallel such that the two lines form a memory for frequency encoded qubits. The same scheme readily extends to higher mode frequency states in atomic ensembles with high ground state angular momentum. For example, the four magnetically sensitive Zeeman levels of the ^{85}Rb ground state (F=2) could be used to store four mode frequency states using the same approach that we demonstrate here with ^{87}Rb.

To achieve high fidelity frequency qubit storage in such a dual-rail GEM it is necessary to balance the effective optical depth of the two Raman lines shown in Fig. 16.2(b) and match the output polarization of each frequency rail. The optical depth of each line depends on the dipole matrix elements associated with the transitions for the coupling and signal fields involved in the relevant two-photon transitions, as well as the polarization of the two beams. In general, for an ensemble of atoms that has a population distributed uniformly across the Zeeman sub-levels, this results in unequal optical depths for the $\pm\delta_0$ Raman transitions. To balance the efficiencies of the two frequency rails we use linear polarizations for the coupling and signal fields which, by symmetry, ensures equal optical depths. In this configuration, however, frequency dependent polarization rotation will produce output modes that are not matched and limit our qubit fidelity.
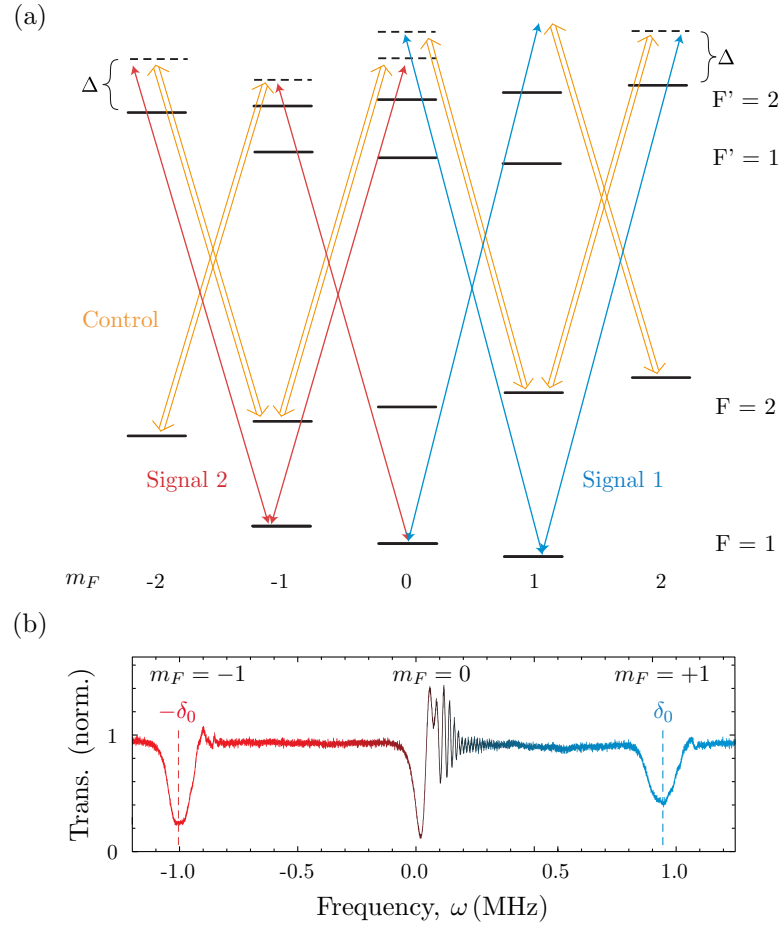
Figure 16.2: (a) Zeeman levels of the ^{87}Rb D1 line split by a bias magnetic field B_0. The control and signal laser fields couple the two ground states F=1 and F=2 via multiple Λ-type Raman transitions. (b) Split Raman absorption lines for the dual-GEM scheme. Non-degenerate lines at $\pm\delta_0$ are produced by the bias magnetic field B_0 according to the level scheme above, and broadened by an additional field gradient B_z that is applied to the atom ensemble for GEM. Free-induction decay can be seen in the centre line. Inhomogeneous broadening by the magnetic field suppresses free induction decay on the two magnetically sensitive lines.

16.2   Polarization rotation

Polarization rotation occurs as a result of interference between coherences driven by the σ^+ and σ^- components of each signal field. To examine the effect of this rotation, we consider below the level structure of the ^{87}Rb atoms, shown in Fig. 16.2(a). Off-resonant dispersion of σ^+ and σ^- will further rotate the signal fields, but the relative Faraday rotation between signals 1 and 2 is negligible so long as their splitting, δ_0, is much smaller than the detuning, Δ.

We assume that the population initially rests entirely in the $F = 1$ ground state, evenly distributed between Zeeman sub-levels, and that there are no coherences within that manifold. These assumptions are valid provided that the probe field is weak and that the splitting, δ_0, is large compared to the Raman linewidth. We proceed by treating each of the signals independently, starting with the signal 1. Referring to Fig. 16.2(a), signal 1 will produce a coherence, $\hat{\sigma}_1$, between the $|F = 1, m_F = 1\rangle$ and $|F = 2, m_F = 1\rangle$

states via three Λ systems with excited states $|F' = 2, m_F = 0\rangle$, $|F' = 2, m_F = 2\rangle$ and $|F' = 1, m_F = 0\rangle$. This last Λ system reduces the absorption asymmetry between σ^+ and σ^- components of the signal. Consequently the σ^+/σ^- absorption ratio approaches unity as the detuning Δ is increased.

The Λ system formed by $|F = 1, m_F = 0\rangle$, $|F' = 2, m_F = 1\rangle$ and $|F = 2, m_F = 2\rangle$ makes a small contribution to the memory process due to weak effective coupling strength. We neglect this contribution in the analysis below because the optical depth associated with this process is ≈ 19 times smaller than the optical depth of the three Λ schemes contributing to the $|F = 1, m_F = 1\rangle \leftrightarrow |F = 2, m_F = 1\rangle$ coherence.

16.3   Equations of motion

Following Eqns. 13.32 to 13.34, the equations of motion for signal 1 are[1]

$$\partial_t \hat{\sigma}_1 = -(\gamma_0' + i\delta')\hat{\sigma}_1 + ig_1^- \hat{\mathcal{E}}_1^- + ig_1^+ \hat{\mathcal{E}}_1^+ , \tag{16.2}$$

$$(\partial_t + c\partial_z)\hat{\mathcal{E}}_1^\pm = ig_1^\pm N\hat{\sigma}_1 , \tag{16.3}$$

with effective coupling strengths

$$g_1^+ \propto \frac{\Omega^+}{\Delta_{22}}\mu_{(1,1;2,2)}\mu_{(2,1;2,2)} , \tag{16.4}$$

$$g_1^- \propto \frac{\Omega^-}{\Delta_{22}}\mu_{(1,1;2,0)}\mu_{(2,1;2,0)} + \frac{\Omega^-}{\Delta_{21}}\mu_{(1,1;1,0)}\mu_{(2,1;1,0)}) , \tag{16.5}$$

where $\mu_{(m,n;p,q)}$ is the dipole matrix element corresponding to the $|F = m, m_F = n\rangle \to |F' = p, m_F = q\rangle$ transition, $\Omega^\pm$ are the Rabi frequencies associated with the right and left circularly polarized components of the control field, $\Delta_{22} = \Delta$ is the control field detuning from the $|F = 2\rangle \leftrightarrow |F' = 2\rangle$ transition and $\Delta_{21} = \Delta + 2\pi \times 816.7$ MHz [408] is the control field detuning from the $|F = 2\rangle \leftrightarrow |F' = 1\rangle$ transition. We can further simplify this system by introducing the signal 1 coupled mode $\hat{\mathcal{E}}_1^{\mathrm{cp}}$

$$g_1^{\mathrm{cp}}\hat{\mathcal{E}}_1^{\mathrm{cp}} \equiv (g_1^- \hat{\mathcal{E}}_1^- + g_1^+ \hat{\mathcal{E}}_1^+) , \tag{16.6}$$

$$g_1^{\mathrm{cp}} \equiv \sqrt{|g_1^-|^2 + |g_1^+|^2} . \tag{16.7}$$

From Eqs. (16.2) and (16.3) we derive Eqs. of motion for the coupled mode

$$\partial_t \hat{\sigma}_1 = -(\gamma_0' + i\delta')\hat{\sigma}_1 + ig_1^{\mathrm{cp}}\hat{\mathcal{E}}_1^{\mathrm{cp}} \tag{16.8}$$

$$(\partial_t + c\partial_z)\hat{\mathcal{E}}_1^{\mathrm{cp}} = ig_1^{\mathrm{cp}}N\hat{\sigma}_1 . \tag{16.9}$$

The component of the input perpendicular to the coupled mode polarization is not stored in the memory. Given a horizontally polarized signal and vertically polarized control, g_1^- and g_1^+ determine the signal 1 coupled mode polarization $|P_1^{\mathrm{cp}}\rangle = 0.51\,|L\rangle + 0.86\,|R\rangle$. Analogous equations exist for signal 2; by symmetry (assuming detunings Δ_{21} and Δ_{22} are approximately the same for signals 1 and 2, and given the same beam polarizations) the coupled mode polarization for signal 2 is $|P_2^{\mathrm{cp}}\rangle = 0.86\,|L\rangle + 0.51\,|R\rangle$. The input and output polarizations of both signals are indicated schematically in Fig 16.3. The por-

---

[1]In this section superscripts $\pm$ denote the circularly polarized components of each signal, as distinct from their use in Sec. 13.3, where we used them to denote forward and backward propagating fields.
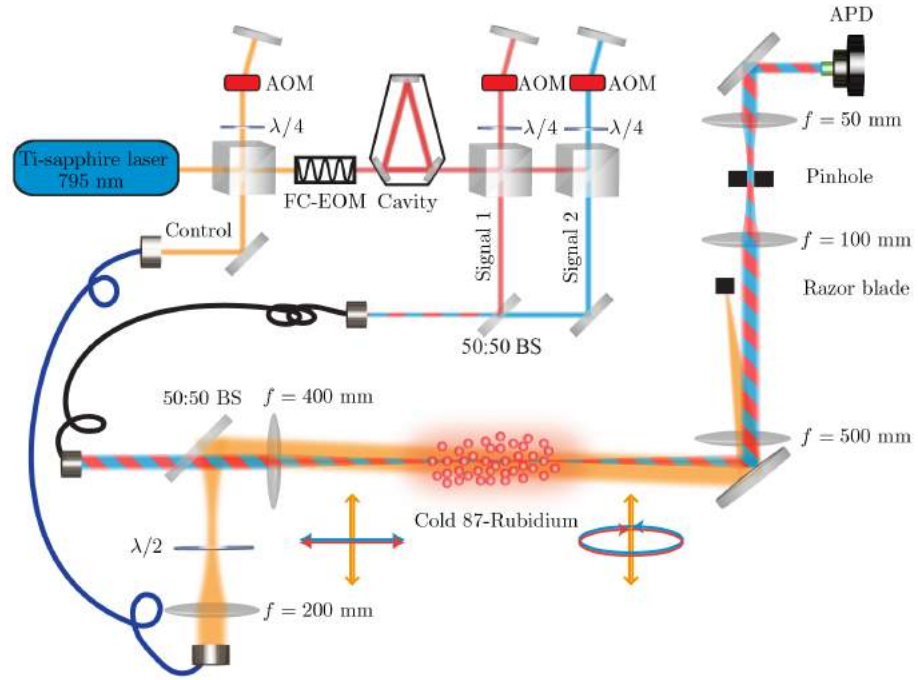
Figure 16.3: The experimental layout for dual-frequency GEM in an ensemble of cold ^{87}Rb atoms. A root signal beam is produced from the control by 6.8 GHz sideband generation (EOM) followed by frequency filtering (cavity). The beam is then split to allow independent gating and frequency control of signals 1 and 2 (AOMs). The two signal beams are recombined and sent to the atomic ensemble through an optical fibre. The ^{87}Rb atoms are cooled and held in a magneto-optical trap setup similar to that in [8, 402]. The signal and control polarizations are indicated schematically before and after storage in the atom ensemble. The output signal polarizations $|P_1^{\mathrm{cp}}\rangle$ and $|P_2^{\mathrm{cp}}\rangle$(defined in the text) are elliptical with major/minor axes ratio 0.97/0.24. After passing through the atom ensemble the coupling field is spatially filtered using a pinhole and razor.

tion of the input orthogonal to the coupled mode is not stored in the memory, therefore the highest efficiency possible in this memory configuration is $|H\rangle \cdot |P_1^{\mathrm{cp}}\rangle = |H\rangle \cdot |P_2^{\mathrm{cp}}\rangle = 0.94$. The interference fringe visibility between the two output modes is limited to the coupled mode overlap $|P_1^{\mathrm{cp}}\rangle \cdot |P_2^{\mathrm{cp}}\rangle = 0.88$.

To eliminate the polarization rotation described above and improve fidelity the memory can be configured with circularly polarized signal and control beams. In this alternative configuration the memory fidelity is limited by recall efficiency asymmetry between the rails, which goes to zero in the high optical depth limit. With low optical depth one could still balance these efficiencies directly by preparing an ensemble population unevenly distributed between the Zeeman sub-levels of the ground state.

16.4 Dual-rail storage

The experiment is carried out in a cold atomic cloud of ^{87}Rb produced by a magneto-optical trap prepared according to Chap. 15. The ensemble is initially prepared in the $F = 1$ hyperfine ground state with a resonant optical depth of $d \approx 300$ on the unsplit D_1 $F = 1 \leftrightarrow F' = 2$ transition. Eddy currents induced in the optical bench when the MOT coils switch off are allowed to die away for 1 ms before the memory experiment begins. The coupling field is turned on 400 μs before the writing stage to pump the atoms to the
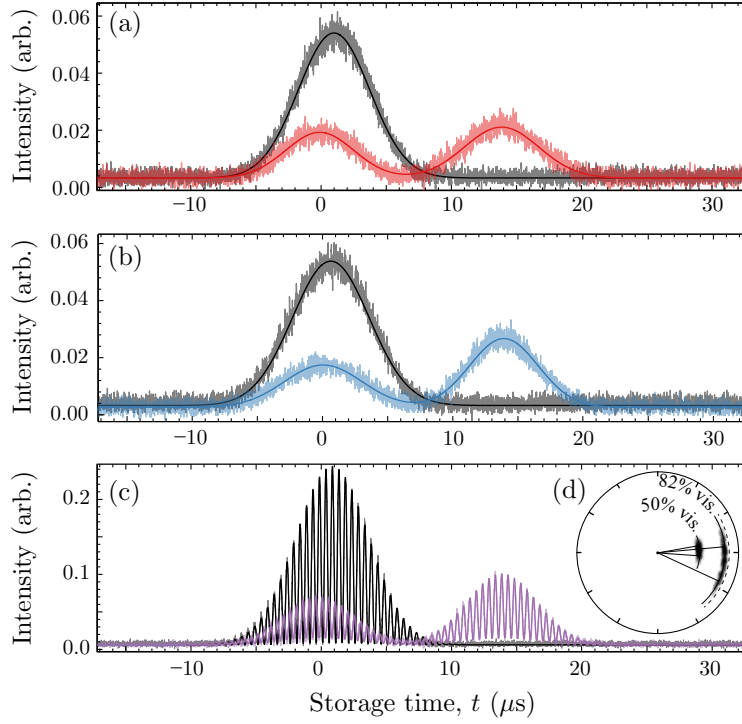
Figure 16.4: Storage and recall of the two signal fields independently and simultaneously. (a) A typical input signal (black, recorded without the atomic ensemble) and echo pulse (red, also with light that has leaked through the memory during the write process) of signal 2 in isolation. (b) A typical input (black) and echo (blue) of signal 1 in isolation. (c) Temporally matched input pulses of both signals (black) and simultaneously recalled echoes (purple) demonstrating parallel frequency rail storage. Inset (d) shows the relative phase and fringe visibility between the two echo signals as an angle and radial displacement respectively. The first set of data has a phase stability of only 15° and visibility of 82%. The black dotted arc is the visibility limit imposed by the polarization distinguishability of the signal outputs. The phase stability of the second set was improved to 6° by mains line triggering, but not optimized for high visibility interference.

$F = 1$ hyperfine ground state and remains on during the writing and reading stages.

The experimental setup is shown schematically in Fig 16.3. The coupling and signal fields are derived from a Ti:Sapphire laser that is 200 MHz blue-detuned from the ^{87}Rb D$_1$ $F = 2 \leftrightarrow F' = 2$ transition. The signal fields are produced by a fibre-coupled phase-modulator followed by a locked cavity. The modulator generates sidebands at $\approx \pm 6.8$ GHz relative to the coupling field and the cavity is used to select only the correct sideband, which is then split into the two signal fields. All three fields pass through separate acousto-optic modulators to allow for fine frequency adjustment as well as gating and pulsing. The signal fields are combined with the same linear polarization (horizontal), passed through an optical fibre and focused to match the size of the atomic cloud (beam waist = 200 μm). The coupling field is polarized orthogonally to the signal fields and is collimated to a larger diameter of 7 mm so that it illuminates the entire ensemble uniformly. The coupling field propagates with a small angle relative to the signal beams and after passing through the cell it is extinguished by ≈ 45 dB using a razor blade and a pinhole. This spatial filtering incidentally reduces the signal field efficiency by 1 dB.

The results of the dual-rail storage and recall experiment are shown in Fig. 16.4. Panels

(a) and (b) show independent storage and recall of each of the signal fields in the absence of the other. Panel (c) shows storage of the two signal fields simultaneously. The input signal pulses have a Gaussian profile with 10 μs width. We record reference traces of the inputs (black) in the absence of the atomic ensemble. Traces showing storage and recall in the atom ensemble (red, blue, purple) are produced by reversing the magnetic field gradient across the MOT as per the GEM scheme described in Sec. 13.2 such that the pulse is stored for approximately one pulse width. The polarization of the control field is tuned to balance the efficiencies of the echoes to compensate for misalignment of the magnetic gradient relative to the optical axis and polarization errors caused by the glass vacuum cell walls.

The recall efficiencies are 39% and 32% for signal fields 1 and 2 respectively. We demonstrate dual-rail storage by sending both signal pulses into the memory simultaneously with matched temporal profiles and amplitudes. The combined signals are recalled with 35% efficiency and the interference fringe visibility between the recalled pulses is 82%, compared to an expected visibility of 85% given the output mode overlap derived earlier (0.88), the measured rail efficiencies (0.32,0.39) and the input temporal matching (0.97). The relative phase between the echo signals is measured by comparing the beat signal phase of the recalled pulses to earlier reference pulses that are not stored and not shown in Fig. 16.4. The storage process produces an overall shift in the phase difference between the two signals with a standard deviation of 15°, Fig. 16.4(d). This variation is due to magnetic field background noise. By triggering the experimental sequence from the mains power supply, which improves the magnetic field stability, this phase noise was later reduced to 6°, Fig. 16.4(d). Unfortunately the output visibility in this second measurement was reduced by an unrelated experimental consideration, namely the exhaustion of our Rb source.

16.5   Summary

These results demonstrate that the dual-rail gradient echo memory can be used to store and recall two frequency separated signals in parallel while preserving the relative phase and amplitude of the optical states. This technique is therefore a suitable memory for frequency qubits with fidelity limited by the frequency-dependent polarization rotation of two signals and the magnetic field stability of the atom ensemble. The alternative circular polarization scheme described above is free of polarization rotation. Instead, the fidelity in this configuration is limited by unbalanced absorption of the two signals, which goes to zero as the optical depth increases and could be addressed even in a low optical depth ensemble by preparing asymmetric initial populations. Achievable improvements to the atom ensemble optical depth and ambient field isolation promise to improve both the efficiency and fidelity of such a frequency-qubit memory.

The optical depth available for this experiment was limited by the exhaustion of our rubidium dispensers. We have since replaced the dispensers, and improved the optical depth available for quantum memory to $d \approx 600$ on the ^{87}Rb D$_1$ $F = 1 \leftrightarrow F' = 2$ transition. With this improvement we are able to substantially enhance the efficiency of our memory, which is the subject of the following chapter.

Bibliography - Dual-rail optical gradient echo memory

1. D. B. Higginbottom, et al., Dual-rail optical gradient echo memory., *Opt. Express* **23**, 24937–44 (2015).

8. J. Geng, et al., Electromagnetically induced transparency and four-wave mixing in a cold atomic ensemble with large optical depth, *New J. Phys.* **16**, 113053 (2014).

327. A. L. Alexander, et al., Photon echoes produced by switching electric fields, *Phys. Rev. Lett.* **96**, 1–4 (2006).

328. G. Hétet, et al., Photon echoes generated by reversing magnetic field gradients in a rubidium vapor, *Opt. Lett.* **33**, 2323–5 (2008).

329. J. J. Longdell, et al., Analytic treatment of controlled reversible inhomogeneous broadening quantum memories for light using two-level atoms, *Phys. Rev. A* **78**, 032337 (2008).

354. Y.-W. Cho, and Y.-H. Kim, Atomic vapor quantum memory for a photonic polarization qubit, *Opt. Express* **18**, 25786–93 (2010).

355. C. Kupchak, et al., Room-temperature single-photon level memory for polarization states, *Sci. Rep.* **5**, 7658 (2015).

357. S. Riedl, et al., Bose-Einstein condensate as a quantum memory for a photonic polarization qubit, *Phys. Rev. A* **85**, 22318 (2012).

386. D. G. England, et al., High-fidelity polarization storage in a gigahertz bandwidth quantum memory, *J. Phys. B* **45**, 124008 (2012).

387. E. Saglamyurek, et al., Broadband waveguide quantum memory for entangled photons, *Nature* **469**, 512–5 (2011).

394. M. Hosseini, et al., Coherent optical pulse sequencer for quantum applications., *Nature* **461**, 241–5 (2009).

402. B. M. Sparkes, Storage and manipulation of optical information using gradient echo memory in warm vapours and cold ensembles, PhD thesis (The Australian National University, 2013).

408. D. A. Steck, Rubidium 87 D line data, 1–29 (2001).

418. C. Clausen, et al., Quantum storage of heralded polarization qubits in birefringent and anisotropically absorbing materials, *Phys. Rev. Lett.* **108**, 190503 (2012).

419. A. Nicolas, et al., A quantum memory for orbital angular momentum photonic qubits, *Nat. Photonics* **8**, 234–238 (2014).

420. J. Roslund, et al., Wavelength-multiplexed quantum networks with ultrafast frequency combs, *Nat. Photonics* **8**, 109–112 (2013).

421. P. C. Humphreys, et al., Continuous-variable quantum computing in optical time-frequency modes using quantum memories, *Phys. Rev. Lett.* **113**, 130502 (2014).

422. A. MacRae, G. Campbell, and A. I. Lvovsky, Matched slow pulses using double electromagnetically induced transparency, *Opt. Lett.* **33**, 2659 (2008).

High efficiency GEM

Bees have to move very fast to stay still.
   – David Foster Wallace, *Brief Interviews with Hideous Men* (1999)

The most efficient quantum memories demonstrated to date operate by gradient echo, with efficiencies of 69% in rare-earth ion crystals [423], 87% in hot vapours [395] and 80% in cold vapours [397] (before this work). The efficiency of cold-atom gradient echo memory has been limited primarily by the available optical depth (OD) [397]. In this chapter we report the operation of a cold-atom GEM with atom number $N \approx 10^{10}$ and optical depth $d = 600$ that improves the efficiency to $87 \pm 2\%$, equalling the best demonstrated quantum memory efficiency. The optical depth is improved by a combination of optical pumping and compression stages.

The storage time of our cold-atom GEM is limited by magnetic field noise and atomic motion to well below the best measured coherence times of the rubidium hyperfine ground states. Ref. [397] found the memory efficiency to decay exponentially with storage lifetime $\tau_s = 117$–$195\ \mu$s. In this chapter we improve the memory lifetime to $\tau_s = 1$ ms by improved cooling and the reduction of eddy currents. We lifted the MOT from the optical bench, the biggest source of eddy currents due to MOT field switching, and drop the vapour for longer before operating the memory to let eddy currents die down completely.

The efficiency and storage time of our memory are now such that we can recall stored pulses with 50% efficiency after 600 μs, surpassing the 50% lifetime of of an ideal fibre-loop delay line by a factor of six. Until now no quantum memory has beaten this time-efficiency limit. This work appears in the publication

[3] "**Highly efficient and long-lived optical quantum memory with cold atoms**" Y.-W. Cho, G. T. Campbell, J. L. Everett, J. Bernu, D. B. Higginbottom, M. T. Cao, J. Geng, N. P. Robins, P. K. Lam, and B. C. Buchler. *Optica* **3**, 100 (2016)."

17.1   Pumped Raman lines

We operate our GEM according to the description in Chap. 15 with same-circular probe and control polarizations, single photon detuning $\Delta = 325$ MHz, and after pumping the ensemble into the $F = 1$, $m_F = 1$ ground state $|g\rangle$. Pumping our vapour into the ground state is considerably less efficient than the single-atom pumping we performed in Chap. 7; inelastic collisions between atoms relax the populations at a rate that determines an equilibrium spin under continuous pumping. Figure 17.1 shows the Raman absorption resonances of the $m_F = -1, 0, +1$ lines after pumping and show residual populations in the other two Zeeman states. In contrast to the unpumped absorption lines in Fig. 16.2(b),
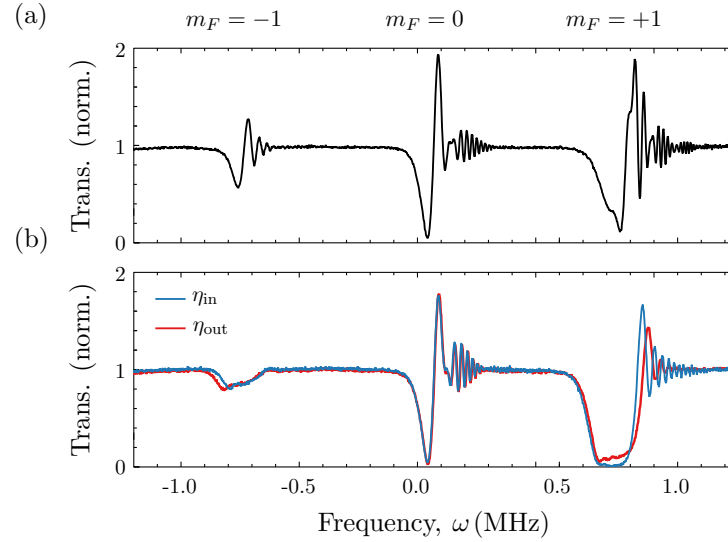
Figure 17.1: (a) The Raman lines after pumping and without broadening by a magnetic field gradient. (b) The pumped Raman lines with magnetic field gradients for the write and recall operations δ_{in} (blue) and δ_{out} (red).

the $m_F = -1$ and $m_F = 0$ lines are considerably suppressed and the $m_F = +1$ line is enhanced. Figure 17.1(a) shows the unbroadened Raman lines under the bias field B_0. The optical depths of the $m_F = -1, 0, +1$ lines are, respectively, 6.3, 38 and 488.

As with all the ensemble optical depth measurements reported in this thesis, the above depths are determined by measuring the absorption of an off-resonant probe pulse as a function of detuning. The resonant absorption is then inferred from a fit to the off-resonant absorption profile. This off-resonant absorption measurement is required whenever on-resonance absorption is effectively saturated, as it is for both the $m_F = 0$ and $m_F = +1$ lines after pumping. Although the optical depth of the $m_F = +1$ line is an order of magnitude larger than the $m_F = 0$ line, this is obscured slightly in Figure 17.1(a) by the presence of free induction decay [424].

Free induction decay is induced as the frequency scans to record these Raman lines because the scan and atomic dynamics have similar timescales. Free induction decay leads to apparent transmissions larger than one, and similarly obscures the true depth of the $m_F = +1$ absorption line in Figure 17.1(a) because the OD is sufficiently large that free-induction decay begins before resonance. Nevertheless, the width of the unbroadened $m_F = +1$ Raman absorption line in Figure 17.1(a) indicates that the true optical depth is larger than the $m_F = 0$ transition. Further evidence is provided by Figure 17.1(b), in which the $m_F = +1$ Raman absorption line is shown to saturate even after being broadened.

During the write and recall memory operations we apply an additional field gradient B_z to broaden the Raman lines by δ_ξ as shown in Fig. 17.1(b). The lines are shown for both the read (blue) and write (red) magnetic field configurations. From this measurement we determined input and output gradients of $\delta_{\mathrm{in}} = 2\pi \times 197$ kHz and $\delta_{\mathrm{out}} = 2\pi \times 210$ kHz, or $\delta_\xi \approx \pm 0.035\,\Gamma$. We calibrated the control field Rabi frequency Ω and atom number N by fitting an analytic model to broadened and unbroadened Raman lines recorded at various control beam powers.

17.2   High efficiency storage

We stored and recalled a Gaussian probe pulse with width 6.66 μs by gradient echo memory. The control field and magnetic field gradient remain on for the entire operation, with the magnetic field gradient switched at the half-way time. The storage and recall magnetic field gradients were unbalanced slightly, as we can see in Fig. 17.1(b), in order to preserve the shape and frequency of the recalled pulse, which would otherwise distort due to the close match between the pulse and memory bandwidths.

Figure 17.2(a) shows the input and recalled pulses as measured on a balanced heterodyne detector. The local oscillator was mode matched to the input signal recorded in the absence of any rubidium vapour. Figure 17.2(b) shows the demodulated heterodyne signals averaged over 15 pulses. The output pulse is only slightly distorted, its envelope overlaps 99.3% with the input pulse. The shot to shot phase drift is 5°, consistent with the phase stability of our dual rail memory in Sec. 16.4 after we introduced mains-line triggering. Including this phase fluctuation the mode overlap is still 99.1%. The efficiency is the square of the ratio of the input and output pulse areas, $\eta = 0.87 \pm 2$. This high-efficiency storage was taken with control field $\Omega = 2\pi \times 7.06$ MHz determined from the Raman line control field calibration.

The heterodyne-measured efficiency is consistent with the intensity efficiency as measured by an APD. However, the control-field intensity noise at the APD is large when the angle θ between probe and control beams is small, due to the increased difficulty of spatial filtering as $\theta \to 0$. Numerically modelling the memory by integrating Eqns. 13.47 and 13.48 with parameters from the Raman line fits to Fig. 17.1, we predict a theoretical efficiency of $\eta = 0.89$, consistent with the measured efficiency.

Noise may be present in the recalled pulse in the form of an idler field produced by FWM. Numerically integrating Eqns. 13.47 and 13.48 with an additional idler field and the same parameters predicts an idler field that is 0.9% of the input power. This FWM analysis was performed by Geoff Campbell, and a detailed explanation is available in his thesis, Ref. [332]. An analysis of FWM in a hot-vapour GEM with similar storage efficiency showed the same result [396].

17.3   Long coherence time storage

Storing the same Gaussian pulse with the control field and magnetic field gradient off, we measure a storage time that is limited by atomic motion. The bias field remains on to reduce dephasing by ambient magnetic field fluctuations. Figure 17.2(c) shows the storage efficiency measured by heterodyne detection as a function of storage time. When the probe and control fields are co-propagating ($\theta = 0°$) the memory lifetime is $\tau_{\rm s} = 1$ ms. The efficiency remains above $\eta = 0.5$ until $t = 600$ μs.

Given the temperature of our ensemble, $T = 100$ μK, the waist of our signal beam $w_0 = 100$ μm, and a maximum spin wave momentum $k = k_0 + \delta_\xi t/(2L)$ where t is the total time the field gradient is on, we predict radial and longitudinal motional time constants from Sec. 15.3 of

$$\tau_{\rm r} = w_0/\langle v \rangle = 1.15 \text{ ms}\,, \qquad \tau_{\rm l} = \frac{1}{\langle v \rangle \left(\delta_\xi t/(2L) + (k_p - k_c) \right)} = 71 \text{ ms}\,. \qquad (17.1)$$

We therefore expect that longitudinal diffusion is inconsequential at $\theta = 0°$ and decoherence is entirely due to atomic motion out of the signal mode. Fitting the atomic motion
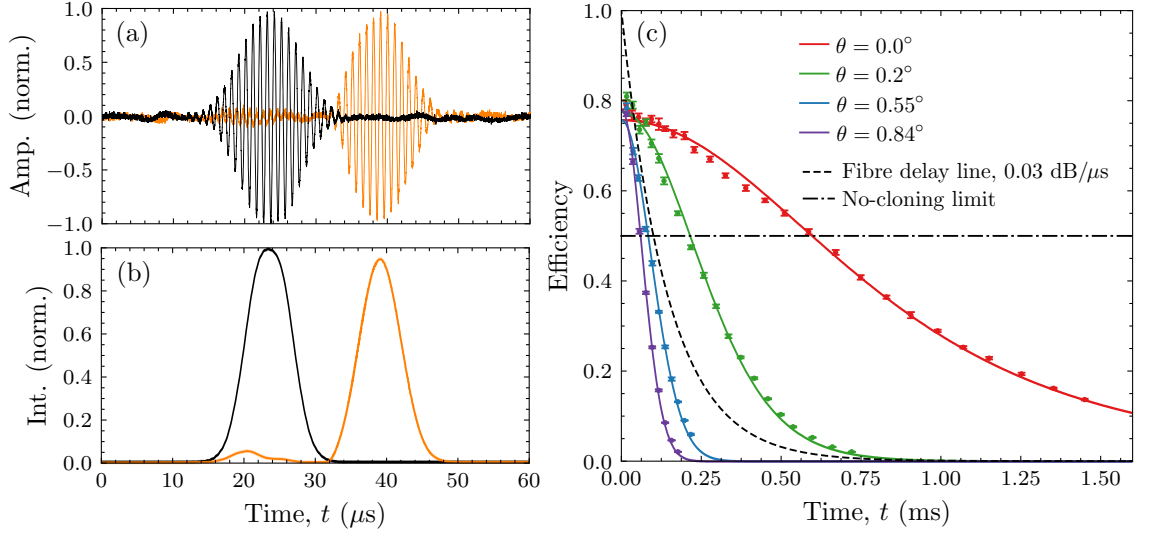
Figure 17.2: Gradient echo memory with a high OD ensemble. (a) The balanced heterodyne trace of the input (black) and recalled (orange) pulse stored for one pulse width. (b) Demodulated heterodyne input (black) and output (orange) signals, averaged over 15 traces. One σ uncertainty shown by shaded region. (c) Recall efficiency as a function of storage time for several angles θ between the probe and control beams. The efficiency is compared to two benchmarks: the efficiency of a fibre loop (dashed) and the no-cloning limit (dot-dashed). Fits and data processing by Young Wook Cho.

storage efficiency model from Eqn. 15.5 to the measured storage efficiency curve at $\theta = 0°$, Fig. 17.2(c), we derive $\tau_r = 1.24$ ms, close to the estimate from our vapour temperature. Fixing τ_r by this measurement and assuming a temperature $T = 100$ μK, the model of Sec. 15.3 fits the measured data well for every measured probe control angle θ. The measured data is consistent with temperatures in the range 90–110 μK.

Because k_s, $k_c \gg k_s - k_s$ even small angles significantly reduce the storage lifetime. At $\theta > 0.06°$, $\tau_l < \tau_r$ and longitudinal motion is the dominant decoherence mechanism. At $\theta = 0.84°$ the storage lifetime is already less than 88 μs. However, when $\theta = 0°$ the longitudinal motion time constant is almost two orders of magnitude larger than the storage lifetime. So long as the memory operates with co-propagating beams the effect of longitudinal atom motion is negligible.

Taking a conservative telecom loss rate of 0.15 dB/km [69] and group velocity of $v_{fibre} = 2 \times 10^8$ km/s, a passive fibre delay line has a loss of 0.03 dB/μs. This is the dashed line in Fig. 17.2(c). Given that the purpose of a quantum repeater network is to extend the range of a lossy fibre network, surpassing the performance of a fibre loop delay line is an essential benchmark for quantum memories. The optical fibre delay line drops below the no-cloning limit (dot-dashed line in Fig. 17.2) after 100 μs. Our cold atom GEM beats this performance by a factor of six, surpassing the no-cloning limit up to 600 μs of storage. A comparison to other published ensemble memories is available in Ref. [3].

17.4 Storage lifetime limits

The coherence time is limited by the temperature of the cold-atom vapour and the waist of the signal beam. In principle, the temperature can be further reduced towards the Bose-Einstein condensate limit at temperatures $< 1 \ \mu$K. At a temperature of 1 μK the characteristic radial motion time constant is 11 ms. Alternatively, a larger ensemble supporting a signal beam with a larger waist would improve the storage time in proportion to w_0. The challenge, however, is to maintain the MOT density and temperature as the cross section increases. Beyond storage times of 3 ms, the gravitational acceleration of the atoms begins to matter. After 5 ms half of the vapour will have fallen out of a beam with $w_0 = 240 \ \mu$m. This problem is overcome with a vertical MOT; in this configuration the atoms fall together along the propagation axis and stay inside the interaction region [425].

Perhaps more importantly, the feasible storage time falls as the number of stored pulses increases. Each pulse being written and read requires a control field that scatters more of the coherence. This can be reduced only with higher depth and greater detuning. Furthermore, the magnetic field gradient is required to be on for every read and write operation. Magnetic field imperfections reduce the efficiency in proportion to the time the gradients are on. Our Helmholtz GEM coil configuration produces fields with a slight nonlinearity, the effect of which is analysed by my colleagues in [3, 332].

17.5 Summary

We have increased both the storage efficiency and storage time of our cold-atom GEM, achieving a recall efficiency of $\eta = 0.87 \pm 0.02$ and storage time of $\tau_s = 1$ ms. This is the first quantum memory to beat the no-cloning limit for storage times that surpass the performance of an ideal fibre delay line. A simple model of atomic motion in the vapour explains the measured coherence times well. The coherence time of the spin wave is largest when the angle between the probe and control, θ, is zero. However at this angle the control field filtering is insufficient to perform single-photon level measurements. To operate in the single-photon, long coherence time regime we require an alternative control filtering method. The control could be filtered spectrally by concatenated etalons, as in Ref. [385], although this is a technically demanding solution. A promising alternative is to use a narrow atomic absorption line, perhaps on one of the ^{85}Rb lines, in a hot vapour cell in combination with a larger single photon detuning to filter control field.

Improving the efficiency further requires higher optical depths so that the memory can operate at larger single photon detuning Δ. Subsequent work by Aaron Tranter has improved the optical depth with the same apparatus by machine learning [426], making still further improvements possible.

Heterodyne measurements of single-photon level coherent pulses have been used by my colleagues to perform a T-V characterization [427, 428] of noise and loss in this memory, and show that the memory is unambiguously in the no-cloning regime, even for storage times longer than 100 μs [3]. The noise performance has not been verified out to 600 μs of storage. This T-V measurement requires a slight probe-control angle to reduce control field noise at the detector, which is inconsistent with the operation of our longest-lived memory. The memory noise is due to shot-to-shot phase fluctuations caused by varying MOT parameters, much as in the dual memory of Chap. 16, and does not depend on storage time. Despite this unambiguous demonstration of efficient, long-lived quantum storage by GEM, no entangled state has yet been stored in this memory. However, new

photon sources operating near our GEM bandwidth promise imminent advances in this space [141].

Bibliography - High efficiency GEM

3. Y.-W. Cho, et al., Highly efficient optical quantum memory with long coherence time in cold atoms, *Optica* **3**, 100 (2016).

69. G. P. Agrawal, *Optical fibers* (John Wiley & Sons, Inc., Hoboken, 2011).

141. M. Rambach, et al., Sub-megahertz linewidth single photon source, *APL Photonics* **1**, 096101 (2016).

332. G. Campbell, Quantum memories and monolithic resonators, PhD thesis (The Australian National University, 2015).

385. D. J. Saunders, et al., Cavity-enhanced room-temperature broadband Raman memory, *Phys. Rev. Lett.* **116**, 090501 (2016).

395. M. Hosseini, et al., High efficiency coherent optical memory with warm rubidium vapour, *Nat. Commun.* **2**, 174 (2011).

396. M. Hosseini, et al., Unconditional room-temperature quantum memory, *Nat. Phys.* **7**, 794–798 (2011).

397. B. M. Sparkes, et al., Gradient echo memory in an ultra-high optical depth cold atomic ensemble, *New J. Phys.* **15**, 085027 (2013).

423. M. P. Hedges, et al., Efficient quantum memory for light., *Nature* **465**, 1052–6 (2010).

424. M. Hosseini, Quantum optical storage and processing using Raman gradient echo memory, PhD thesis (The Australian National University, 2012).

425. X.-H. Bao, et al., Efficient and long-lived quantum memory with cold atoms inside a ring cavity, *Nat. Phys.* **8**, 517–521 (2012).

426. A. D. Tranter, et al., Multiparameter optimisation of a magneto-optic trap using deep learning, *Nat. Commun.* **9**, 4360 (2018).

427. T. C. Ralph, and P. K. Lam, Teleportation with bright squeezed light, *Phys. Rev. Lett.* **81**, 5668–5671 (1998).

428. G. Hétet, et al., Characterization of electromagnetically-induced-transparency-based continuous-variable quantum memories, *Phys. Rev. A* **77**, 1–16 (2008).

Ensemble-light couplers: Conclusions and outlook

Those who have hitherto pursued science, have in general no very reasonable grounds of complaint; they knew, or should have known, that there was no demand for it, that it led to little honour, and to less profit.

– Charles Babbage, *Reflections* (1830)

As a quantum memory platform, cold-atom vapours have the advantage of long coherence times and high optical depths. We demonstrated a cold-atom gradient echo memory that matches the performance of the most efficient quantum memories, with efficiencies up to $87 \pm 2\%$, while simultaneously improving the memory lifetime to 1 ms. This quantum memory beats the 50% efficiency no-cloning limit after 600 μs of storage. An ideal optical fibre delay line, with conservative losses, loses 50% of the input field after only 100 μs. Until this work, no universal quantum memory had surpassed the performance of a fibre delay line in the no-cloning regime.

The storage lifetime of our memory is well predicted by numerical simulations, and by a simple model that accounts for atomic motion, control field scattering and magnetic field non-linearities. To further improve the coherence time for single-mode storage requires either colder atoms, or a larger MOT to support a larger signal beam. Conceivably, the coherence time of cold-atom gradient echo memory could reach 6 ms by doubling the size of the MOT and cooling the vapour to 10 μK. The peak efficiency is limited by control field scattering and magnetic field inhomogeneity. To reduce control field scattering requires still higher optical depths allowing large detunings, which have since been achieved.

Subsequent work has demonstrated that the memory is unambiguously quantum, but gradient echo memory is yet to demonstrate the storage of entangled qubits. This remains an important hurdle for GEM to clear before it can be used for any sort of quantum repeater. The best prospect for practical quantum memories are solid-state memories, with recent advances in rare-earth ion crystal engineering, a REIC GEM could likely surpass the performance of our cold-atom memory.

In addition to improving and characterizing the performance of our gradient echo memory, we have extended the protocol to store frequency qubits in a dual-rail configuration. We recalled dual-rail signals with 35% efficiency and 82% interference fringe visibility. The visibility is limited by frequency-dependent polarization rotation, for which we derived an analytical model that well-characterizes our memory. The same circular-configuration we used for our high efficiency GEM is rotation free, but the same-circular dual rail memory has asymmetric optical depths. The efficiency of each rail can be balanced by optical pumping, so that the same-circular dual-rail memory should be a high fidelity memory for frequency qubits with this preparation. The fidelity of such a memory is limited only by

ambient magnetic field noise, which produces 5-6° of phase fluctuation for both the dual and single rail memories.

We also introduced a stationary-light effect that can be generated in GEM using counter-propagating, two-colour control fields. This is a means of engineering the spatial distribution of bright fields in an atomic ensemble. These stationary light fields have since been produced and measured, matching the expectations of our model [348]. Such work extends the prospects of gradient-echo techniques not only as memories, but also as a platform for qubit operations and two-qubit gates.

In combination, these results show gradient echo quantum memories inching towards the benchmarks required for useful repeaters [351] for time-bin, polarization, frequency or spatial mode qubits, albeit in the laboratory and not the field. The gradient echo memory is approaching useful efficiencies, leveraging the enhanced interaction strength between photonic qubits and atom ensembles to not only store, but manipulate optical qubits. Using a cold, trapped vapour we limit the decoherence typical of atom ensembles and achieve storage lifetimes sufficient for short-range repeaters.

We've now considered atom-light couplers that operate by two very different mechanisms: tight-focussing by high-aperture optics and collective interactions with atomic ensembles. By addressing single atoms in trapped-ion registers, tight-focussing allows us to couple single-atom qubits almost noiselessly. Feasible coupling efficiencies, however, remain limited by the availability of precise, high aperture optics. In contrast, ensemble-based atom-light couplers are approaching unit efficiency, but compared to a single trapped atom the ensemble introduces new noise sources and decoherence mechanisms. Each approach lends itself to different middle-term applications; tight-focussing to networking trapped-ion quantum processors and atom-ensembles to repeaters for optical fibre QKD networks. Although there remains considerable work to be done, the capabilities demonstrated and prospects explored in this thesis light a clear path towards useful quantum devices.